

Nanoarchitecture: Morphogenesis and Applications of Nanostructured Materials

A thesis submitted for the degree of

Doctor of Philosophy

By

Katla Sai Krishna



**Chemistry and Physics of Materials Unit
Jawaharlal Nehru Centre for Advanced Scientific Research
(A Deemed University)
Bangalore, India
December 2010**

Dedicated

to

my family and teachers

DECLARATION

I hereby declare that this thesis entitled '**Nanoarchitecture: Morphogenesis and Applications of Nanostructured Materials**' is an authentic record of research work carried out by me under the supervision of Dr. M. Eswaramoorthy, at the Chemistry and Physics of Materials Unit, Jawaharlal Nehru Centre for Advanced Scientific Research, Bangalore, India and that it has not been submitted elsewhere for the award of any degree or diploma.

In keeping with the general practice of reporting scientific observations, due acknowledgements has been made whenever work described here has been based on the findings of other investigators. Any oversight due to error of judgement is regretted.

Katla Sai Krishna

CERTIFICATE

I hereby certify that the work described in this thesis entitled **‘Nanoarchitecture: Morphogenesis and Applications of Nanostructured Materials’** has been carried out by Katla Sai Krishna, under my supervision at the Chemistry and Physics of Materials Unit, Jawaharlal Nehru Centre for Advanced Scientific Research, Bangalore, India and that it has not been submitted elsewhere for the award of any degree or diploma.

Dr. Muthusamy Eswaramoorthy

(Research Supervisor)

ACKNOWLEDGEMENTS

Firstly, I would like to thank my research supervisor Dr. M. Eswaramoorthy, for his valuable guidance and constant support that has resulted in shaping up of this research work. Without his support, this thesis would not have seen the light.

I thank Prof. C. N. R. Rao, for his valuable suggestions from time to time during the course of my research. I also thank him for his kind encouragement and support extended to me in completing my research successfully.

I thank Prof. G. U. Kulkarni for his valuable suggestions and favours that he has been kind enough to extend to me on many an occasion.

I thank the present and past chairmen of CPMU for allowing me to use the facilities of the centre.

I thank Prof. G. U. Kulkarni, Prof. S. Balasubramanyam, Prof. A. Sundaresan of CPMU, Prof. Swapan K. Pati of TSU and Prof. T. N. Guru Row of SSCU (IISc), Prof. N. Ravishankar of MRC (IISc), for their courses.

I thank Prof. K. S. Narayan, Prof. N. Chandrabhas, Prof. S. M. Shivaprasad, Dr. A. Govindaraj, Dr. Tapas K. Maji of CPMU, Dr. Subi George of NCU, and Dr. N. S. Vidhyardhiraja of TSU for useful discussions on various topics. I also thank Prof. Umesh Waghmare of TSU, for extending his support and guidance as hostel warden during my tenure as a student representative.

I am indebted to various technical staff especially, Mrs. N. R. Selvi (FESEM) for spending her valuable time and patience in capturing attractive microscope images of my research works. Mrs. Usha (TEM), Mr. Basavaraj (SEM), Mr. Vasu (Spectroscopy), Mr. Anil (XRD) and Mr. Srinath, Mr. Srinivas and Mr. Srinivasa Rao (technical assistance). I also thank Mr. Arokianathan, Mr. Moorthy and Mr. Sunil for their assistance.

I thank the JNCASR Library, Complab, Hostel, Academics and Administration staff for providing and maintaining the various facilities that have helped me immensely. Special thanks are due to IISc library, SERC and National Nanoscience Initiative from IISc for their facilities. I am thankful to Prof. Vikram Jayaram (MSE) and Mr. Amit for their help in utilizing the nanocentre facility at IISc.

I thank my collaborators Prof. Reji Philip, Dr. C. S. Suchand Sandeep, of RRI for extending their help in carrying out experiments in their lab.

I have been fortunate to have excellent lab mates with whom i had a wonderful time; my heartfelt thanks to Mr. K.K.R. Datta, Mr. Kalyan, Mr. Piyush, Mr. Pawan, Ms. Josena, Mr. Amritroop for their cooperation and help. I also thank all the visiting scientists, summer research fellows (SRFs), POCE students especially Dr. Vivekanandan and Ms. Uzma for their contributions in my research work.

Special thanks are due to Dr. A. Gomathi, Ms. Neenu, Dr. V. P. Bhat for Raman measurements, Ms. Surbhi Dhar for antibacterial studies, Dr. G.V. Pavan Kumar for SERS measurements, Mr. Chandramohan (Veeco) for AFM imaging and Mr. S. P. Pal (Quantachrome) for surface area instrumentation.

I thank Gurunath (Toulouse), Madhu (Colorado), Rajashekarayya (Bristol), Ujjal Goutam (Japan) for sending me papers for which i do not have electronic access.

I thank all my friends who made my stay at JNC comfortable with their cordial ambience, specially gomathi, claudy, urmi, nitesh, jayaram, sundaraya, matte, ajmala, ankita, shipra, pranab, rakesh, leela, subbu, sudip, prakash, arif, bharath, himadri, malik, anil, mighfar, nisha, abhishek, anupama, basanth, neenu, bhat, jyoti, barun, sandeep, datta, radha, narendra, ritu, sachi, monojit, vini, anshuman, avinash, mohit, venkat, manoj, jithesh, sathish,

I thank my past friends and batchmates (Drs.) dinesh, vivek, thiru, gopal, arun, manu, sairam, anand, dhriti, kalyani, vengadesh, reji, ved, neena, vijay, bhuvana

I thank gopal, surbhi, dhriti, kalyan, manu, srini, Prof. VKS for the joyous moments that we spent playing volley ball. I also thank Umesh (gym master) for his assistance in physical training.

I thank all my teachers from Jawahar Navodaya Vidyalaya and Sri Sathya Sai Institute of Higher Learning for their exceptional teaching that has inspired me for choosing science as my career.

I am especially grateful to my parents and my family for all their love, affection, support and strength.

For all my humble achievements till date, I am thankful to Bhagawan Sri Sathya Sai Baba, for showering his choicest blessings on me always.

PREFACE

This thesis presents creation of diverse morphologies of nanomaterials utilizing novel synthetic approaches and studies their applications. Making of nanoscale shapes such as rings, bowls, sponges, drums, pencils, and pillared arrays were studied for the thesis work.

Chapter 1 of the thesis explains the importance of shape and size at nanoscale focusing on the synthesis, shape control of nanomaterials and properties emerging at nanoscale. **Chapter 2** investigates the formation of nanorings of amorphous carbon through evaporation-induced self-assembly of carbon nanofibers that are generated within mesoporous silica. **Chapter 3** deals with formation of bowls (sub-micron size) by three different approaches viz., (a) Temperature-induced self-assembly and growth of ZnO nanoparticles during calcination of zinc nitrate-polymer composite film (b) Spontaneous formation of ordered mesoscopic MnSO₄ salt bowls by gas-bubble templating (c) Template-based synthesis of gold bowls using colloidal silica spheres. **Chapter 4** explains generic and simple route to make high surface area metal sponges and their applications in broadband optical limiting. **Chapter 5** presents synthesis of drums and pencil-shaped ZnO nanostructures and their use as templates to make silica, gold and carbon analogues, which are otherwise difficult to make by the conventional methods. **Chapter 6** describes the synthesis of nanopillar arrays of amorphous carbon nitride and their applications for nanoparticle immobilization and surface functionalization.

CONTENTS

DECLARATION	I
CERTIFICATE.....	II
ACKNOWLEDGEMENTS	III
PREFACE	VI
CONTENTS.....	VII
LIST OF ABBREVIATIONS.....	XII

1. Importance of shape and size at nanoscale

1.1 Introduction.....	2
1.2 Synthesis of nanomaterials with shape control.....	3
1.3 Properties induced by shape and size.....	17
1.3.1 Electronic structure.....	17
1.3.2 Optical properties.....	21
1.3.3 Catalytic properties.....	24
1.4 Conclusions.....	26
1.5 References.....	27

2. Rings: Novel synthesis of carbon nanorings and their characterization

Summary.....	34
2.1 Introduction.....	35
2.1.1 Importance of nanoring morphology.....	37

2.2 Synthetic methods of forming nanoring structures.....	42
2.3 Scope of the present investigation.....	46
2.4 Experimental section.....	46
2.4.1 Synthetic procedure for carbon nanorings.....	46
2.4.2 Sample characterization.....	47
2.5 Results and discussion.....	47
2.6 Conclusions.....	54
2.7 References.....	55

3. **Bowls:**

Part 1: Temperature induced self-assembly and growth of ZnO nanoparticles into zeptolitre bowls and troughs

Summary.....	60
3.1 Introduction.....	61
3.2 Scope of present investigation.....	61
3.3 Experimental section.....	62
3.3.1 Synthetic procedure for ZnO bowls.....	62
3.3.2 Synthetic procedure for gold bowls and silica nanorings.....	62
using ZnO bowls and nanorings as templates	
3.3.3 Sample characterization.....	63
3.4 Results and discussion.....	64
3.5 Conclusions.....	81
3.6 References.....	81

Part 2: Spontaneous formation of ordered manganous sulphate salt

bowls

Summary.....	85
3.1 Introduction.....	86
3.2 Scope of present investigation.....	87
3.3 Experimental section.....	88
3.3.1 Synthetic procedure for MnSO ₄ bowls.....	88
3.3.2 Synthetic procedure for gold bowls using MnSO ₄ bowls.....	88
as water soluble template	
3.3.3 Sample characterization.....	89
3.4 Results and discussion.....	89
3.5 Conclusions.....	105
3.6 References.....	106

Part 3: Large-scale synthesis of ordered gold bowl arrays using colloidal silica spheres as template

Summary.....	109
3.1 Introduction.....	110
3.2 Scope of present investigation.....	112
3.3 Experimental section.....	113
3.3.1 Synthetic procedure for colloidal silica spheres.....	113
3.3.2 Synthetic procedure for ordered Au bowl arrays.....	113
3.4 Results and discussion.....	114
3.5 Conclusions.....	120
3.6 References.....	121

4. Sponges: A generic and rapid synthesis of high surface area nanoporous noble metals showing broadband nonlinear optical response

Summary.....	124
4.1 Introduction.....	125
4.2 Scope of present investigation.....	126
4.3 Experimental section.....	127
4.3.1 Synthetic procedure for sponges.....	127
4.3.2 Z-scan experiment.....	128
4.3.3 Surface enhanced Raman scattering.....	130
4.3.4 Antibacterial studies.....	131
4.3.5 Sample characterization.....	131
4.4 Results and discussion.....	132
4.5 Conclusions.....	157
4.6 References.....	157

5. Drums & Pencils: ZnO as a versatile template to obtain unusual morphologies of silica, gold and carbon nanostructures

Summary.....	163
5.1 Introduction.....	164
5.2 Scope of present investigation.....	165
5.3 Experimental section.....	165
5.3.1 Synthetic procedure for ZnO drums.....	165
5.3.2 Synthetic procedure for ZnO pencils.....	166
5.3.3 Silica-coating of ZnO structures.....	167

5.3.4 Gold-coating of ZnO structures.....	167
5.3.5 Carbon-coating of ZnO structures.....	168
5.3.6 SiO ₂ @Fe ₂ O ₃ hollow tubes.....	168
5.3.7 Sample characterization.....	169
5.4 Results and discussion.....	169
5.5 Conclusions.....	180
5.6 References.....	181
6. <u>Pillar arrays</u>: Synthesis, characterization and applications of nanopillar arrays of amorphous carbon nitride	
Summary.....	184
6.1 Introduction.....	185
6.2 Scope of present investigation.....	186
6.3 Experimental section.....	186
6.3.1 Synthetic procedure for nanopillar arrays.....	186
6.3.2 Sample characterization.....	187
6.4 Results and discussion.....	187
6.5 Conclusions.....	199
6.6 References.....	199
List of publications.....	202

LIST OF ABBREVIATIONS

AAO – Anodic alumina oxide

ALD- Atomic layer deposition

BET – Brunauer Emmett Teller

CCD – Charge coupled device

CNPs – Carbon nitride nanopillars

CNT – Carbon nanotubes

CTAB – Cetyltrimethylammonium bromide

DCC - 1, 3-Dicyclohexylcarbodiimide

DMPG- Dimyristoyl-*L*- α -phosphatidyl-*DL*-glycerol

DNA – Deoxyribonucleic acid

EELS – Electron energy loss spectroscopy

ED – Electron diffraction

EDX/EDAX – Energy dispersive X-ray (analysis)

FESEM – Field emission scanning electron microscope

FTIR – Fourier transform infrared spectroscopy

HREM – High resolution transmission electron microscopy

MOCVD – Metal organic chemical vapour deposition

NaAOT - Sodium bis-(2-ethylhexyl)-sulfosuccinate

NLO – Non-linear optics

PXRD – Powder X-ray diffraction

P123 – Pluronic 123 [(polyethelene oxide)₂₀-(polypropelene oxide)₇₀-
(polyethelene oxide)₂₀]

PL – Photoluminescence

PVP – Polyvinylpyrrolidone

PVA – Polyvinyl alcohol

PS – Polystyrene

PEG – Polyethylene glycol

SEM – Scanning electron microscope

STEM – Scanning transmission electron microscope

SBA – 15 – Santa Barbara Amorphous – 15

SDS - Sodium dodecylsulfonate

SWNT – Single-walled carbon nanotubes

SERS – Surface enhanced Raman spectroscopy

TEM – Transmission electron microscope

TGA – Thermogravimetric analysis

TEOS – Tetraethylorthosilicate

TOPO – Tetraoctylphosphonium oxide

TTAB - Tetradecyltrimethylammonium bromide

UV-Vis – Ultraviolet and visible

XPS – X-ray photoelectron spectroscopy

XRD – X-ray diffraction

List of publications

From Thesis:

1. **Katla Sai Krishna** and M. Eswaramoorthy, Novel synthesis of carbon nanorings and their characterization, *Chem. Phys. Lett.*, 433, 327 - 330 (2007).
2. **Katla Sai Krishna**, Uzma Mansoori, N. R. Selvi and M. Eswaramoorthy, Form emerges from formless entities: Temperature-induced self-assembly and growth of ZnO nanoparticles into zeptoliter bowls and troughs, *Angew. Chem. Int. Ed.*, 46, 5962 - 5965 (2007).
3. **Katla Sai Krishna**, C. S. Suchand Sandeep, Reji Philip and M. Eswaramoorthy, Mixing does the magic: A rapid synthesis of high surface area noble metal nanosponges showing broadband nonlinear optical response, *ACS Nano*, 4, 2681 - 2688 (2010).
4. **Katla Sai Krishna**, G. Vivekanandan, D. Ravinder and M. Eswaramoorthy, ZnO: A versatile template to obtain unusual morphologies of silica, gold and carbon nanostructures, *Chem. Comm.*, 46, 2989–2991 (2010).
5. **Katla Sai Krishna** and M. Eswaramoorthy, A Book Chapter on 'Nanorings', *CRC Handbook of Nanophysics*, Taylor & Francis Group Publishers (Oct 2010).
6. **Katla Sai Krishna** and M. Eswaramoorthy, Shaping up: Spontaneous formation of ordered mesoscopic salt bowls (Submitted).
7. **Katla Sai Krishna** and M. Eswaramoorthy, Nanopillar arrays of amorphous carbon nitride (Submitted).
8. **Katla Sai Krishna** and M. Eswaramoorthy, Large-scale synthesis of gold nanobowl arrays using colloidal silica spheres as template (Manuscript under preparation).

Other publications:

1. Anupama Ghosh, K. S. Subrahmanyam, **Katla Sai Krishna**, Sudipta Dutta, A. Govindaraj, Swapan K. Pati and C. N. R. Rao, Uptake of H₂ and CO₂ by graphene, *J. Phys. Chem. C*, 112, 15704 (2008).
2. K. Jayaramulu, **Katla Sai Krishna**, M. Eswaramoorthy and Tapas K. Maji, Nanocage structure of squarate based metal-organic frameworks (Submitted).

Patent:

Katla Sai Krishna and M. Eswaramoorthy, International patent (PCT) under process for 'Template free, simple and scalable synthesis of high surface area metal (Ag, Au, Pt, Pd and Cu/Cu₂O) nanosponges/nanostructures'.

Chapter 1

Importance of Shape and Size at Nanoscale

1.1 Introduction

Nanomaterials are materials with at least one of their dimension in the nanometre ($1 \text{ nm} = 10^{-9} \text{ m}$) range and *nanoscale* is usually defined as smaller than one tenth of a micrometer, though this term is sometimes used for materials smaller than one micrometer. Figure 1 gives an illustration of objects correlating to different sizes (1).

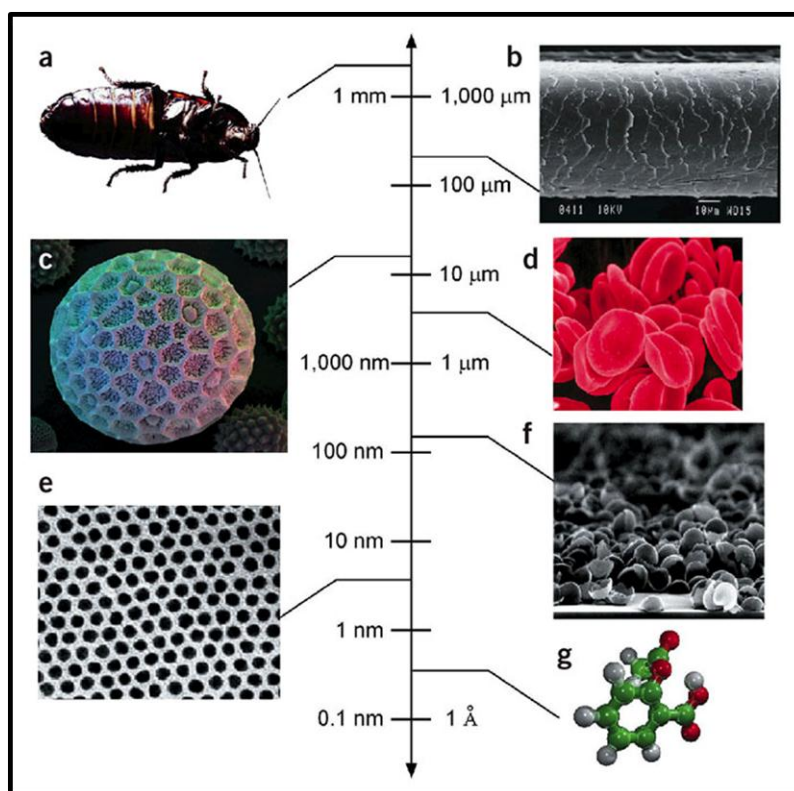


Figure 1: Sizes of representative objects at different length scales (a) A cockroach (b) A human hair (c) *Polygonum* pollen grain (d) Red blood cells (e) Cobalt nanocrystal superlattice (f) An aggregate of half-shells of palladium (g) Aspirin molecule (ref 1).

Nanomaterials are of immense scientific interest as they effectively bridge the gap between bulk materials and atomic or molecular structures. Bulk materials have constant physical properties regardless of its size, but at the nanoscale, this is often not the case. However, at nanoregime, many of the properties (electronic, optical, thermodynamic, magnetic and mechanical) of metals and semiconductors are in between bulk and atoms (2-4). For example, bending of bulk copper wires/ribbons occurs with movement of copper atoms/clusters at about 50 nm scale. Copper nanoparticles smaller than 50 nm are considered super hard materials that do not exhibit the same malleability and ductility as bulk copper (5). The change in properties is not always desirable. Ferroelectric materials smaller than 10 nm can switch their magnetization direction using room temperature thermal energy, thus making them useless for memory storage (6). Decrease in melting temperature has been observed with decreasing nanocrystal size in the case of Au, Sn, Pb and CdS nanoparticles (7-9). Sintering is also possible for nanoparticles at lower temperatures and over shorter durations than for larger particles (5).

1.2 Synthesis of nanomaterials with shape control

In the last few years, researchers have been extensively studying efficient synthetic methods to obtain nanostructures of different shapes and sizes (2, 10-12). Synthesis of nanomaterials broadly falls into either a top down method, where

material is removed from the bulk, leaving only the needed nanostructures, or a bottom up method, where the atoms are assembled to generate nanostructures.

Table 1 gives various synthetic methods normally used to produce nanostructures through top-down and bottom-up approaches (10):

Top-down methods	
Method	Description
Ball milling	Production of nanoparticles by mechanical attrition to produce grain size < 5 nm. High energy ball milling uses steel balls to transfer kinetic energy by impact to the sample.
Atomization	Conversion of a liquid into aerosol particles by forcing through a nozzle at high pressure.
Mechanical machining, polishing, grinding and ultra microtome	It is also known as conventional machining, resolution limit is 5 μm . Other techniques analogous to mechanical machining perform the same function with laser beams, focused ion beams, and plasmas. Mechanical grinders/cutters are used to thin TEM samples. These include dimple grinders, diamond saws, ultrasonic disc cutters, and ultramicrotones (<100 nm).
Electrospinning	A high voltage is applied to a polymer melt solution to induce charging. Polymer solutions at room temperature are also used routinely. At an acquired threshold, an electrospun fluid jet emerges from a needle tip to form a taylor cone. The substrate, held at high a lower potential, is covered by the charged polymeric solution.
Evaporation	Evaporation of solid metal or other material samples to form thin films. It is usually performed under high vacuum (10^{-6} Torr). Heat is produced by electrical resistance. If nanoclusters are formed during the evaporation process, it

	is top-down. If atoms or molecules are formed during the evaporation process that recombines to form thin layer without any chemical reaction, it is a cross over technique.
Thermolysis/ Pyrolysis	Decomposition of bulk solids at high temperature (top-down). These terms are also applied to the decomposition of molecules. Nanomaterials are also formed after decomposition in a bottom-up way by agglomeration. Because of this crossover, it is hard to place pyrolysis/thermolysis into one category or the other. The most common sense of the terms implies that molecules are simply converted into other molecules. In this sense, pyrolysis and thermolysis are neither top-down nor bottom-up methods. In such reactions (like decomposition), chemical change does occur.
Combustion	Chemical combustion is top-down process in which there is chemical conversion of bulk organic materials + impurities into molecules like CO ₂ , H ₂ O and nanomaterials such as ash with micron to submicron dimensions. The process of combustion involves oxygen.
Carbonization	Heating the samples at high temperatures in the absence of oxygen thus enriching the carbon content in them.
Arc discharge	High energy electrical discharge directed on a graphite target (anode) + catalyst to produce single-walled carbon nanotubes that accumulates on the cathode.
Laser ablation	High-intensity laser beam directed on a graphite target + catalyst to produce SWNTs. The process is considered to be thermal and high-energy method.
RF sputtering	Ion bombardment of metal, oxide or other material targets to form thin film coatings. Usually performed under moderate vacuum (10 ⁻³ torr). Atoms, molecules, and clusters are formed by this process

Photolithography	Light is used to transfer patterns onto light-sensitive photoresist substrates. Photo lithography is primarily used in the manufacture of integrated circuits and MEMS devices. The wavelength range of optical lithography techniques ranges from the visible to near ultraviolet (ca. 300 nm). The resolution of photolithography techniques is ~100 nm
Electron beam lithography (EBL)	An electron beam source is used instead of light to generate patterns. Although e-beams can be generated below few nanometers, the practical resolution is determined by the electron scattering at the photoresist material. Just like in SEM, electron line width is < 20 nm and electron energy : 10 - 50 keV
Bottom-up methods	
Method	Description
Molecular-self assembly	This generic process is supported in liquid media. From some perspectives, supramolecular chemistry is subset of molecular self-assembly. Almost all molecular self-assembly takes place in liquids. This liquid plays role in supporting intramolecular interactions and intermediate metastable species
Nucleation	Precursor chemicals in a supersaturated state combine by self-assembly or chemical reaction to form seed particles. Thermodynamics drives a nucleation process that forms nanoparticles. The nucleation process depends on prevailing conditions of pH, temperature, ionic strength, and time.
Sol-gel process	Sol-gel methods are irreversible chemical reactions of homogenous solutions that result in a three-dimensional polymer. Sol-gel methods yield nanostructured materials of high purity and uniform nanostructures formed at lower

	temperatures. Negative replicas of colloidal hierarchical structures, upon drying, yield aerogels or xerogels. Such gels can be back-filled to produce nanocomposites or hybrid materials.
Reduction of metal salts	Noble metal clusters and colloids are formed by reduction of metal salts like HAuCl_4 and H_2PtCl_6 . Common reducing agents come in the form of organic salts like sodium citrate. By means of phase transfer reactions (consisting of an interface between two immiscible liquids), metal clusters and colloids are stabilized by the addition of organic ligands. For example, phosphine or thiols are adsorbed onto gold-55 to produce a stable cluster.
Single-crystal growth	Nucleation process to form single crystals in liquid media.
Electrodeposition/ Electroplating	Direct deposition of metals from metal salt solutions to form thin layers or films on a solid conducting substrate. It is an electrolytic process that forms thin metal films on the cathode of the cell.
Electroless deposition	Autocatalytic deposition of metals without electrical assistance.
Liquid template synthesis	Liquid templates (micelles and reverse micelles) are used to make nanoparticles from bottom up.
Solid template synthesis	Provides a solid template substrate for electrochemical, chemical, polymerization and other liquid phase reactions. Most methods are accomplished in a liquid medium. Final nanomaterial size, shape and orientation predetermined by template parameters.
Chemical vapour deposition (CVD)	CVD involves the formation of nanomaterials from the gas phase, usually at elevated temperatures, onto a solid substrate or catalyst. For example, carbon nanotubes are formed by catalytic decomposition of carbon feedstock gas in inert carrier gas at elevated temperature.

Atomic layer deposition (ALD)	ALD is an incredibly sequential surface chemistry layer deposition method to form thin films on conductors, insulators and ceramics. The layer formed by ALD conforms to surface topography. Precursor materials are kept separate until required. Atomic scale control pinhole-free layers are formed. Layer thickness: 1 - 500 nm.
Metal oxide (MOCVD). Organometallic vapour phase epitaxy (OMVPE)	Chemical characteristics of precursor materials utilize reactive gas-phase-organometallic compounds that decompose to form nanometer-scale thin films or nanoparticles.
Molecular beam epitaxy (MBE)	MBE is thin film growth process conducted under high vacuum. A heated Knudsen cell or effusion cell is used to introduce reactants to molecular beams. MBE is able to deposit one atom layer per application.
Nanopore template methods (shadow mask evaporation)	Use of porous alumina membrane templates to form arrays of nanoparticles. The size of the nanoparticles can be controlled from 5 nm to > 200 nm. The space between nanoparticles can also be adjusted. Nanoparticle aspects are adjusted by the height of the mask, pore size and the direction of evaporation

Table 1: Different methods of top-down and bottom-up approaches (ref 10)

Nanostructures of various materials have been prepared using several of these methods. A brief overview of some of the nanostructures and their synthesis methods are given below:

Gold: There are many synthetic methods for controlling the shape of Au nanocrystals. In general, the selection of reductant, reaction conditions, and stabilizer are critical to forming a particular shape. Polyhedral shapes of Au nanocrystals such as octahedrons, truncated tetrahedrons, icosahedrons, decahedrons and Au nanocubes are generally formed using polyol process (13). Au hexagonal and triangular nanoplates/prisms were produced at room temperature by using mild reductants such as phenylenediamine (14), lemongrass (*Cymbopogon flexuosus*) extract (15), PVP (16), or aspartate (17). Anionic phospholipid dimyristoyl-*L*- α -phosphatidyl-*DL*-glycerol (DMPG) has also been shown to promote the formation of hexagonal Au nanoplates (18). Au nanobelts can be prepared by reducing HAuCl_4 with ascorbic acid in a mixed surfactant system containing sodium dodecylsulfonate (SDS) and CTAB (19). Gold nanorods were formed from micelles of cetyltrimethylammonium bromide (CTAB) using seed mediated growth (20, 21). Tadpole-shaped particles of gold have been synthesized through the reduction of AuCl_4^- in the presence of sodium dodecylsulfonate (SDS) (22). Seed mediated growth has been used to obtain Au monopods, multipods, flower-like, dog bone, dumb-bell and bipyramid structures (23-28). Figure 2 shows some of the shapes obtained for Au by using different techniques.

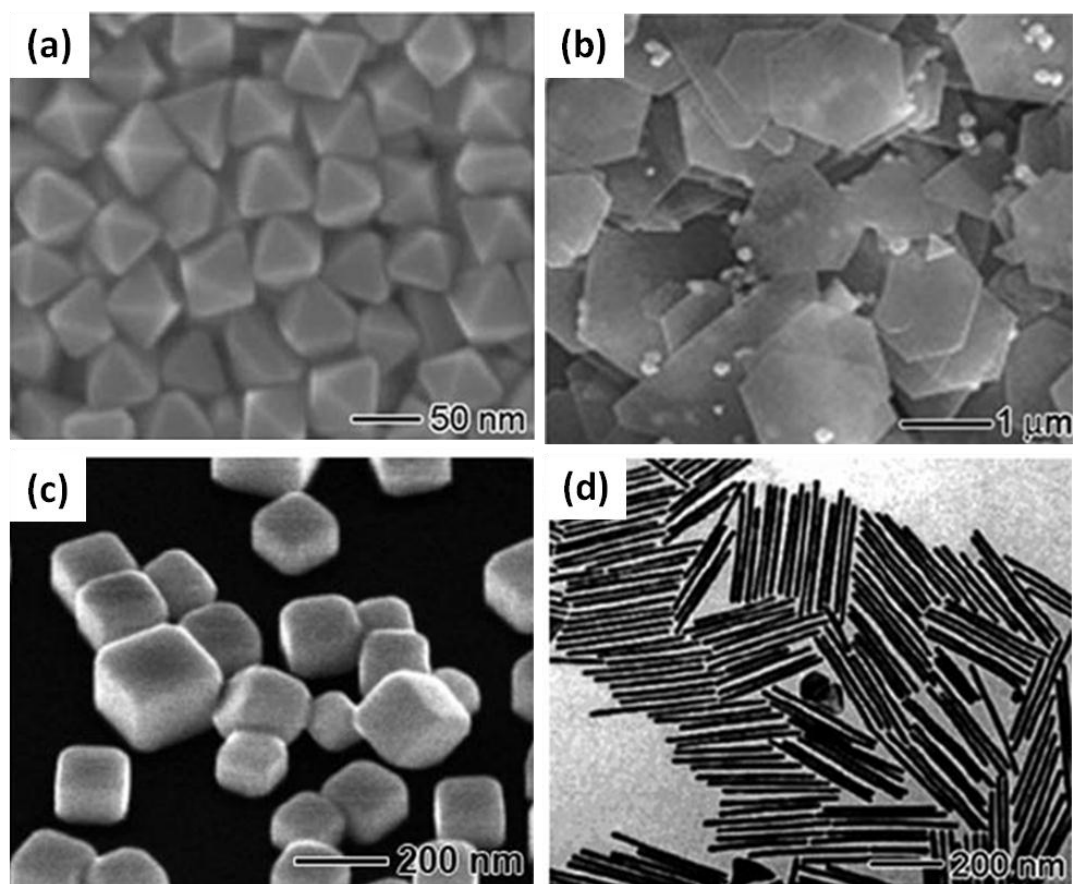


Figure 2: Electron microscopy images of Au nanocrystals: (a) octahedrons prepared with PVP as a capping agent in polyethylene glycol (b) hexagonal nanoplates prepared with ortho-phenylenediamine as a reductant (c) nanocubes prepared in 1, 5-pentanediol in the presence of Ag^+ ions with PVP as a capping agent (d) five-fold twinned nanorods prepared by a seeding process with CTAB as a capping agent (ref 11).

Silver: Different shapes such as icosahedra, decahedra, cuboctahedra and nanocube of Ag were formed using polyol process using PVP as a capping agent (29). Seed mediated growth was used to form 1-D Ag nanostructures such as, nanorods and nanowires (30). Polyol synthesis is also used to form nanorods and nanowires with

pentagonal cross-section (31). Ag nanoplates were prepared by using -OH terminated PVP, ascorbic acid, or glycylglycine. (32). CTAB micelles were used in the synthesis of triangular and circular nanodisks of silver (33, 34). Silver nanodisks have also been produced using reverse micelles of sodium bis (2-ethylhexyl) sulfosuccinate (AOT) in an octylamine–water bilayer (35, 36). Figure 3 shows some of the shapes obtained for Ag by using different techniques.

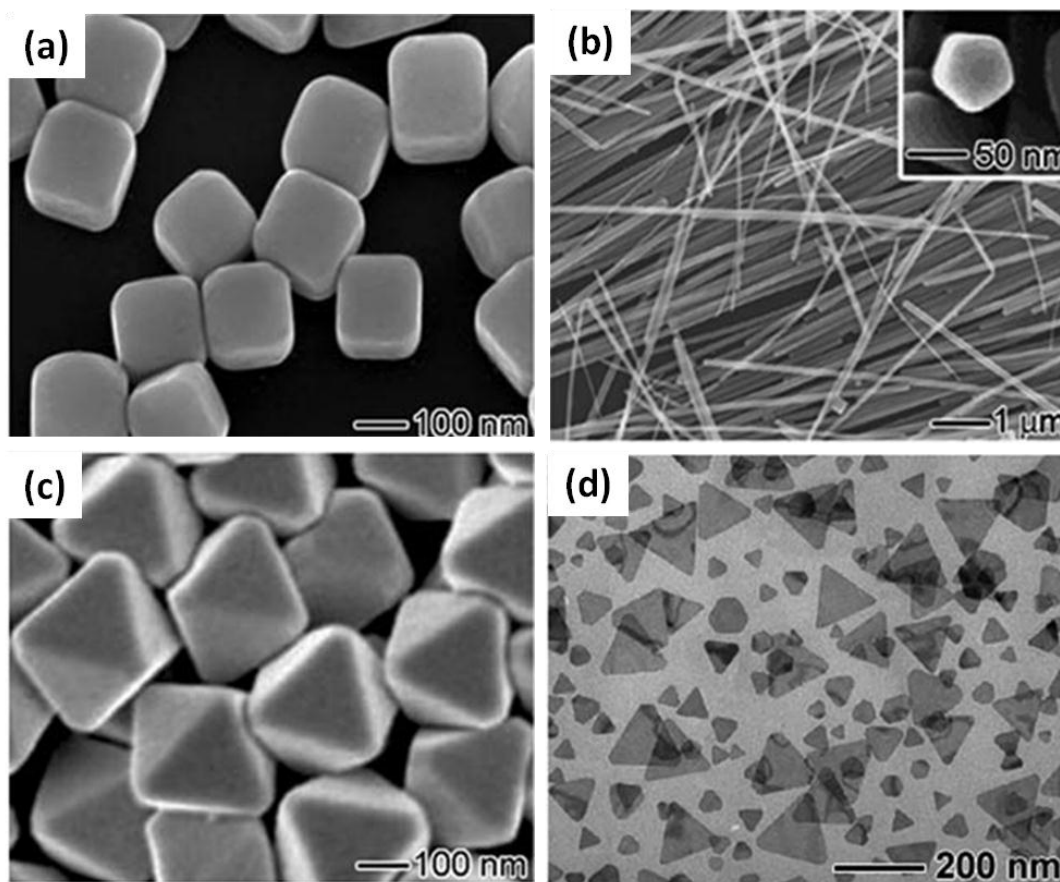


Figure 3: Electron microscopy images of Ag nanocrystals: (a) nanocubes prepared in ethylene glycol with PVP as a capping agent (b) five-fold twinned nanorods prepared in ethylene glycol with PVP as a capping agent (c) octahedrons prepared in 1,5-pentanediol in the presence of PVP and Cu^{2+} ions (d) nanoplates prepared by light-induced conversion of Ag nanospheres (ref 11)

Platinum: Pt cubes, tetrahedrons, and truncated octahedrons were formed using a solution based approach (37). Pt nanorods and nanowires were synthesized using a γ -irradiation method (38) and a Pd-seeding process (39) respectively.

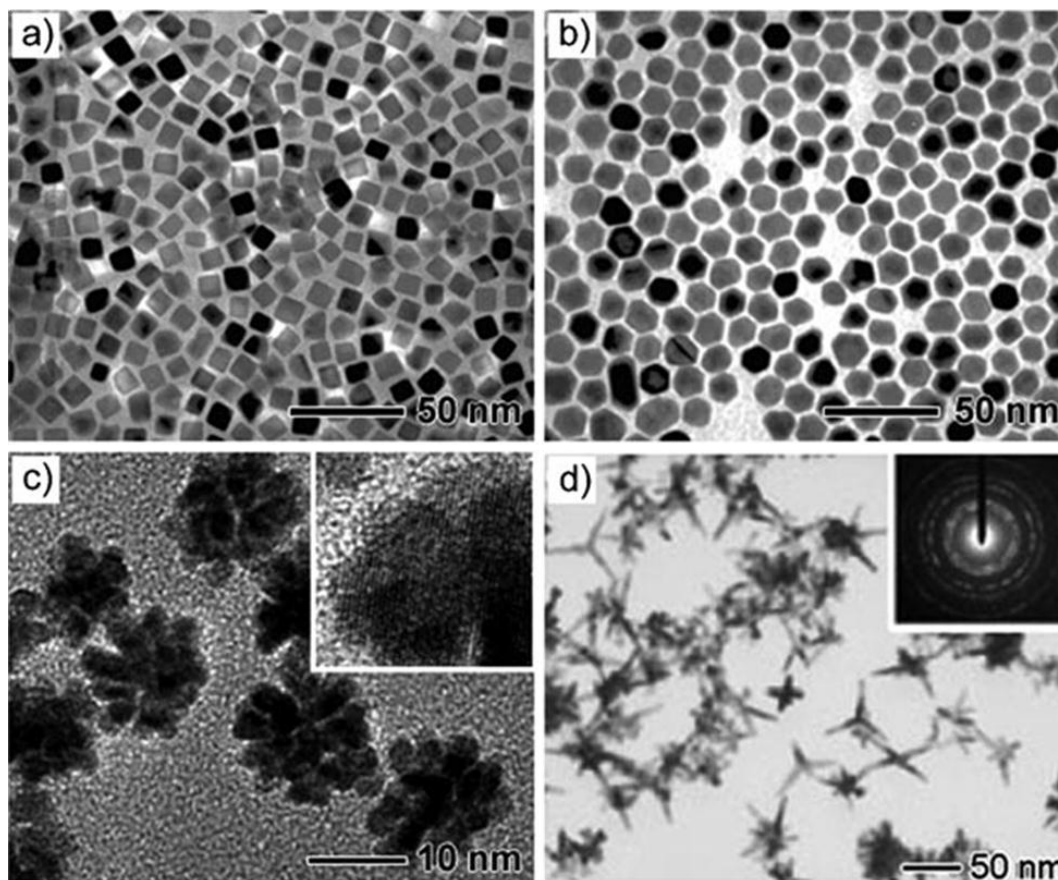


Figure 4: Electron microscopy images of Pt nanocrystals with different shapes: (a) nanocubes prepared in the presence of tetradecyltrimethylammonium bromide (TTAB) with a high concentration of NaBH_4 (b) cuboctahedrons prepared in the presence of TTAB with a low concentration of NaBH_4 (c) nanodendrites prepared with ascorbic acid as a reducing agent (d) tetrapods prepared by a polyol process using Fe (III) species to reduce the number of seeds at the nucleation stage (ref 11)

Single-crystal star-like Pt nanostructures were prepared from tetrahedral Pt seeds (40). Interconnected Pt nanowires were synthesized in a two-phase water–chloroform system containing CTAB (41). Pt nanoplates were formed by using Pd nanoplates as seeds for heteroepitaxial deposition of Pt (42). Mono-, bi- and tripods of Pt from Pt seeds were produced from the reduction of Pt(acac)₂ in the presence of adamantanecarboxylic acid, hexadecylamine, and various 1,2-alkanediols (43). Figure 4 shows some of the shapes obtained for Pt by using different techniques.

Palladium: Polyhedral shapes of Pd nanocrystals are generally formed using the polyol process (44). Pd nanocubes with edge lengths up to 50 nm were prepared by adding Fe (III) species to a polyol synthesis at 90 °C (45). Pd nanobars enclosed by {100} facets with a square cross-section were synthesized from a reaction containing ethylene glycol, water, PVP, and KBr (46). Pd nanoneedles with a rectangular cross-section were prepared in water with ascorbic acid and sodium citrate as co reductants and CTAB as a capping agent (47). Triangular nanoplates of Pd were prepared using ethylene glycol in the presence of FeCl₃ and HCl (48). Hexagonal Pd nanoplates in high yields were generated through slow decomposition of Pd–octanedionate complex in the presence of various tetraalkylammonium salts (49). Figure 5 shows some of the shapes obtained for Pd by using different techniques.

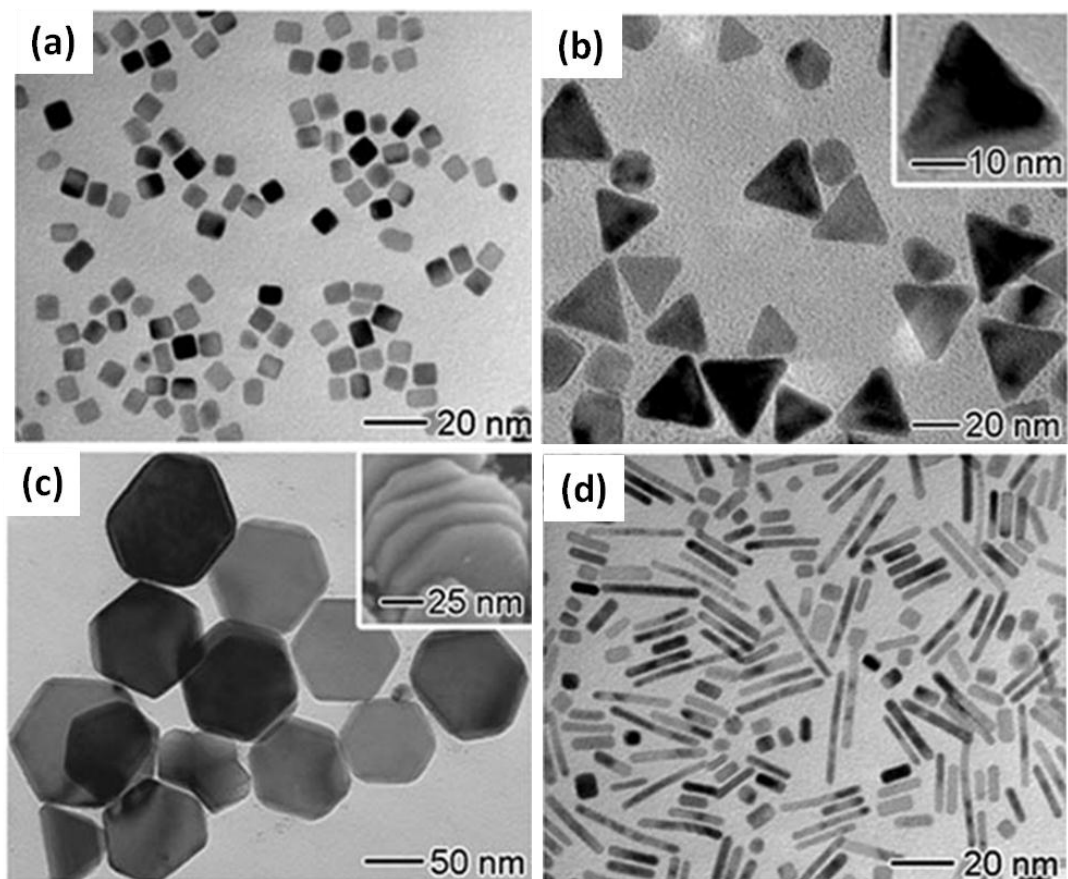













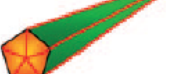


Figure 5: Electron microscopy images of Pd nanocrystals: (a) nanocubes prepared with PVP as a reductant in water and in the presence of KBr (b) triangular nanoplates prepared in ethylene glycol and in the presence of FeCl_3 and HCl (c) hexagonal nanoplates prepared with PVP as a reductant in water (d) nanorods prepared in a mixture of 72.7% ethylene glycol and 27.3% water, in the presence of KBr (ref 11)

Copper: Cu nanocubes of 100 ± 25 nm in edge length were formed from a modified polyol process (50). Synthesis of five-fold twinned nanorods were also formed by polyol reduction where 1,2-hexadecanediol was used to reduce $\text{Cu}(\text{acac})_2$ at temperatures higher than 190°C in octyl ether using oleic acid and oleyl amine as

capping agents (51). Pentagonal Cu nanowires were grown on solid supports using an MOCVD method (52). Cu nanoplates were prepared by reduction of $\text{Cu}(\text{CH}_3\text{CO}_2)_2$ by hydrazine in acetonitrile at 80 °C under an inert atmosphere (53).

Other metals: Iron nanocubes of ~ 7 nm in size were prepared through the decomposition of $[\text{Fe}\{\text{N}(\text{SiMe}_3)_2\}_2]$ with hexadecylamine (HDA) and oleic acid or hexadecylammonium chloride (HDAC) as capping agents in mesitylene at 150 °C (54). Synthesis of Fe nanowires through anisotropic growth was reported by reduction of Fe-containing salts in the presence of 1, 10-phenanthroline as a coordinating ligand (55). Co nanodisks were prepared through the rapid decomposition of $[\text{Co}_2(\text{CO})_8]$ in the presence of linear alkylamines (56). Hexagonal and triangular Ni nanoplates were prepared by the reduction of Ni-formate (57).

Table 2 summarizes some of the faceted morphologies obtained for the metal nanoparticles.

Structures	Shapes	Schematic drawings	Metals
single-crystal	perfect/truncated cube ^[a]		Pd, Ag, Au, Pt, Cu, Rh, Bi, Fe
	perfect/truncated octahedron ^[a]		Pd, Ag, Au, Pt
	perfect/truncated tetrahedron ^[a]		Ag, Au, Pt, Rh
	rectangular bar		Pd, Ag, Pt
	octagonal rod		Pd, Au, Fe, Co, Ni
singly twinned	rectangular or octagonal wire		Pb, In, Sn, Sb, Fe, Co
	right bipyramid		Pd, Ag
multiply twinned	beam		Ag
	decahedron ^[a]		Pd, Ag, Au
	icosahedron ^[a]		Pd, Au
	five-fold twinned pentagonal rod		Pd, Ag, Au, Cu
	five-fold twinned pentagonal wire		Ag, Au, Cu
	triangular/hexagonal plate		Pd, Ag, Au, Cu, Pb, Bi, Co, Ni
	disc		Sn, Co

[a] Platonic solid.

Table 2: Various shapes formed by metal nanocrystals (ref 11)

Metal oxides/chalcogenides/pnictides: Like metals, metal oxides, chalcogenides and pnictides were also synthesized with different morphologies at nanoscale by various techniques. For example, interesting nanostructures of ZnO such as belts, rings, combs, springs, helices, bows, propellers and cages were reported by Wang and co-workers using a vapour-liquid-solid method (58) (Figure 6) .

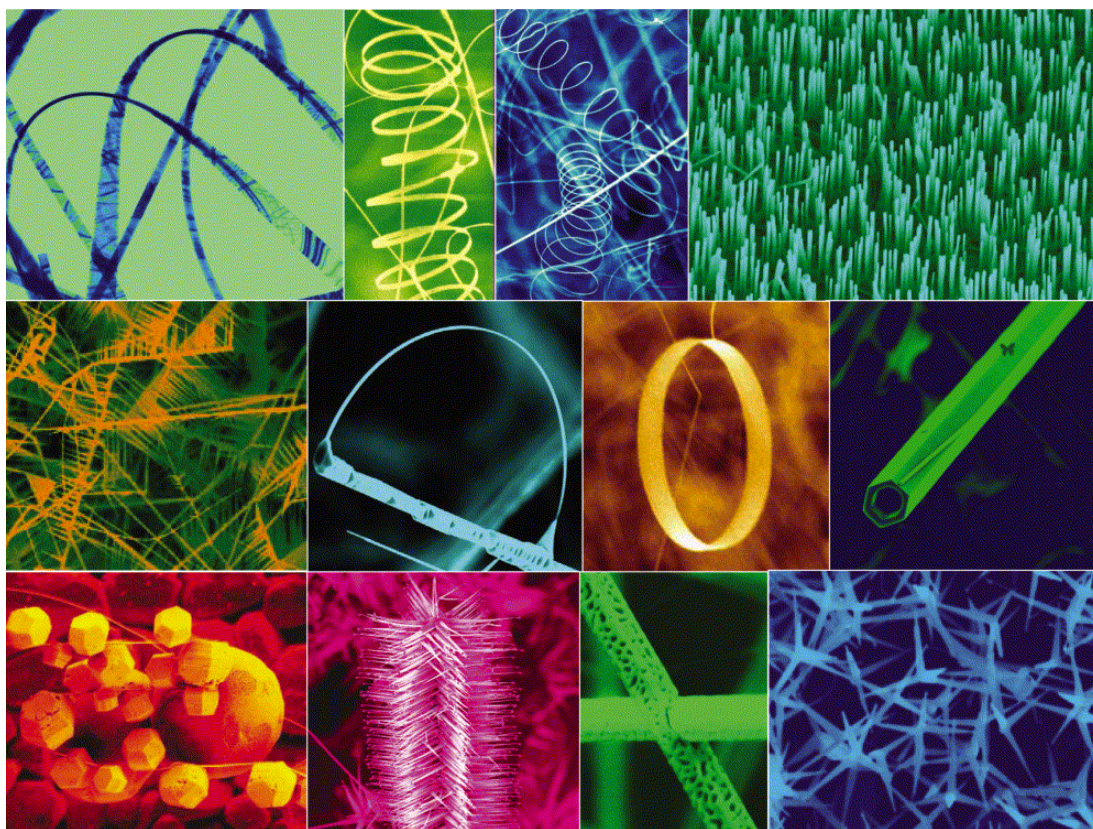


Figure 6: Different shapes of ZnO obtained by vapour-liquid-solid method (ref 58)

Cube-shaped CoFe_2O_4 is formed under mild growth conditions from acetyl acetonate complexes of Co and Fe in presence of oleic acid and oleyl amine as capping agents (59). Harsh growth conditions like high temperature and pressure leads to the formation of spheres. Similarly triangular metal oxides of Co_3O_4 , Cr_2O_3

and NiO were produced from their carboxylate precursors in organic solutions (12, 60). Triangular, diamond like, truncated octahedron $\gamma\text{-Fe}_2\text{O}_3$ nanocrystals could be produced from $[\text{Fe}(\text{CO})_5]$ using various concentrations of dodecyl amine as capping agent (Figure 7(a-d)) (61).

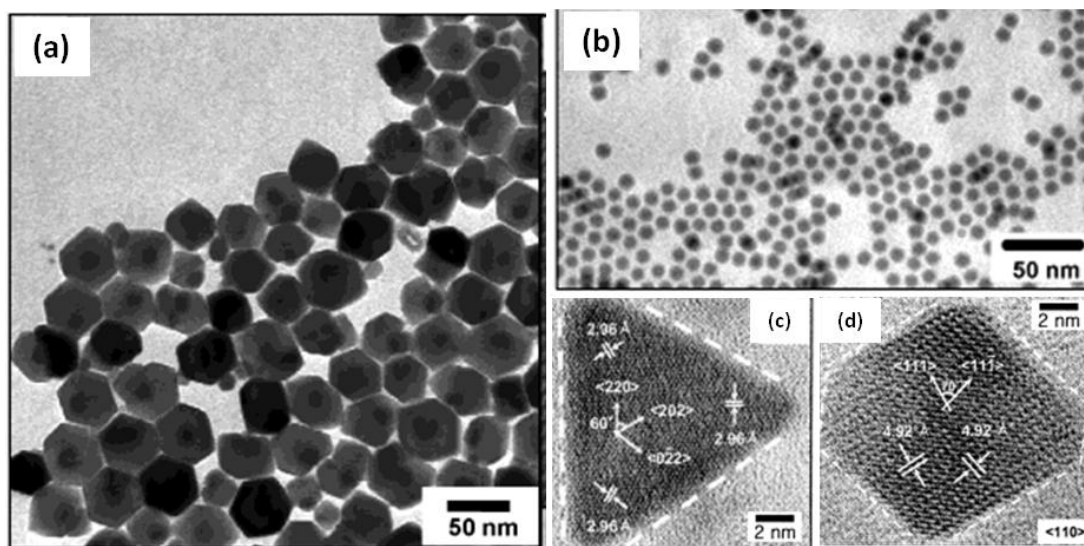


Figure 7: Various shapes of $\gamma\text{-Fe}_2\text{O}_3$ nanocrystals. TEM images of (a) hexagonal nanocrystals (b) spheres (c) triangle and (d) diamond (ref 61).

Alivisatos and co-workers reported CdSe nanorods from a thermal reaction of CdMe_2 and TOPSe in a hot surfactant mixture of TOPO and hexylphosphonic acid (HPA) (62). In the absence of HPA, formation of CdSe nanospheres is preferred. Furthermore, by increasing the concentration of HPA, the shape systematically changes to pencil shape, arrow shape, and pine-tree shape. Murray and co-workers formed radially branched nanowires from star shaped PbSe nanocrystals by linking the star-shaped nanocrystals together along their [100] direction (63). They also demonstrated that the formation of PbSe nanorings is possible by a similar oriented attachment approach. Brock and co-workers synthesized colloidal metal phosphide

nanospheres by thermal decomposition of metal precursors in the presence of trioctylphosphine (TOP) (64). O'Brien and co-workers synthesized CoP nanowires through thermal decomposition of $[\text{Co}(\text{acac})_2]$ (acac=acetylacetonate) and tetradecylphosphonic acid in a mixture of TOPO and HAD (65).

1.3 Properties induced by shape and size

The interest in nanoscale materials stems from the fact that new properties are acquired at this length scale and, that these properties change with their shape. Shape plays a key role in control of electronic, optical and catalytic properties of nanostructured materials (2). The changes in the properties at this length scale are not a result of scaling factors, but originate from different causes in different materials.

1.3.1 Electronic Structure

Electronic properties of nanomaterials are determined by their electronic energy levels and density of states (66). Metals when in bulk possess a partially filled electronic band and their ability to conduct electrons is due to the availability of a continuum of energy levels above the Fermi energy, E_F . However, at nanoscale continuum of electronic states breaks, making the material insulating (Figure 8).

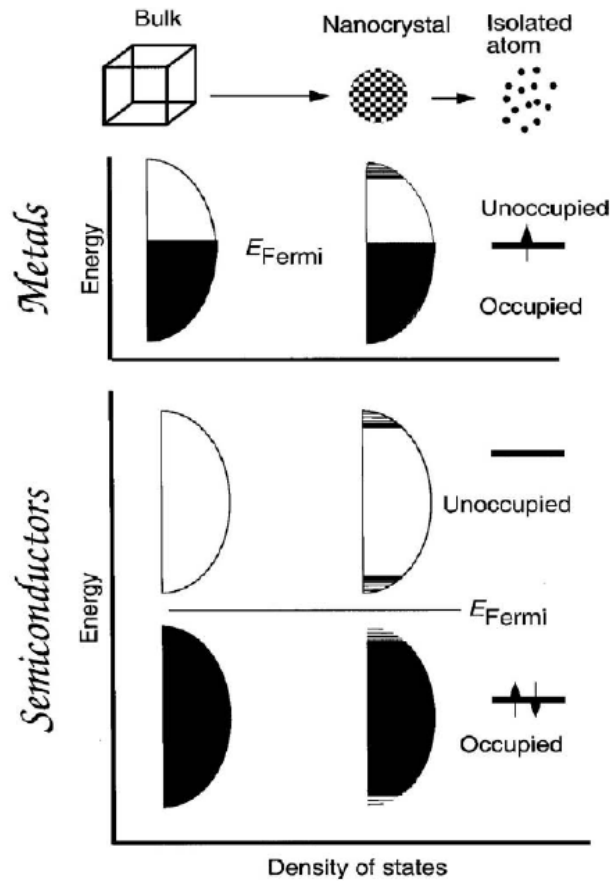


Figure 8: Schematic illustration of density of states of metals and semiconductors

In the case of semiconductors in bulk state, the E_F is in between the filled and the unfilled levels (Figure 8). Thus, excitation induces the formation of an electron and a hole, which are delocalized over a number of atoms or ions constituting the material. Since the material has high dielectric constant these delocalized pairs have relatively small binding energy. The distance between the hole and the electron is known as the Bohr radius and is on the nanometer length scale. The minimum amount of energy required for the formation of these charge carriers is the band gap energy of the semiconductor. It is the energy difference between the top of the

valence band and the bottom of the conduction band. When the size of the semiconductor material becomes smaller than the Bohr radius, it would decrease the space in which the charge carriers move and thus confine their motion. The situation is equivalent to the motion of an electron in a box. The solution to the Schrodinger equation of an electron in a box of length L gives the Eigen functions:

$$\varphi_n(x) = \sqrt{\frac{1}{L}} \sin(k_n x) ; \quad k_n = \frac{n\pi}{L} \quad (1)$$

Whose corresponding energy eigen values are given by

$$E_n = \frac{\hbar^2 n^2}{8mL^2} \quad (2)$$

Where, m is the effective mass. As the size of the box is reduced, the energy level spacing increases since it is inversely proportional to L^2 . Thus, the kinetic energy, E_n , and the excitation energy i.e. separation between two energy levels ($E_{n1} - E_{n2}$), of this particle increases upon confinement. Nanocrystals exhibiting quantum confinement are called quantum dots (QDs). The density of states (DOS), $\rho(E)$, of inorganic crystals simultaneously evolve from continuous levels into discrete states as the dimensionality is decreased from 3D to 0D as described by the relationship:

$$\rho(E) \approx E^{D/2-1} \quad (3)$$

(Where, D = dimensionality; see in **Figure 9**) (12). In 3D crystals as in the case of bulk materials $\rho(E)$ is a smooth square-root function of energy. 2D crystals and 1D crystals show staircase and saw-tooth like DOS, respectively, while 0D crystals show a δ -function like DOS. (**Figure 9**) This sudden variation of density of states with change of dimensionality imparts nanomaterials with interesting electrical and optical properties.

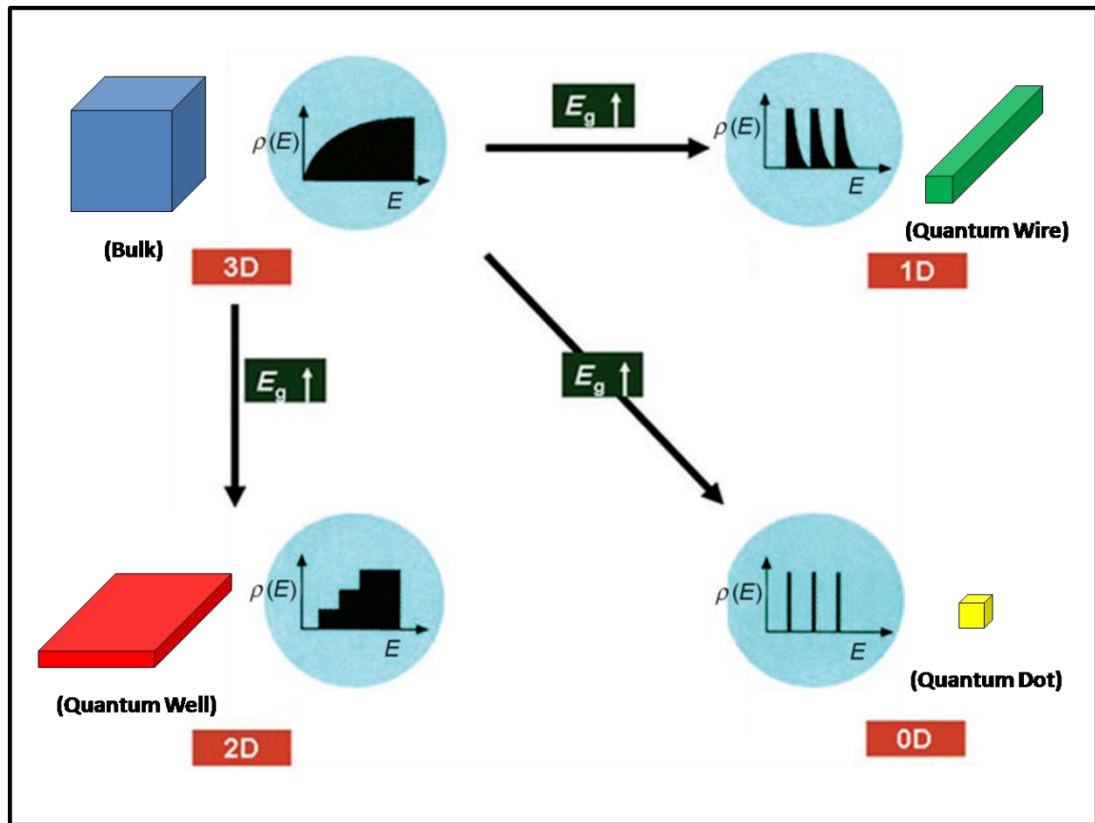


Figure 9: Shape evolution of crystals and their shape-dependent properties. Shape evolution of crystals and their shape-dependent properties. The plot of density of state (DOS) versus energy is a continuous curve for 3D crystals and changes to a discrete line for 0D crystals. The band-gap energy of semiconductors and metal oxides gradually increases as dimensionality and size reduces (ref 12)

Shape of nanocrystals also influences their electronic properties. For example, emission from CdSe nanocrystals gradually changes from circular to linearly polarized as the nanocrystal shape evolves from spherical to rod-like (Figure 10) (67).

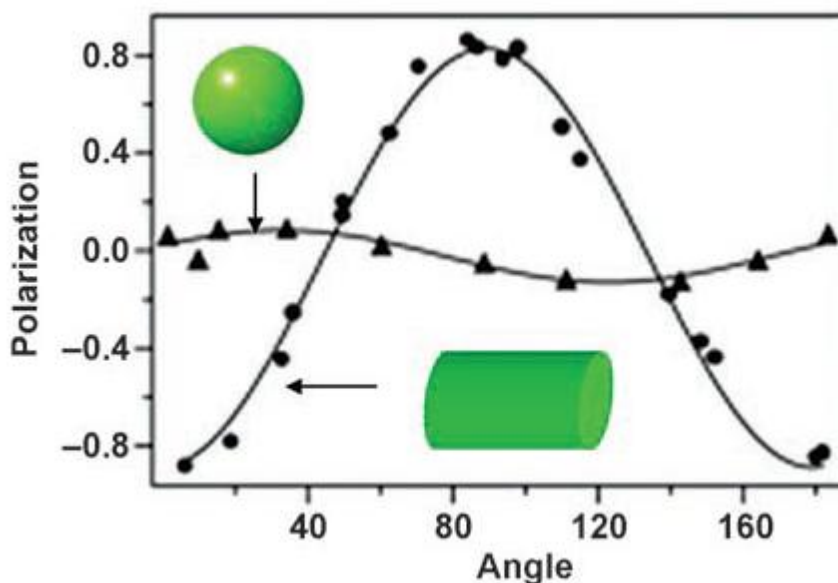


Figure 10: CdSe nanorods shows linearly polarized emission properties, while circularly polarized emission is observed from spherical CdSe nanoparticles. (ref 67).

1.3.2 Optical properties

The interaction of electromagnetic radiation with metallic nanostructures varies significantly resulting in the distinctive optical properties (68). For example, Au, Ag and Cu metal nanoparticles show surface plasmon resonance (SPR), which is a unique phenomenon at nanoscale and is absent in bulk. Metal nanoparticles are

well known for their strong interactions with visible light through the resonant excitations of the collective oscillations electrons. As a result, local electromagnetic fields near the particle can be many orders of magnitude higher than the incident fields and the incident light around the resonant-peak wavelength is scattered very strongly. This coherent oscillation of the metal electrons in resonance with light (Figure 11) of a certain frequency is known as localized *surface plasmon resonance* (SPR) (69).

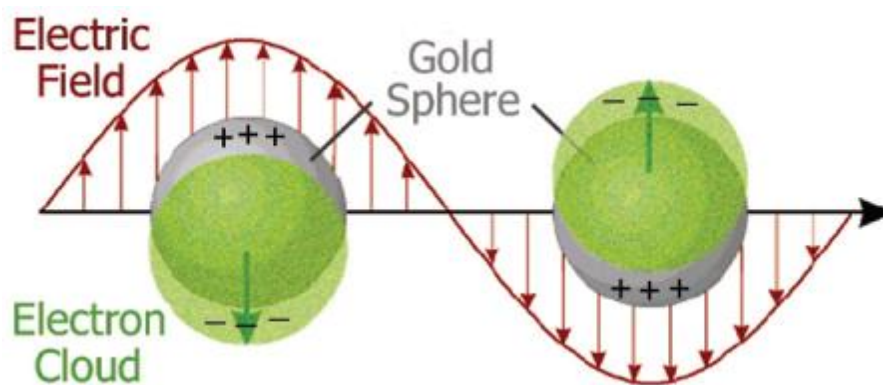


Figure 11: Origin of surface plasmon resonance due to coherent interaction of the electrons in the conduction band of gold nanoparticle (sphere) with light (ref 69).

Changing the shape of metal nanocrystals changes their optical absorption. For example, the plasmon resonance for Au nanorods splits into two bands. Figure 12 shows the experimentally observed absorption spectrum of a nanospheres and nanorods having different aspect ratios. In case of nanospheres, only one plasmon absorption band is observed whereas in case of nanorods, there are two plasmon absorption bands, one corresponding to oscillation of the electrons perpendicular to

the major axis of the nanorods (transverse plasmon absorption) and the other corresponding to the oscillation of the electrons along the minor axis of the nanorods (longitudinal surface plasmon). As the aspect ratio increases, the energy separation between the resonance frequencies of the two plasmon bands also increases (68). The transverse plasmon absorption band is relatively insensitive to the nanorod aspect ratio and coincides spectrally with the surface plasmon oscillation of the nanospheres whereas longitudinal transverse plasmon mode varies linearly with aspect ratio.

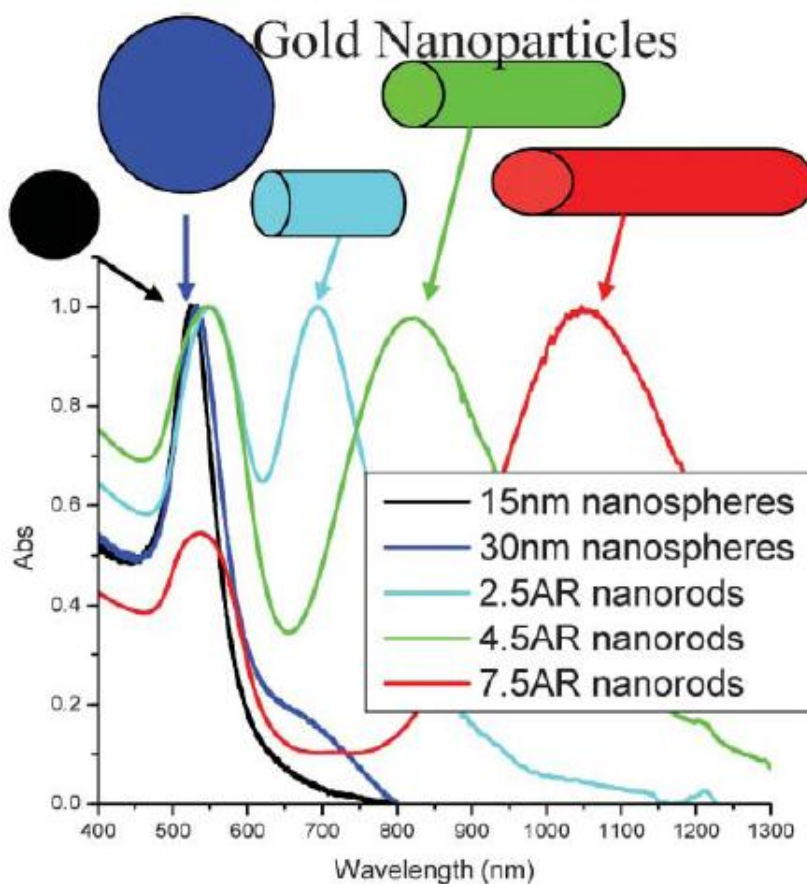


Figure 12: Absorption spectra of gold nanospheres and gold nanorods (AR = aspect ratio) of different sizes (ref 68).

Not only among spheres and rods, different shapes of nanostructures also differ in their absorption spectra. Figure 13 gives the extinction efficiency (absorption) of differently shaped nanostructures (70).

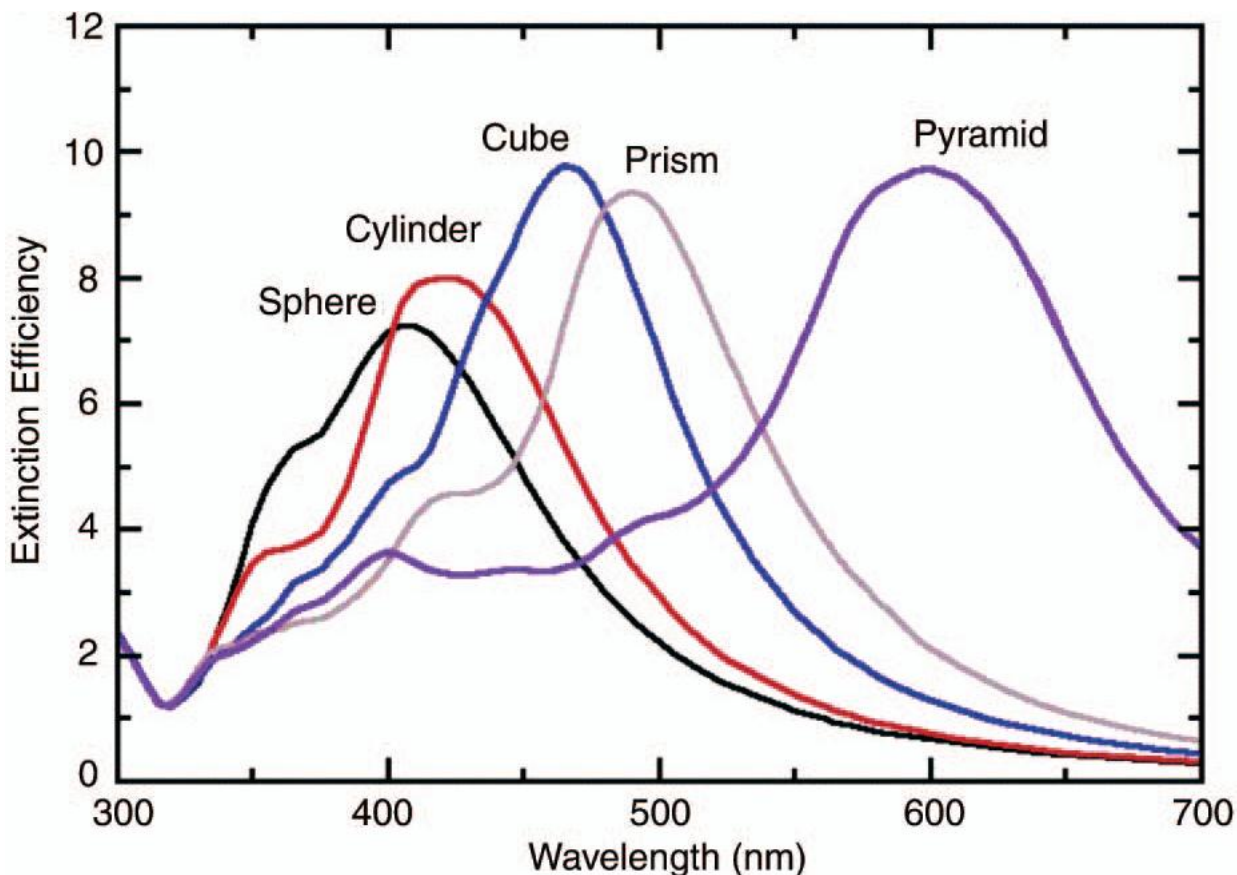


Figure 13: Extinction efficiency (ratio of cross section to effective area) of silver nanoparticles in vacuum having the shapes indicated. Each particle has the same volume, taken to be that of a sphere with a radius of 50 nm (ref 70).

1.3.3 Catalytic properties

Catalysis drives many reactions, with the ability to lower the activation energy of the reaction, and thus increases the rate of reaction and the yield of the

desired products. The use of nanoparticles as catalysts has increased exponentially as nanoparticle properties and reactions are better understood and having different properties for different shapes of nanoparticles is very attractive. Nanocrystals of noble metals are constantly being used as catalysts because of their high surface-to-volume ratios and high surface energies, which in turn cause their surface atoms to be highly active (71). Various noble metal nanocrystals are widely used to catalyze many types of reactions including oxidation, cross-coupling, electron-transfer, and hydrogenation (72). Shape control could enable the properties of a nanocrystal to be tuned with a greater versatility than can be achieved otherwise. For example, both the reactivity and selectivity of a nanocatalyst can be tailored by controlling the shape, as shape determines the number of atoms located at the edges or corners (71, 73) (Figure 14).

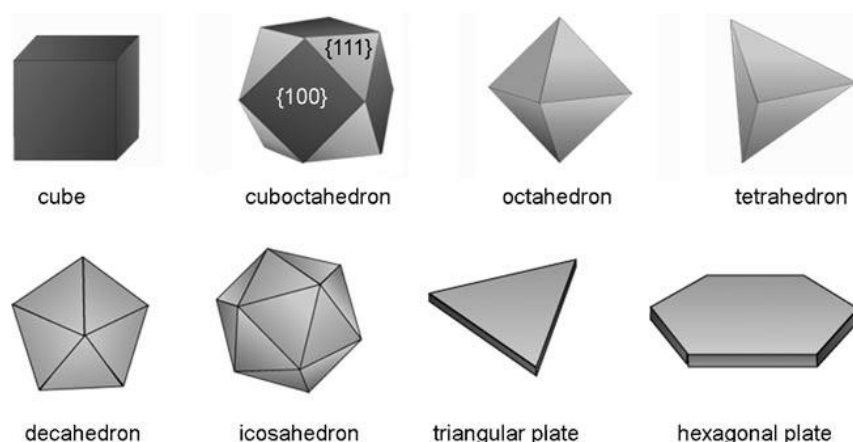


Figure 14: Conventional shapes of face-centered cubic (fcc) metals whose surface is enclosed by $\{100\}$ and/or $\{111\}$ facets. Black and gray colors represent the $\{100\}$ and $\{111\}$ facets, respectively (ref 73).

In general, high-index planes have a greater density of unsaturated atomic steps, ledges, and kinks which can serve as active sites for breaking chemical bonds. Correlation of the catalytic activity of Pt nanocrystals with the number of surface atoms indicates that a large number of edge and corner atoms hold the key to improving their catalytic performance. Fundamental studies on the single-crystal surfaces of bulk Pt have shown that high-index planes exhibit much higher catalytic activity than common, stable, low-index planes, such as {111} and {100}. For example, a bulk Pt (210) surface possesses extremely high catalytic reactivity for electro-reduction of CO₂ (74) and electro-oxidation of formic acid (75). The bulk Pt (410) surface exhibits unusual activity for catalytic decomposition of NO, a major pollutant of automobile exhaust (76). The reactant molecules in these cases selectively adsorb onto specific growth planes of the nanocrystals before converting into products. The maximization of high-index surfaces and abundant corner and edge sites in a catalyst is expected to perform as a good nanocatalyst, although the catalytic activity depends upon the type of the reaction and support.

1.4 Conclusions

Research in the field of nanomaterials gained momentum in the last two decades, primarily because of the availability of new synthetic methods, as well as the tools for characterization and manipulation. Different shapes of materials, which are earlier not known, are being discovered continuously from time to time using various methods. Due to the promising applications of the nanostructured materials

in the devices, there is a lot of interest in developing nanomaterials of different shapes and sizes. This thesis investigates variety of nanostructures of complex morphology like rings, bowls, drums, pencils and pillar arrays and explores their properties and applications.

1.5 References

1. G. M. Whitesides, *Nat. Biotechnol.* **2003**, *21*, 1161.
2. C. Burda, X. Chen, R. Narayanan and M. A. El-Sayed, *Chem. Rev.* **2005**, *105*, 1025.
3. G. Schmid Ed., *Nanoparticles: From Theory to Applications*, Wiley-VCH Verlag, GmbH & Co. KGaA. Weinheim, **2004**.
4. C. N. R. Rao, A. Muller and A. K. Cheetham Ed., *Nanomaterials Chemistry: Recent Developments*, Wiley-VCH Verlag, GmbH & Co. KGaA. Weinheim, **2007**.
5. P. Dutta and S. Gupta Ed. *Understanding of Nano Science and Technology*, Global Vision Publishers, New Delhi, **2006**.
6. Sergey P. Gubin, *Magnetic nanoparticles*, Wiley-VCH Verlag, GmbH & Co. KGaA. **2009**.
7. Ph. Buffat and J. P. Borel, *Phys. Rev. A.* **1976**, *13*, 2287.
8. W.H. Qi, *Physica B* **2005**, *368*, 46.
9. A. N. Goldstein, C. M. Echer and A. P. Alivisatos, *Science* **1992**, *256*, 1425.

10. G. Hornyak, J. Dutta, H. F. Tibbals, A. K. Rao, *Introduction to Nanoscience*, CRC Press Taylor & Francis group, **2008**.
11. Y. Xia, Y. Xiong, B. Lim, and S. E. Skrabalak, *Angew. Chem. Int. Ed.* **2009**, *48*, 60.
12. Y-W. Jun, J-S. Choi and J. Cheon, *Angew. Chem. Int. Ed.* **2006**, *45*, 3414.
13. R. Jin, S. Egusa, N. F. Scherer, *J. Am. Chem. Soc.* **2004**, *126*, 9900.
14. X. Sun, S. Dong, and E. Wang, *Angew. Chem. Int. Ed.* **2004**, *43*, 6360.
15. S. S. Shankar, A. Rai, B. Ankamwar, A. Singh, A. Ahmad and M. Sastry, *Nat. Mater.* **2004**, *3*, 482.
16. Y. Xiong, I. Washio, J. Chen, H. Cai, Z.-Y. Li, Y. Xia, *Langmuir* **2006**, *22*, 8563.
17. Y. Shao, Y. Jin, S. Dong, *Chem. Commun.* **2004**, 1104.
18. D. Ibane, Y. Yokota, and T. Tominaga, *Chem. Lett.* **2003**, *32*, 574.
19. N. Zhao, Y. Wei, N. Sun, Q. Chen, J. Bai, L. Zhao, Y. Qin, M. Li, L. Qi, *Langmuir* **2008**, *24*, 991.
20. B. Nikoobakht, M. A. El-Sayed, *Chem. Mater.* **2003**, *15*, 1957.
21. N.R. Jana, L. Gearheart, and C.J. Murphy, *Adv. Mater.* **2001**, *13*, 1389.
22. Y. Zhang, B. Liu, J. Liu, H. Zhou, Y. Xu, Y. Jiang, Z. Yang, and Z.Q. Tian, *J. Am. Chem. Soc.* **2004**, *126*, 9470.
23. E. Hao, R. C. Bailey, G. C. Schatz, J. T. Hupp, S. Li, *Nano Lett.* **2004**, *4*, 327
24. J. Hu, Y. Zhang, B. Liu, J. Liu, H. Zhou, Y. Xu, Y. Jiang, Z. Yang, Z.-Q. Tian, *J. Am. Chem. Soc.* **2004**, *126*, 9470
25. J. H. Song, F. Kim, D. Kim, P. Yang, *Chem. Eur. J.* **2005**, *11*, 910

26. X. Xu, M .B. Cortie, *Adv. Funct. Mater.* **2006**, *16*, 2170
27. X. Kou, S. Zhang, Z. Yang, C.-K. Tsung, G. D. Stucky, L. Sun, J. Wang, C. Yan, *J. Am. Chem. Soc.* **2007**, *129*, 6402
28. B. K. Jena, C. R. Raj, *Langmuir* **2007**, *23*, 4064.
29. Benjamin Wiley, Yugang Sun, Jingyi Chen, Hu Cang, Zhi-Yuan Li, Xingde Li, and Younan Xia, *Mater. Res. Bull.* 2005, *30*, 356.
30. N. R. Jana, L. Gearheart, C. J. Murphy, *Chem. Comm.* **2001**, 617.
31. B. Wiley, Y. Sun, Y. Xia, *Langmuir* **2005**, *21*, 8077.
32. I. Washio, Y. Xiong, Y. Yin, Y. Xia, *Adv. Mater.* **2006**, *18*, 1745
33. S. Chen and D.L. Carroll, *Nano Lett.* **2002**, *2*, 1003.
34. S. Chen, Z. Fan, and D.L. Carroll, *J. Phys. Chem. B.* **2002**, *106*, 10777.
35. M. Maillard, S. Giorgio, and M.-P. Pileni, *Adv. Mater.* **2002**, *14*, 1084.
36. D.O. Yener, J. Sindel, C.A. Randall, and J.H. Adair, *Langmuir* **2002**, *18*, 8692.
37. T. S. Ahmadi, Z. L. Wang, T. C. Green, A. Henglein, M. A. El-Sayed, *Science* **1996**, *272*, 1924.
38. R. Krishnaswamy, H. Remita, M. Imperor-Clerc, C. Even, P. Davidson, B. Pansu, *ChemPhysChem* **2006**, *7*, 1510.
39. E. P. Lee, J. Chen, Y. Yin, C. T. Campbell, Y. Xia, *Adv. Mater.* **2006**, *18*, 3271.
40. M. A. Mahmoud, C. E. Tabor, M. A. El-Sayed, Y. Ding, Z. L. Wang, *J. Am. Chem. Soc.* **2008**, *130*, 4590.

41. Y. Song, R. M. Garcia, R. M. Dorin, H. Wang, Y. Qiu, E. N. Coker, W. A. Steen, J. E. Miller, J. A. Shelnut, *Nano Lett.* **2007**, *7*, 3650.
42. B. Lim, J. Wang, P. H. C. Camargo, M. Jiang, M. J. Kim, Y. Xia, *Nano Lett.* **2008**, *8*, 2535.
43. S. Maksimuk, X. Teng, H. Yang, *J. Phys. Chem. C* **2007**, *111*, 14312.
44. Y. Xiong, J. Chen, B. Wiley, Y. Xia, S. Aloni, Y. Yin, *J. Am. Chem. Soc.* **2005**, *127*, 7332.
45. Y. Xiong, J. Chen, B. Wiley, Y. Xia, Y. Yin, Z.-Y. Li, *Nano Lett.* **2005**, *5*, 1237.
46. Y. Xiong, H. Cai, B. J. Wiley, J. Wang, M. J. Kim, Y. Xia, *J. Am. Chem. Soc.* **2007**, *129*, 3665.
47. Y. Sun, L. Zhang, H. Zhou, Y. Zhu, E. Sutter, Y. Ji, M. H. Rafailovich, J. C. Sokolov, *Chem. Mater.* **2007**, *19*, 2065.
48. Y. Xiong, J. M. McLellan, J. Chen, Y. Yin, Z.-Y. Li, Y. Xia, *J. Am. Chem. Soc.* **2005**, *127*, 17118.
49. P.-F. Ho, K.-M. Chi, *Nanotechnology* **2004**, *15*, 1059.
50. Y. Wang, P. Chen, M. Liu, *Nanotechnology* **2006**, *17*, 6000.
51. D. Mott, J. Galkowski, L. Wang, J. Luo, C.-J. Zhong, *Langmuir* **2007**, *23*, 5740.
52. J.-H. Wang, T.-H. Yang, W.-W. Wu, L.-J. Chen, C.-H. Chen, C.-J. Chu, *Nanotechnology* **2006**, *17*, 719.
53. A. C. Curtis, D. G. Duff, P. P. Edwards, D. A. Jefferson, B. F. G. Johnson, A. I. Kirkland, A. S. Wallace, *Angew. Chem. Int. Ed. Engl.* **1988**, *27*, 1530.

54. F. Dumestre, B. Chaudret, C. Amiens, P. Renaud, P. Fejes, *Science* **2004**, 303, 821
55. Y. Xiong, Y. Xie, Z. Li, R. Zhang, J. Yang, C. Wu, *New J. Chem.* **2003**, 27, 588.
56. V. F. Puntes, D. Zanchet, C. K. Erdonmez, A. P. Alivisatos, *J. Am. Chem. Soc.* **2002**, 124, 12874.
57. Y. Leng, Y. Wang, X. Li, T. Liu, S. Takahashi, *Nanotechnology* **2006**, 17, 4834.
58. Q. Song, Z. J. Zhang, *J. Am. Chem. Soc.* **2004**, 126, 6164.
59. N. R. Jana, Y. Chen, X. Peng, *Chem. Mater.* **2004**, 16, 3931.
60. J. Cheon, N.-J. Kang, S.-M. Lee, J.-H. Lee, J.-H. Yoon, S. J. Oh, *J. Am. Chem. Soc.* **2004**, 126, 1950.
61. Z. L. Wang, *Mater. Today*, **2004**, 7, 26.
62. L. Manna, E. C. Scher, A. P. Alivisatos, *J. Am. Chem. Soc.* **2000**, 122, 12700.
63. K.-S. Cho, D. V. Talapin, W. Gaschler, C. B. Murray, *J. Am. Chem. Soc.* **2005**, 127, 7140.
64. S. L. Brock, S. C. Perera, K. L. Stamm, *Chem. Eur. J.* **2004**, 10, 3364.
65. Y. Li, M. A. Malik, P. O'Brien, *J. Am. Chem. Soc.* **2005**, 127, 16020.
66. C. N. R. Rao, G. U. Kulkarni, P. J. Thomas, P. P. Edwards, *Chem. Eur. J.* **2002**, 8, 28-35.
67. J. Hu, L.-s. Li, W. Yang, L. Manna, L.-w. Wang, A. P. Alivisatos, *Science* **2001**, 292, 2060.
68. S. Eustis and M. A. El-Sayed, *Chem. Soc. Rev.* **2006**, 35, 209.

69. Y. Xia and N. Halas, *Mater. Res. Bull.* **2005**, 30, 338.
70. A. J. Haes, C. L. Haynes, A. D. McFarland, G. C. Schatz, R. P. Van Duyne, and S. Zou, *Mater. Res. Bull.* **2005**, 30, 368.
71. R. Narayanan, M. A. El-Sayed, *J. Phys. Chem. B.* **2005**, 109, 12663.
72. L. N. Lewis, *Chem. Rev.* **1993**, 93, 2693.
73. Y. Xiong, B. J. Wiley, and Y. Xia, *Angew. Chem. Int. Ed.* **2007**, 46, 7157.
74. N. Hoshi, S. Kawatani, M. Kudo, Y. Hori, *J. Electroanal. Chem.* **1999**, 467, 67.
75. S. G. Sun, J. Clavilier, *Chem. J. Chin. Univ.* **1990**, 11, 998.
76. W. F. Banholzer, R. I. Masel, *J. Catal.* **1984**, 85, 127.

Chapter 2

**Rings: Novel Synthesis of Carbon Nanorings
and their Characterization**

Summary

Amorphous carbon nanorings, different from the tubular and graphitic SWNT nanorings, formed through the fusion of carbon nanostructures derived from the carbonization of Pluronic P123 polymer inside the mesoporous SBA-15 rods grown in a porous alumina membrane is investigated in this chapter. The mechanism of formation of these carbon rings is investigated in greater detail. Properties and applications of other metal and metal oxide nanorings are also discussed. Further, the importance of the nanoring morphology in general is also reviewed in detail.

Papers based on the above study have been published in (i) *Chem. Phys. Lett.* **2007**, 433, 327. (ii) *Nanorings*, in *CRC Handbook of Nanophysics*, Taylor and Francis Publishers, 2010.

2.1 Introduction

The exciting size- and shape-dependent properties associated with many materials at the nanometer scale evoked a great deal of interest in synthesizing materials of different sizes and shapes (1–9). Spheres, wires, rods, and tubes are the common morphologies prevalent in the nanomaterial world as against uncommon shapes like rings, bowls, and other complex architects. Nanostructured materials with ring-like morphology (*Nanorings*) are expected to display unique features different from the rod, ribbon, wire or sphere-type structures (10-15). Nanorings, as the name implies, are the nanoscale entities with ring-shaped geometry, (i.e. the inner diameter of the ring is larger than the width and thickness of the rim) having one of its dimensions (either the width or thickness of the rim) in the nanometre regime (Figure 1). Molecular nanorings are the ones where the size of the ring-shaped molecule is in the nanometer scale.

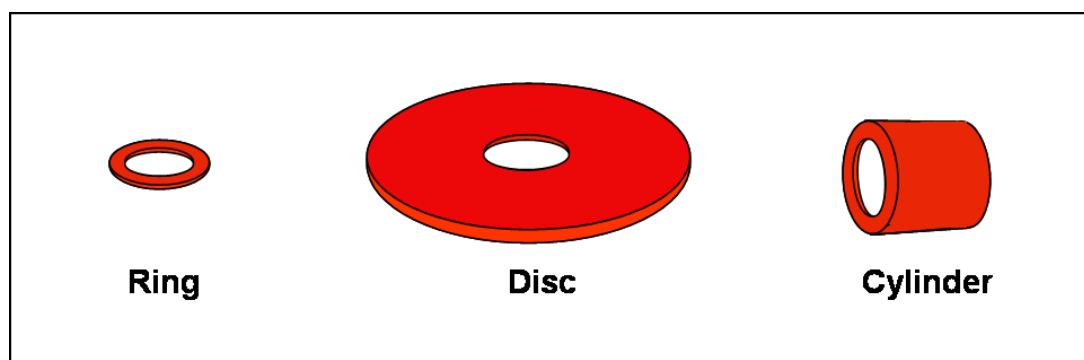


Figure 1: Illustration of a Ring, Disc and a Cylinder

A nanoring can be of a single entity with an end to end closed (a perfect tori structure) or coiled, or a superstructure formed by the self-assembly of smaller

entities such as molecules and nanoparticles (Figure 2). In the case of superstructures, the resulting symmetry is often determined by the shape of the smaller entities used to build the structure. Since the prevalent shapes of the smaller units are mostly spherical, disc/tile and rod-like, it would be difficult to pack them in the form of ring like superstructure.



Figure 2: Schematic showing the single ring, coiled ring and self-assembled ring

For example, opaline structures are commonly resulted from the packing of (monodispersed) spherical entities (Figure 3). Stacked pancake structures (discotic phase) are obtained from the packing of disc shaped entities. Nematic, smectic or hexagonal phase superstructures are built from the packing of rod like entities. These type of superstructures usually observed in controlling the mesophases in colloidal suspensions and superlattices in nanocrystals dispersions (16, 17). Nevertheless, organization of sphere-, disc- and rod shaped entities into ring-like superstructures (18) were also reported under certain conditions which will be discussed later in this chapter.

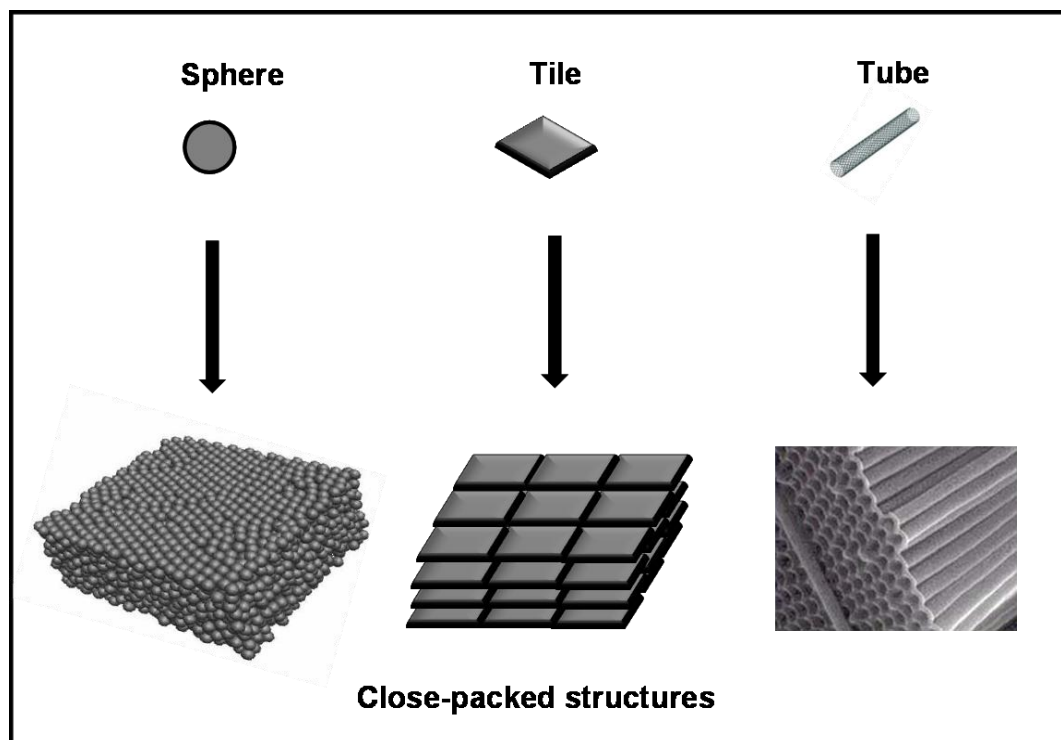


Figure 3: Scheme illustrating the packing of spheres, tiles and tubes

2.1.1 Importance of nanoring morphology

Metal nanoparticles such as Ag, Au and Cu are known to absorb and emit certain wavelength of light depending upon their size and shape (19). Among various shapes, ring-shaped nano objects of similar size exhibit several novel properties due to their unique structural features. For example, gold nanorings are shown to display tunable plasmon resonance in the near infrared which is not possible with the solid gold particles of similar size (20, 21). Further, the optical and electromagnetic properties of the gold nanorings can be varied by varying the ratio of the ring radius and wall thickness. When light falls on a gold nanoring the electrons get excited and oscillate collectively as a wave (plasmon) which can be tuned by tuning the

wavelength of light and the geometry of the ring. By tuning the wavelength of the incoming light, the pool of electrons in the ring can be made to resonate in the same wavelength. This resonance generates a strong and uniform electromagnetic field which will oscillate within the ring cavity. If the field inside the ring cavity is optimised to near infrared, it (cavity) can be used as a container for holding and probing smaller nanostructures in sensing and spectroscopy applications. Conducting the experiments inside the nanoring will give amplified infrared signals and better results which would be of interest to drug industry and biochemical researchers (22).

Another interesting phenomenon observed in the metal nanorings is called Aharonov-Bohm effect (23-25) which cannot be explained by classical mechanics. It is a quantum mechanical phenomenon. It predicts that if a coherent electron beam splits into two parts and the path encloses a finite magnetic flux (magnetic field B on the path of the electrons is zero), a phase difference will occur in the electron wave packets travelling along the two parts which in turn would manifest in an interference pattern at the other end due to the non-zero magnetic vector potential (Figure 4).

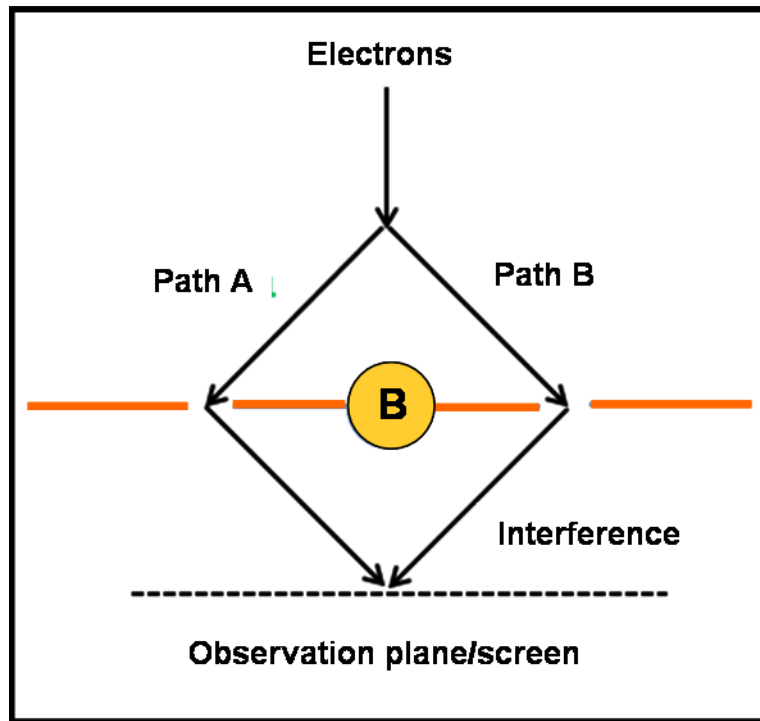


Figure 4: Schematic of double-slit experiment in which Aharonov–Bohm effect can be observed: electrons pass through two slits, interfering at an observation screen. The interference pattern will shift when a magnetic field, B is turned on in the cylindrical solenoid

Similarly, the phase coherent electrons travelling around the magnetic field, B through the arms of the metal nanorings (remember the magnetic field in the conductor regions, the arms of the rings, is zero) should show oscillations in the magnetoresistance because of the interference between the wave packets of electrons of the two arms (Figure 5). The electrons phase shift occurs in both arms of the ring and can be tuned by changing the magnetic flux encircled by the ring.

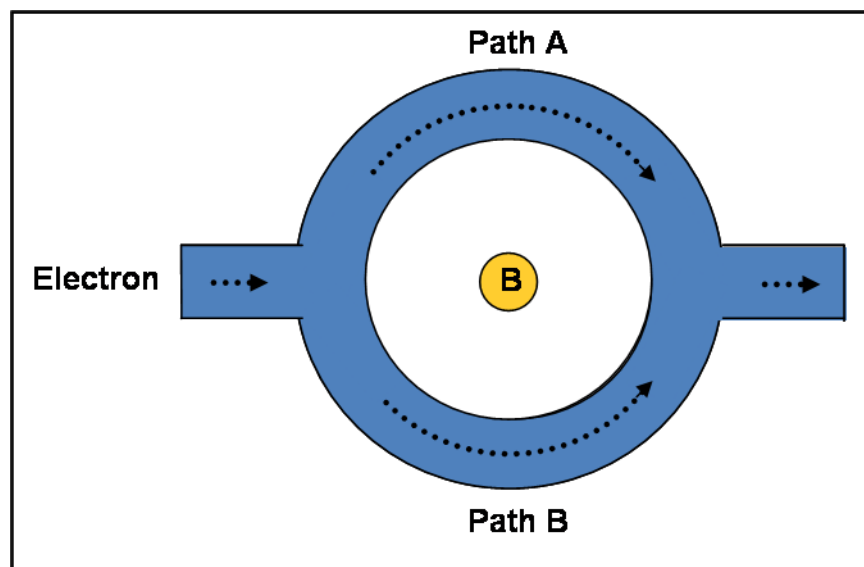


Figure 5: Schematic of Aharonov-Bohm effect in a nanoring

Nanorings made up of metallic carbon nanotubes are expected to possess giant paramagnetic moment in presence of an applied magnetic field (perpendicular to the plane of the ring) owing to the effective interplay between the ring geometry and the ballistic motion of π -electrons in the nanotube (11). Theoretical studies predict that at 0 K and at applied magnetic fields of ~ 0.1 T, the rings of metallic carbon nanotube can exhibit very large paramagnetic moments, three orders of magnitude higher compared to the diamagnetic moment of graphite.

Magnetic nanorings have been proposed for applications in high-density magnetic storage and vertical magnetic random access memory (V-MRAM) (26, 27) due to their ability to retain the vortex states. Larger magnetic elements such as microdiscs have rich domain structures determined by their geometry. On the other hand very small nano entities generally have single domain state, with all spins point to one direction (Figure 6a). Further, the microdiscs form vortex state, whose

magnetic moments form a closure structure where no stray field is leaked out. The center of the vortex, called vortex core, have the magnetic moments pointing out of the plane, either up or down (Figure 6b).

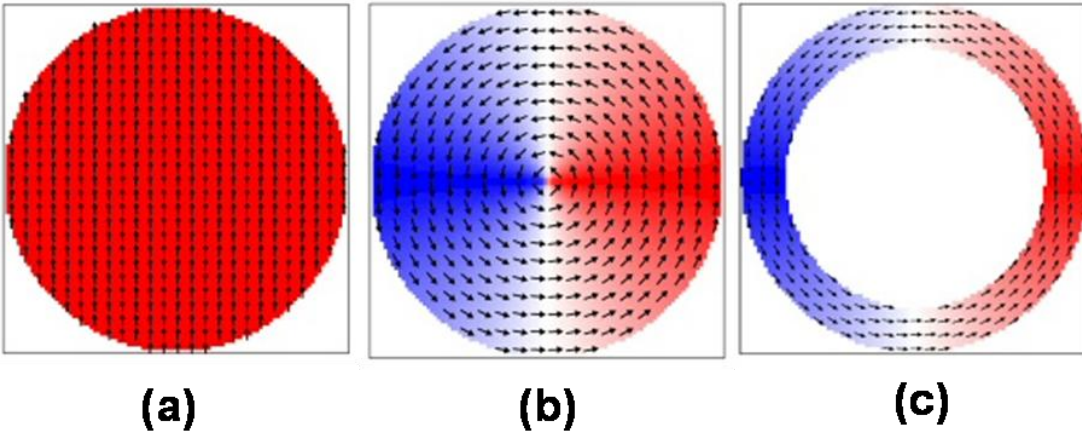


Figure 6: (a) Vortex state in single circular domain (all spins pointing upwards), (b) Vortex state in a circular disc (with a vortex core where spins are out of planarity and (c) Vortex state of a nanoring (with a missing vortex core). In both the circular disc and nanoring, the left side spins are pointing downwards and right side spins are pointing upwards.

As the size of the discs shrinks laterally, the vortex core becomes unstable and finally transforms to a single domain state below a certain critical size. The competition between the exchange energy (dominant at small scale) and the magneto static energy (dominant at large scale) basically decides such transition. Since there is no vortex core, a stable vortex states can be achieved in the case of magnetic nanorings. All moments are completely confined within the plane and form a closure (Figure 6c). The vortex chirality (clockwise and anti-clockwise) in the magnetic nanorings can be used for information storage.

Nanorings made up of porphyrin entities through π - π stacking and supramolecular self-assembly (28, 29) are reported to show excellent fluorescence properties and are being explored for optical applications (30). All these applications clearly demonstrate the significance of ring morphology at the nanoscale.

2.2 Synthetic methods of forming nanoring structures

Nanorings can either be made from a single entity or from self-assembly of multiple entities like molecules, nanoparticles etc. Various approaches are being adopted to make the nanoring structures of different components. Among these, evaporation induced self-assembly, electrostatic interactions induced coiling, template-based synthesis, and chemical reactions are the most common approaches to make nanorings. In evaporation induced self assembly, physical processes such as dewetting, surface tension, solvent and solute dynamics play a major role in the ring formation. Mainly two kinds of mechanisms operate in such cases, (i) Coffee stain mechanism and (ii) Pin-hole mechanism.

Coffee stain mechanism explains the formation of ring-like stains (31) from the solution (containing nanocrystals/polymers/nanowires) drop on evaporation. Enrichment of solute at the edges of the droplet will occur during the evaporation of solvent (from the solution), if the contact line of the solution with the solid substrate is pinned. The solvent at the edge of a solution droplet evaporate faster than the bulk. This evaporation loss at the perimeter will be offset by an outward flow of fluid from the core which draws the solute (dispersed material) from the interior to the edge of the drop and deposits it as a solid ring (Figure 7).

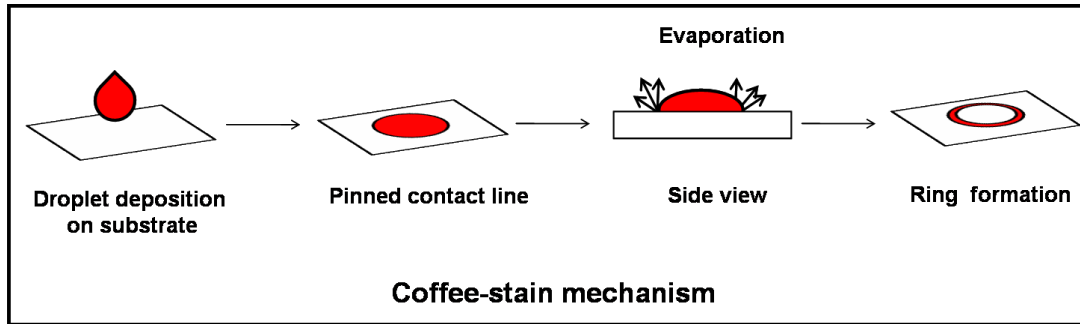


Figure 7: Schematic showing the coffee-stain mechanism (ref 28)

In the pinhole mechanism, formation of holes in the liquid films during evaporation is responsible for ring-formation (28). Holes nucleate when the evaporating solution film on a wetted substrate reaches a critical thickness where there is a balance between thinning of liquid and wetting of the surface. The holes then open up and expands outward (in order to retain the optimum film thickness while evaporation continues) and push the solute particles towards the growing inner perimeter. As the evaporation continues, the solution around the rim becomes more and more concentrated. Finally, the resulting ring of particles gets stuck when the friction between the particles and the substrate can no longer be overcome by the force acting radially outward to thicken the film. Further, the evaporation rate at the edge of the pinhole is higher than in the bulk of the solution film, an inward flow of solute occurs to compensate this loss which will enrich the concentration of the solute at the inner edge of the ring. This process will continue till complete evaporation of solvent occurs leaving the dispersed materials in the form of rings (Figure 8).

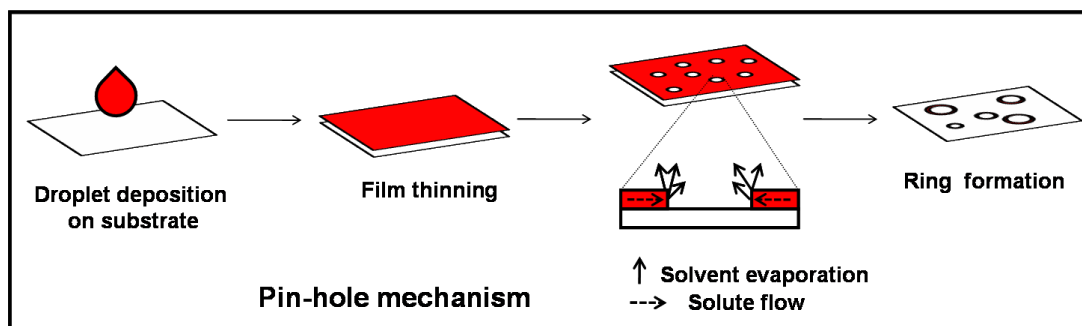


Figure 8: Schematic showing the Pin-hole mechanism (adapted from ref 28)

In certain cases, the functional groups present over the nanostructures would also induce the formation of ring-like superstructures. The electrostatic interactions between the charged surfaces of the nanostructures have been reported to give ring shaped morphology in some cases. For example, the cylindrical micelles obtained with a negatively charged amphiphilic polymer undergo a shape change from a cylindrical to toroid shape on interaction with the positively charged divalent counter ion (32). Electrostatic interaction of the charges over the ZnO nanobelt edges leads to ring formation through self-coiling process at high temperature (33). Colloidal crystal templating, a well known method to produce ordered porous structures (34) has been tuned to obtain TiO₂ nanorings (35) by depositing the titania around the contact points of two spheres (36, 37).

Carbon nanorings were first observed during the laser assisted synthesis of single-walled carbon nanotubes (SWNTs) in the year 1997 by Smalley and co-workers (38) (Figure 9a). Avouris and co-workers have later reported the formation of SWNT rings by the curling of nanotube ropes (no end-to-end fusion) (39). Rings in their case were produced by ultrasonically treating a solution containing SWNTs in a

mixture of concentrated sulphuric acid and hydrogen peroxide (Figure 9b). Chemical reaction between the end-to-end functionalized carbon nanotube was also shown to produce nanorings of SWNTs. These SWNTs were first functionalized with carboxylic acid at both ends by ultrasonating them in concentrated $\text{H}_2\text{SO}_4/\text{HNO}_3$ solution (40) followed by end-to-end ring closure using 1, 3-dicyclohexylcarbodiimide (DCC) as the coupling agent (Figure 9c and 9d).

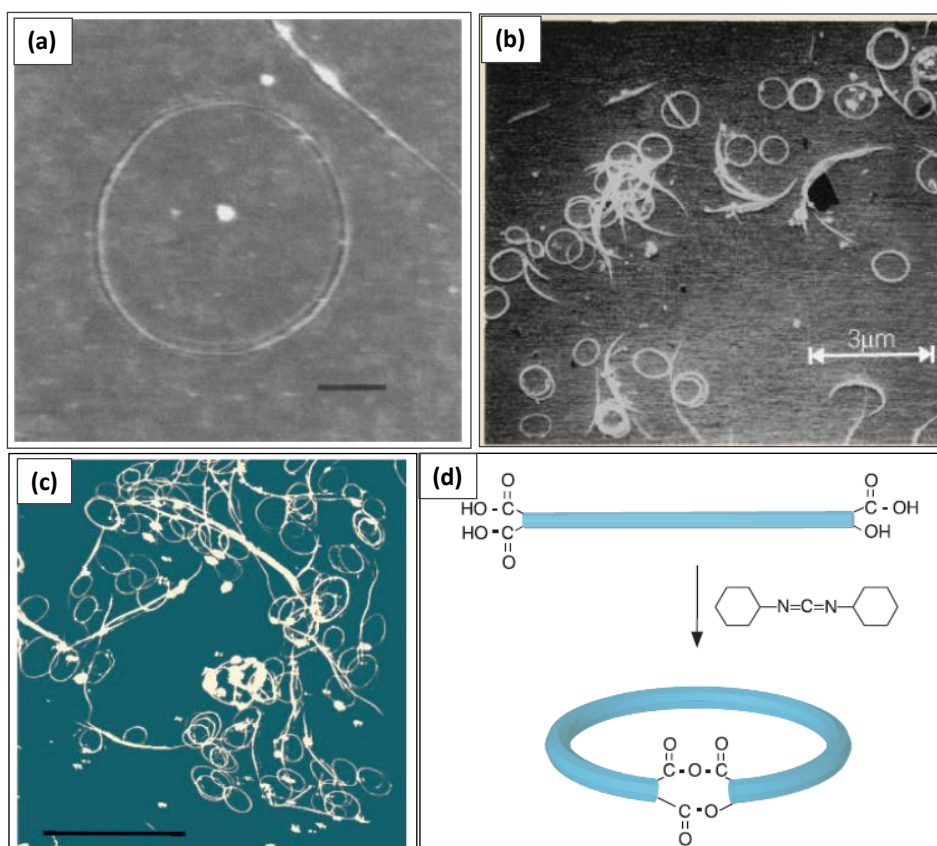


Figure 9: (a) Scanning force micrograph (SFM) of nanoring formed from SWNTs by laser assisted growth of SWNT (Scale bar: 100 nm) (b) Scanning electron micrograph of a SWNT sample dispersed on a hydrogen-passivated silicon substrate (c) AFM images of carbon nanotube rings (prepared using DCC) cast on mica (Scale bar: 2 mm) (d) A possible scheme for the ring-closure reaction with DCC (ref 38, 39, 40)

2.3 Scope of the present investigation

Nanorings have several exciting and novel size- and shape-dependent properties that are discussed in the previous section. They are expected to play a prominent role in the advanced technologies of future owing to their potential applications in VMRAM devices, nanocontainers for spectroscopy, and as nanoscale sensors. The present investigation is focused on the formation of amorphous carbon nanorings, a possible template to make metal and metal oxide nanorings. This work reports a new method to form nanorings of amorphous carbon and discusses their formation mechanism.

.

2.4 Experimental section

2.4.1 Synthetic procedure for carbon nanorings

SBA-15 mesoporous silica rods were synthesized inside the porous anodic alumina membrane (AAM) using a literature procedure (41). In a typical synthesis, 0.6 g of Pluronic P123 (Aldrich) was dissolved in 1 ml of ethanol followed by the addition of 1 ml of tetraethoxyorthosilicate (TEOS) (Aldrich) and 0.4 ml of 0.1 M HCl solution. Anodic alumina membrane (13 mm diameter, 60 μm thick with a uniform pore size of 200 nm, Whatman® Anodisc 13) was soaked in the above sol for overnight. The membrane was dried after taking out of the sol and calcined at 500 °C for 5 h at a heating rate of 1 °C/min. The calcined membrane was then treated

in 1.5 ml of 6 M HCl solution for 24 h and then taken out of acid solution, dried and ground in a mortar with the addition of 1 – 2 ml of CCl₄ into it. The solution was drop-casted on a carbon coated copper grid and used for the transmission electron microscope (TEM).

2.4.2 Sample characterization

The as-prepared carbon nanorings samples were characterized using field-emission scanning electron microscope (FE-SEM, FEI Nova-Nano SEM-600, The Netherlands) and transmission electron microscope (JEOL JEM-3010 with an accelerating voltage at 300 kV). Electron energy loss spectra (EELS) were recorded using transmission electron microscope (FEI, TECNAI F30) equipped with an energy filter for (EELS) operating at 300 kV.

2.5 Results and discussion

Nanorings were observed on TEM grids (carbon coated copper grids) when solution containing the residue of the acid etched anodic alumina membrane in carbon tetrachloride was drop-casted onto them. Figure 10a shows the FESEM image of the sample obtained after 24 h acid treatment. The rings were different sizes with diameter ranging from 0.5 to 20 μm. The histogram (Inset figure) shows the wide distribution of the ring sizes with the maximum at 2 μm diameter. Rings of smaller diameter (< 2 μm) are clearly seen in the higher magnification image. The

smaller rings are exhibiting a smooth, but slightly tapered rim surface of thickness about 140 nm (Figure 10b) whereas, the larger ones (above 5 μm diameter) show a rope like rim structures of width about 80 nm (Figure 12b). Occasionally, rims of fiber like morphology with pinched holes also appear for larger rings (Figure 10c).

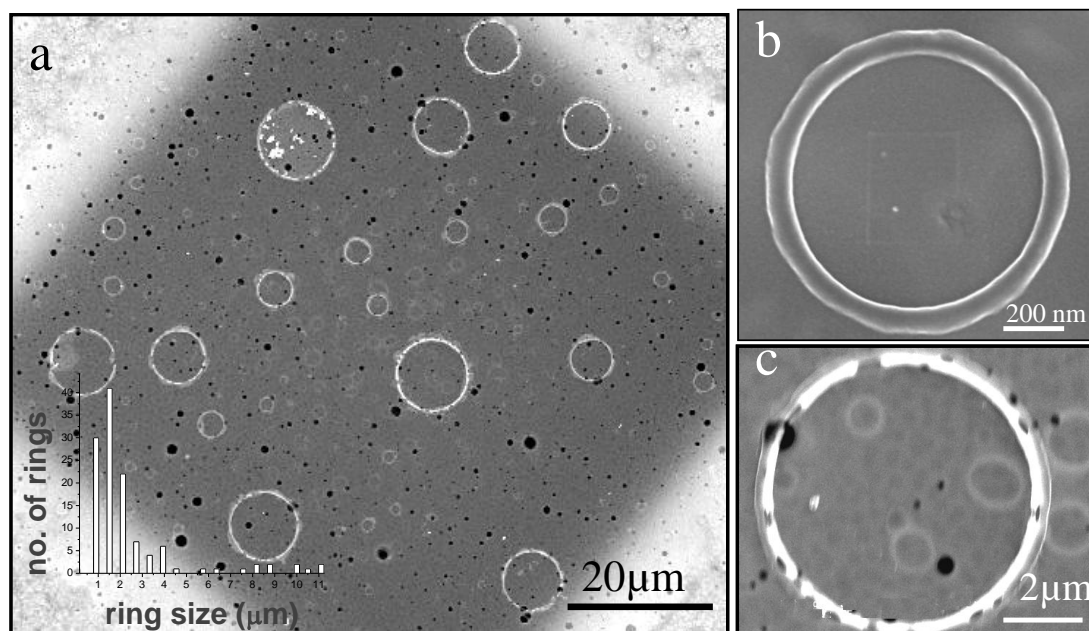


Figure 10: FESEM image of carbon nanorings obtained after 24 h HCl treatment (a) low magnification image (b) image of a single carbon nanoring (c) rings formed within a ring. Inset shows the size distribution profile

In many cases, the inner circle of the larger rings was decorated with smaller rings (Figure 10c). The tilted FESEM image (Figure 11) of a 1 μm diameter ring indicates that the height of the rim could be around 50 nm. TEM images of the unstained rings show a perfect tori structure with no beginning or end (Figure 12a and 12b). The thickness of the rim falls between 50 and 230 nm irrespective of the diameter of the rings. Occasionally, overlapping of the rings was also observed

(Figure 12c). Incomplete/open rings were also found randomly over the substrate during their formation (Figure 12d). This observation led us to the conclusion that the mechanism of ring formation in our case is different from that of coffee-stain or pin-hole mechanism since in either of these two mechanisms there is no possibility of forming rings within rings.

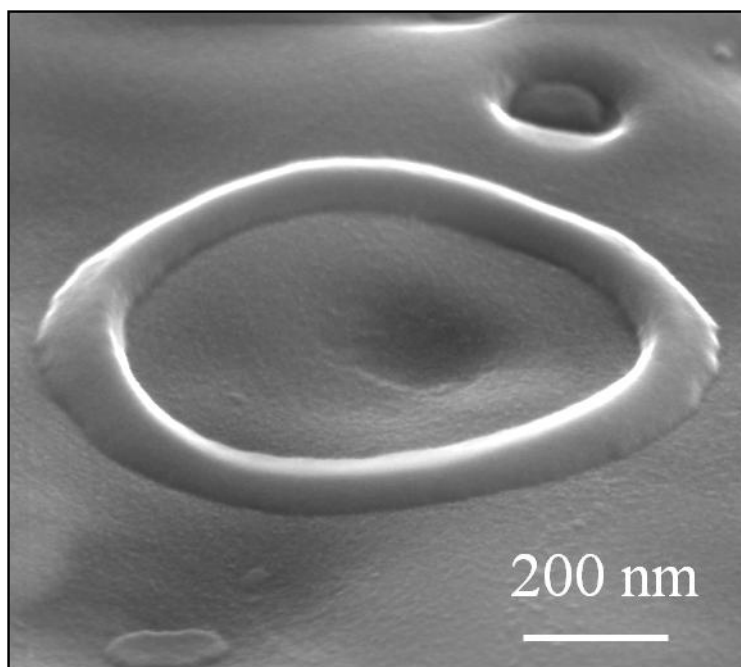


Figure 11: High magnification image of a single carbon nanoring tilted at 60° showing 3-D ring structure.

Invariably, the rings observed in TEM are near-perfect circles except, in a few cases where unclosed loop structures are seen (Figure 12d). In almost all the cases, the inner edge of the rings appears to be smooth compared to the rough outer edge. The smaller rings further display a near-uniform thickness around the circumference whereas, local variations in thickness are observed for the larger rings

(of sizes above $5\ \mu\text{m}$) along the circle. High resolution electron microscope (HREM) images of some of these rings show the presence of pores of diameter less than $1\ \text{nm}$ (Figure 12e).

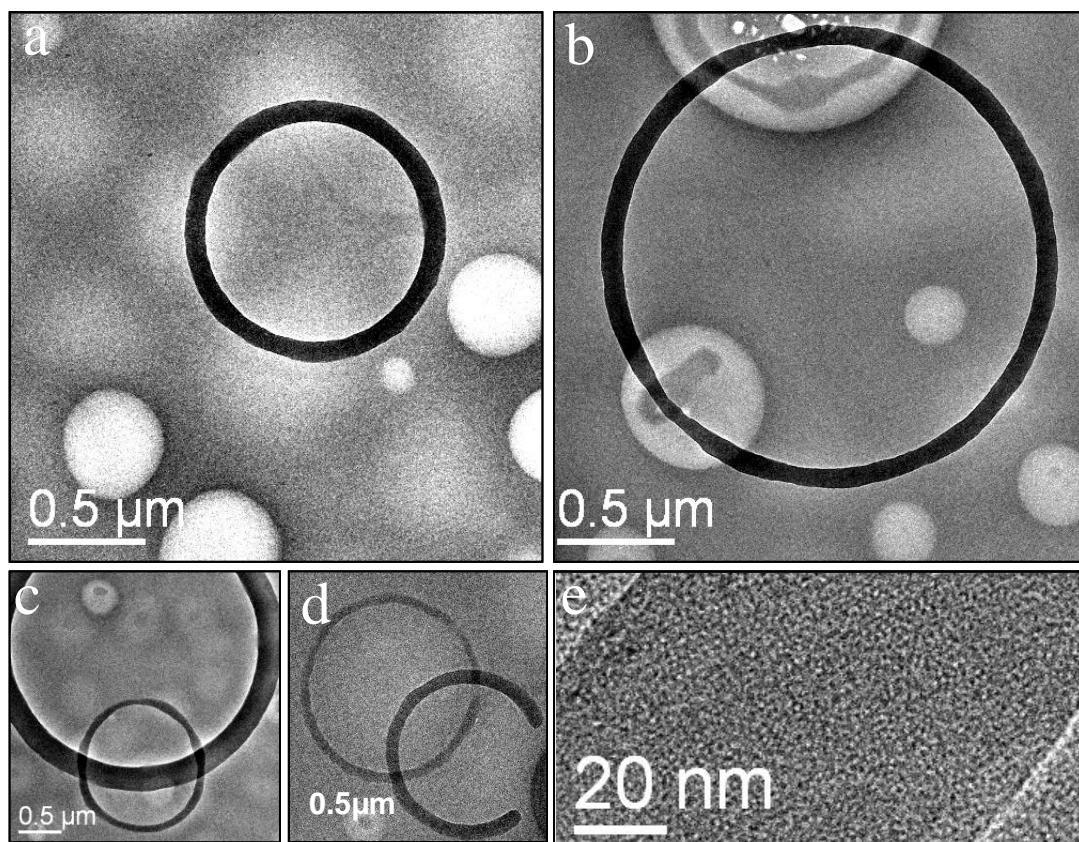


Figure 12: TEM images showing (a, b) perfect carbon tori structure, (c) overlapping rings, and (d) an incomplete ring. (e) HREM image of a carbon nanoring showing its amorphous nature.

The elemental composition of the rings has been found using Electron energy loss spectra (EELS). Figure 13 shows the EELS spectra of the carbon nanorings which corroborates the presence of carbon and oxygen. The characteristic peak for C 1s is observed at $284\ \text{eV}$ and for O 1s at $538\ \text{eV}$.

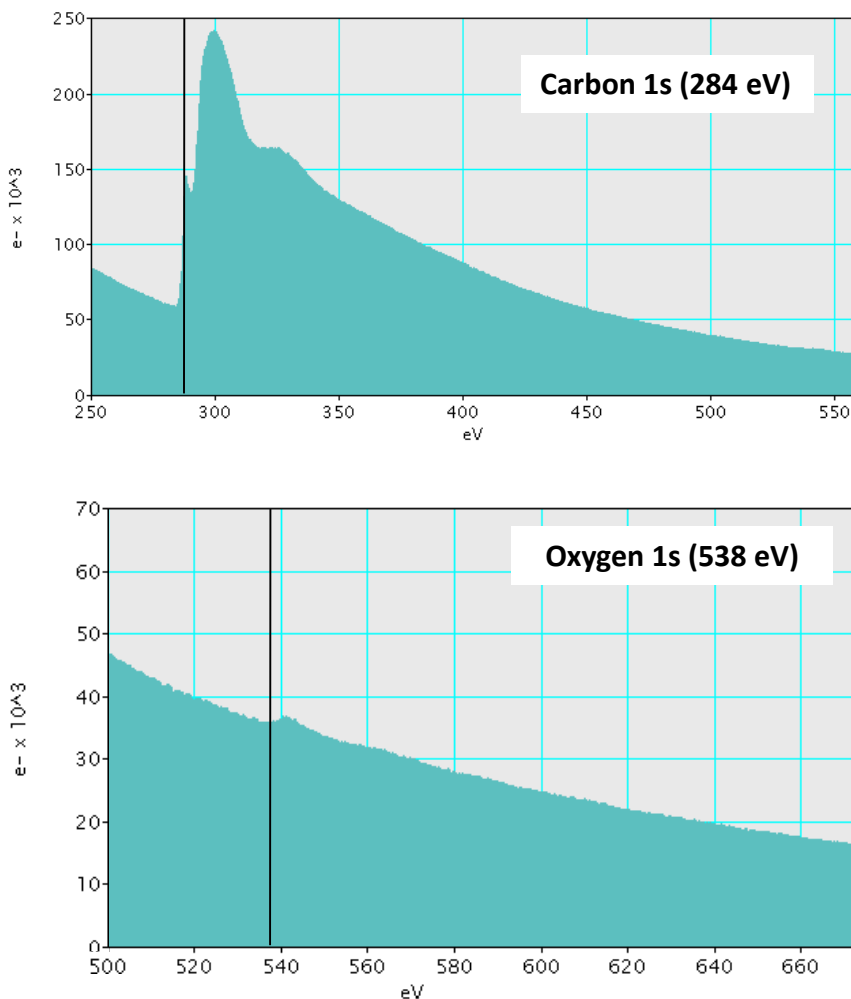


Figure 13: Electron energy loss spectra (EELS) of the rings showing the characteristic peaks for carbon and oxygen.

It is evident from our experiments that the presence of P123 is necessary for ring formation. Separate experiments making silica under the same conditions without adding P123 did not yield any ring structure. Similarly, P123 alone in the alumina membrane on calcination at 500 °C failed to show any ring structures (Figure 14a). In order to check the role of SBA-15 in the formation of ring structure, we carried out the same experiments in the bulk as-synthesized SBA-15 (without

alumina membrane). The TEM analysis does not show formation of rings (Figure 14b). Moreover, P123 polymer kept in a crucible at 500 °C in presence of air for 5 h did not leave any residue. However, under a nitrogen atmosphere at 500 °C, the crucible turned black indicating carbon deposition on the surface of the crucible. Analysis of this residue by TEM failed to show ring like structures.

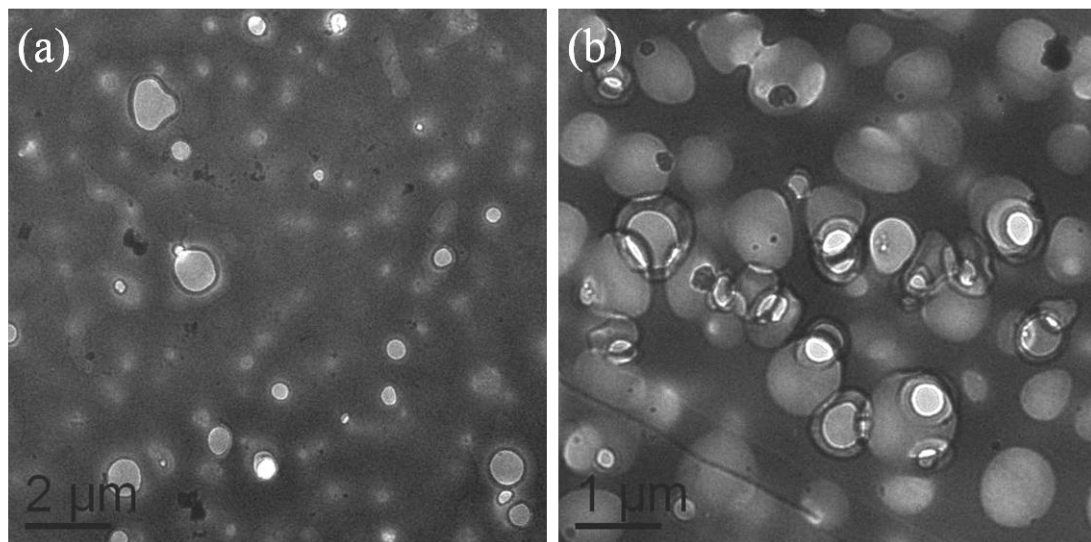


Figure 14: TEM images of the samples obtained with (a) P123 alone without using SBA-15 and (b) SBA-15 without using alumina membrane.

We believe that the presence of alumina and silica walls obstruct the oxygen diffusion into the mesopores. Calcination in such an oxygen deficient environment carbonizes the P123 polymer inside the mesopores of SBA-15. Acid treatment partially etches the mesopores facilitating the removal of compartmentalized carbonized nanostructures from the mesopores. The carbonized structures are rendered hydrophilic during the acid treatment process. On grinding with CCl_4 , the carbonized nanostructures get dispersed into the solvent. Drop casting the solution on a carbon coated copper grid containing nucleated water droplets on its

hydrophobic surface, result in the displacement of water droplets by the high density CCl_4 . The carbonized nanostructures revolve around the water droplets and form the ring structures on evaporation. The formation process of the amorphous carbon ring structures is shown in the schematic diagram (Figure 15).

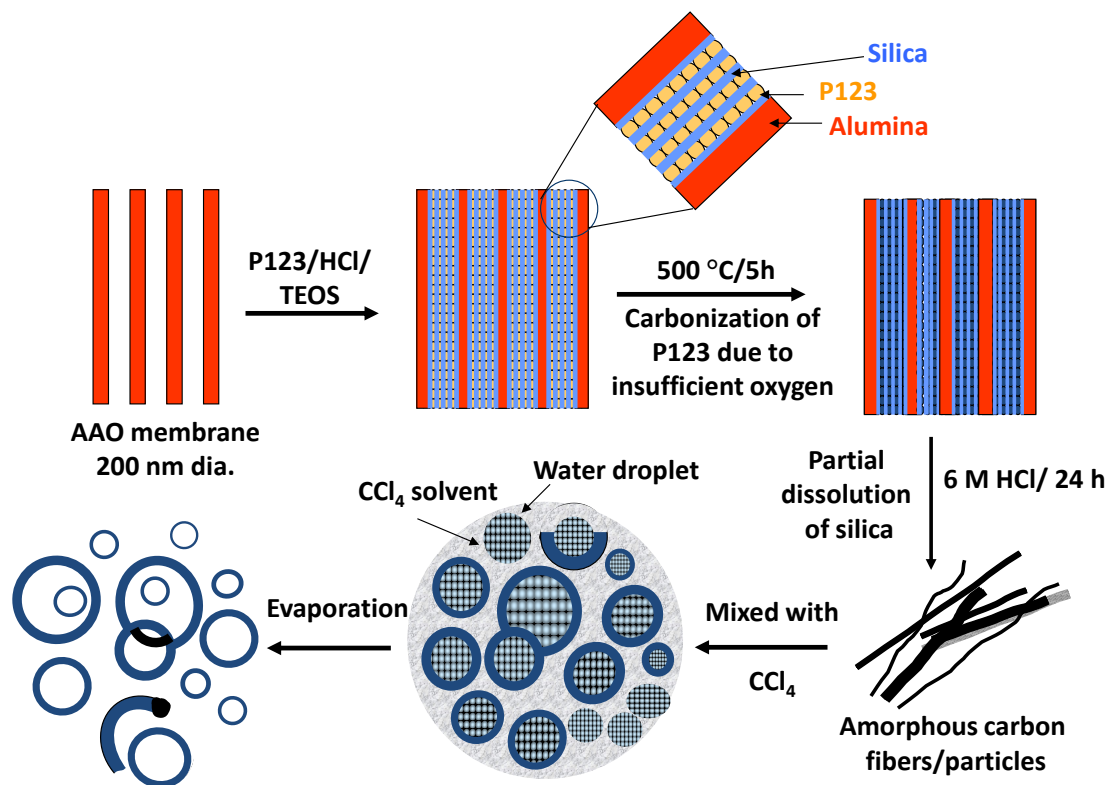


Figure 15: Schematic of amorphous carbon nanorings formation

This is analogous to ring formation by the carbon nanotubes around sonication- induced cavities (39). At temperatures above 500 °C, the continuity of the ring structure is not maintained in many of the rings due to the loss of the carbon structure as shown in Figure 16a and 16b.

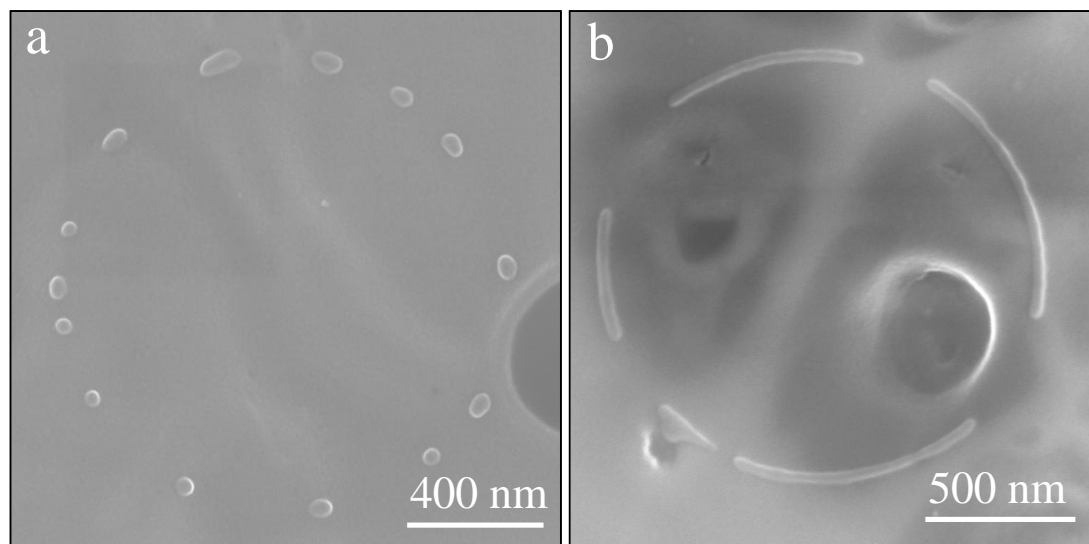


Figure 16: FESEM images showing discontinuous ring structure at 550 °C with (a) carbon nanoparticles (b) amorphous carbon fibers at the periphery.

2.6 Conclusion

In summary, this chapter describes about a novel method of formation of amorphous carbon nanorings. The rings are formed from the carbon nanostructures that have been organized to form rings at the liquid–liquid interface. These nanostructures were obtained by carbonizing the Pluronic P123 template of mesostructured SBA-15 confined in an anodic alumina membrane. The carbon nanorings can be envisaged as templates to make metal and metal oxide replica with hollow ring structures that have interesting optical and magnetic properties.

2.7 References

1. S. Mann and G. A. Ozin, *Nature* **1996**, 382, 313.
2. S. Mann, *Angew. Chem.*, **2000**, 112, 3532-3548; *Angew. Chem. Int. Ed.*, **2000**, 39, 3392.
3. Z. L. Wang, *J. Phys: Condens. Matter.*, **2004**, 16, R829.
4. H. Yang, N. Coombs and G. A. Ozin, *Nature* **1997**, 386, 692.
5. Y. Xia, Y. Xiong, B. Lim and S. E. Skrabalak, *Angew. Chem. Int. Ed.*, **2009**, 48, 60.
6. S. Mann, in *Biomineralization: principles and concepts in bioinorganic materials chemistry* Oxford University Press, Oxford, **2001**.
7. K. S. Krishna, U. Mansoori, N. R. Selvi and M. Eswaramoorthy, *Angew. Chem. Int. Ed.*, **2007**, 46, 5962.
8. J. Dinesh, U. Mansoori, P. Mandal, A. Sundaresan and M. Eswaramoorthy, *Angew. Chem. Int. Ed.*, **2008**, 47, 7685.
9. C. Sanchez, H. Arribart and M.G. Guille, *Nature Mater.* **2005**, 4, 277.
10. H.R. Shea, R. Martel and Ph. Avouris, *Phys. Rev. Lett.* **2000**, 84, 4441.
11. L. Liu, G. Y. Guo, C. S. Jayanthi and S.Y. Wu, *Phys. Rev. Lett.*, **2002**, 88, 217206.
12. L. Liu, G.Y. Guo, C.S. Jayanthi and S.Y. Wu, *Phys. Rev. B* **2001**, 64, 033412.
13. N. Chen, M.T. Lusk, A. C. T. van Duin and W. A. Goddard III, *Phys. Rev. B* **2005**, 72, 085416.
14. A. Ceulemans, L.F. Chibotaru, S.A. Bovin and P.W. Fowler, *J. Chem. Phys.* **2000**, 112, 4271.

15. D-H. Oh, J. M. Park and K.S. Kim, *Phys. Rev. B* **2000**, 62, 1600.
16. C. Murray, C. Kagan and M. Bawendi, *Science*, **1995**, 270, 1335.
17. X. Peng, L. Manna, W. Yang, J. Wickham, E. Scher, A. Kadavanich and A. P. Alivisatos, *Nature* **2000**, 404, 59.
18. T. Vossmeier, S-W. Chung, W. M. Gelbart, and J. R. Heath, *Adv. Mater.*, **1998**, 10, 351.
19. G. Schmid, *Nanoparticles: From theory to Applications*, Wiley-VCH Publications, **2004**.
20. J. Aizpurua, P. Hanarp, D. S. Sutherland, M. Kall, G. W. Bryant and F. J. Garcí a de Abajo, *Phys. Rev. Lett.*, **2003**, 90, 057401.
21. J. Aizpurua, L. Blanco, P. Hanarp, D.S. Sutherland, M.K. Garnett, W. Bryant and F. J. Garcí a de Abajo, *J. Quant. Spec. Rad. Trans.*, **2004**, 89, 11.
22. Y. Rondelez, G. Tresset, K. V. Tabata, H. Arata, H. Fujita, S. Takeuchi and H. Noji, *Nat. Biotechnol.* **2005**, 23, 361.
23. Y. Aharonov and D. Bohm, *Phy. Rev.*, **1959**, 115, 485.
24. R. A. Webb, S. Washburn, C. P. Umbach and R. B. Laibowitz, *Phys. Rev. Lett.*, **1985**, 54, 2696.
25. H. Hu, J - L Zhu, D - J Li and J - J. Xiong, *Phys. Rev. B* **2001**, 63, 195307.
26. F. Q. Zhu, D. Fan, X. Zhu, J. G. Zhu, R. C. Cammarata and C-L-Chien, *Adv. Mater.*, **2004**, 16, 2155.
27. F. Q. Zhu, G. W. Chern, O. Tchernyshyov, X. C. Zhu, J. G. Zhu and C. L. Chien, *Phys. Rev. Lett.* **2006**, 96, 027205.

28. M. C. Lensen, K. Takazawa, J. A. A. W. Elemans, C. R. L. P. N. Jeukens, P. C. M. Christianen, J. C. Maan, A. E. Rowan and R. J. M. Nolte, *Chem. Eur. J.*, **2004**, *10*, 831.
29. H. A. M. Biemans, A. E. Rowan, A. Verhoeven, P. Vanoppen, L. Latterini, J. Foekema, A. P. H. J. Schenning, E.W. Meijer, F. C. de –Schryver and R. J. M. Nolte, *J. Am. Chem. Soc.*, **1998**, *120*, 11054.
30. A. P.H.J. Schenning, F. B. G. Benneker, H.P.M. Geurts, X. Y. Liu and R. J. M. Nolte, *J. Am. Chem. Soc.*, **1996**, *118*, 8549.
31. R. D. Deegan, O. Bakajin, T. F. Dupont, G. Huber, S. R. Nagel and T. A. Witten, *Nature (London)*, **1997**, *389*, 827.
32. D. J. Pochan, Z. Chen, H. Cui, K. Hales, K. Qi and K. L. Wooley, *Science*, **2004**, *306*, 94.
33. X. Y. Kong, Y. Ding, R. Yang and Z. L. Wang, *Science*, 2004, *303*, 1348.
34. O. D. Velev, E. W. Kaler, *Adv. Mater.* **2000**, *12*, 531.
35. H. Xu, W. A. Goedel, *Angew. Chem. Int. Ed.*, **2003**, *42*, 4696.
36. F. Yan, W. A. Goedel, *Angew. Chem. Int. Ed.*, **2005**, *44*, 2084.
37. F. Yan, W. A. Goedel, *Nano lett.*, **2004**, *4*, 1193.
38. J. Liu, H. Dai, J. H. Hafner, D. T. Colbert, R. E. Smalley, S. J. Tans and C. Dekker, *Nature* **1997**, *385*, 780.
39. R. Martel, H.R. Shea and P. Avouris, *Nature* **1999**, *398*, 299.
40. M. Sano, A. Kamino, J. Okamura and S. Shinkai, *Science* **2001**, *293*, 1299.
41. D. Wang, R. Kou, Z. Yang, J. He, Z. Yang and Y. Lu, *Chem. Comm.* **2005**, 166.

Chapter 3

Chapter 3 of the thesis investigates the synthesis of bowl-shaped structures employing three different synthetic approaches. The chapter therefore is divided into 3 parts:

Part 1: ZnO Bowls

Part 2: MnSO₄ Bowls

Part 3: Au Bowls

Chapter 3: Part 1

**Bowls: Temperature-Induced Self-Assembly
and Growth of ZnO Nanoparticles into
Zeptoliter Bowls and Troughs**

Summary

This first part of the chapter deals with the temperature-induced self assembly and growth of ZnO nanoparticles to form superstructures like bowls and troughs. Calcination of zinc nitrate – polymer (polyvinylpyrrolidone) composite film produces ZnO nanoparticles within the polymer at the initial stage which then coalesces to give interesting bowl and trough shaped structures at high temperatures. The formation process occurs via intermediates blade-like and mesoporous disc-like structures. The mechanism of bowls formation has been elucidated by carrying out experiments at different temperatures and studying their intermediate morphologies. Further, the chapter deals with the application of the bowls and ring-like structures as templates to form SiO₂ and gold analogues.

Paper based on the above study has been published in *Angew. Chem. Int. Ed.* **2007**, *46*, 5962.

3.1 Introduction

Construction of complex morphologies by controlled growth and organization of nanoparticles at multiple-length scales is one of the challenging tasks in materials synthesis (1, 2). Inorganic nano- and microstructures of prevalent shapes like rods, tubes, and spheres can be readily built from colloidal and ligand-stabilized nanoparticles (3-5) through self-assembly processes. However, engineering complex forms to parallel naturally existing biominerals is not a simple task and demands many new synthetic approaches (6-8). ZnO, an important wide-band-gap semiconductor, finds applications in catalysis (9), solar cells (10), sensors (11), UV lasing (12) and photoelectronics (13). The properties of ZnO are closely related to its microstructures, particularly its crystal size, orientation, and morphology (14). Though a variety of ZnO nano- and microstructures of various shapes have been obtained by solid–vapor phase growth (SVG) (15-21), microemulsion (22), and hydrothermal methods (23), bowl and triangular trough-shaped structures have not explored so far. In this chapter, we investigate formation of unusual bowl-, trough-, and ring-shaped structures through a temperature-induced self-assembly and growth of ZnO nanoparticles.

3.2 Scope of present investigation

The current investigation focuses on a new method to form bowl and ring-shaped nanostructures of ZnO. The process involves temperature-induced self-assembly and growth of ZnO nanoparticles formed during the calcination of zinc

nitrate – PVP polymer composite film. The ZnO bowls and rings thus obtained were also used as a template to make gold and silica bowls and rings respectively.

3.3 Experimental section

3.3.1 Synthetic procedure for ZnO bowls

In a typical synthesis, $\text{Zn}(\text{NO}_3)_2 \cdot 6\text{H}_2\text{O}$ (0.50 g, Merck) was dissolved in ethanol (10 ml) and mixed with polyvinylpyrrolidone (1.00 g, Aldrich, $M_w=13,00,000$) to make a homogeneous, viscous slurry. The slurry was then poured into a glass petri dish (50 mm diameter) and aged for 10 h in an oven at 80 °C. The transparent film of zinc nitrate–PVP composite thus obtained was calcined at different temperatures (250, 370, 420, 470, and 600 °C) for a duration of 5 h with a heating rate of 1 °C/min. Calcinations at 470 °C for different durations (1, 5, and 8 h) were also carried out to understand the bowl formation. In all the cases the sample was cooled to room temperature at a rate of 3 °C/min.

3.3.2 Synthetic procedure for gold bowls and silica nanorings using ZnO bowls and nanorings as templates

a) To prepare gold replicas of the ZnO bowls, gold was sputtered onto a sample of ZnO bowls (10 mg) by using a plasma-induced sputtering technique for 2 minutes in an argon atmosphere, which resulted in a coating (*ca.* 60 nm) of gold over

the bowls. The ZnO was removed by soaking the gold sputtered sample in concentrated HCl solution for 5 min. Finally, the sample was washed thoroughly with deionized water and dried at room temperature.

b) Silica nanorings were obtained by dispersing ZnO nanorings (30 mg) in 2-propanol (3 ml). De-ionized water (0.4 ml), ammonia solution (0.1 ml), and tetraethylorthosilicate (TEOS, 0.06 ml) were consecutively added with stirring. The stirring was allowed to continue for 3 h, and a white product was collected after 3 h. The product was filtered and the precipitate was washed several times with de-ionized water and subsequently anhydrous ethanol. The product (ZnO/SiO₂ core-shell nanorings) was then dried at room temperature. Soaking the product in 6 M HCl solution at room temperature for 3 h removed the ZnO and left the silica rings intact. The solution was filtered and the precipitate was washed several times with de-ionized water and anhydrous ethanol to obtain silica nanorings.

3.3.3 Sample characterization

The morphologies of the samples obtained were examined with field-emission scanning electron microscope (FESEM, FEI Nova-Nano SEM-600, The Netherlands) and transmission electron microscope (JEOL JEM-3010 with an accelerating voltage at 300 kV). Powder X-ray diffraction (XRD) patterns were obtained using a Rich-Siefert 3000-TT diffractometer employing CuK α radiation. Thermogravimetric analysis (TGA) was carried out with a Mettler Toledo TGA 850

instrument. N₂ adsorption–desorption isotherms were measured using a Quantachrome Autosorb-1C surface-area analyzer at liquid nitrogen temperature (77 K). Atomic force microscope images of the nanobowls were acquired in tapping mode on a Digital Instruments CP II AFM (Veeco Instruments Inc., Santa Barbara, CA).

3.4 Results and discussion

ZnO bowls were obtained by calcination of zinc nitrate/polyvinylpyrrolidone composite film (wt/wt ratio 0.5) at 600 °C for 5 h. Figure 1a shows a field-emission scanning electron microscopy (FESEM) image of the ZnO bowls formed in good yield. The outer diameter of the bowls varies from 300 nm to 1 μm. The background of the image shows a porous network made up of ZnO nanoparticles of size 30 to 80 nm. The bowls are not fully circular and in some cases they are faceted. The widths of the rims are in the range of 80 to 100 nm (Figure 1b). The bowls have a coarse inner surface owing to variation in the sizes and shapes of the particles from which they are made. The inner core of the bowl shown in Figure 1b is composed of small particles, and its outer edge is formed by the fusion of large, elongated particles, which resembles the formation of microstructures of cocolith by the fusion of nanometer-scale calcite particles (6).

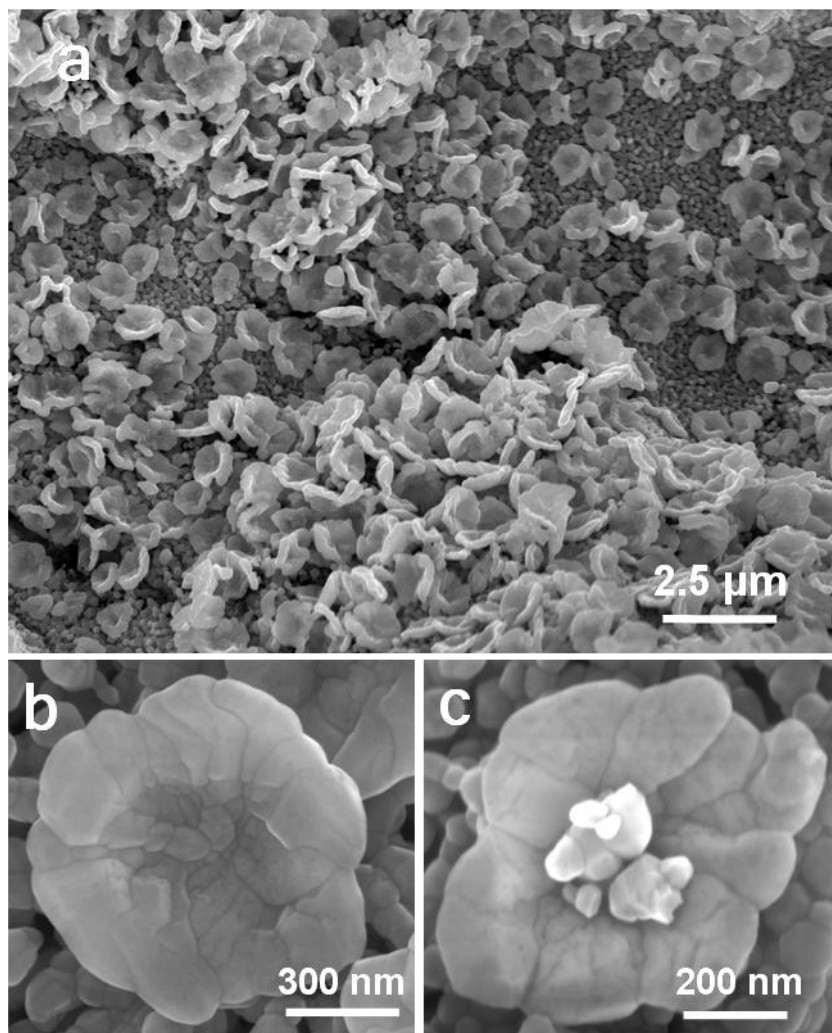


Figure 1: Field emission scanning electron microscopy (FESEM) images of ZnO bowls formed at 600 °C. (a) low magnification image showing high yield of sub-micron ZnO bowls (b) High magnification image of a single bowl shows that it is formed by the fusion of irregular shaped ZnO nanoparticles (c) ZnO bowl holding nanoparticles of ZnO.

An ultra-small container fortuitously holding the ZnO nanoparticles of different sizes between 50 and 150 nm is shown in Figure 1c. An atomic force microscopy (AFM) image and the height-profile analysis of a single bowl of size 300

nm show its depth to be around 90 nm. The volume calculated for a single bowl of size 300 nm is about 1 zeptoliter (Figure 2).

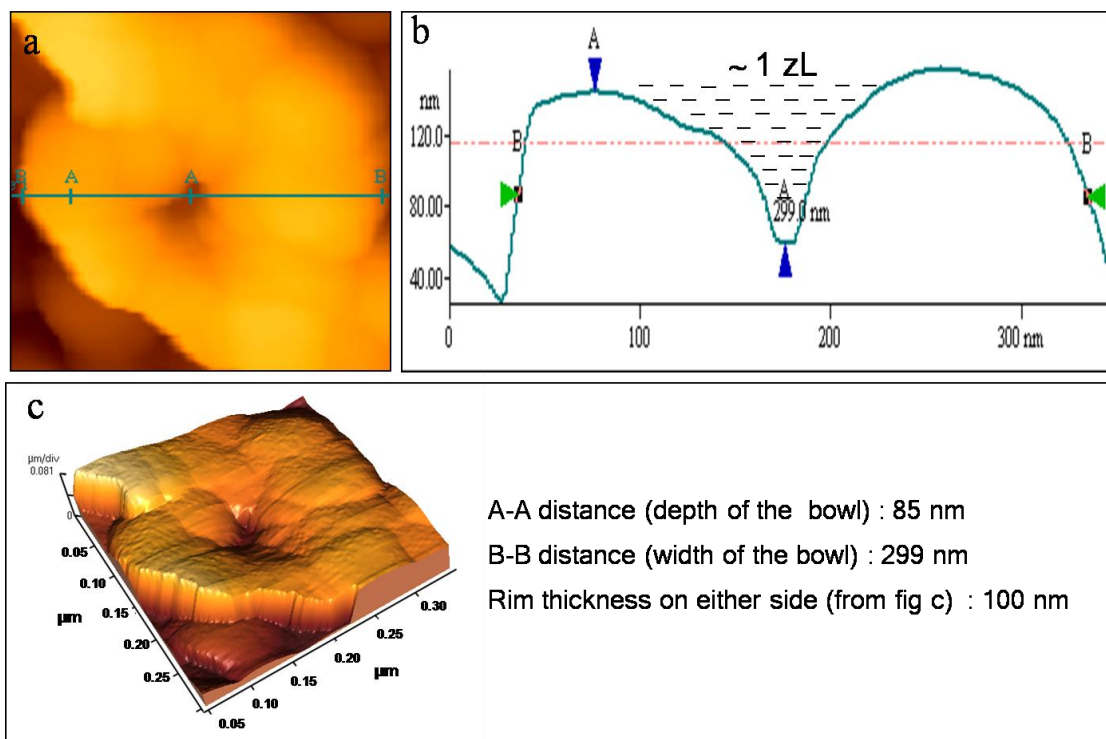


Figure 2: AFM tapping mode image showing (a) Top-view of a single bowl of size 300 nm (b) Height profile showing the bowl dimensions (c) Topographic profile of the bowl seen in 3-D.

Synthesis of ZnO using low-molecular-weight ($M_w=40,000$) PVP polymer also resulted in bowl-shaped structures in good yield. The magnified image of one bowl of approximate size 500 nm is again made up of nanoparticles of various sizes and shapes (Figure 3a). However, the yield of ZnO bowls is decreased when the PVP ($M_w=13,00,000$) to zinc nitrate weight ratio is 0.75 (Figure 3b).

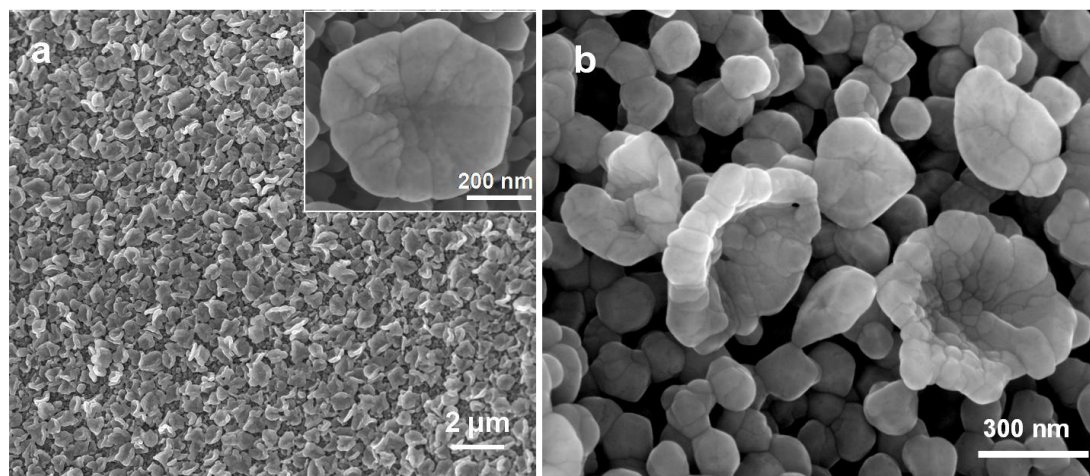


Figure 3: FESEM images of (a) ZnO bowls synthesized using low molecular weight polymer, polyvinylpyrrolidone (PVP to zinc wt. ratio is 0.5). Inset shows a single bowl of size 500 nm. (b) ZnO bowls synthesized at different PVP to zinc nitrate weight ratio (0.75). A closer look at the edges of a bowl shows that it is formed by the fusion of nanoparticles of size 70 to 100 nm.

To understand the role of PVP in the formation of ZnO bowls, we studied the morphology of ZnO–PVP composites calcined at different temperatures: 250, 370, 420, and 470 °C. These temperatures were selected on the basis of the decomposition temperatures of the precursors, zinc nitrate, and PVP, as obtained from thermogravimetric analysis (TGA; Figure 4). TGA shows that, at 370 °C, the zinc nitrate decomposes to ZnO, whereas the decomposition of PVP just begins. At 420 °C, the polymer is partially decomposed and, at 470 °C, it is decomposed completely.

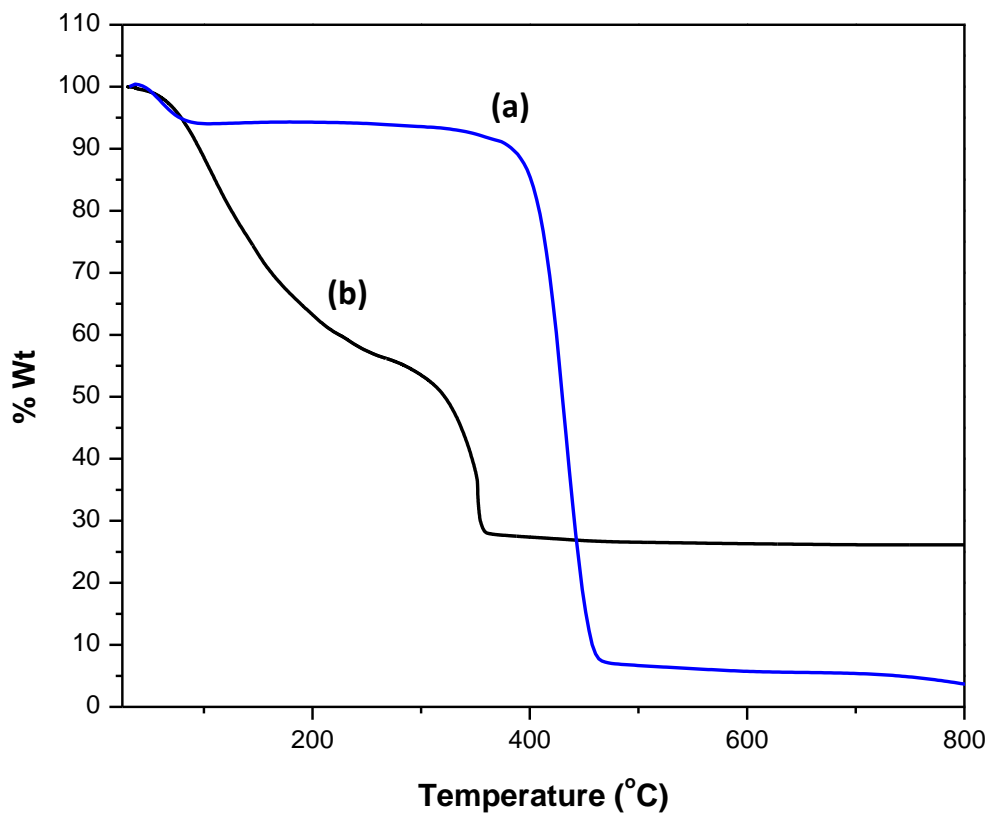


Figure 4: TGA curves of (a) Polymer, polyvinylpyrrolidone (blue line), (c) Zinc nitrate (black line)

The powder X-ray diffraction (PXRD) pattern (Figure 5) confirms the formation of ZnO nanoparticles in the composite even at 250 °C. The peak broadening at lower calcination temperatures is associated with the formation of smaller nanoparticles. At higher calcination temperatures, the well-resolved peaks obtained can be indexed to the ZnO wurtzite phase. The size of the ZnO nanoparticles increases with an increase in calcination temperatures, which is reflected in the sharpening of the peak line width in the PXRD pattern.

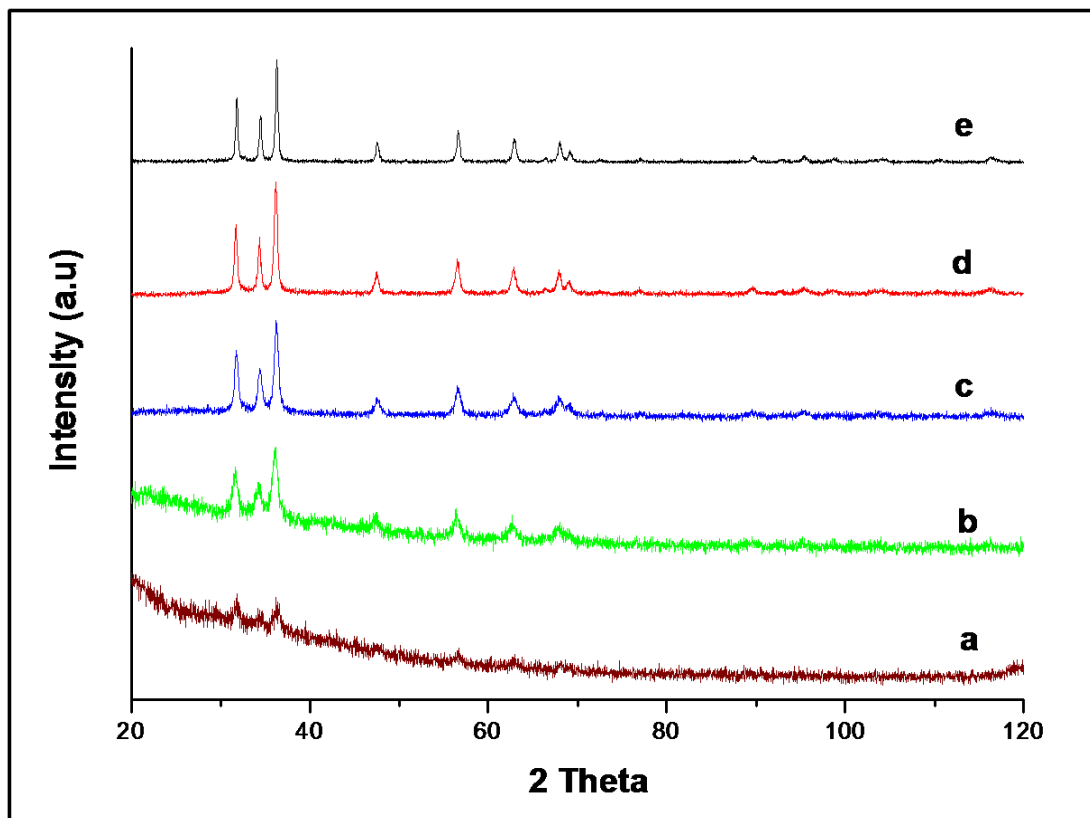


Figure 5: XRD pattern of ZnO bowls obtained at (a) 250 °C (brown curve), (b) 370 °C (green curve), (c) 420 °C (blue curve), (d) 470 °C (red curve), (e) 600 °C (black curve).

FESEM images of the samples calcined at 370 °C show that ZnO nanoparticles of size around 10 to 30 nm are well interspersed within the organic matrix (Figure 6a). Calcination at 420 °C for 5 h resulted in the formation of nanocomposite structures on the surface with blade-like morphologies of sizes between 100 and 400 nm (Figure 6b). A higher magnification image confirms the presence of an organic matrix studded with ZnO nanoparticles of sizes in the range 10 to 30 nm. Energy-dispersive X-ray analysis (EDX) of a blade-like nanostructure

confirms the presence of carbon and nitrogen from the polymer matrix. Further growth and organization of these blade-like structures with concomitant removal of the polymer during calcination at 470 °C for 5 h resulted in the formation of mesoporous disks (Figure 7).

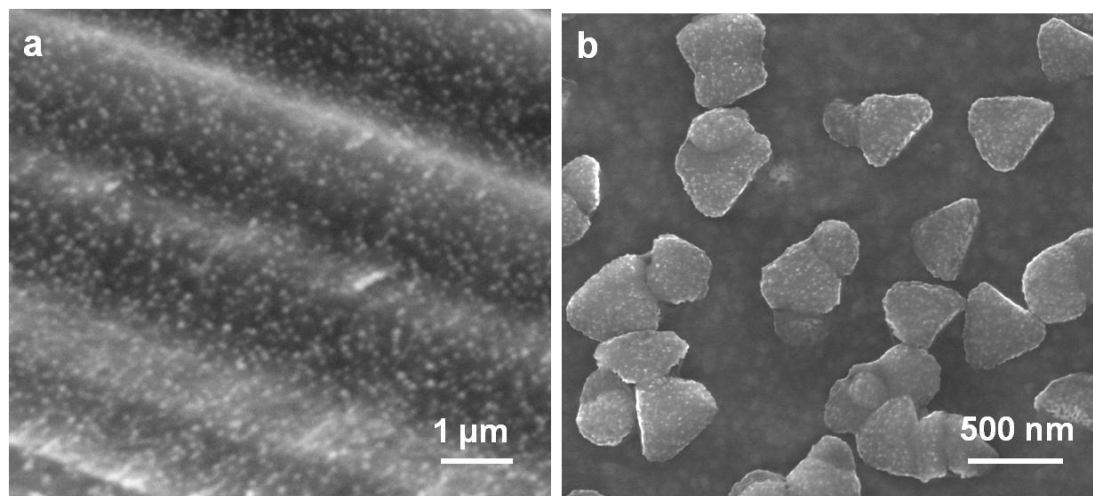


Figure 6: FESEM images showing intermediate morphologies at different calcination temperatures during the bowl formation. (a) at 370 °C (5 h), the precursor zinc nitrate in the composite film is completely decomposed into ZnO nanoparticles of size around 30 nm which are well dispersed within the partially decomposed polymer matrix (b) at 420 °C (5 h), a large number of ZnO-polymer nanocomposites of blade-like morphology in the size range of 100 to 200 nm emerges from the surface

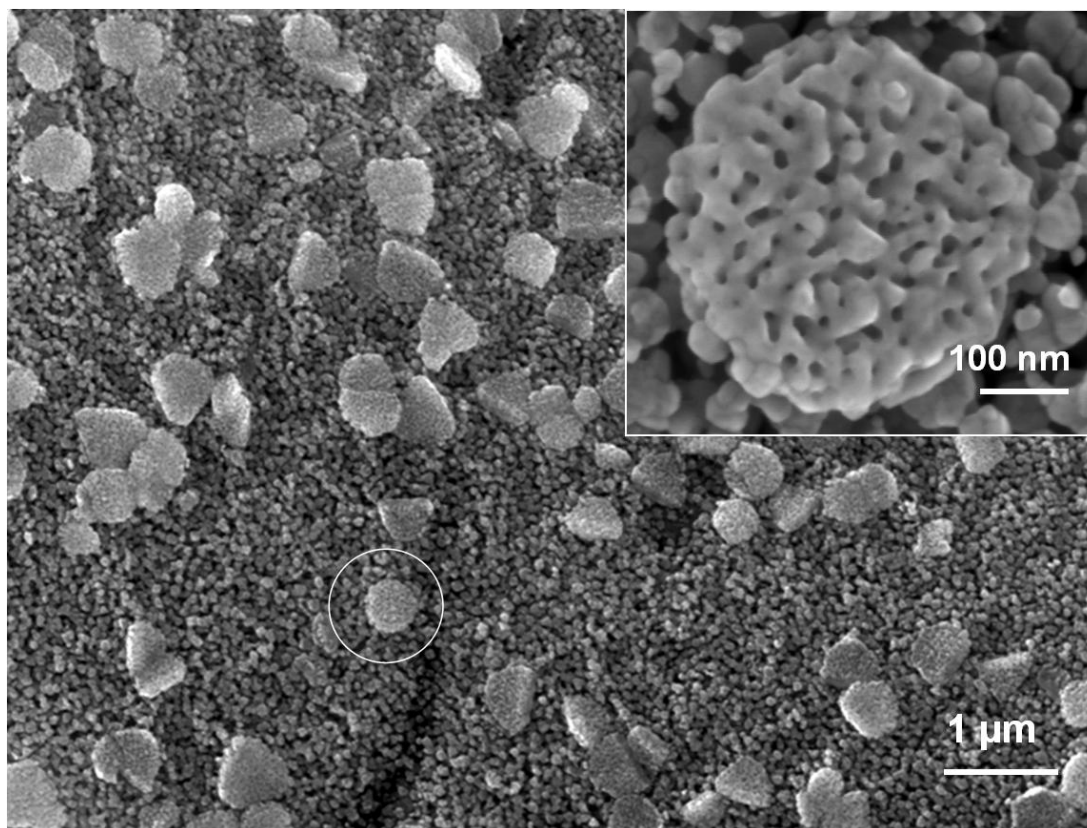


Figure 7: FESEM images of intermediates obtained at 470 °C (5 h), aggregation of blade-like structures and concomitant removal of polymer resulted in nanoporous ZnO discs. Inset: high magnification image of the encircled portion shows a single mesoporous disc. The sizes of the nanopores are in the range of 15-25 nm.

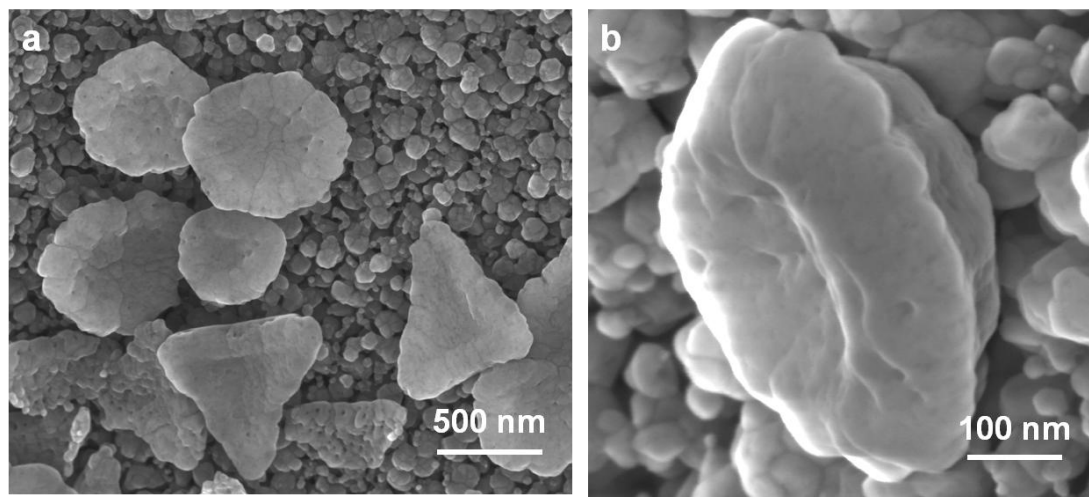


Figure 8: FESEM of the structures obtained at 470 °C (a) for longer duration (8 h) yields ZnO bowls and triangular troughs (b) side-on-view of a single ZnO bowl obtained at 470 °C with a rim thickness of 100 nm.

The enlarged image of a disk shown in the inset of Figure 7 indicates that the network of pores is made by the fusion of ZnO nanoparticles. The pore sizes in the disk are in the range 15 to 25 nm, and the thickness of the walls is about 20 nm. Extending the calcination time beyond 5 h at 470 °C up to 8 h modified these porous architectures into exotic morphologies such as bowls and triangular troughs (Figure 8a). The side-on view of a bowl shown in Figure 8b displays a rim thickness of about 100 nm. Prolonged heating (8 h) at the same temperature leaves no interconnected pores in these morphologies. However, the presence of many nanodents in the bowls is manifested from the lower electron-density contrast observed in the TEM image (Figure 9a). The electron diffraction pattern shows that the ZnO bowls are polycrystalline in nature (Figure 9b). A scanning transmission electron microscopy (STEM) image of a bowl with a nonporous surface shows many low-electron-density

spots, suggesting the existence of nanocavities inside the walls of the bowls (Figure 9c and 9d).

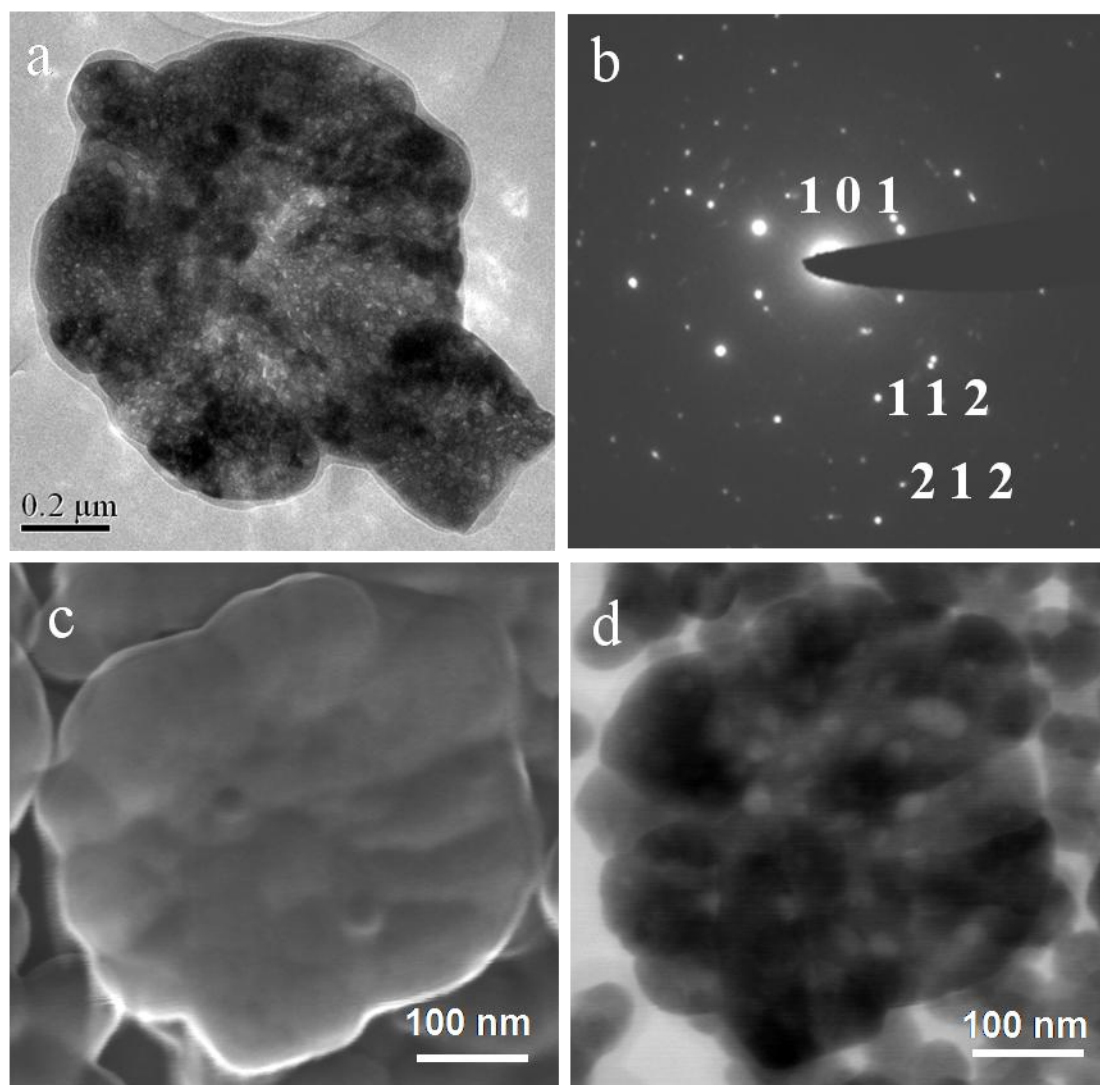


Figure 9: (a) TEM image of a single ZnO bowl with a handle (b) ED pattern showing the polycrystalline nature of the bowl (c) & (d) shows the FESEM and STEM image of the same bowl. White patches in the STEM image shows the low electron density regions indicating the presence of cavities inside the walls.

The Brauner–Emmett–Teller (BET) surface area for the samples calcined at 370 °C is well below 10 m²/g, mostly owing to the nonporous nature of the ZnO–PVP composite film. Removal of polymer upon calcination at 470 °C for 5 h increases the surface area to about 40 m²/g. The pore size analysis shows the appearances of additional mesopores of size 15 to 25 nm (Figure 10), which is in accordance with the pore size observed in the FESEM image (Figure 7). These larger pores, however, disappeared upon calcination of the samples at 600 °C, thus lending support to the transformation of mesoporous disks into sub-micrometer-sized bowls of ZnO. The corresponding BET surface area of the sample is around 28 m²/g.

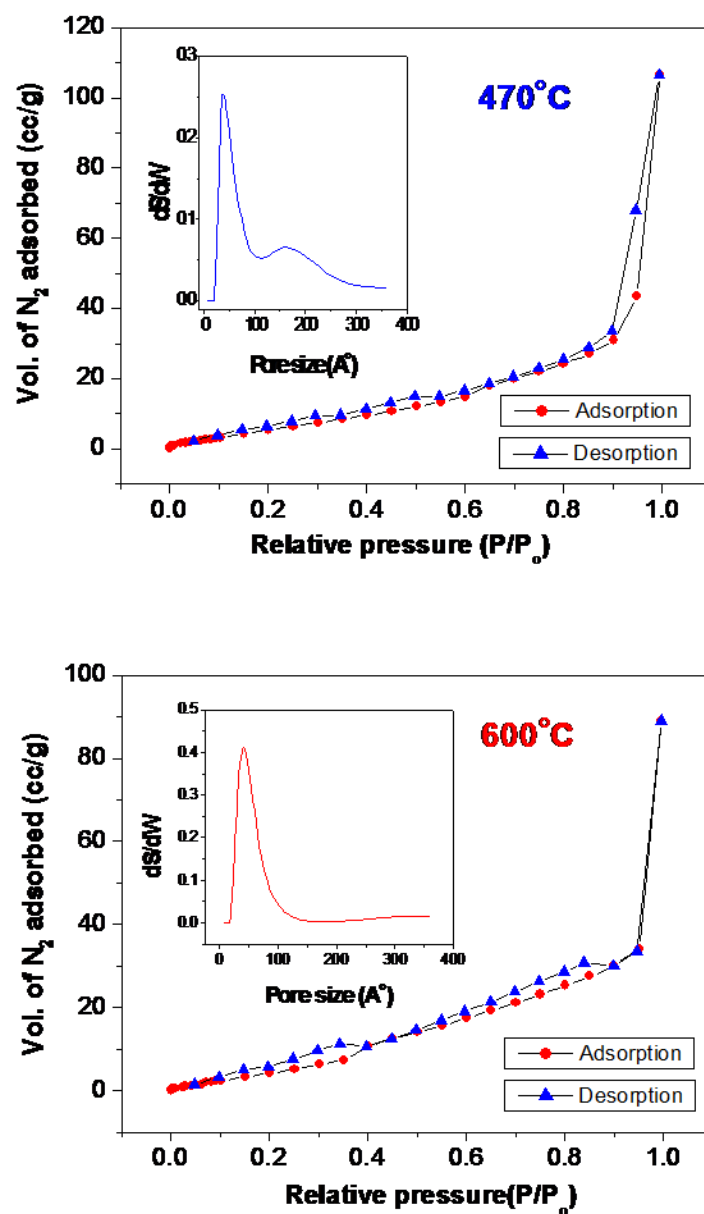


Figure 10: N₂ adsorption isotherms of the samples calcined at 470 °C and 600 °C. Inset in the figures shows the pore size distribution obtained by the density functional theory (DFT) method. The DFT pore size analysis shows the presence of mesopores of size in the range of 15 to 25 nm at 470 °C which are removed on calcination at 600 °C.

We have also studied the effect of heating rate on the morphology by increasing the calcination temperature of the zinc nitrate–PVP composite to 600 °C at a heating rate of 20 °C/min and kept at that temperature for 1 h before it was cooled to room temperature. Interestingly, we observed the formation of ring-shaped ZnO nanostructures (Figure 11 and 12).

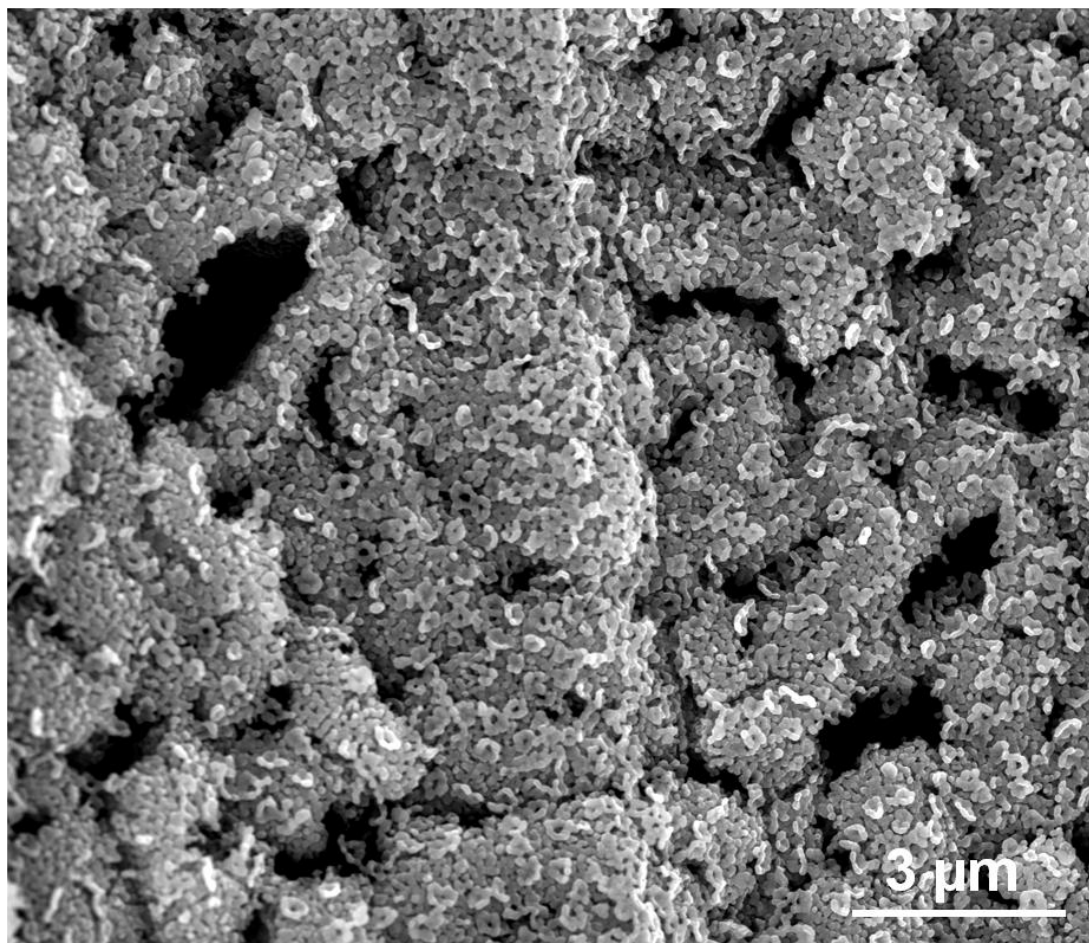


Figure 11: FESEM image of corrugated ring-shaped ZnO nanostructures obtained by calcination of the ZnO-PVP composite at 600 °C for 5 h duration with a faster rate of heating, 20 °C / min.

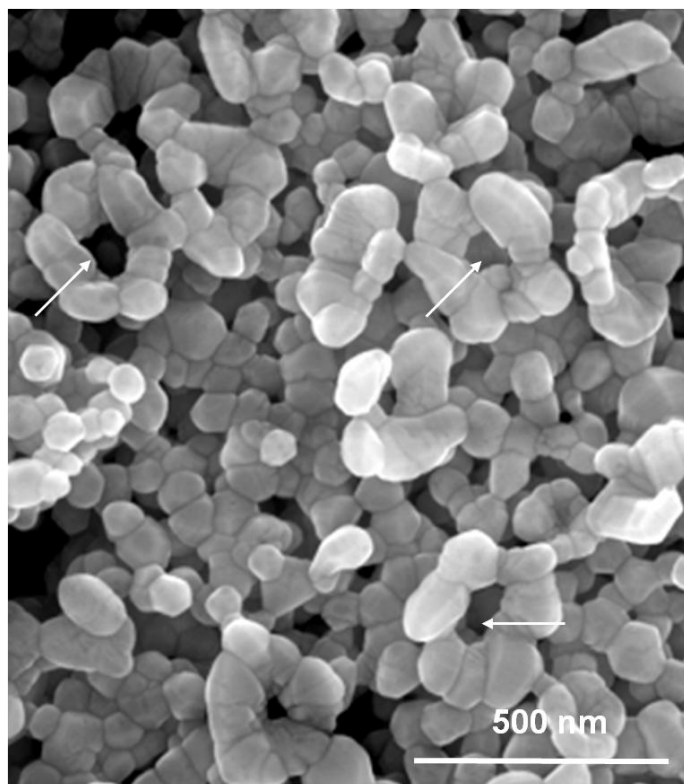


Figure 12: Higher magnification FESEM image shows the rings with arrows pointing towards the holes.

These nanorings are corrugated in shape and each ring is made up of around 10 to 12 nanoparticles of approximate size 50 to 80 nm. The outer diameters of the rings are between 200 and 300 nm, with the inner hole between 50 and 100 nm. The intermediate morphologies obtained at different calcinations temperatures and different time durations led us to believe that the bowls and triangular troughs emerge from the aggregation of two or three blade-like secondary structures (Figure 13). Figure 14 gives a schematic of the formation of these microbowls.

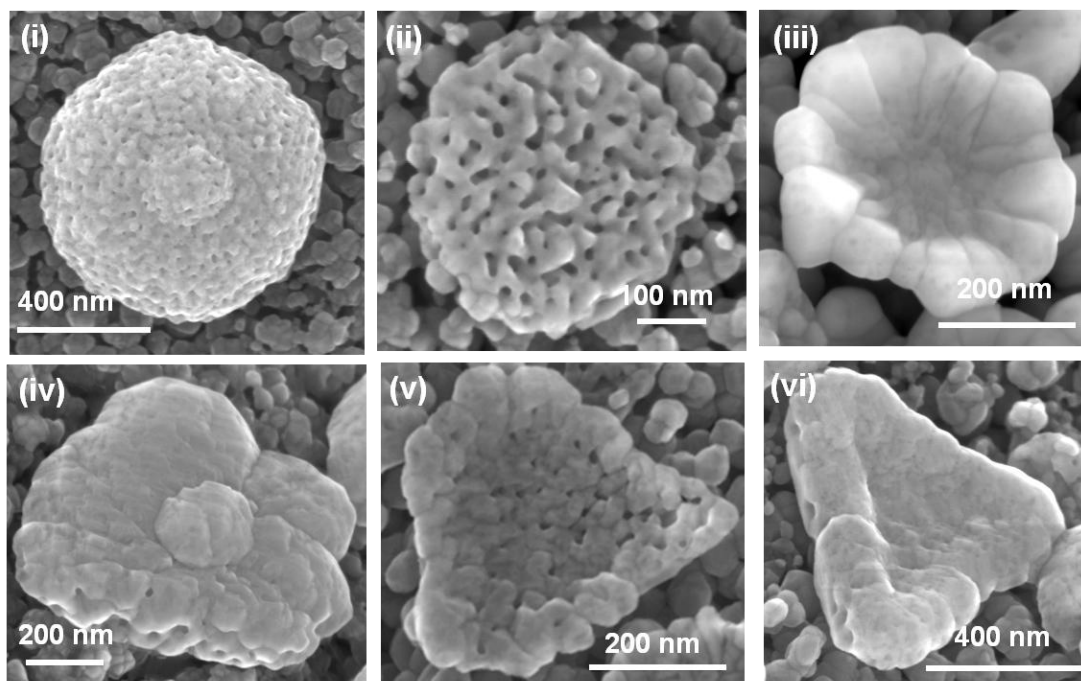


Figure 13: Extraction of intermediate morphologies for different calcination times at 470 °C: Emergence of bowl- and trough-like morphologies from the blade-like ZnO–PVP composite. (i, iv) Calcination of the composite at 470 °C for 1 h resulted in the formation of circular and triangular composite structures; (ii, v) calcination at 470 °C for 5 h resulted in a porous morphology owing to the removal of the polymer; (iii, vi) calcination at 470 °C for 8 h transformed these porous structures into zeptoliter bowls and triangular troughs.

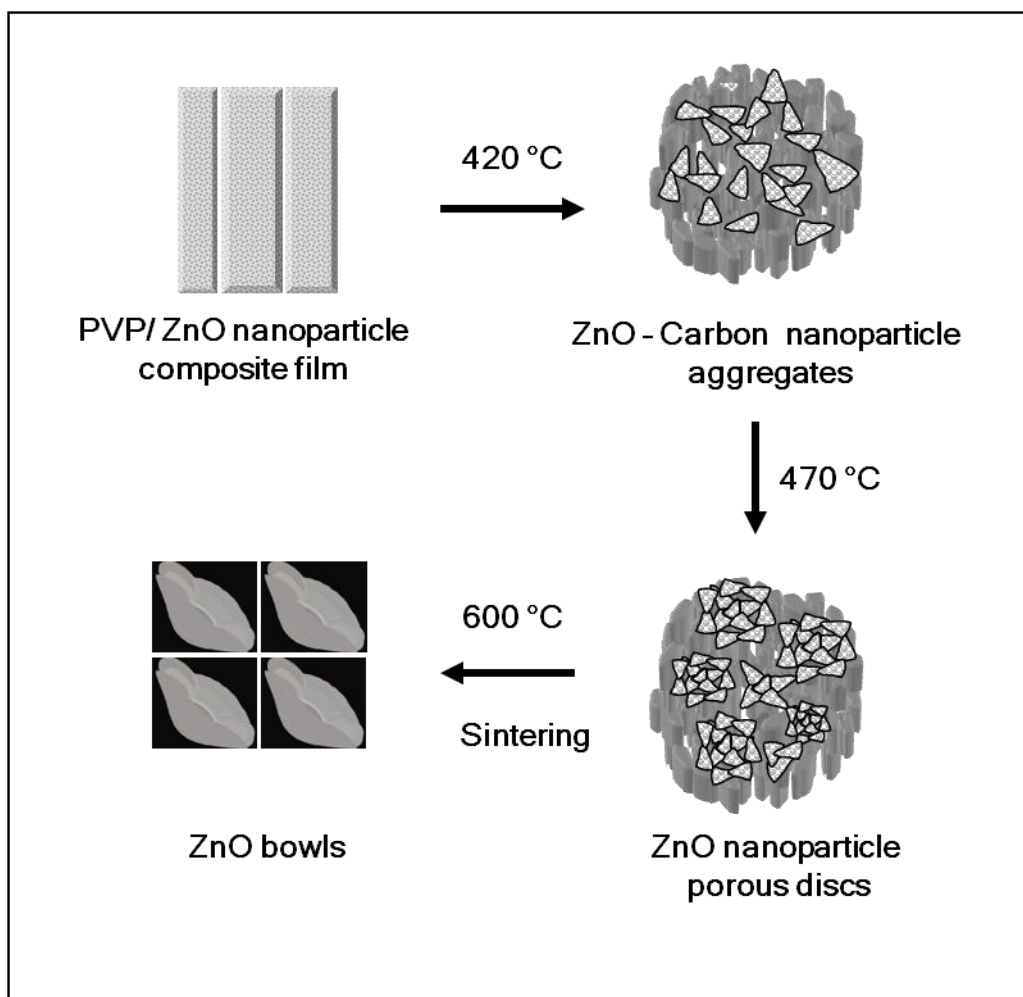


Figure 14: Schematic illustration of the formation of ZnO bowls.

The bowls could also be used as a template to synthesize various metal and metal oxide bowls. To prove this point, gold replicas were made by coating the ZnO bowls with gold by using plasma induced sputtering and subsequently etching the ZnO with concentrated HCl solution. Figure 15 shows the gold replicas of the bowls. The EDX analysis shows only gold peaks after acid treatment. Similarly, silica rings were also made by using ZnO nanorings as the template. The pearl-like silica

structures shown in Figure 15b are composed of 12 to 15 nanoparticles of about 50 nm in diameter.

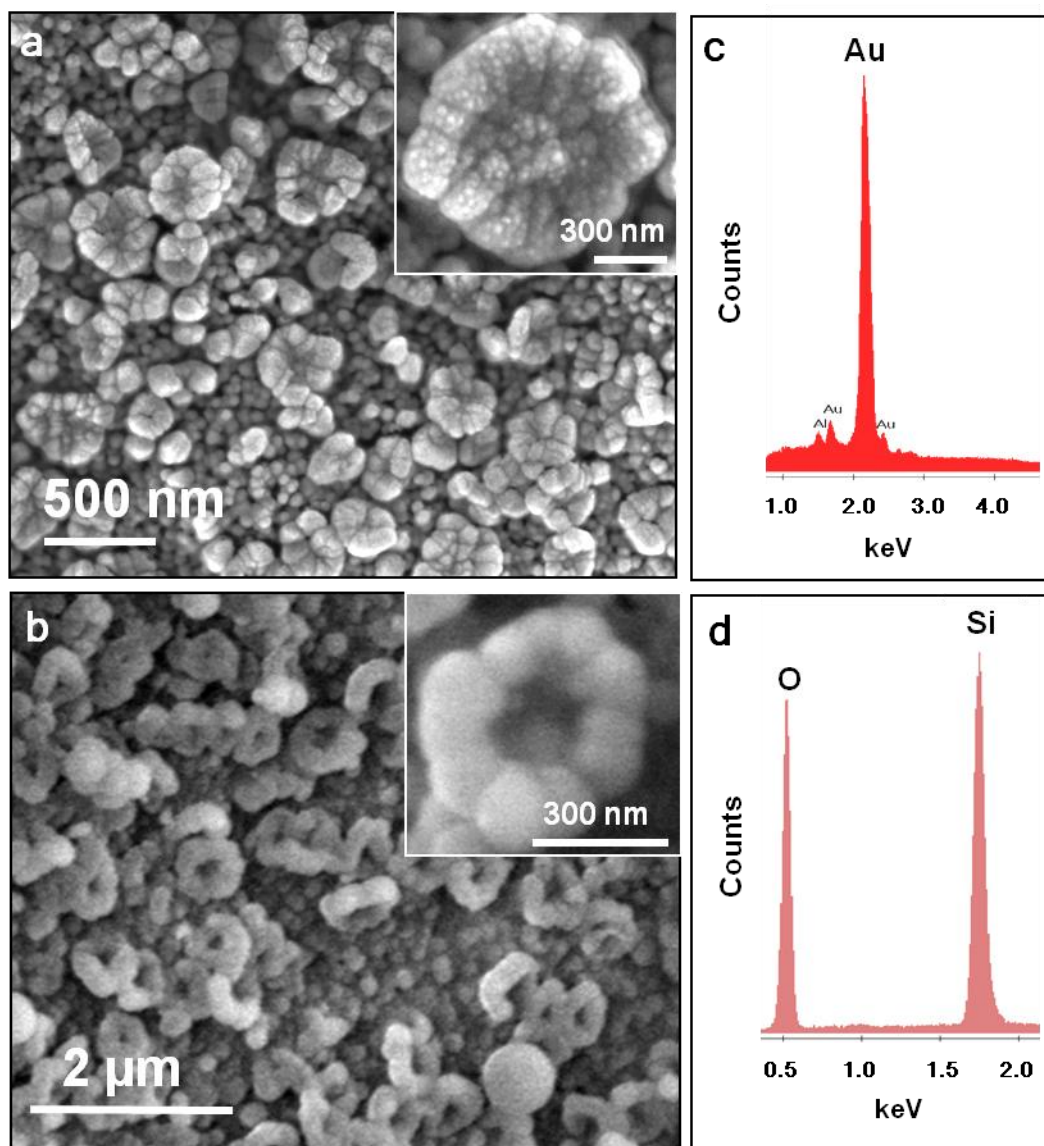


Figure 15: Metal and metal oxide replicas synthesized using ZnO bowls and rings as templates. (a) Gold bowls synthesized using ZnO bowls as the template. (b) Silica rings templated by ZnO rings. (c, d) The corresponding EDAX profile for Au

bowls and silica rings after the removal of ZnO. The Al peak arises from the sample holder.

3.5 Conclusions

In summary, this chapter describes a temperature induced self-assembly method to prepare zeptoliter bowls and troughs of ZnO. The tiny bowls are envisaged not only to hold fluids of ultralow volume (24), but also to be used to grow nanoparticles (25), immobilize biomolecules (26), and screen sub-micrometer-sized particles (27). In principle, it would be possible to prepare zeptoliter bowls of various metal oxides with this method by optimizing the synthesis conditions.

3.6 References

1. S. Mann and G. A. Ozin, *Nature* **1996**, 382, 313.
2. H. Yang, N. Coombs and G. A. Ozin, *Nature* **1997**, 386, 692.
3. J. Park, V. Privman and E. Matijevic, *J. Phys. Chem. B* **2001**, 105, 11630.
4. M. Li, H. Schnablegger and S. Mann, *Nature* **1999**, 402, 393.
5. C. Pacholski, A. Karnowski and H. Weller, *Angew. Chem. Int. Ed.* **2002**, 41, 1188.
6. S. Mann, *Biomineralization: Principles and Concepts in Bioinorganic Materials Chemistry*, Oxford University Press, Oxford, **2001**.
7. C. Sanchez, H. Arribart and M. G. Guille, *Nat. Mater.* **2005**, 4, 277.

8. S. Mann, *Angew. Chem. Int. Ed.* **2000**, 39, 3392.
9. T. Nakajima, H. Nameta, S. Mishima, I. Matsuzaki and K. A. Tanabe, *J. Mater. Chem.* **1994**, 4, 853.
10. W. J. E. Beek, M. M. Wienk and R. A. J. Janssen, *Adv. Mater.* **2004**, 16, 1009.
11. X. Wang, C. J. Summers and Z. L. Wang, *Nano Lett.* **2004**, 4, 423.
12. M. Huang, S. Mao, H. Feick, H. Yan, Y. Wu, H. Kind, E. Weber, R. Russo and P. Yang, *Science* **2001**, 292, 1897.
13. J. Reemts and A. Kittel, *J. Appl. Phys.* **2007**, 101, 013709.
14. Z. L. Wang, *J. Phys. Condens. Matter* **2004**, 16, R829.
15. J. Y. Lao, J. G. Wen and Z. F. Ren, *Nano Lett.* **2002**, 2, 1287.
16. Z. L. Wang, *Mater. Today* **2004**, 7, 26.
17. Z.W. Pan, Z. R. Dai and Z. L. Wang, *Science* **2001**, 291, 1947.
18. W. L. Hughes and Z. L. Wang, *J. Am. Chem. Soc.* **2004**, 126, 6703.
19. X. Y. Kong and Z. L. Wang, *Nano Lett.* **2003**, 3, 1625.
20. C. X. Xu, X.W. Sun, Z. L. Dong and M. B. Yu, *Appl. Phys. Lett.* **2004**, 85, 3878.
21. X. Y. Kong, D. Yong, R. Yang and Z. L. Wang, *Science* **2004**, 303, 1348.
22. F. Li, Y. Ding, P. Gao, X. Xin and Z. L. Wang, *Angew. Chem. Int. Ed.* **2004**, 43, 5238.
23. C.-L. Kuo, T. J. Kuo and M. H. Huang, *J. Phys. Chem. B* **2005**, 109, 20115.
24. N. S. John, N. R. Selvi, M. Mathur, R. Govindarajan and G. U. Kulkarni, *J. Phys. Chem. B* **2006**, 110, 22975.

25. J. E. Barton and T.W. Odom, *Nano lett.* **2004**, *4*, 1525.
26. Y. Rondelez, G. Tresset, K. V. Tabata, H. Arata, H. Fujita, S. Takeuchi and H. Noji, *Nat. Biotechnol.* **2005**, *23*, 361.
27. S. H. Im, U. Jeong and Y. Xia, *Nat. Mater.* **2005**, *4*, 671.

Chapter 3: Part 2

**Bowls: Spontaneous Formation of Ordered
Mesoscopic Salt Bowls**

Summary

The second part of this chapter deals with spontaneous formation of hexagonally ordered mesoscopic salt bowls during the calcination of salt-polymer (MnSO_4 -PVP) composite film. The decomposition of composite leaves strikingly beautiful mesoscopic structures of MnSO_4 salt. The formation mechanism of these structures is explained by a gas bubble template approach in which the crystallization of salt occurs around the gas bubble during calcination of the polymer leading to bowl and disc-shaped morphologies.

3.1 Introduction

Synthesis of inorganic materials with complex patterns will have significant implications in separation, catalysis and biomedicine areas (1). Inorganic biominerals are known to display stunning structural patterns at different length scale defying their rigid geometric symmetry (2-4). Mimicking such complex forms in inorganic synthesis is still a challenging task, though the guiding principles involved in the formation of many biological minerals were well understood by now than ever before. Nevertheless, some progress has been made in generating inorganic structures with complex form and pattern by mimicking the biological design principles (5). Synergistic synthesis, transcriptive synthesis, metamorphic reconstruction and microphase separation mechanisms are usually identified with inorganic morphosynthesis (1, 6). For example, the synergistic assembly of organic molecules and the inorganics has been the basis for the formation of zeolites and meso-structured materials (7). To take the complexity to higher levels, the vesicle-based synthesis, in which nature masters the art of patterning skeletons at multiple length-scales in a spatio-temporal process, has been used to create mesoscale inorganic structures of different shapes and patterns (8). Assembly of inorganic nanoparticles into mesoscale structures was possible by template directed or surfactant/polymer mediated self-assembly process (9-11). Similarly, individual components of micrometer and millimeter sizes have also been tailored to self-assemble (mesoscale self-assembly) into complex 3-D structures through capillary, electrostatic, optical, gravitational or magnetic interactions (11). However, the great

challenge in making individual components of different shapes other than spherical and plate like forms limit this strategy to be employed in microfabrication (12).

In this chapter, we investigate a spontaneous formation of ordered, mesoscale structures made up of inorganic salt bowls. These tiny bowls are generating a lot of interest due to their unique application as ‘containers’ to hold ultra low volumes (13-19). Array of these ultra-low volume containers are applied in molecular biology (20) for screening and bio-sensing of proteins and DNA.

3.2 Scope of the present investigation

In the previous part of this chapter, we have seen the formation of ZnO bowls through the calcination zinc nitrate-PVP composite film. The zinc nitrate salt in that case has a lower decomposition temperature than the PVP polymer and hence it decomposes to ZnO before the polymer decomposes completely. In this work, we wanted to find out what happens by replacing zinc nitrate salt with a salt having higher decomposition temperature than the polymer. For this purpose, we chose manganous sulphate salt whose decomposition temperature is ~ 850 °C, well above the decomposition temperature of PVP (~ 470 °C). The present investigation deals with elucidating the mechanism of the formation of the salt bowls and other interesting structures during calcination of the salt-polymer composite film. Since the MnSO_4 salt is water soluble, these salt bowls were also utilized as water soluble template to make gold replicas.

3.3 Experimental section

3.3.1 Synthetic procedure for MnSO₄ bowls

In a typical synthesis, 0.50 g of MnSO₄.H₂O salt (Merck) dissolved in 10 ml ethanol was mixed with 1.00 g polyvinylpyrrolidone (Aldrich, M_w=13,00,000) polymer to make a homogeneous, viscous slurry. The slurry was then poured into a glass petri dish (50 mm diameter) and aged for 10 h in an oven at 80 °C. The transparent film of manganous sulfate–PVP composite thus obtained was calcined at different temperatures (200, 370, 420, 470, and 550 °C) for a duration of 5 h with a heating rate of 1 °C min⁻¹. In all the cases the sample was cooled to room temperature at a cooling rate of 3 °C min⁻¹.

3.3.2 Synthetic procedure for gold bowls using MnSO₄ bowls as water-soluble template

To prepare gold replicas of the MnSO₄ bowls, gold was sputtered onto MnSO₄ bowls (10 mg) sample by using a plasma-induced sputtering technique for 2 minutes in an argon atmosphere, which resulted in a coating (ca. 60 nm) of gold over the bowls. The MnSO₄ salt is later removed by soaking the gold sputtered sample in water for 1 h followed by washing with excess water and drying at room temperature.

3.3.3 Sample characterization

The morphologies of the samples obtained in all the experiments were examined with field emission scanning electron microscope (FESEM, FEI Nova-NanoSEM-600, The Netherlands), scanning electron microscope (SEM, LeicaS-440-I Instrument, U.K), and transmission electron microscope (TEM, JEOL, JEM-3010 with an accelerating voltage of 300 kV). Powder X-ray diffraction (XRD) patterns were measured by using Rich-Siefert 3000-TT diffractometer employing Cu $K\alpha$ radiation. Thermo gravimetric analysis (TGA) was performed using Mettler Toledo TGA 850 instrument. SEM analysis of the samples was done after a mild gold coating to avoid charging as per the standard procedure.

3.4 Results and discussion

Ordered bowl array of manganous sulphate salt are formed during the calcination of the $MnSO_4$ -PVP composite film. The composite film is made by mixing of the salt with poly (vinyl pyrrolidone) polymer in 1: 2 wt/wt ratio. Figure 1 shows the scanning electron microscope (SEM) image of the bowl array obtained at 550 °C for 5 h. Since the decomposition temperature of $MnSO_4$ salt is around 850 °C, it is highly unlikely that $MnSO_4$ will undergo any change at this temperature.

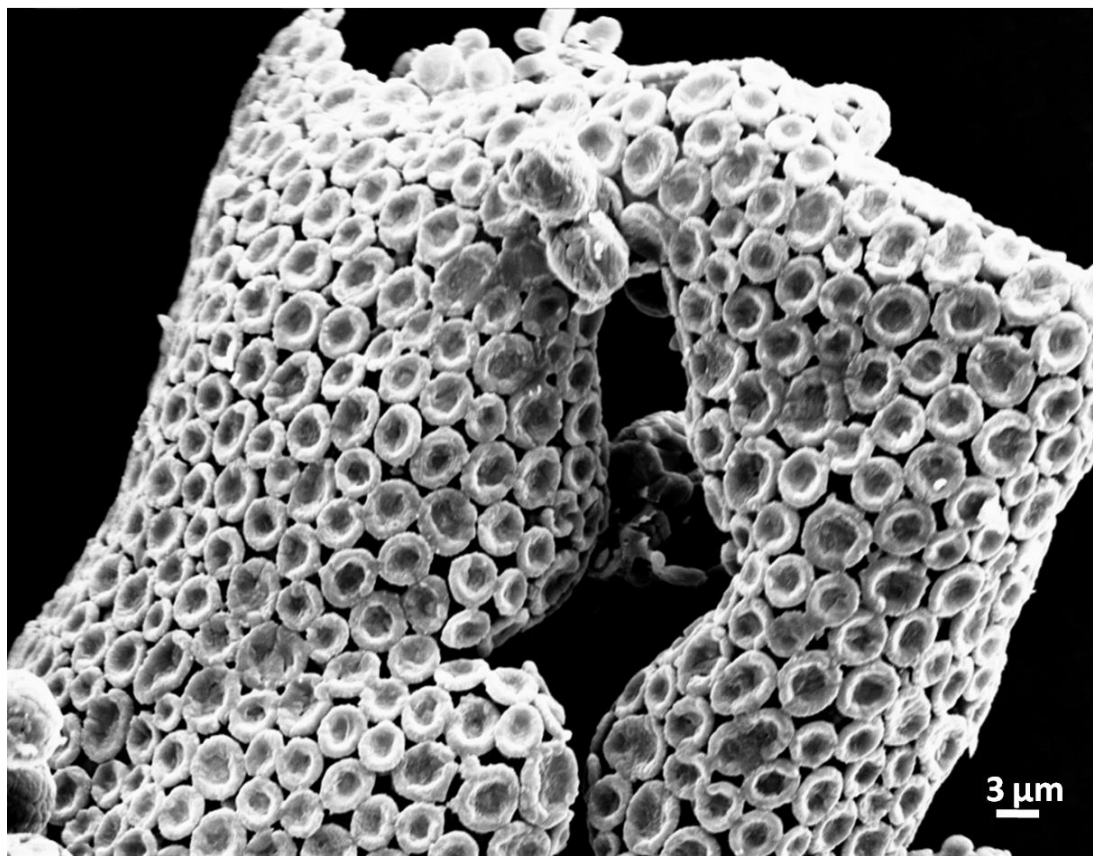


Figure 1: SEM image of an ordered array of MnSO₄ bowls obtained after calcination of MnSO₄–PVP composite film at 550 °C for 5 h.

Calcination of the composite at 550 °C for 5 h removes the polymer, PVP, leaving the film composed of salt bowls to curl (Figure 2). The transmission electron microscope (TEM) image shows that each bowl is made up of several smaller particles. The electron diffraction (ED) pattern confirms the polycrystalline nature of a single bowl (Figure 3a). Powder X-ray diffraction (PXRD) pattern of the calcined sample confirms the presence of crystalline MnSO₄ salt (Figure 3b).

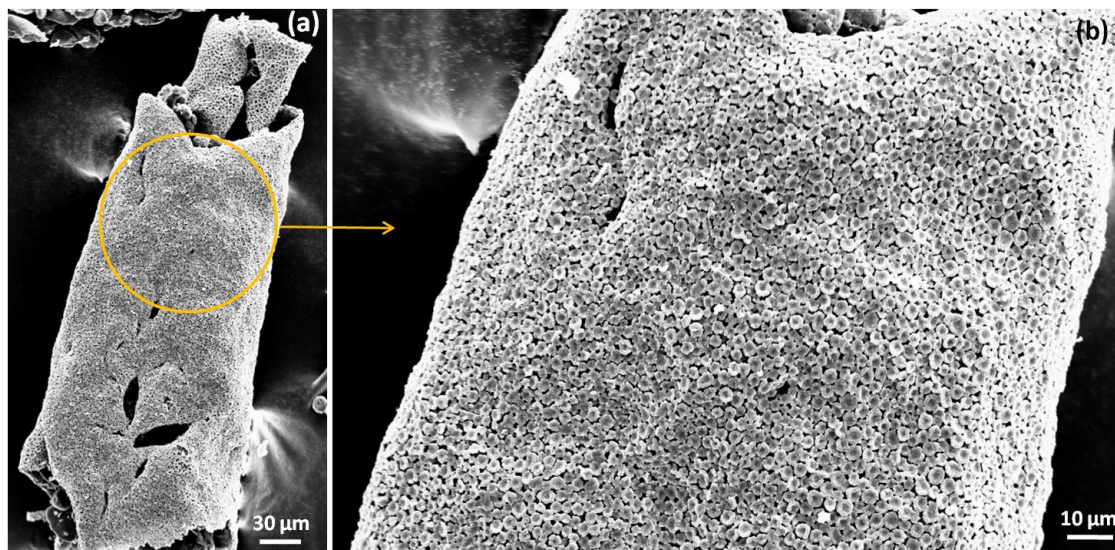


Figure 2: (a) Low magnification SEM image of a curled film containing ordered array of MnSO_4 bowls. (b) Higher magnification SEM image of the encircled portion.

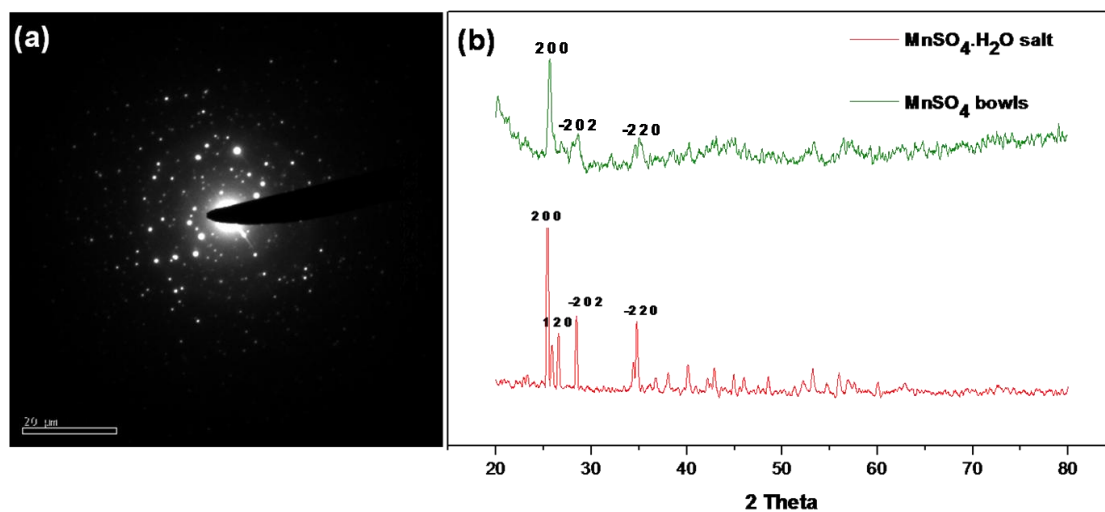


Figure 3: (a) Electron diffraction pattern of the MnSO_4 bowls showing their polycrystalline nature. (b) Powder X-ray diffraction (PXRD) pattern of the MnSO_4 bowls sample in comparison with the MnSO_4 salt precursor.

The mesoscopic bowls of size around 3 to 5 μm are exquisitely arranged in a hexagonal pattern, though in many cases the bowls are not making direct contact with the six neighboring bowls as shown in Figure 4. In some cases the rims of the bowls are not perfectly circular. The wall thickness of the bowls is in the range of 500 – 700 nm and the depth of the bowls is about 500 nm.

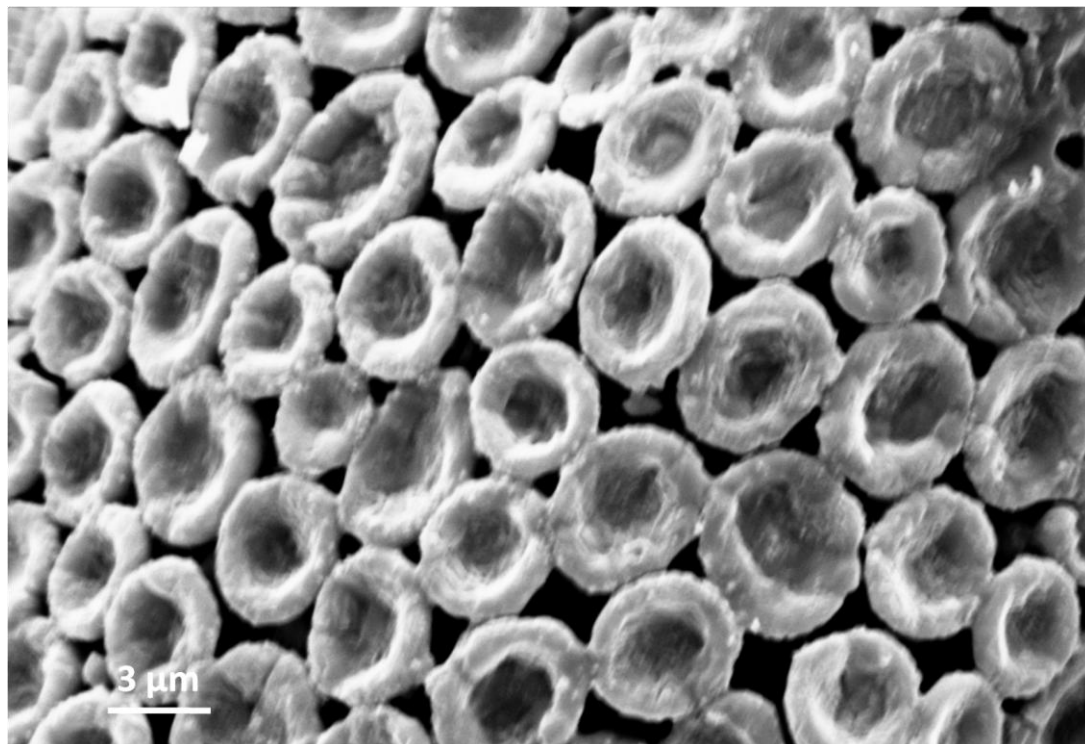


Figure 4: Higher magnification SEM image showing the closer-view of the hexagonally-ordered array of MnSO_4 bowls.

To understand the formation mechanism of the ionic salt into mesoscopic bowls upon removal of the polymer, calcination of the composite film was carried out at different temperatures. Figures 5(a-d) and 6 show the field-emission electron microscope (FESEM) images of various structures (other than bowls) occasionally formed during the calcinations at 470 $^\circ\text{C}$ and 550 $^\circ\text{C}$. Calcination at 200 $^\circ\text{C}$ for 5 h

shows formation of flakes with several microns size (~20 to 200 μm) originating from the cracking of a large film which is quite understandable because, at that temperature neither the polymer nor MnSO_4 salt decomposes.

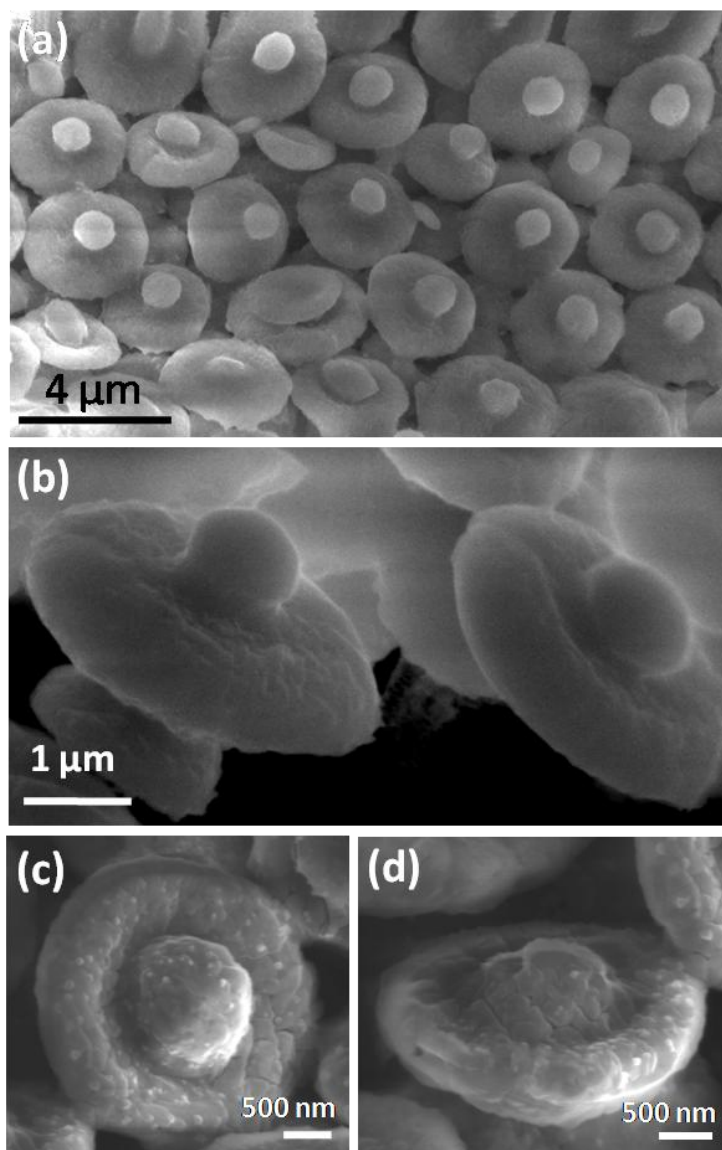


Figure 5: (a) Low magnification FESEM image of ball-in-bowl shaped structures formed by calcination of the composite film at 470 °C for 5 h (b), (c) and (d) higher magnification images showing the close view of these structures

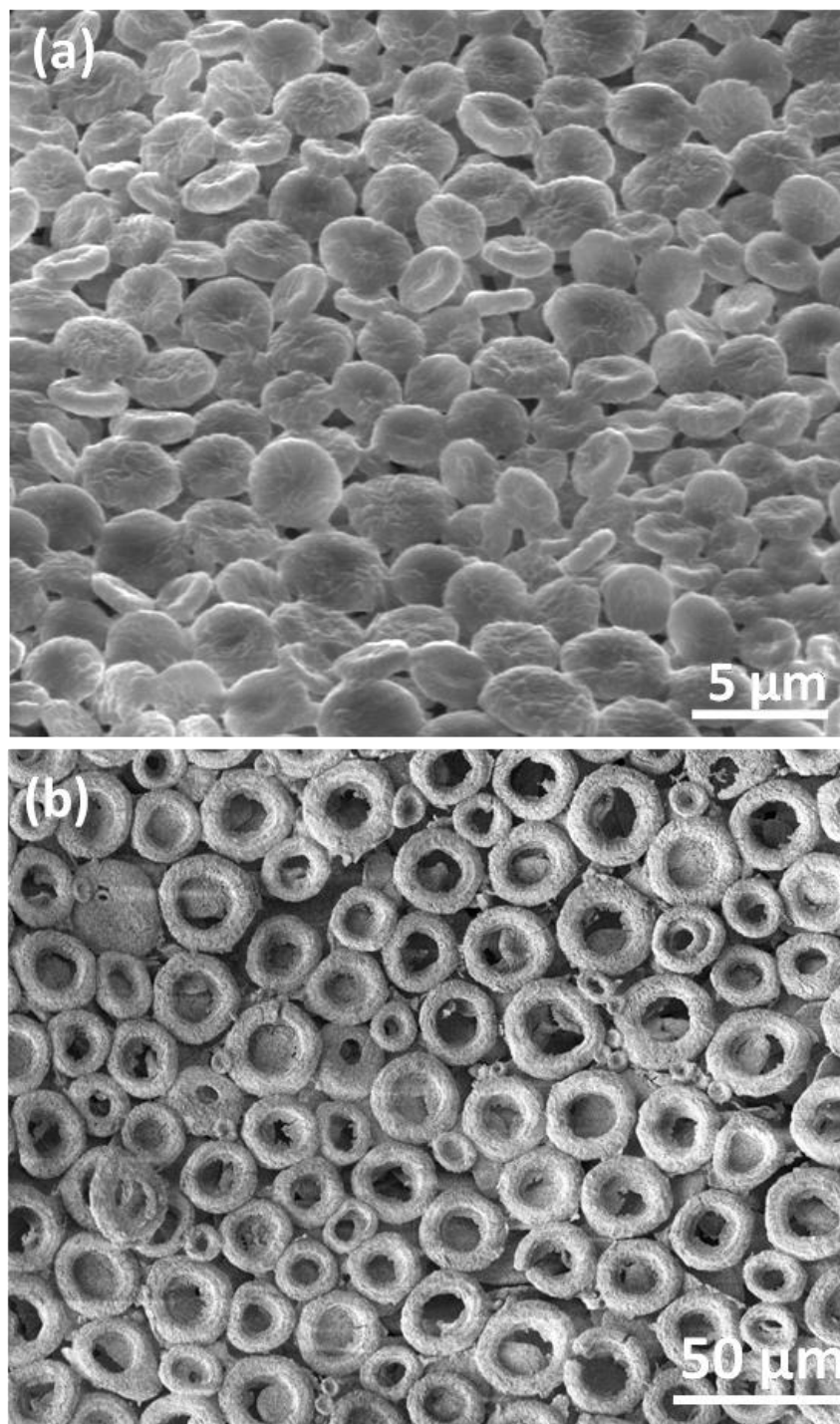


Figure 6: FESEM images of (a) Circular discs with partial dents in their center formed at 470 °C for 5 h. (b) Ring shaped structures formed at 550 °C for 5 h.

Thermo gravimetric analysis (TGA) (Figure 7) shows that the degradation of polymer starts at 370 °C and completes at around 470 °C. The composite film calcined at 370 °C for 5 h was showing the signature for the ball-like structures embedded within the matrix, probably emerged from the partial crystallization of MnSO_4 salt around the gas bubbles generated by the decomposition of the polymer (encircled portions of Figure 8).

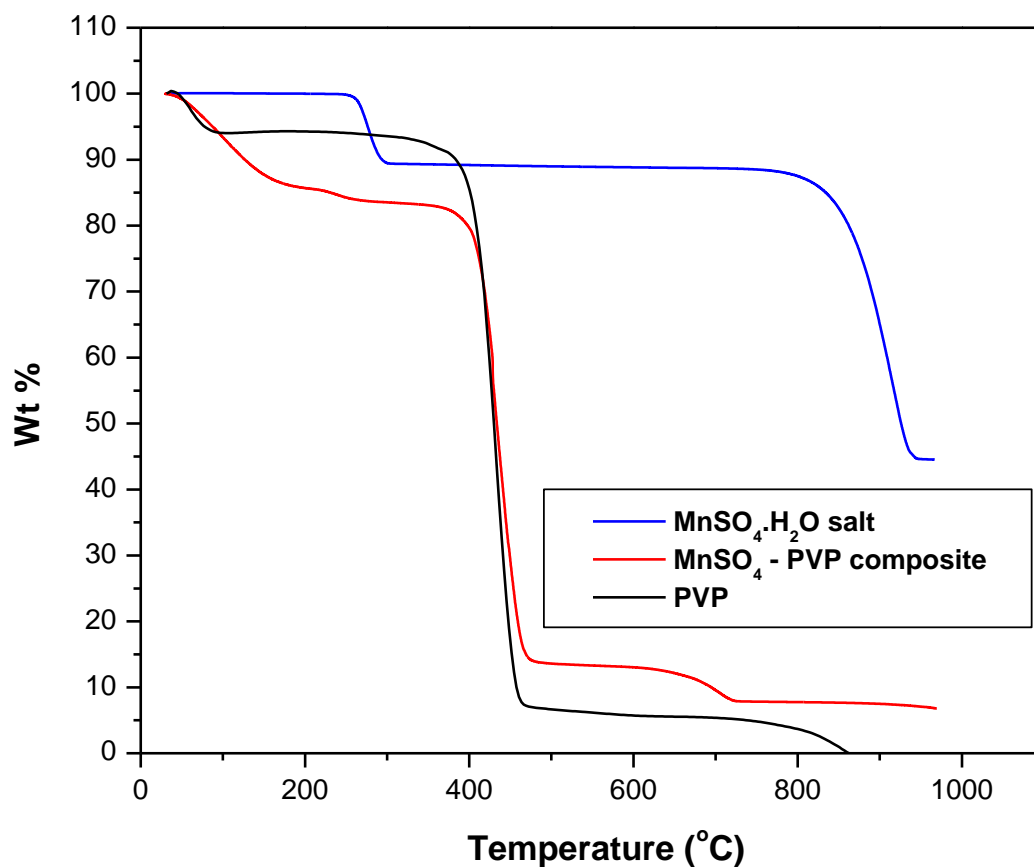


Figure 7: Thermo gravimetric analysis (TGA) curves of MnSO_4 salt (blue), MnSO_4 salt – PVP composite (red) and PVP polymer (black).

At 420 °C for 5 h, further crystallization of salt in association with the removal of carbonaceous layer leaves the bubbles burst open at the top leading to the formation of large number of hemi-spherical structures (Figure 9a and 9b). TGA shows that only about 50% of the polymer was removed at this temperature (Figure 7). Further heating of this composite to 550 °C for 5 h gives rise to hexagonally organized bowls (Scheme A in Figure 10). There are regions in which the bowls are less organized probably due to the presence of large unevenness on the surface of the initial PVP-MnSO₄ film (Figure 11).

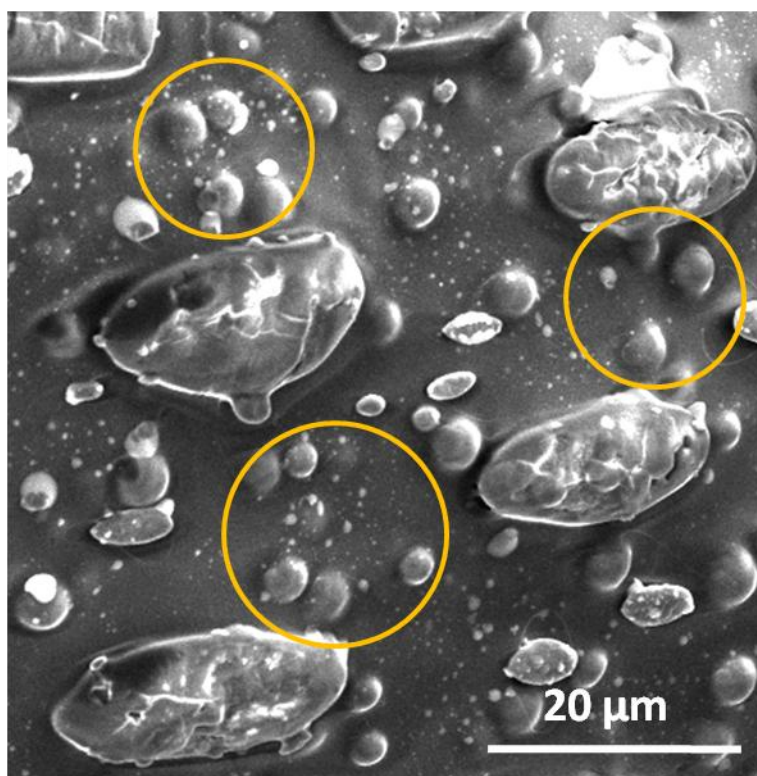


Figure 8: FESEM image showing the emergence of spherical ball-shaped structures from the film on calcination of the composite film at 370 °C for 5h. Encircled regions show the bubbles emerging out from the film.

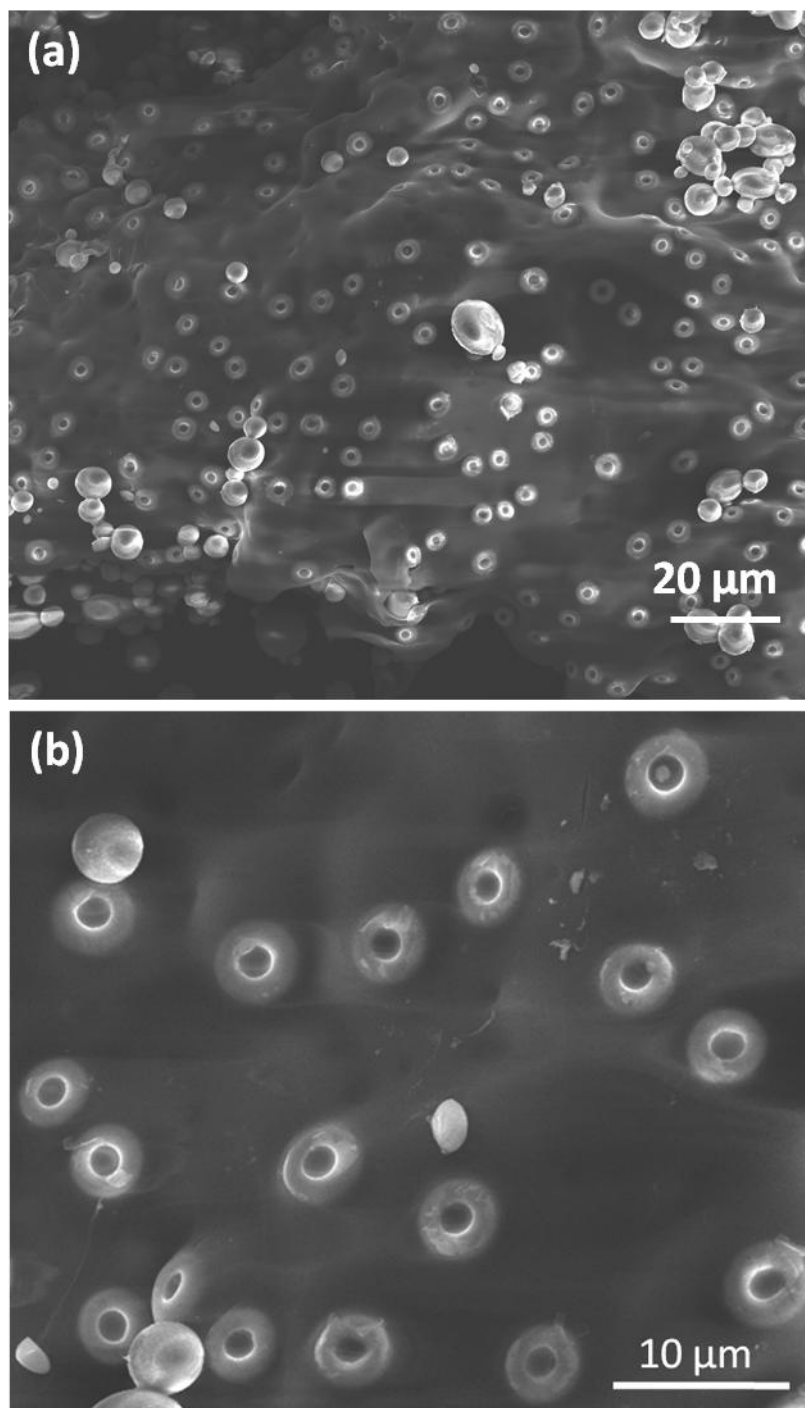


Figure 9: (a) and (b) Low and High magnification FESEM images respectively of the top-view of the hemi-spherical bowls that are emerging out of the polymer film after calcining at 420 °C for 5 h.

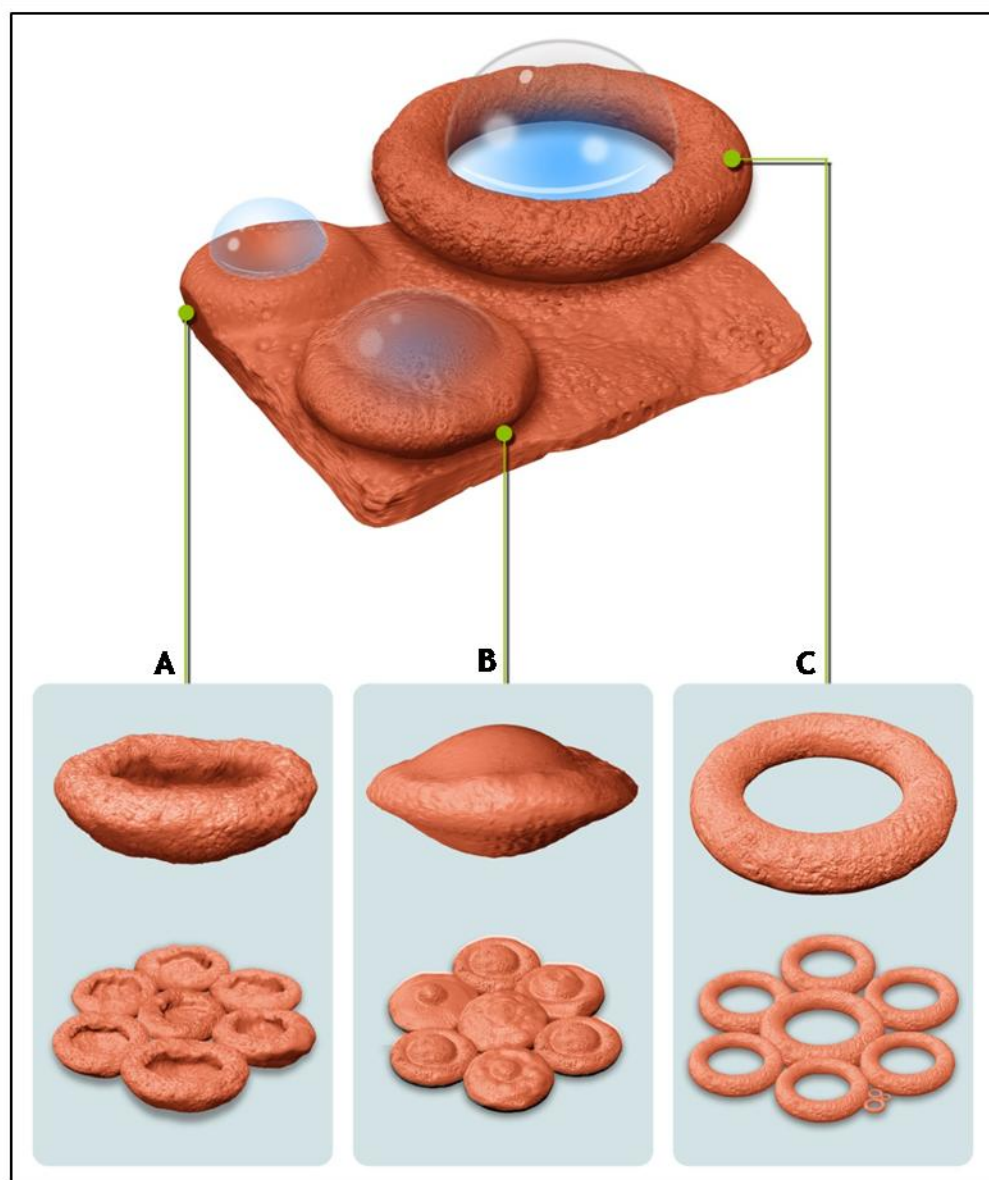


Figure 10: Scheme showing formation process of different MnSO₄ morphologies through gas-bubble template method, Scheme A: Bowls, Scheme B: Ball-in-bowl shaped structures, Scheme C: Ring shaped structures (for convenience, all morphologies are shown to be evolved from the same film).

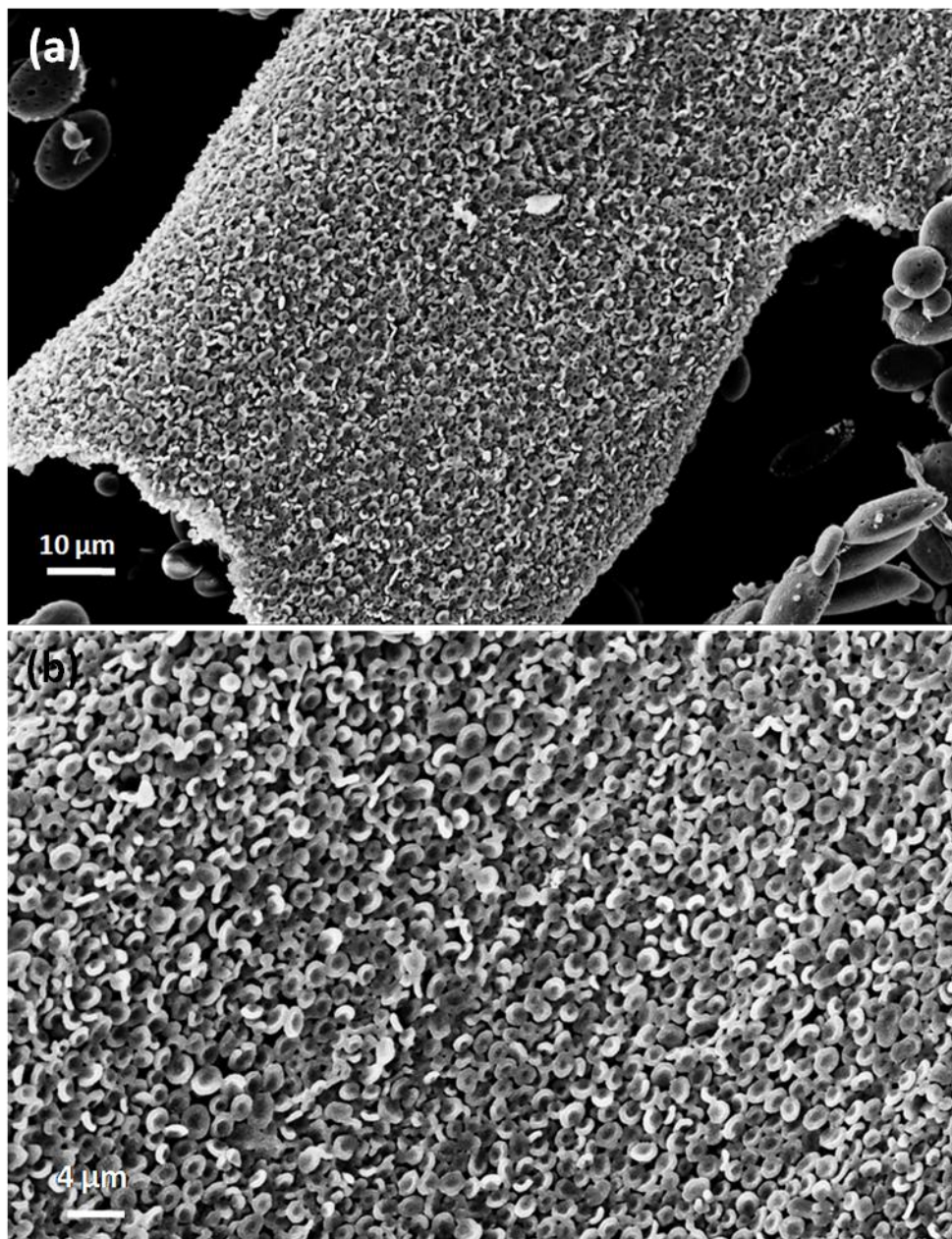


Figure 11: (a) and (b) Low and high magnification SEM images respectively of the bowls showing the uneven surface of the polymer film after calcination at 550 °C for 5 h leading to the less organized bowls.

In some cases, the crystallization of manganous sulphate salt around the bubbles deforms them to oblate spheroids (Figure 12) which are not able to burst

open while heating. Instead, these spheroids during the process of polymer removal shrink inwards to form disc-shaped morphology (Figure 6a). If the thickness of spheroid wall is high due to salt crystallization, the buckling will not be complete leading to ball-in-bowl shaped structures (Figures 5 and 13, Scheme B in Figure 10). On the other hand, if the bubbles formed during calcination are larger than the thickness of the film, hexagonally arrayed ring like structures of diameter around 20 microns are obtained (Figure 6b and Scheme C in Figure 10).

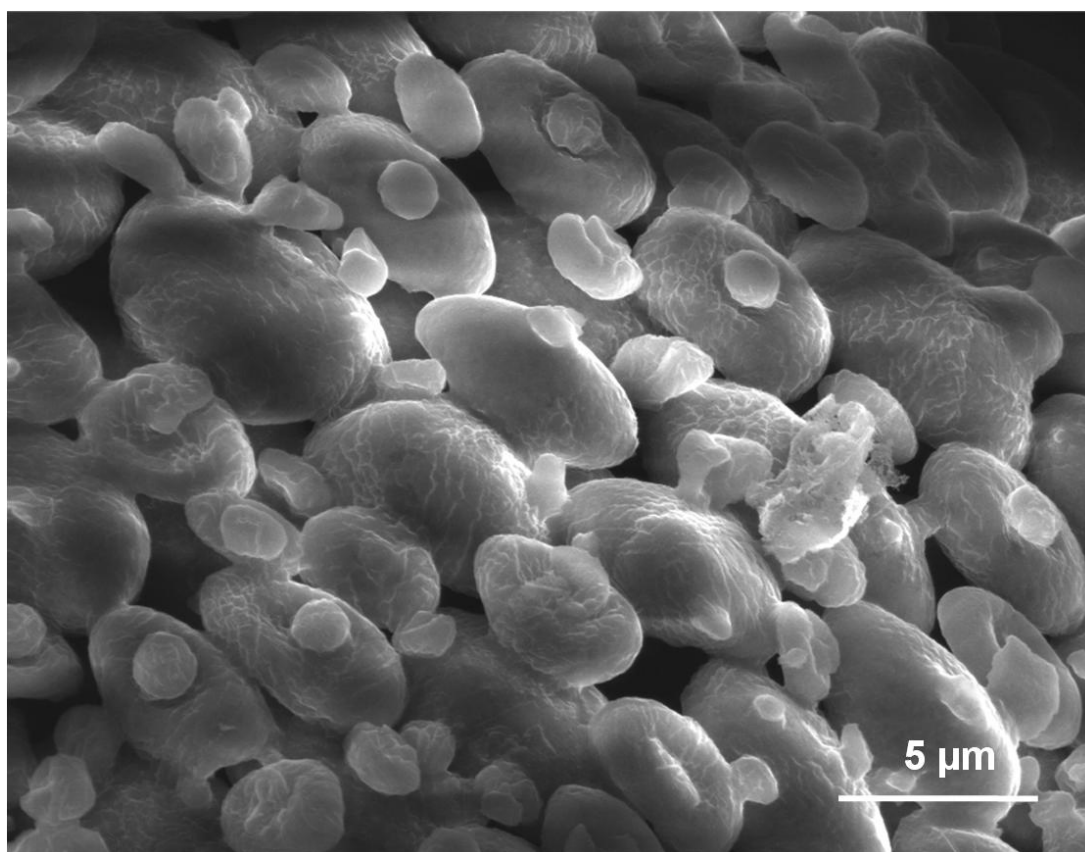


Figure 12: FESEM image of some intermediate, oblate-shaped structures obtained upon heating at 470 °C for 5h.

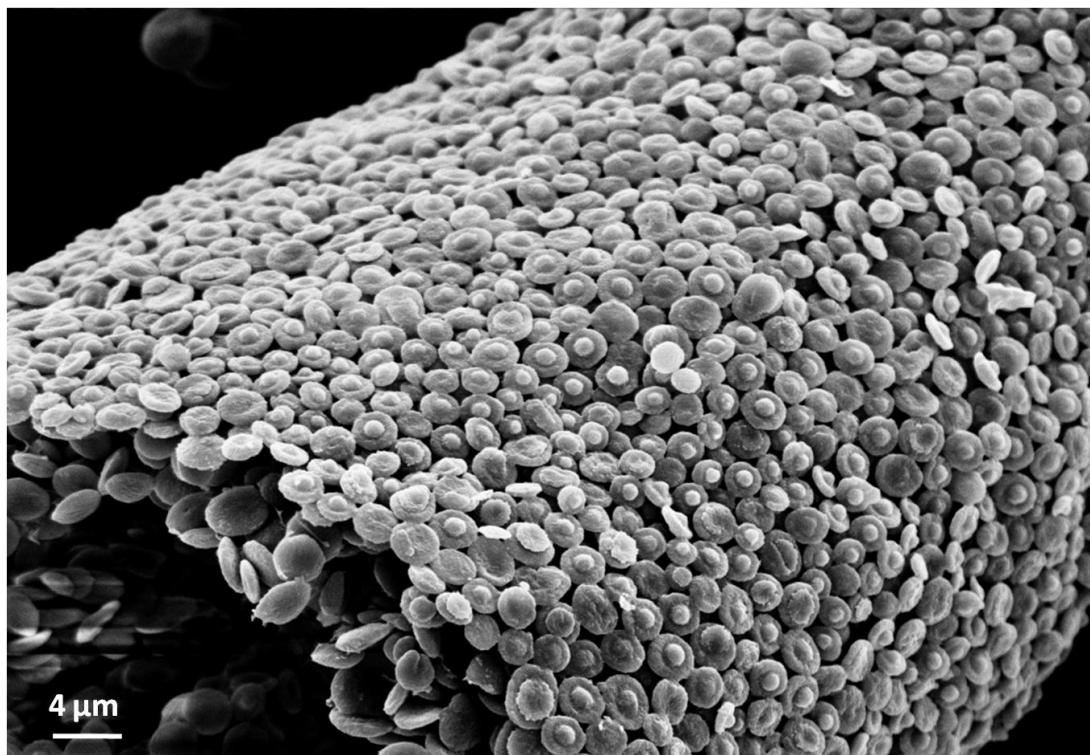


Figure 13: SEM image of the ordered arrays of ball-in-bowl shaped microstructures formed from shrinking of the oblate spheroids.

The effect of solvent on the shape formation is checked by replacing ethanol with water in the synthesis step which resulted in ring-shaped structures (Figure 14). When the reaction was carried out with more amount of polymer, MnSO_4 : PVP ratio (wt/wt) was 1 : 4, no bowl formation was observed instead, a flaky solid product was obtained. On the other hand, when the MnSO_4 : PVP ratio was 1 : 1, the bowl morphology was still retained indicating the optimum salt concentration necessary for the crystallization to occur around the bubble during calcination. Heating MnSO_4 without PVP did not result any bowl shaped structures, but yielded micron-sized irregular structures. Similarly, when the polymer PVP was replaced with polyvinylalcohol (PVA), calcination of the composite at 550 °C for 5 h yielded

MnSO₄ with large, ring-shaped structures of diameter 20 to 30 microns (Figure 15a and 15b). This suggests that the carbonaceous film formed during the decomposition of the polymer plays an important role in controlling the bubble formation around which the crystallization of the salt occurs.

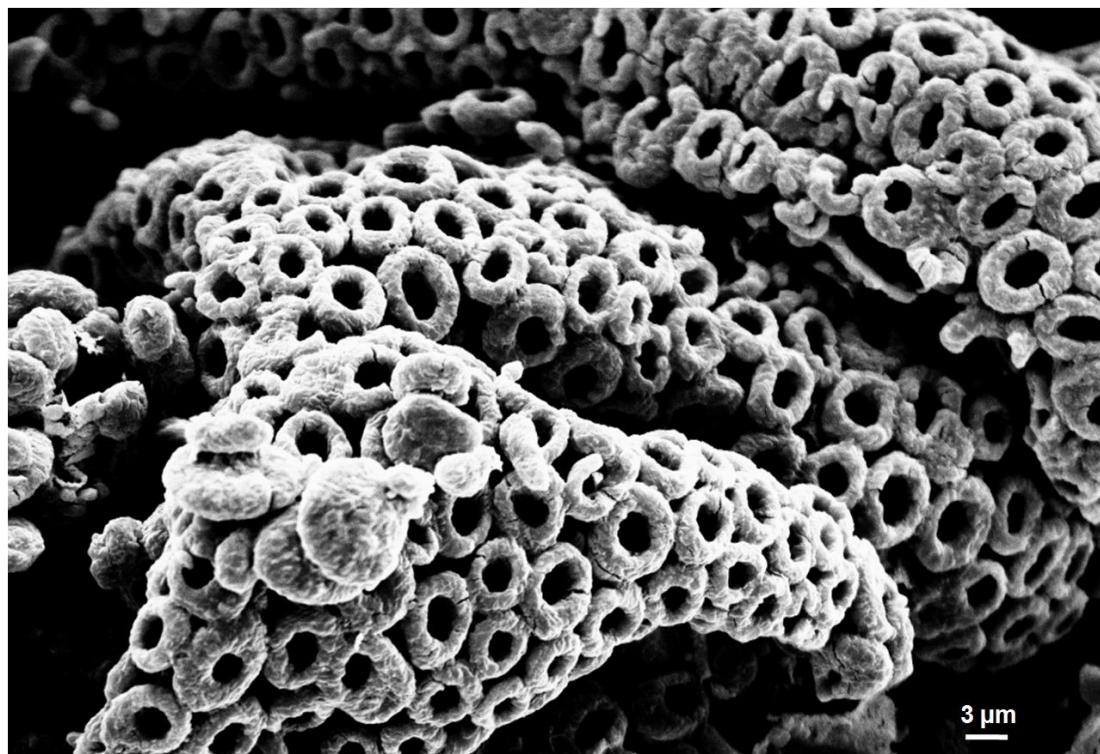


Figure 14: SEM image of the ring shaped microstructures obtained by using only water as the solvent.

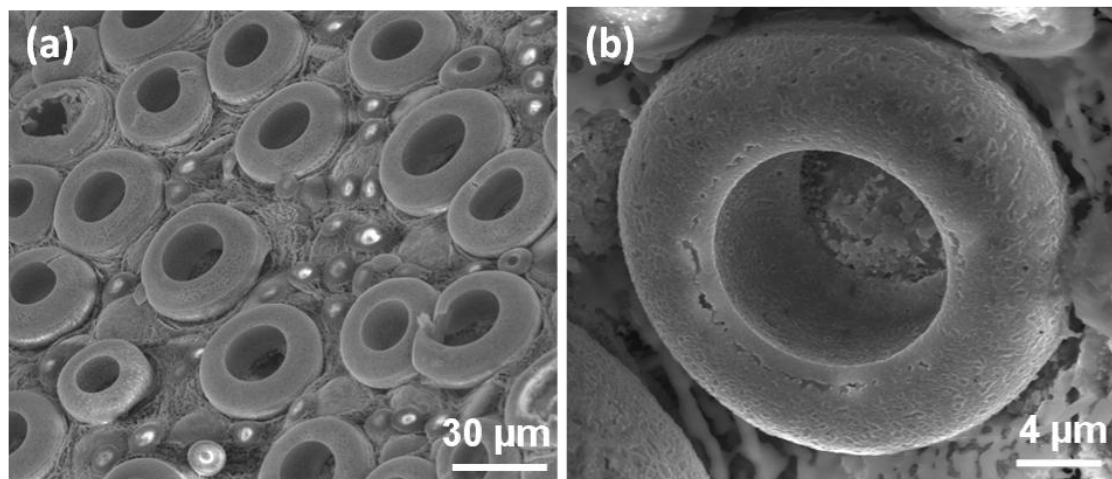


Figure 15: FESEM images of the (a) ring shaped microstructures obtained by using poly vinyl alcohol (PVA) polymer instead of PVP (b) higher magnification of a single ring.

Considering the effective solubility of the MnSO_4 salt in water, we used these MnSO_4 bowls as water soluble template for the generation of gold bowls. For this purpose, gold is sputter-coated onto the MnSO_4 bowls to form a thick layer (~ 60 nm) followed by dipping them in water for 1 h to remove the salt. Figure 16a shows a FESEM image of the gold coated MnSO_4 bowls. The hollow gold bowls (Figure 16b) formed after the removal of MnSO_4 core and their EDAX profile (Figure 17) clearly demonstrate the possibility of using these MnSO_4 bowls as water soluble template to prepare other metal and metal oxide bowls.

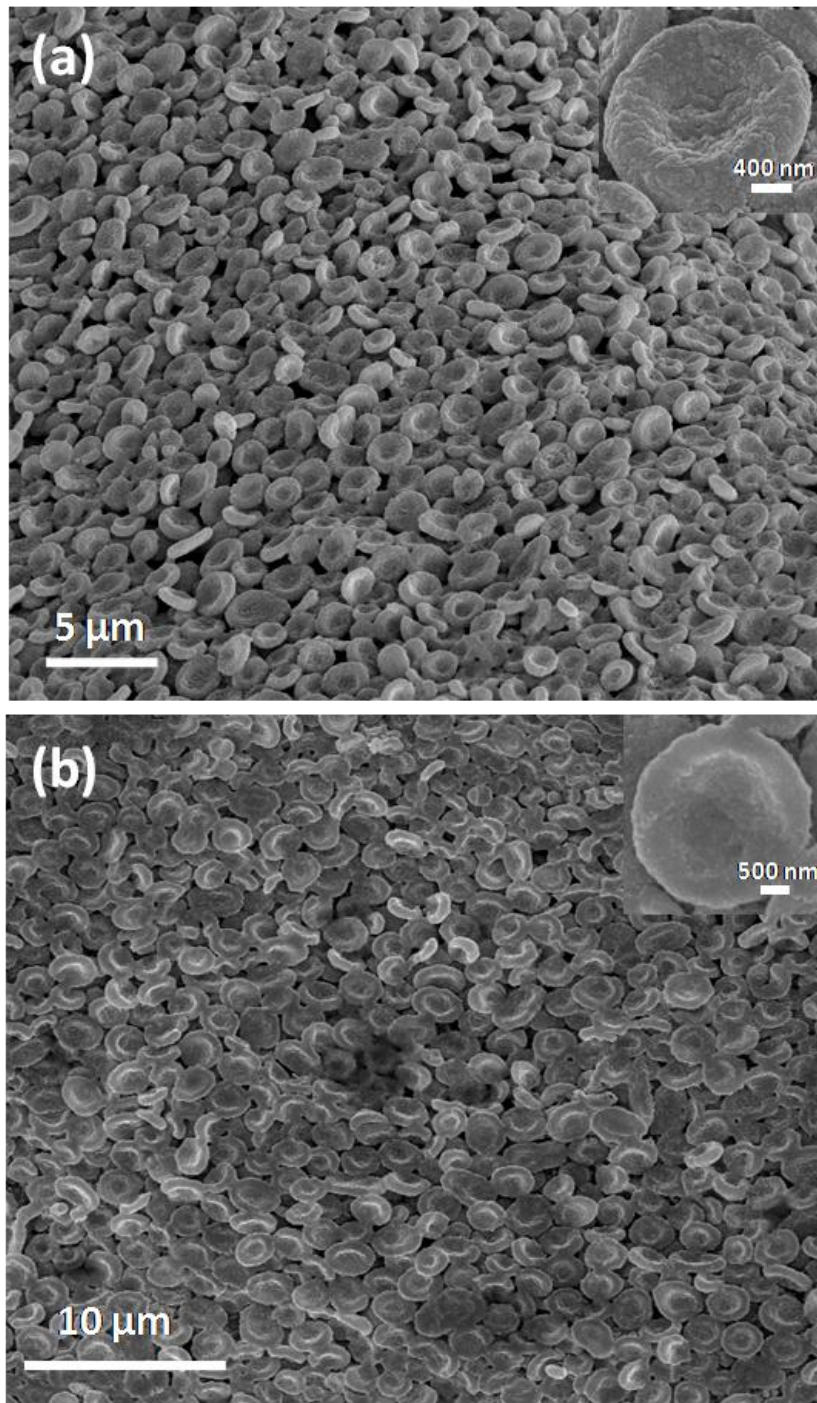


Figure 16: (a) Gold-coated $MnSO_4$ bowls (b) gold bowls formed after the removal of $MnSO_4$ salt core.

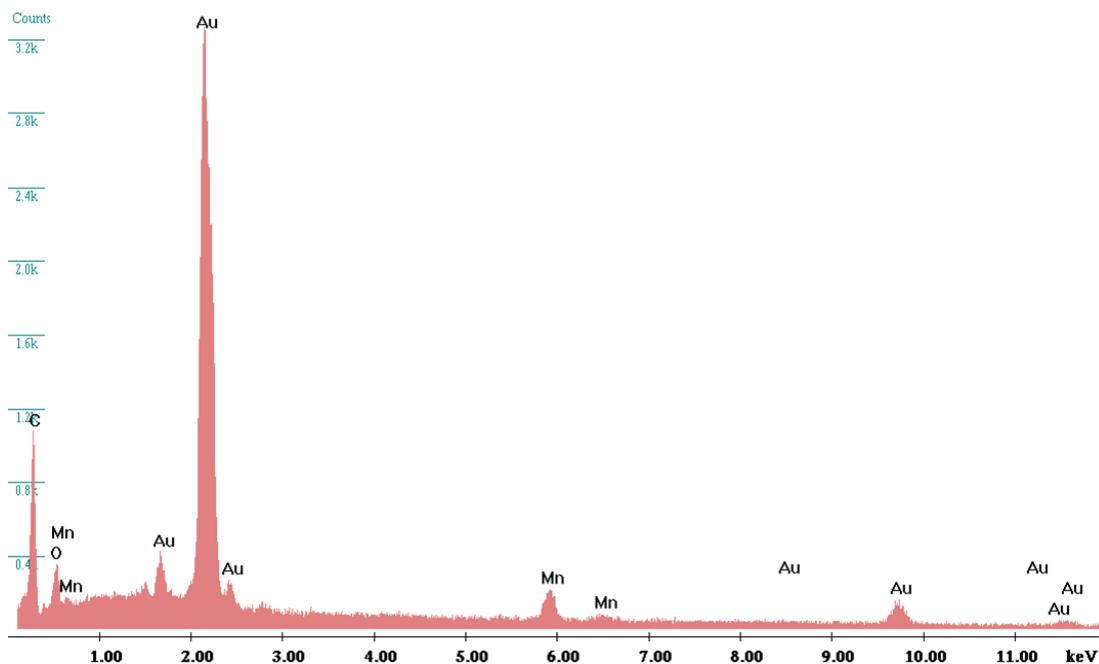


Figure 17: EDAX profile of the gold bowls obtained after dissolving the MnSO_4 core (the minor peaks for 'Mn' are from the negligible amount ($\sim 4\%$) of salt left over after its dissolution).

3.5 Conclusions

In summary, this second part of the chapter describes a novel method to form ordered micro-bowls of manganous sulphate salt. These salt bowls were formed by crystallization of MnSO_4 salt around the gas bubble. The bowls are spontaneously formed into hexagonal arrays during the synthesis stage. Such arrays would find application as ultra-low volume containers. Further, due to water solubility of the salt, these bowls were successfully used as water-soluble template to make replicas of gold bowls.

3.6 References

1. S. Mann and G. A. Ozin, *Nature* **1996**, 382, 313.
2. G. A. Ozin, *Acc. Chem. Res.* **1997**, 30, 17.
3. S. Mann, *Angew. Chem. Int. Ed.* **2000**, 39, 3392.
4. C. Sanchez, H. Arribart and M. G. Guille, *Nat. Mater.* **2005**, 4, 277.
5. S. Mann in *Biomaterialization: Principles and Concepts in Bioinorganic Materials Chemistry*, Oxford University Press, Oxford, **2001**.
6. H. Yang, N. Coombs and G. A. Ozin, *Nature* **1997**, 386, 692.
7. C. T. Kresge, M. Leonowicz, W. J. Roth, J. C. Vartuli and J. C. Beck, *Nature* **1992**, 359, 710.
8. E. Dujardin and S. Mann, *Adv. Eng. Mater.* **2002**, 4, 461.
9. M. Li, H. Schnablegger and S. Mann, *Nature* **1999**, 402, 393.
10. H. Cölfen and S. H. Yu, *Mater. Res. Bull.* **2005**, 30, 727.
11. M. Boncheva and G. M. Whitesides, *Mater. Res. Bull.* **2005**, 30, 736.
12. G. M. Whitesides and M. Boncheva, *Proc. Natl. Acad. Sci.* **2002**, 99, 4769.
13. K. S. Krishna, U. Mansoori, N. R. Selvi and M. Eswaramoorthy, *Angew. Chem. Int. Ed.* **2007**, 46, 5962.
14. J. Dinesh, U. Mansoori, P. Mandal, A. Sundaresan and M. Eswaramoorthy, *Angew. Chem. Int. Ed.* **2008**, 47, 7685.
15. N. S. John, N. R. Selvi, M. Mathur, R. Govindarajan and G. U. Kulkarni, *J. Phys. Chem. B.* **2006**, 110, 22975.

16. R. J. Jackman, D. C. Duffy, E. Ostuni, N. D. Willmore and G. M. Whitesides, *Anal. Chem.* **1998**, 70, 2280.
17. J. E. Barton and T.W. Odom, *Nano lett.* **2004**, 4, 1525.
18. S. H. Im, U. Jeong and Y. Xia, *Nat. Mater.* **2005**, 4, 671.
19. X. D. Wang, E. Graugnard, J. S. King, Z. L. Wang and C. J. Summers, *Nano Lett.* **2004**, 4, 2223.
20. Y. Rondelez, G. Tresset, K. V. Tabata, H. Arata, H. Fujita, S. Takeuchi and H. Noji, *Nat. Biotechnol.* **2005**, 23, 361.

Chapter 3: Part 3

**Bowls: Large-scale synthesis of ordered gold
bowl arrays using colloidal silica spheres
as template**

Summary

This third part of the chapter deals with the formation of large-scale ordered gold bowl arrays through sputter deposition process using colloidal silica spheres as a template. The process involves sputter-deposition of gold over a closely packed silica spheres on a glass substrate followed by removal of the silica by HF solution etching.

3.1 Introduction

Some of today's nanotechnological needs include fast electronic systems, extremely sensitive sensor devices to probe confined environments and multiplexed techniques for high-throughput analysis. The ultimate realization of these technological advancements will be based on our ability to synthesize and organize matter into controlled geometries at micro- and nanoscale. Since the physical and chemical properties of metal nanostructures show strong correlation with their geometries, controllable variations in morphology have great importance for their applications. In this regard, ordered micro- and nanobowl arrays are generating a lot of interest due to their potential applications in nanoparticles selection (1), biomedical applications (2), and coercivity enhancement (3). For instance, Love *et al* have used a lithographically formed micro-well array for rapid selection of single cells producing antigen specific antibodies thus cutting down their detection time drastically (4). In a different approach, Odom and co-workers have shown nanobowl arrays formed using laser-assisted embossing could be used to grow inorganic crystals in nanosize by mass-limited growth (5). Considering their prospective applications, synthesis of nanobowls arrays has been reported by researchers using various approaches (6-12). The most common method employs metal coating on the top half of the colloidal micro-/nanosphere arrays followed by the removal of the spheres. For example, Whitesides and coworkers have fabricated disordered metal (Au, Pt and Pd) bowls by evaporating a thin metal film (thickness smaller than 20

nm) onto a monolayer of spherical silica colloids followed by silica removal (13).

Figure 1a shows the schematic illustration of their synthetic process.

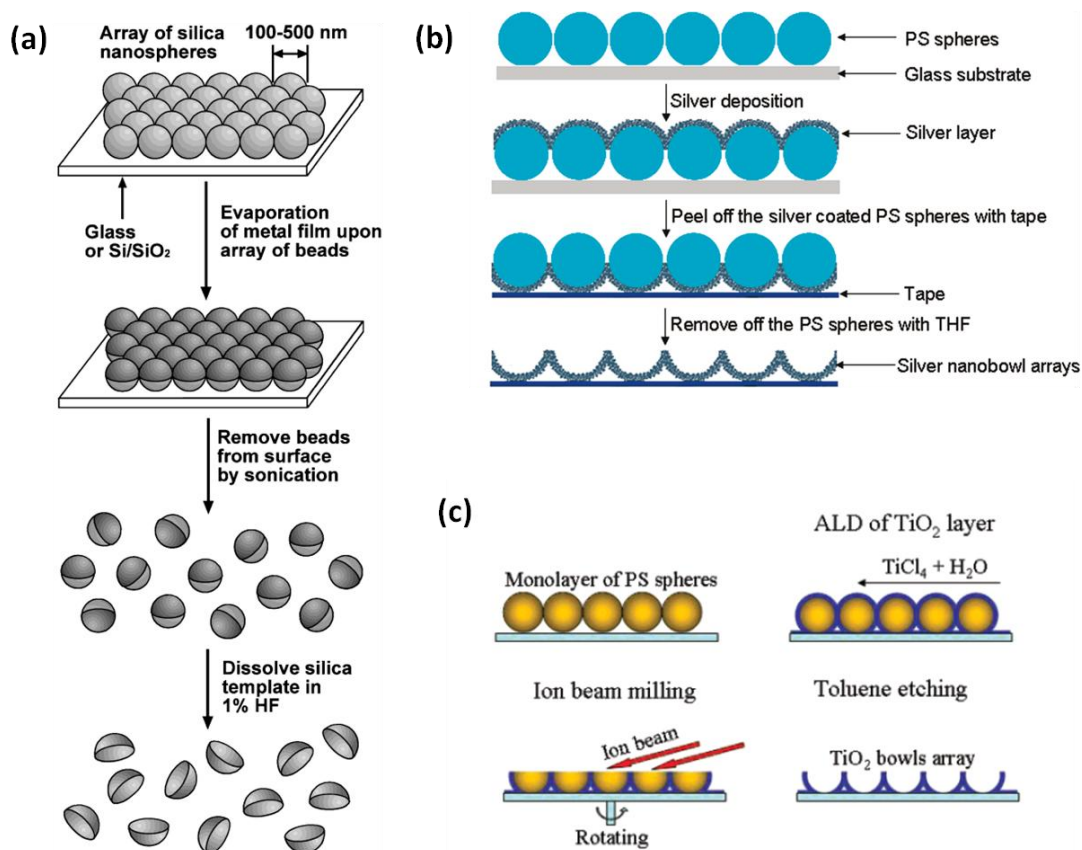


Figure 1: Schematic illustrations of different procedures for fabricating nanobowl arrays

Similarly, L. Chi and co-workers (6) have synthesized silver nanobowls arrays by sphere lithography. Their process involves thermal evaporation of silver over monolayer of polystyrene (PS) spheres followed by peeling of the silver coated PS spheres with a sticking tape. The PS spheres are then removed with THF to obtain silver nanobowls arrays (Figure 1b). In a different approach, C. J. Summers

and co-workers have made ordered TiO₂ bowl arrays by coating TiO₂ over monolayer of PS spheres through atomic layer deposition (ALD) process followed by ion-beam milling and toluene etching (Figure 1c) (1).

Most of these methods described above to generate nanobowl arrays are limited by the high cost and sophisticated techniques such as atomic layer deposition, electroforming etc. In this part of the chapter, we describe synthesis of large-scale gold bowl arrays by a sputter coating method using colloidal silica spheres as template.

3.2 Scope of present investigation

The present investigation explores a facile method for the fabrication of ordered nanobowl arrays of gold using colloidal silica spheres as template. The method involves sputter deposition of gold over a close packed silica spheres (on glass substrate) followed by the removal of the template. The formation process of large arrays of ordered gold bowls is also being investigated.

3.3 Experimental section

3.3.1 Synthetic procedure for colloidal silica spheres

Silica spheres were synthesized following the procedure reported by Stober *et al.* (14). In a typical procedure, 1.5 ml of tetraethylorthosilicate (TEOS) was added to a mixture of 50 ml absolute ethanol, 20 ml NH₃ (about 30% in water) and 1 ml de-ionised water (Milli-Q®) at 40 °C. After 3 h of reaction at 40 °C, an additional 1 ml of TEOS was added. This was followed by another 3 h of reaction at 40 °C. Silica spheres were then washed using three rounds of centrifugation (13,000 rpm for 15 min) interspersed with absolute ethanol.

3.3.2 Synthetic procedure for ordered gold bowl arrays

The as-synthesized silica spheres were redispersed in water and drop-casted onto a freshly cleaned glass wafer and dried in air for 1 h to form the colloidal crystal packing. To prepare gold bowls, gold was sputtered onto the closely packed spheres by a DC sputter coater instrument (Figure 2) in an argon atmosphere. The optimum deposition rate is around 100 mTorr of the argon gas pressure and sputtering voltage is 1 kV. Finally, the silica core was removed by soaking the gold sputtered sample in 5 ml of 5 % HF for 10 h. The sample was then washed with de-ionized water and dried at room temperature.

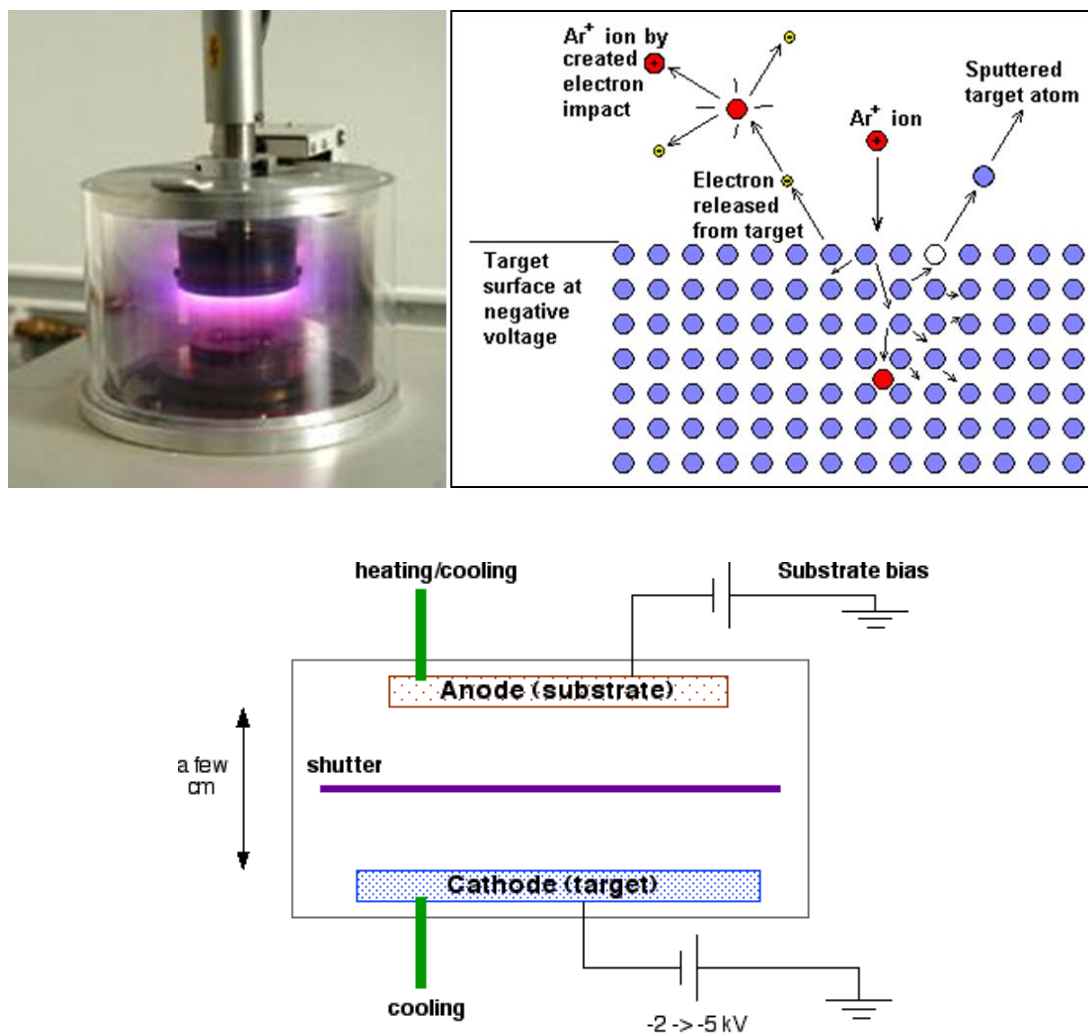


Figure 2: Sputter-coating chamber and schematic of sputtering process

3.4 Results and discussion

The silica spheres obtained by the Stober's process were nearly monodispersed in size (~ 375 nm diameter). The size of the spheres could be varied by varying the amount of ammonia addition during the synthesis. Figure 3 shows a

field emission scanning electron microscope (FESEM) image of a hexagonally packed colloidal crystal of monodispersed silica spheres.

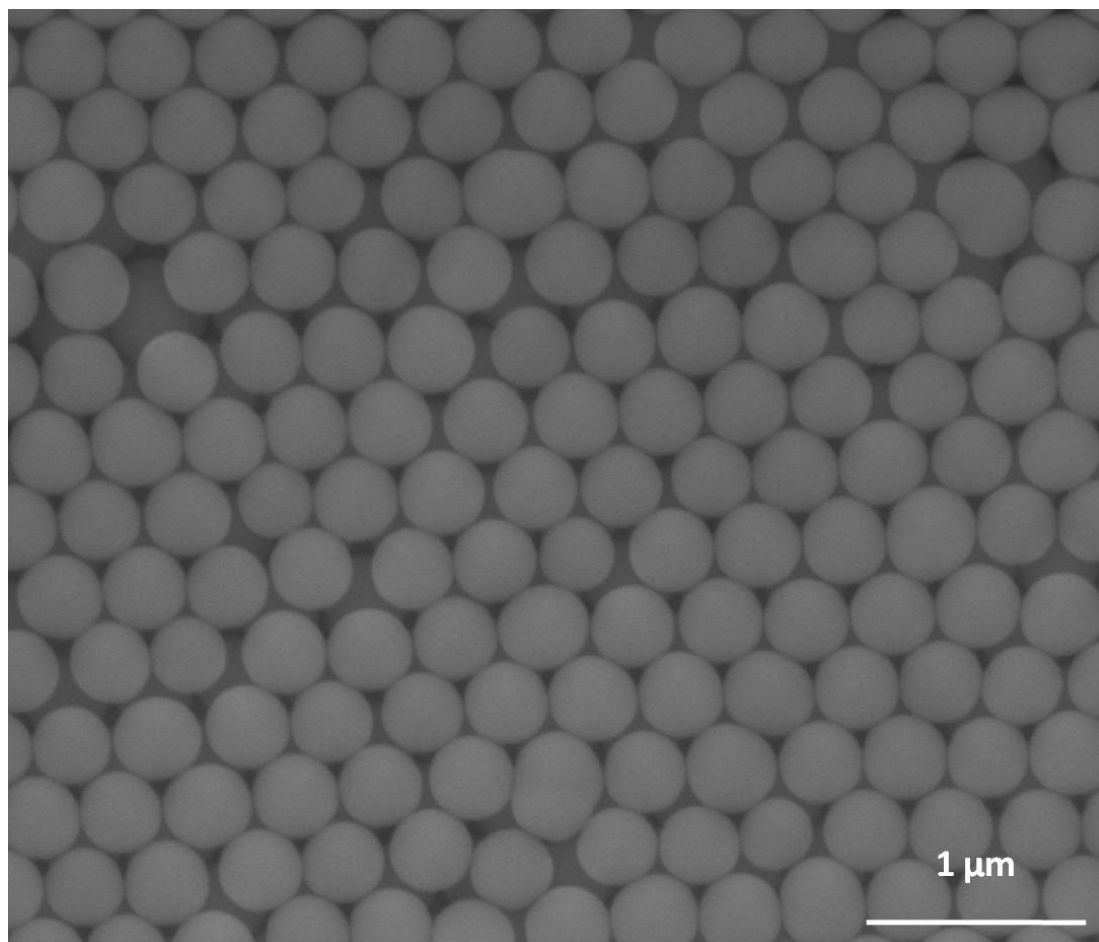


Figure 3: FESEM image of the silica spheres of size ~ 375 nm

The colloidal spheres laden glass wafer was placed inside the sputter coater chamber and gold was sputter deposited on to the sample using the DC sputter coater instrument. Figure 4 shows FESEM image of gold coated silica spheres with size of ~ 435 nm resulting in a coating thickness of ~ 30 nm over the spheres. The gold deposition on the spheres occurs with 15 – 20 nm size gold particles forming over the spheres resembling raspberry-like features. Unlike thermal evaporation or atomic

layer deposition, during sputter-deposition, gold deposits as charged clusters. These clusters are positively charged and hence are driven to the cathode surface when voltage bias is applied across the anode and cathode within the sputtering chamber. As a result, coating occurs from bottom of the spheres.

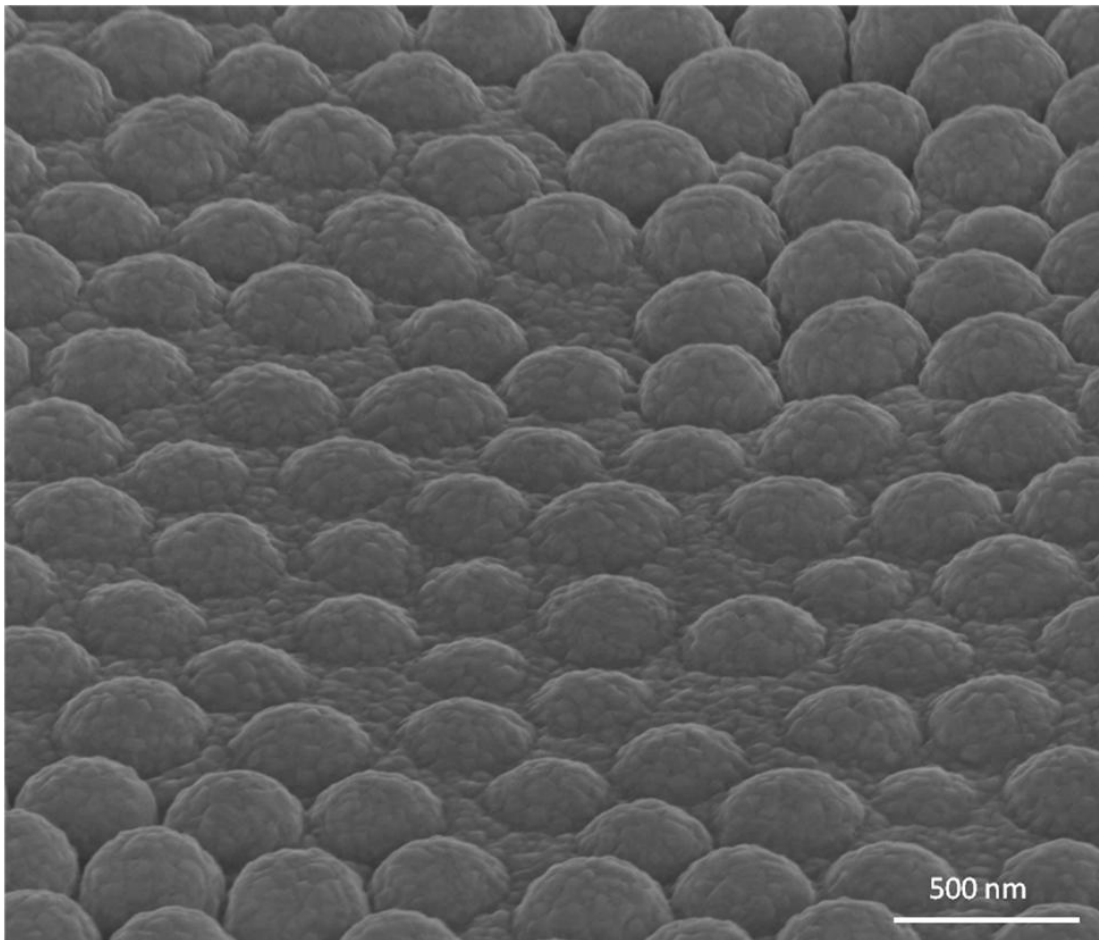


Figure 4: FESEM image of the gold coated silica spheres

. During the sputter coating, gold clusters are deposited in between the packed spheres resulting in adjacent spheres sharing common gold walls. This leads to increase in wall thickness of the bottom half of the spheres compared to top surface of the spheres. The coating on the top of the spheres is lesser in thickness

than the sides of the spheres hence during the acid etching with 5 % HF solution, the top of the gold coated spheres fractured to give bowls. Figure 5 and 6 shows the ordered gold bowl arrays after the silica removal.

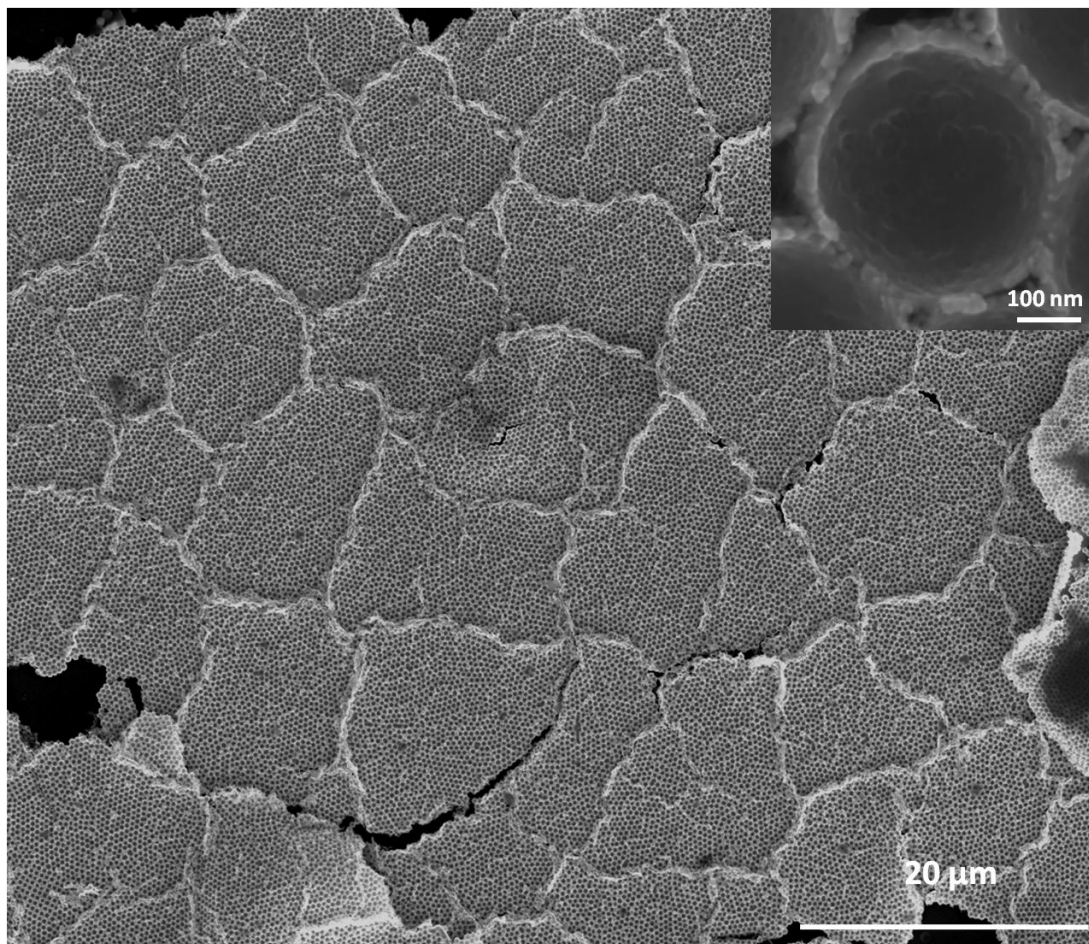


Figure 5: FESEM images of a low magnification of the gold bowl arrays. Inset shows a single bowl with a thickness of ~ 30 nm.

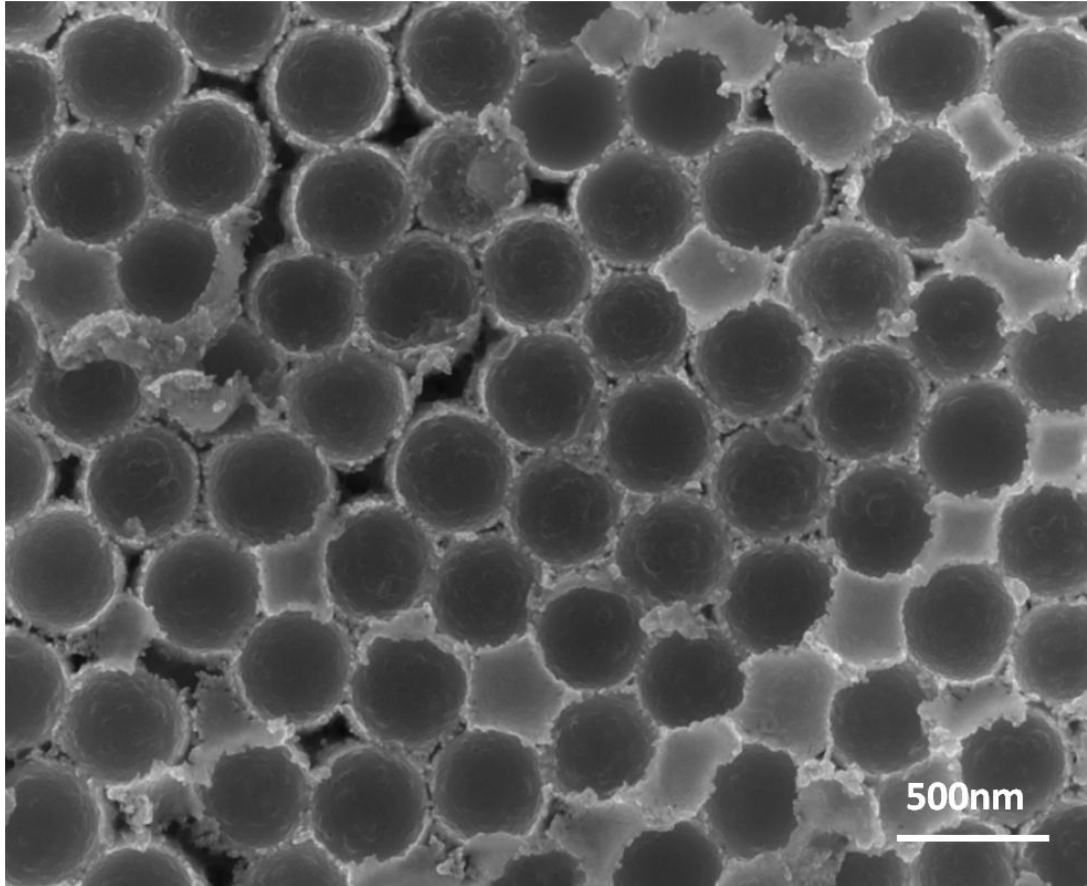


Figure 6: Higher magnification FESEM image of the gold bowl arrays.

The bowls are uniform in size with the inner diameter matching the size of the silica spheres. The outer diameter is ~ 30 nm in most of the bowls (Inset of figure 5). The depth of these bowls varies from 150 to 200 nm. The inner walls of the bowls are comparatively smoother than the outer walls. Also, bowls on the periphery of the array have uneven rim surface whereas, the bowls formed in the center have a smooth hemi-spherical rim surface (Figure 7), probably due to the differences in the coating level. The schematic of the formation of gold bowl arrays is given in Figure 8.

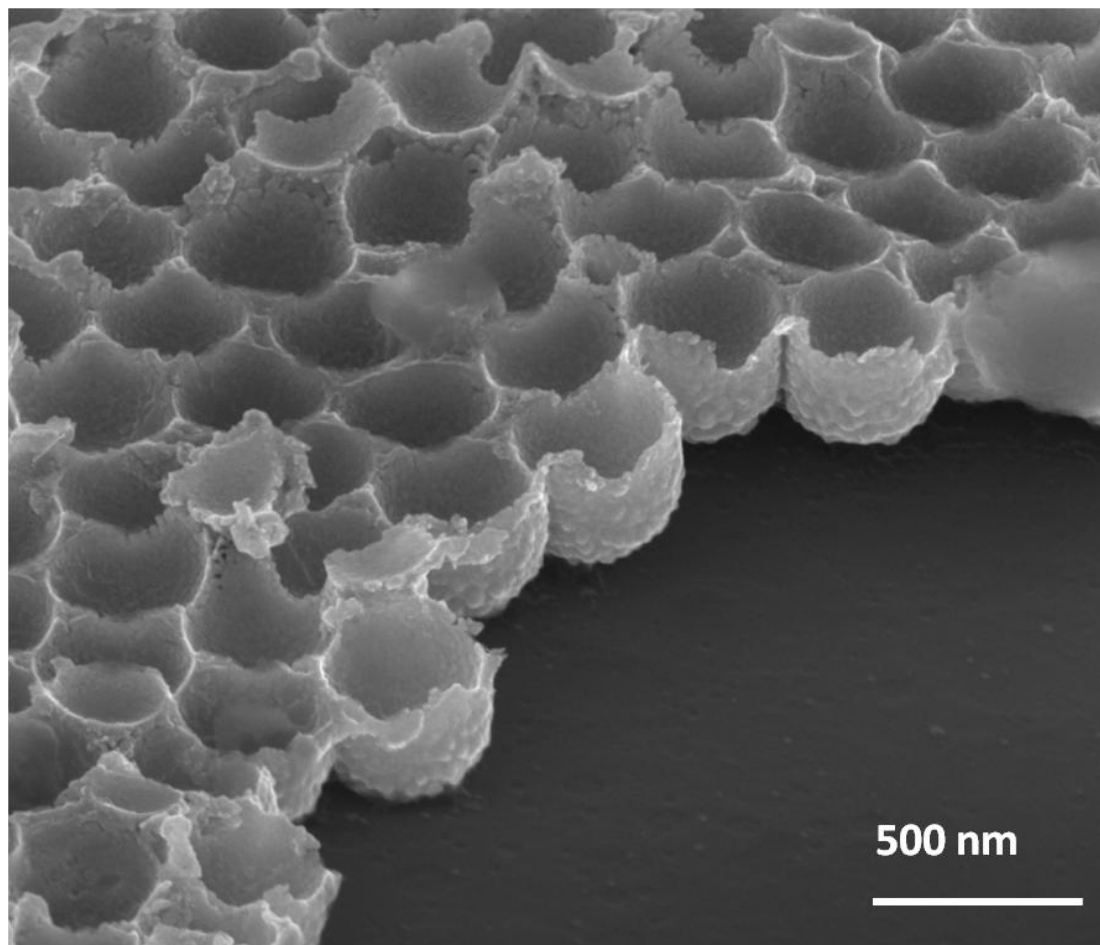


Figure 7: FESEM image of gold bowls shown on the periphery of the array

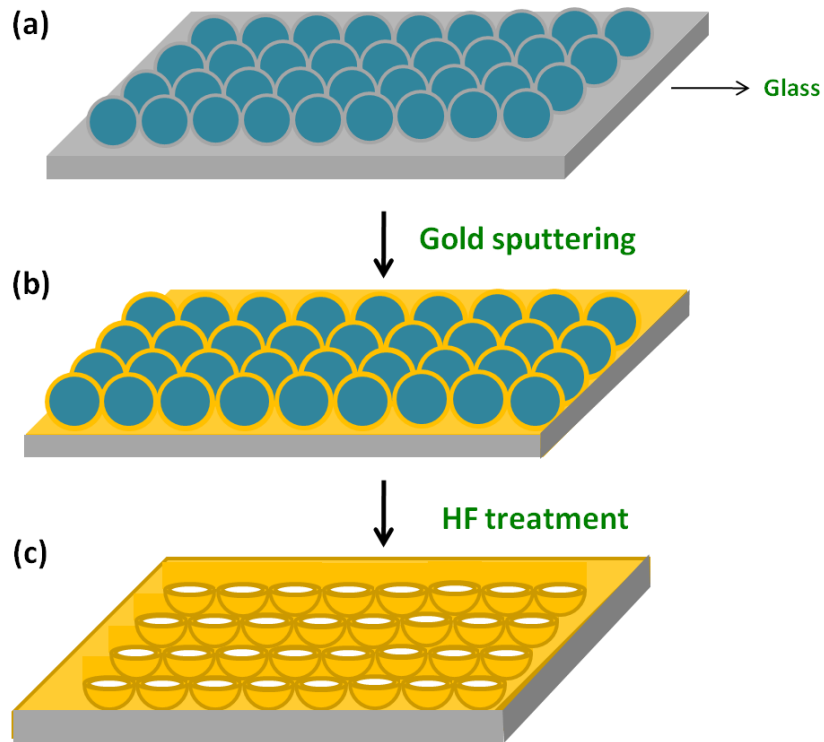


Figure 8: Schematic illustration of the synthetic process (a) Silica colloidal spheres dried on a glass substrate (b) Gold coating over the spheres using sputtering process (c) Removal of the silica spheres using HF treatment.

3.5 Conclusions

In conclusion, this chapter describes a simple method for fabrication of ordered gold nanobowls over large area using sputter deposition of gold over colloidal silica spheres. This method is unique from the other deposition methods, in which the coating of gold clusters starts from the bottom of the spheres. This will

avoid the separation (inversion) process usually adopted to get the ordered bowls from other methods.

3.6 References

1. X. D. Wang, E. Gruagnard, J. S. King, Z. L. Wang and C. J. Summers, *Nano Lett.* **2004**, *4*, 2223.
2. Y. Rondelez, G. Tresset, K. V. Tabata, H. Arata, H. Fujita, S. Takeuchi and H. Noji, *Nat. Biotechnol.* **2005**, *23*, 361.
3. A. K. Srivastava, S. Madhavi, T. J. White and R. V. Ramanujan, *J. Mater. Chem.* **2005**, *15*, 4424.
4. J. C. Love, J. L. Ronan, G. M. Grotenbreg, A. G. van der Veen and H. L. Ploegh, *Nat. Biotechnol.* **2006**, *24*, 703.
5. J. E. Barton and T. W. Odom, *Nano Lett.* **2004**, *4*, 1525.
6. M. Xu, N. Lu, H. Xu, D. Qi, Y. Wang and L. Chi, *Langmuir* **2009**, *25*, 11216.
7. J. Ye, P. V. Dorpe, W. V. Roy, G. Borghs and G. Maes, *Langmuir* **2009**, *25*, 1822.
8. Y. Li, W. Cai and G. Duan, *Chem. Mater.* **2008**, *20*, 615.
9. X. Chen, X. Wei and K. Jiang, *Optics Express* **2008**, *16*, 11888.
10. R. J. Jackman, D. C. Duffy, E. Ostuni, N. D. Willmore and G. M. Whitesides, *Anal. Chem.* **1998**, *70*, 2280.
11. X. D. Wang, C. Lao, E. Gruagnard, C. J. Summers and Z. L. Wang, *Nano Lett.* **2005**, *5*, 1784.

12. Y. Li, C. C. Li, S. O. Cho, G. T. Duan and W. P. Cai, *Langmuir* **2007**, *23*, 9802.
13. J. C. Love, B. D. Gates, D. B. Wolfe, K. E. Paul, and G. M. Whitesides, *Nano Letters*, **2002**, *2*, 891.
14. W. Stober, A. Fink and E. Bohn, *J. Colloid Interface Sci.* **1968**, *26*, 62.

Chapter 4

Sponges: A generic and rapid synthesis of high surface area nanoporous noble metals showing broadband nonlinear optical response

Summary

This chapter focuses on the synthesis, characterization and broadband nonlinear optical properties of nanoporous noble metals like Au, Ag, Pd and Pt. It highlights instantaneous formation of high surface area noble metal nanosponges through a one-step inexpensive method in a green solvent, water. Employing simple, sodium borohydride reduction route, three-dimensional porous structures made up of nanowire networks were generated. The process is generic, involves room temperature reduction of metal salts with sodium borohydride, and is therefore scalable to any amount. Further, these nanoporous metals because of their network structures show optical limiting behavior of a true broadband nature that would find applications in optoelectronic nanodevices.

Paper based on the above study has been published in *ACS Nano* **2010**, *4*, 2681.

4.1 Introduction

Porous metals with sponge-like nanostructures, for their high surface area, low density, high gas permeability, and thermal conductivity, find immense applications in catalysis (1), fuel cells (2, 3), membranes (4), sensors (5, 6), electrodes (7), and actuators (8, 9). Though significant progress has been made in making and manipulating many porous, high surface area metal oxides (10-12), the same is not true for the metals. The most versatile template-based approach used for the synthesis of porous, high surface area metal oxides does not give the desired results with metals, in particular, noble metals such as Ag, Au, Cu, Pt, and Pd, which are industrially more valuable considering their use in the production of hydrogen from methane (13), reduction of pollutants from automobiles (14), CO oxidation (15-17), and in fuel cells (2, 3). Nevertheless, template-based methods employing both soft and hard templates were routinely used to make porous noble metals with very low surface area ($\sim 2 \text{ m}^2/\text{g}$) (18-22). Other methods such as selective dissolution of a metal from an alloy (23, 24), pH-controlled reduction by glucose (25), fusion of nanoparticles at the interface of a biphasic oil-water mixture (26), reaction-limited aggregation (27), and emulsion-based synthesis in presence of a surfactant (28) were also used to make porous noble metal nanostructures. In a different approach, fusion of preformed noble metal nanoparticles into network structures was also being explored recently. For example, Nadja *et al.* have reported the formation of porous noble metal network structures (aerogel) by treating the preformed citrate-stabilized nanoparticles with hydrogen peroxide (29) for a week followed by supercritical CO_2

drying to remove the solvent. Grzybowski and co-workers reported the self-assembly of long-chain dithiol-connected, deformable, spherical aggregates of metal nanoparticles into macroscopic nanostructured materials which, on thermal hardening, yields polycrystalline monolith with controlled porosity (30). All of these processes reported so far are either multistep, non-scalable processes and/or restricted to one or two metals or yield only a very low surface area. In this chapter, we are exploring for the first time, kinetically controlled sodium borohydride reduction process (without any capping agent) to obtain high surface area nanostructured networks of noble metals. Sodium borohydride reduction is an age-old method to obtain metal nanoparticles from their precursors in the presence of a capping agent but seldom used to obtain porous noble metal nanostructures. By carefully controlling the concentration of metal precursors and the sodium borohydride, the fusion of bare metal nuclei formed during the reduction process can be induced to form a three dimensional sponge-like network of noble metals instantaneously. The process involves room temperature reduction of metal salts in water and is, therefore, scalable to any amount.

4.2 Scope of the present investigation

Making of nanoporous metals with high surface areas has been a challenging task for scientists. There is a huge demand for noble metals that are extensively used in catalysis, fuel cells, electrodes, membranes and many other applications. Making of noble metals with high surface areas often involves multiple steps which increases

the cost of synthesis. A single step, general process to produce high surface area noble metal nanostructures is the scope of present investigation.

4.3 Experimental section

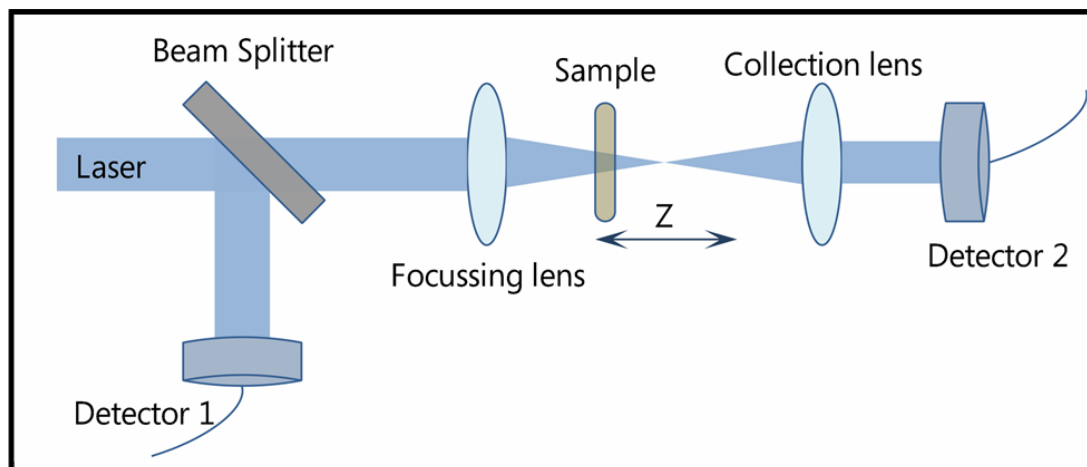
4.3.1 Synthetic procedure for sponges

Gold nanosponge was synthesized by adding 10 ml aqueous solution of 0.1 M HAuCl_4 (Aldrich) to 50 ml aqueous solution of 0.1 M NaBH_4 (1 : 5 v/v ratio of $\text{HAuCl}_4/\text{NaBH}_4$ solution) with stirring. Addition of auric chloride solution to the borohydride solution resulted in the formation of effervescence (due to the release of hydrogen) with a black spongy solid floating on the reaction medium. The stirring was continued for about 5 min until the entire solution became colorless. The floating solid was filtered and washed with distilled water and dried at room temperature.

In a similar method, Ag, Pd and Pt nanosponges were synthesized by adding 50 ml of 0.1 M NaBH_4 solution with 10 ml of 0.1 M metal precursor solution with stirring. AgNO_3 , PdCl_2 and H_2PtCl_6 were used as the precursors for synthesis of Ag, Pd, Pt nanosponges respectively.

4.3.2 Z-scan experiment

The experiments on nonlinear optical properties of the nanosponges were carried out using well-known Z-scan method (A schematic of the Z-scan experiment is given below). The Z-scan is a widely used technique developed by Sheik Bahae *et al* (31) to measure the nonlinear absorption coefficient and nonlinear refractive index of materials. In the “open-aperture” Z-scan, a Gaussian laser beam is focused using a convex lens, and its propagation direction is taken as the z-axis. The focal point is taken as $z = 0$. This focused beam will have maximum energy density at the focus, which will symmetrically reduce towards either side of it, for the positive and negative values of z. The experiment is done by placing the sample in the beam at different positions with respect to the focus (different values of z), and measuring the corresponding transmission. The position vs. transmission curve is known as the open-aperture Z-scan curve. The sample sees different laser intensity at each position, and hence, the position-dependent transmission data can be converted to the intensity-dependent transmission data. From the Z-scan curve the nonlinear absorption coefficient of the sample can be calculated.



Schematic showing the Z-scan experimental set-up

In our Z-scan setup, stepper-motor was used to control linear translation stage to move the sample through the beam in precise steps. The samples were taken in 1 mm glass cuvette (Hellma GMBH). The transmission of the sample at each point was measured by means of two pyroelectric energy probes (RjP7620, Laser Probe Inc.). One energy probe monitored the input energy, while the other monitored the transmitted energy through the sample. The second harmonic output (532 nm) of a Q-switched Nd:YAG laser (Minilite, Continuum) was used for exciting the samples. The nominal pulsewidth of the laser was 5 nanoseconds. For 1064 nm excitation, we used the fundamental output from another Q-switched Nd:YAG laser (Quanta Ray, Spectra Physics). The nominal pulse width at 1064 nm was 8 nanoseconds. The pulses were fired in the “single shot” mode, allowing sufficient time between successive pulses to avoid accumulative thermal effects in the sample.

The equation for nonlinear transmission due to three-photon type absorption is given by: (32)

$$T = \frac{(1-R)^2 \exp(-\alpha L)}{\sqrt{\pi p_0}} \int_{-\infty}^{+\infty} \ln \left[\sqrt{1 + p_0^2 \exp(-2t^2)} + p_0 \exp(-t^2) \right] dt \quad (1)$$

Where, T is the transmission of the sample, R is the Fresnel reflection coefficient at the sample-air interface, α is the absorption coefficient, and L is the sample length. p_0 is given by $[2\gamma(1-R)^2 I_0^2 L_{\text{eff}}]^{1/2}$ where γ is the three-photon absorption coefficient, and I_0 is the incident laser intensity. L_{eff} is given by $[1 - \exp(-2\alpha L)]/2\alpha$. By numerically fitting the experimental data to the above equation, the effective three-photon absorption coefficient could be calculated.

4.3.3 Surface-enhanced Raman spectroscopy (SERS)

The as-prepared nanosponges of silver and gold were tested for SERS activity. For this purpose, 20 μl of Rhodamine 6G (both 10^{-4} M and 10^{-6} M) was drop casted onto a glass slide containing 10 mg of the nanosponge sample. Raman spectra were recorded at room temperature using 632 nm HeNe laser as a source.

4.3.4 Anti-bacterial studies

To study the anti-bacterial activity of the silver, a silver nanosponge–Whatman® composite membrane was prepared by dipping a Whatman® filter paper (125 mm Ashless circles obtained from Whatman® Schleicher & Schuell) in 10 ml of 0.1 M AgNO₃ solution for 30 minutes and followed by dipping it in a 50 ml 0.1 M NaBH₄ solution. Immediate reaction resulted in a dark grey colored membrane. The membrane was washed several times with Millipore water and dried at room temperature prior to the study of anti-bacterial activity.

Anti-bacterial study was done using *E.Coli* (DH5α). The bacteria were inoculated in LB (Luria Bertani) broth and grown overnight at 37 °C in a shaker incubator. The bacterial cells were spread plated on an agar medium (1.5% agar plates were made for the purpose).

4.3.5 Sample characterization

The morphologies of the samples obtained in all the experiments were examined with a field-emission scanning electron microscope (FESEM, FEI Nova-Nano SEM-600, The Netherlands) and TEM (JEOL JEM-3010 with an accelerating voltage at 300 kV). Powder X-ray diffraction (XRD) patterns were measured using a Rich-Siefert 3000-TT diffractometer employing CuKα radiation. N₂ adsorption–desorption isotherms were measured (using nearly 1 gm of sample) with a Quantachrome Autosorb-1C surface-area analyzer at liquid nitrogen temperature (77

K). Absorption studies were carried out using Perkin-Elmer instruments Lambda 900 UV/Vis/NIR spectrometer. Raman spectra were recorded with LabRAM HR Raman spectrometer at an excitation wavelength of 632 nm (HeNe laser as source).

4.4 Results and discussion

Figure 1a shows the low-magnification FESEM image of a gold nanosponge of about 200 μm size obtained by adding 0.1 M auric chloride solution to 0.1 M sodium borohydride solution (1:5 v/v). The cross-sectional image of the nanosponge with 12 μm thickness is shown in Figure 1b. Higher magnification image shows that the nanosponge is made up of porous, interconnected networks (Figure 2). The sizes of the ligaments creating the nanoporous network are in the range of 20 to 50 nm.

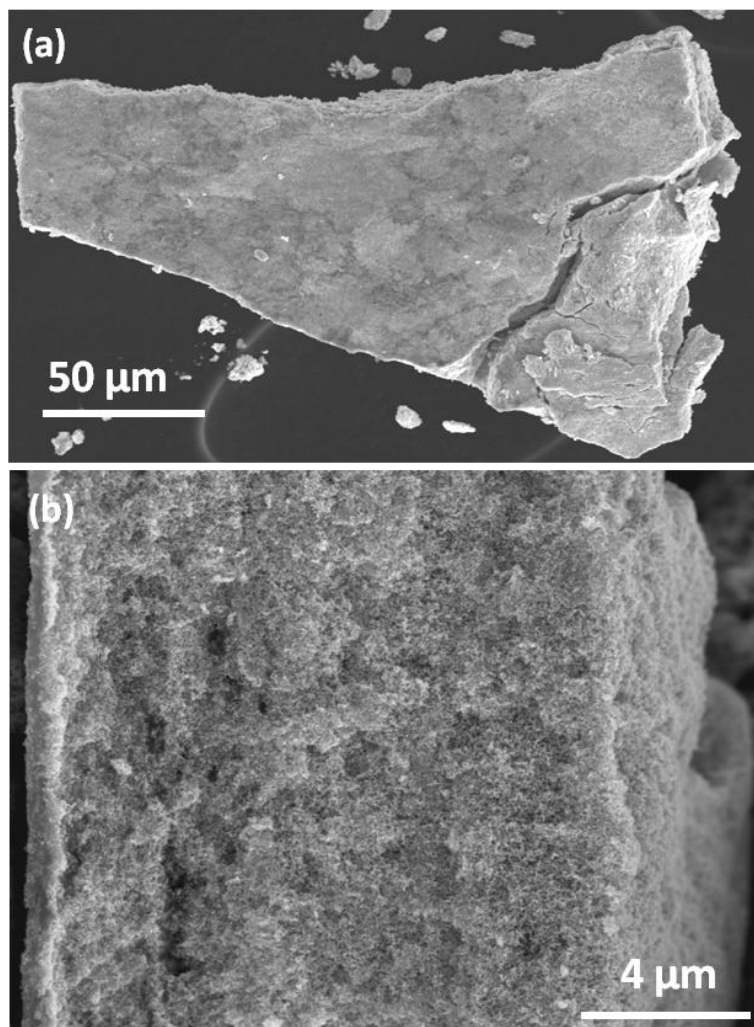


Figure 1: (a) Low-magnification FESEM image of a gold nanosponge in a monolithic form (b) Cross-sectional view of the gold nanosponge

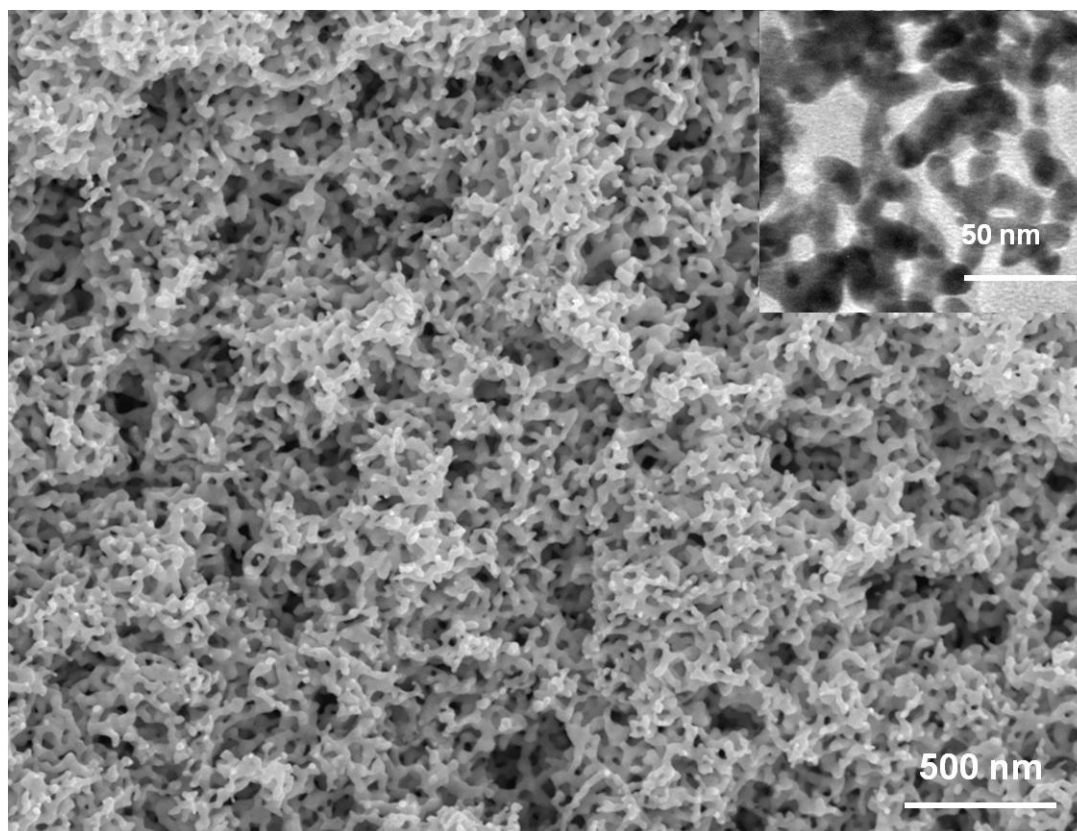


Figure 2: Higher magnification FESEM image of the gold nanosponge showing porous interconnected networks with ligaments of size 20–50 nm. Inset shows the TEM image of the gold nanosponge.

Close observation of these networks shows that the ligaments are not of uniform size and often figured with many branches suggesting their formation through the fusion of nanoparticles. The TEM image (inset of Figure 2) further confirms that the pores created by the interconnected ligaments are in the order of 50 - 150 nm. The polycrystalline nature of the sponge observed from the ED pattern also suggests that the nano networks were originated from the fusion of nanoparticles (inset of Figure 3).

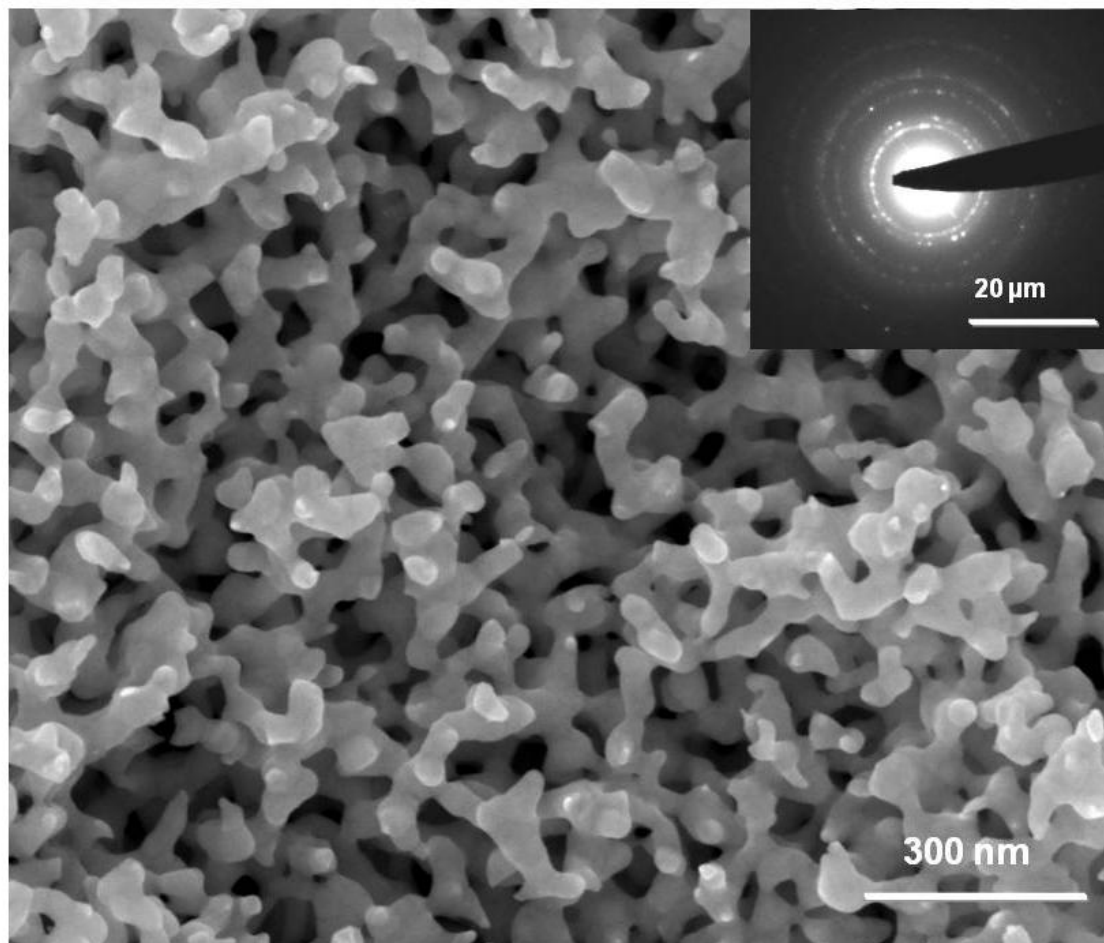


Figure 3: FESEM image showing gold nanostructure with highly interconnected ligaments of size 20 – 50 nm. Inset shows the ED pattern.

The porous, spongy morphology of gold nanostructure is retained even when the reduction of gold chloride (0.1 M) was carried out with higher concentration of sodium borohydride (2 M) (Figure 4). Higher magnification FESEM image further shows that the porous networks are made up of nanoligaments of size around 20 - 50 nm (Figure 5). Similar type of spongy network was obtained with silver when silver nitrate (0.1 M) was mixed with sodium borohydride of equimolar concentration in 1:5 volume ratio (Figure 6a). The sizes of ligaments obtained in this case are in the

range of 50 - 80 nm and are well connected three dimensionally. TEM image (Figure 6b) shows that the sizes of pores are between 50 and 100 nm and are formed by the extended network of fused nanostructure. ED pattern (Figure 6c) further confirms the polycrystalline nature of the silver nanosponge.

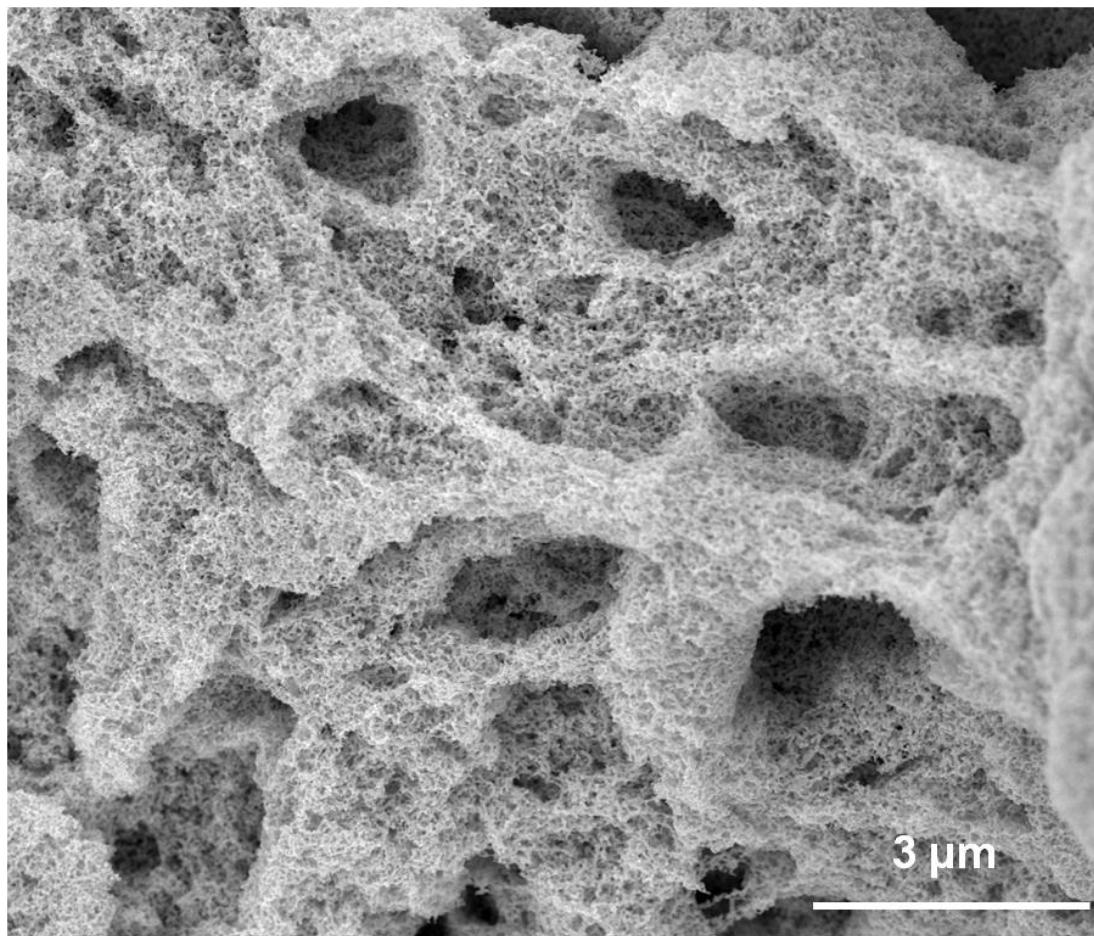


Figure 4: Low-magnification FESEM image of gold nanosponge prepared using 2M NaBH₄ solution showing the spongy networks

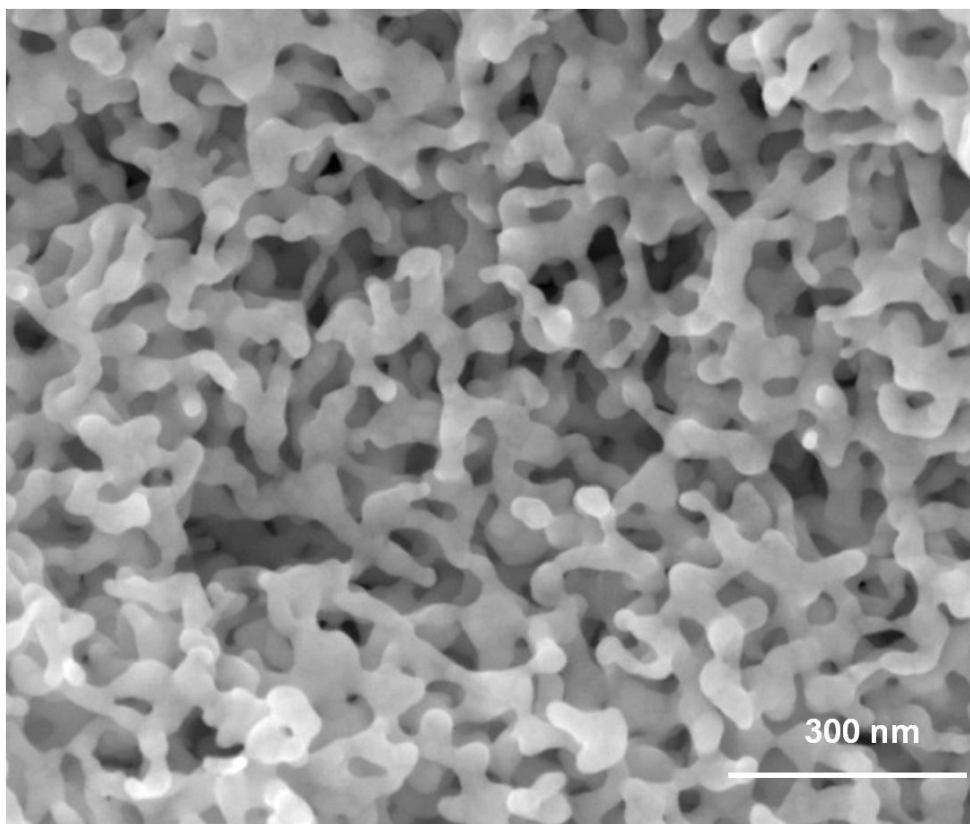


Figure 5: Higher magnification FESEM image of the gold nanosponge

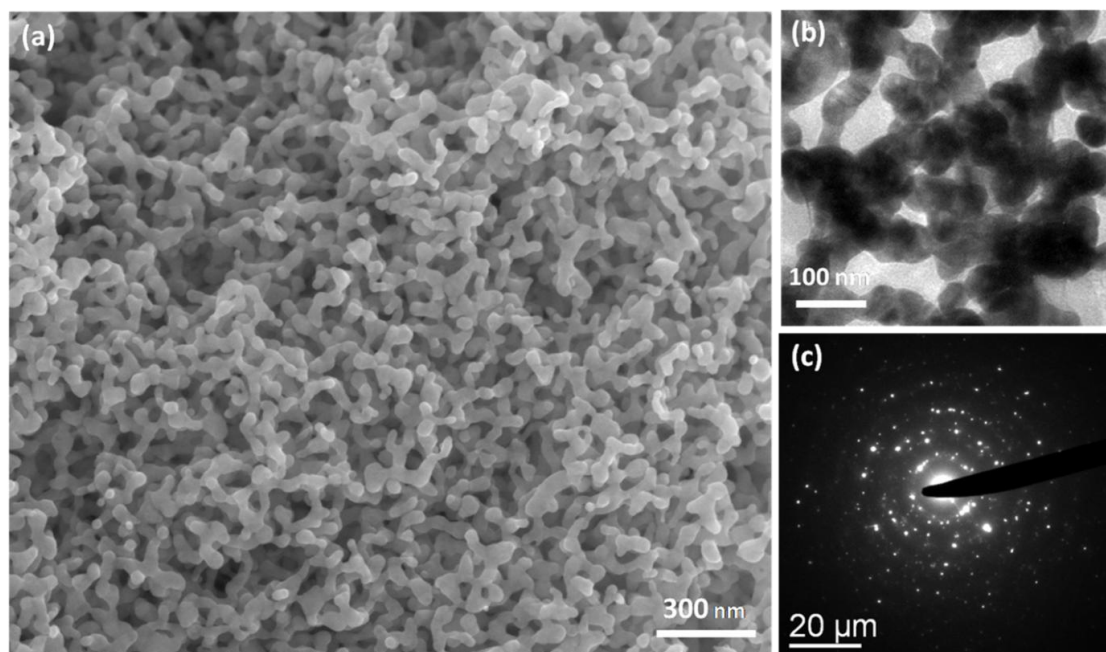


Figure 6: (a) FESEM image of silver nanosponge showing the highly interconnected ligaments. (b) TEM image of the silver nanosponge showing network of ligaments of size 50–60 nm (c) ED pattern showing the polycrystallinity of the silver nanosponge.

Figure 7a shows the spongy structure of Pd made up of thread-like nanoligaments. The network is formed by the fusion of nanoparticles of size around 5 nm (Figure 7b). The interconnected ligaments are significantly smaller in size when compared to Ag and Au ligaments, probably due to the variation in growth kinetics of different metal nanoparticles. In a similar way, platinum also forms a three-dimensional network nanostructure shown in Figure 8a. TEM image (Figure 8b) shows that these networks are of the size around 30 nm and are composed of very fine particles of size less than 5 nm. The particles are fused in such a way that even after sonication they stand together and retain the network morphology.

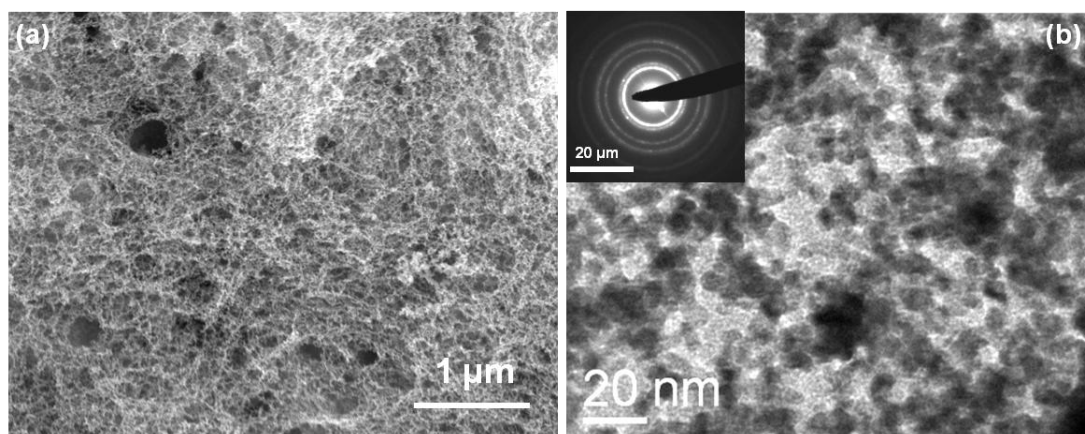


Figure 7: (a) Low-magnification FESEM image of palladium nanosponge (b) TEM image showing palladium nanoparticles of 5–10 nm size fused to form a network structure. Inset shows its ED pattern

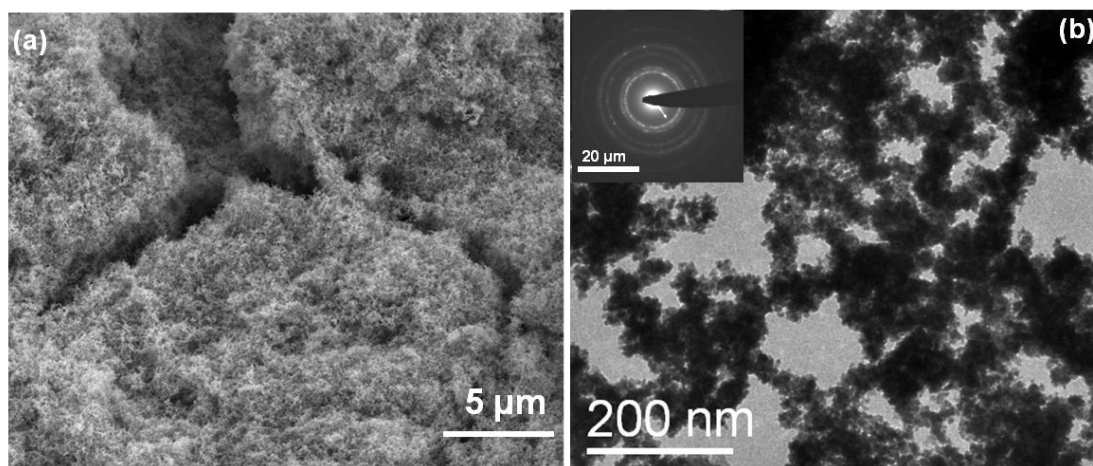


Figure 8: (a) Low-magnification FESEM image showing the platinum nanosponge (b) TEM image showing the platinum networks made up of nanoparticles of size 5–10 nm. Inset shows its ED pattern.

The powder X-ray diffraction pattern (PXRD) shows the peaks corresponding to the cubic phase for all of the metal nanosponges (Figure 9). The peak broadening observed in the XRD patterns is associated with the nanostructured ligaments present in the metal sponges.

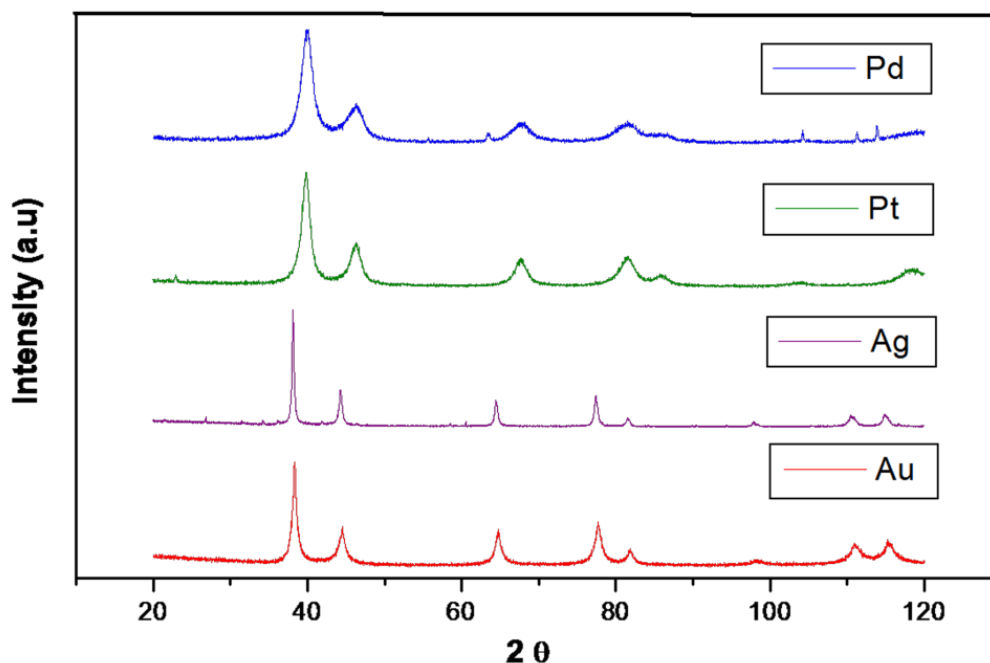


Figure 9: X-ray diffraction pattern of the metal nanosponges

The nitrogen adsorption - desorption isotherms obtained at liquid nitrogen temperature (77 K) show type II behavior for all of the metal nanosponges. The specific surface area measured using the BET method shows 41, 16, 81, and 51 m²/g, respectively for Au, Ag, Pd, and Pt nanosponges (Figure 10). To the best of our knowledge, these are the highest surface areas reported so far for any self-supported Au, Ag, Pd, and Pt nanostructures in one simple, template-free method. Since the

networks were formed through the fusion of metal nanoparticles/clusters (of size 5 nm or less in the case of Pd and Pt) emerged during the nucleation step, they were expected to have surface roughness at the nanoscale which would contribute to their high BET surface area.

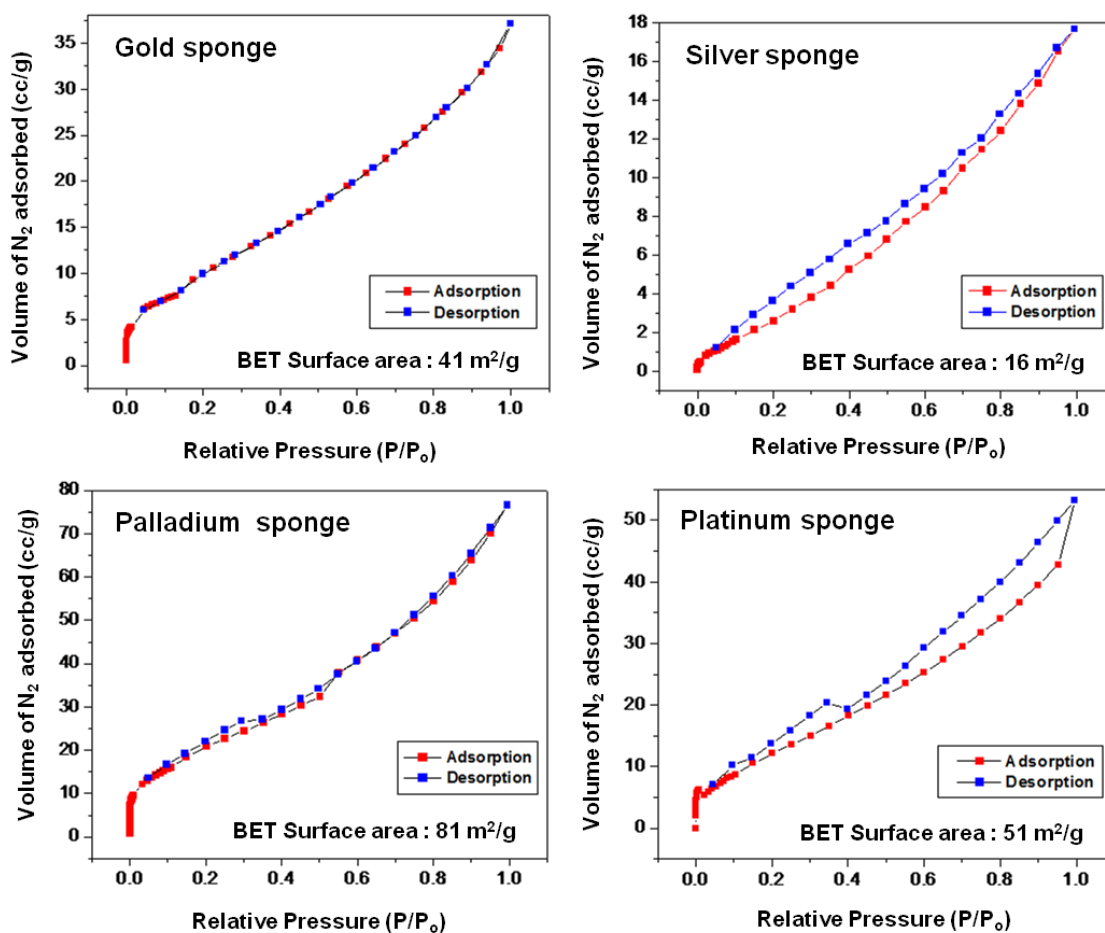


Figure 10: Nitrogen adsorption/desorption isotherms (at 77 K) of the metal nanosponges.

The UV-Vis absorption spectra show near flat absorption for all of the samples for the entire visible region as well as in the IR region associated with the surface plasmon resonance for the extended network nanostructures (Figure 11a).

Size- and shape-dependent surface plasmon resonances in Ag and Au nanoparticles were well studied. For example, spherical Ag and Au nanoparticles were known to show one principal plasmon band around 420 and 520 nm, respectively. However, rod-like nanoparticles, depending on the aspect ratio, will show an additional band at higher wavelength associated with the longitudinal plasmon absorption (33-35). Since the nanoligaments that constitute the network structures produced in our method have all length scales, it shows surface plasmon resonance (a convolution of plasmon absorption bands) over the entire visible region as well as in the IR region of the spectrum. This will also explain the near black color observed for the as-prepared materials. Further, these nanosponge powders (Figure 11b) can be pressed into pellet shape without compromising much of its surface area and porosity (Figure 11c).

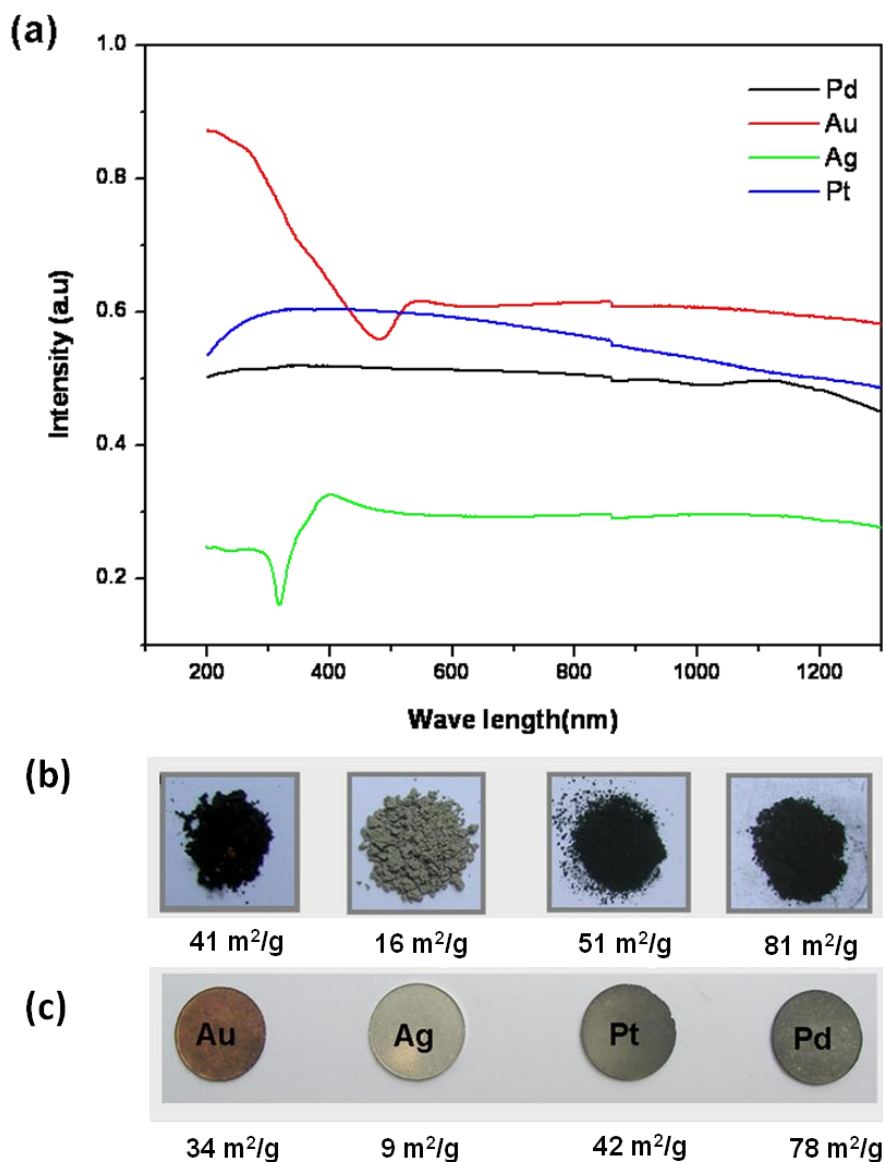


Figure 11: (a) UV-Vis spectra of the nanosponges. Photograph of the nanosponges in (b) Powder form and (c) Pellet form (applied pressure 10 kN)

The specific surface areas of porous discs of Au, Ag, Pd, and Pt nanosponges are measured after applying a mechanical pressure of 10 kN (Figure 12), and except for the Ag disc, all of the porous discs retain more or less the same surface area. In

the case of Ag, nearly 40% reduction in the surface area was observed at 10 kN pressure. However, the Ag discs made by applying 1 kN pressure show only 25% reduction in surface area ($12 \text{ m}^2/\text{g}$). Further, the effect of temperature on the nanosponge was studied for silver, which shows a drastic decrease in the surface area with an increase in temperature. This significant reduction in surface area at $500 \text{ }^\circ\text{C}$ is attributed to the formation of micrometer sized ligaments due to the sintering of the nanostructure (Figure 13a and 14).

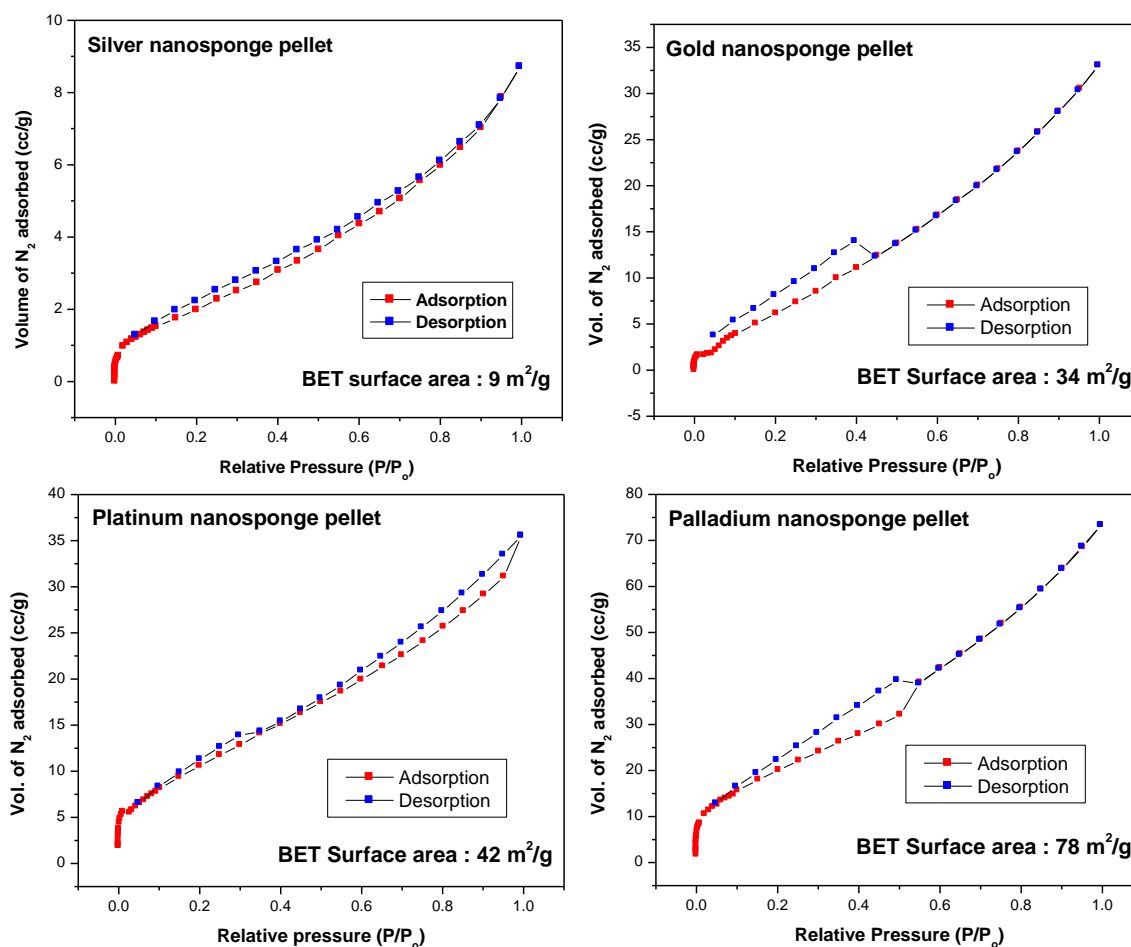


Figure 12: Nitrogen adsorption/desorption isotherms (at 77 K) of metal nanosponge pellets (pressed by applying a pressure of 10 kN)

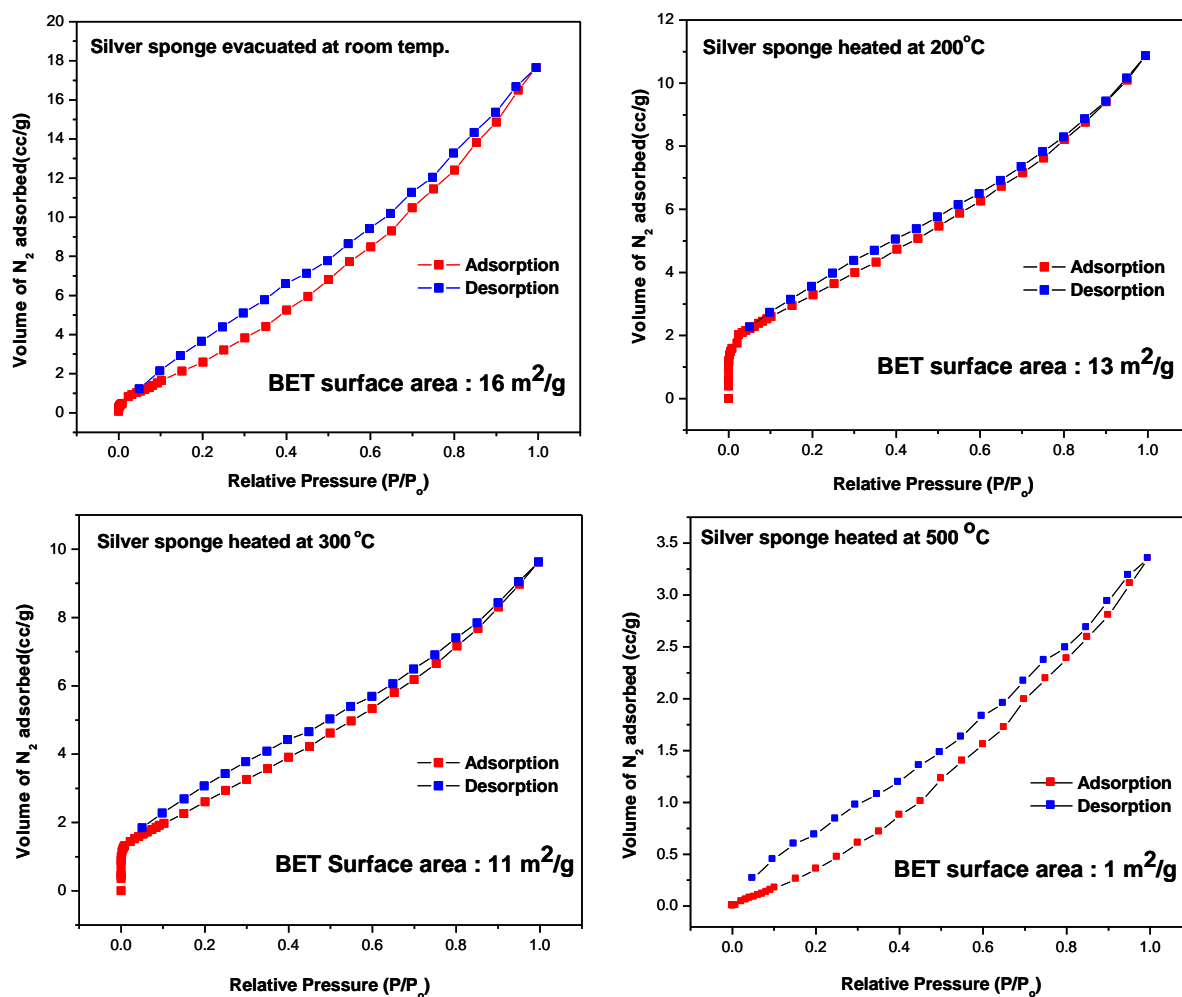


Figure 13: Nitrogen adsorption/desorption isotherms (at 77 K) of silver nanosponge heated at different temperatures

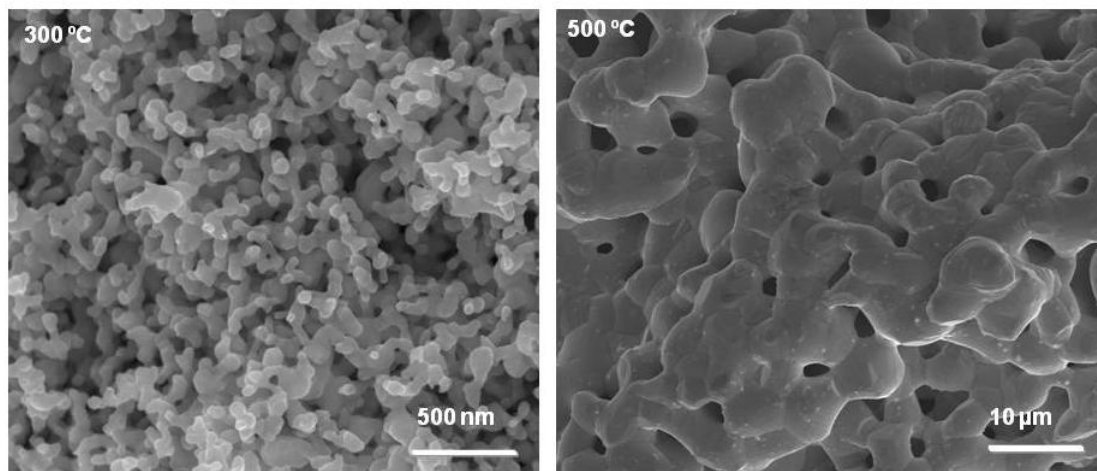


Figure 14: FESEM images of silver nanosponge heated in vacuum at 300 °C and 500 °C for 3 h.

The effect of precursor concentration and the reducing agent, NaBH_4 on the formation of porous network was studied using silver nitrate as the model system. Silver nanosponge with high surface area can be readily formed by mixing the solutions of silver nitrate and borohydride of optimum concentration and amount. If the concentration of silver nitrate is low, around 1.0 mM, porous silver network does not form, no matter how much amount of sodium borohydride is added (Table 1).

Conc. of AgNO ₃ solution	Conc. of NaBH ₄ solution	Volume ratio of Ag ⁺ : BH ₄ ⁻	Product
0.1 M	0.1 M	1 : 1	White micron-sized particles
0.1 M	0.1 M	1 : n , n = 2,3,4,5	Dark grey silver sponge
0.1 M	0.1 M	2 : 1	White micron-sized particles
0.1 M	0.2 M	1 : 1	Dark grey silver sponge
0.2 M	0.1 M	1 : 1	White micron-sized particles
0.001 M	0.001 M	1 : 5	No sponge, nanoparticles

Table 1: Summary of the silver products formed for different precursor concentrations.

If the concentration of silver nitrate is 0.1 M, addition of equal volume of 0.1 M sodium borohydride resulted in micron-sized ligament silver networks. However, mixing a equimolar concentrations (0.1 M and above) of AgNO₃ and NaBH₄ solutions in a 1 : 2 v/v ratio gives a very porous network made up of nanosized ligaments. Further, mixing of equal volumes of 0.2 M AgNO₃ and 0.1 M NaBH₄ solution resulted in micron-sized silver particles and mixing equal volumes of 0.1 M AgNO₃ and 0.2 M NaBH₄ solution resulted in a spongy nanostructure (Figure 15). It is clear from our studies that the formation of silver nanosponge depends not only on the initial concentration of silver nitrate and sodium borohydride solution, but also

on the amount of borohydride ions present in the solution in relation to metal ions. If the concentration of metal ions is below the critical level (*i.e.* below 0.1 M), it favours the formation of colloidal nanoparticles stabilized in solution. For example, 1.0 mM colourless silver nitrate solution gives yellow to dark green colour solution on reduction with sodium borohydride solution of 1 mM or 0.1 M concentration (1 : 5 v/v ratio).

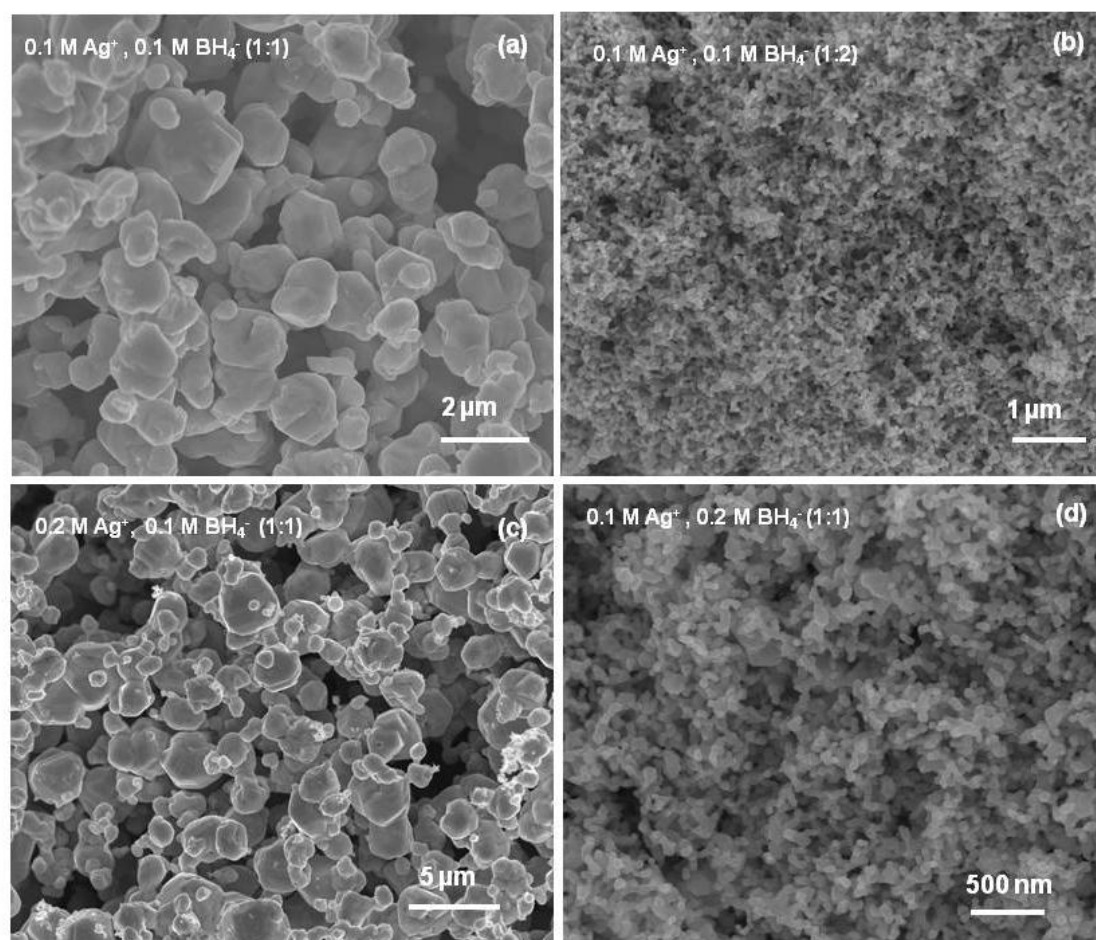


Figure 15: Variations in the silver morphologies obtained with different concentrations of the precursors indicated in the respective images.

Addition of sodium borohydride solution to the silver nitrate solution creates many silver nuclei (clusters) which act as the nucleation centers for further growth. The number of nucleation sites (reduced silver sites) formed is directly proportional to the amount of borohydride added. Rapid fusion and growth of the bare nanoparticles leads to interconnected networks of silver (if the concentration of silver nitrate is around 0.1 M and above), which is then transformed into a black spongy solid that floats on the solution. It is important to note that these three-dimensional networks are not loosely aggregated nanoparticle structures but are fused architects, as can be seen from the TEM and FESEM images (Figures 5 and 6b) and are stable even after sonication. Drying of the uncapped Ag nanoparticle solution (obtained by mixing 1 mM AgNO₃ and 1 mM NaBH₄ solution), however, did not give any network structure.

Unlike for metals in the bulk and nanoparticle form, a broad optical absorption is observed for the metal nanosponges over the entire visible region, which prompted us to study their broadband optical limiting behavior (36-38). In a passive optical limiter, the optical transmittance is progressively reduced when the input light intensity increases, which can be used for safeguarding sensitive optical detectors and eyes from accidental exposure to intense laser beams. For instance, an optical limiter based on heavy-metal-substituted naphthalocyanine has been used to protect a silicon CCD array (39). Some of the optical limiters are referred to as “broadband” devices in literature (40, 41), but to our knowledge, there is no report yet on a nanomaterial-based optical limiter which is truly broadband, that is, capable of limiting laser beams of well-separated wavelengths with similar efficiencies for

the same range of input intensities. We observed an optical limiting behavior of nearly the same efficiency in the present nanosponges at 532 and 1064 nm, showing that these are true broadband devices (Figure 16).

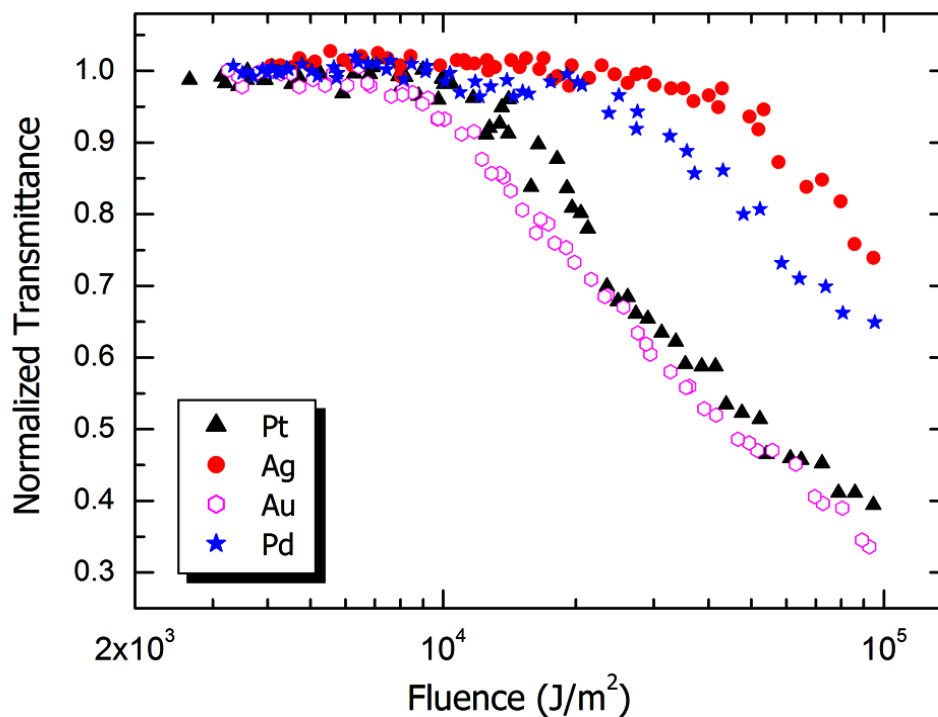


Figure 16: Optical limiting shown by the metal nanosponges at 532 nm excitation.

This is attributed to the almost flat absorption spectra of the metal nanosponges in the visible and near-IR spectral regions. The strong optical limiting behavior for gold nanosponge at two different excitations (532 nm and 1064 nm) is shown in Figure 17a and 17b. A three-photon absorption (3PA)-type process gives the best fit to the experimental data (Figure 18), and the effective three-photon absorption coefficients calculated from the numerical fits are $1.3 \times 10^{-22} \text{ m}^3/\text{W}^2$ for 532nm excitation and $1 \times 10^{-22} \text{ m}^3/\text{W}^2$ for 1064nm.

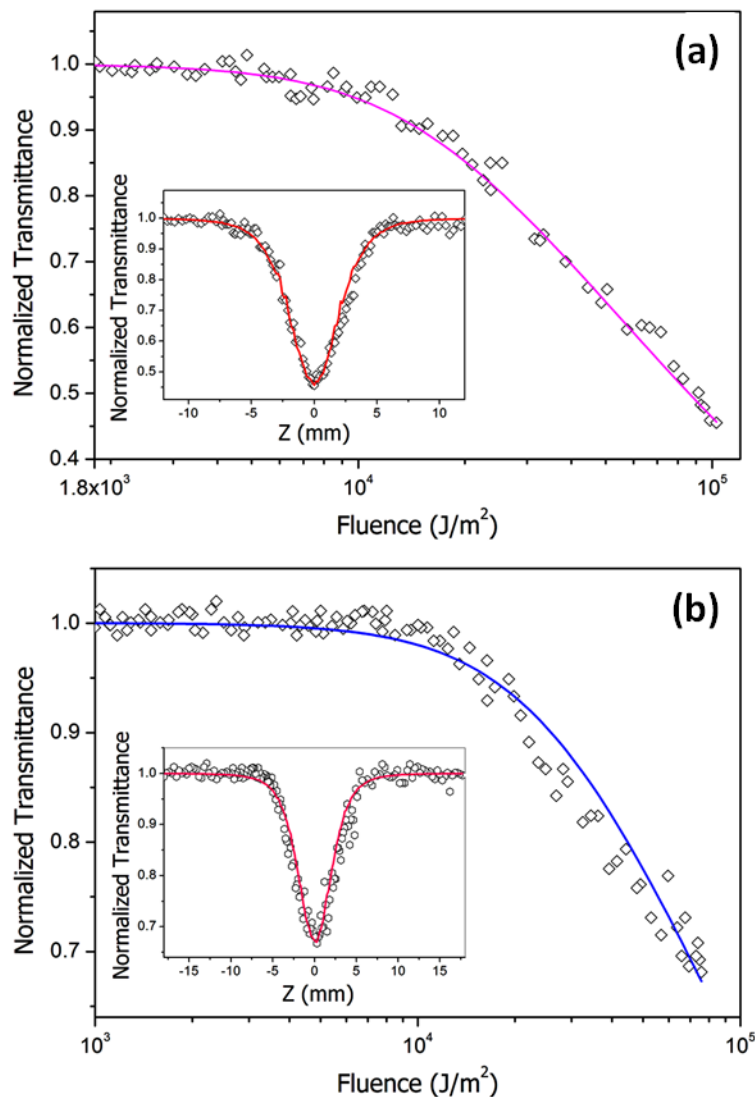


Figure 17: Input laser fluence vs. normalized transmittance curve for the gold nanosponge sample when excited with (a) 532 nm, 5 ns and (b) 1064 nm, 8 ns laser pulses. Open squares show experimental data and the solid curve shows the best fit to the data assuming a 3PA process. The insets show the corresponding open-aperture Z-scan curves.

Considering the absorption spectra of the nanosponges and recalling that pure three-photon absorption cross sections are generally very low, it appears that the

observed nonlinearity arises from sequential three-photon absorption involving real excited states, rather than from a pure three-photon absorption process. Two photon absorption followed by excited state absorption is another possibility. Therefore, the nonlinearity can be considered as an “effective” three-photon absorption process. Such absorptive nonlinearities involving real excited states have been reported earlier in C_{60} , carbon nanotube hybrid structures (42), semiconductors, metal nanoclusters (33, 43, 44), *etc.* To estimate the contribution of nonlinear scattering to the observed optical limiting, we did Z-scan experiments at relatively lower energies, where nonlinear scattering was negligible (Figure 19). The gold nanosponge still showed significant optical limiting, confirming that the optical limiting primarily arises from absorptive nonlinearities in the system, though it may be augmented by nonlinear scattering at the higher intensities used.

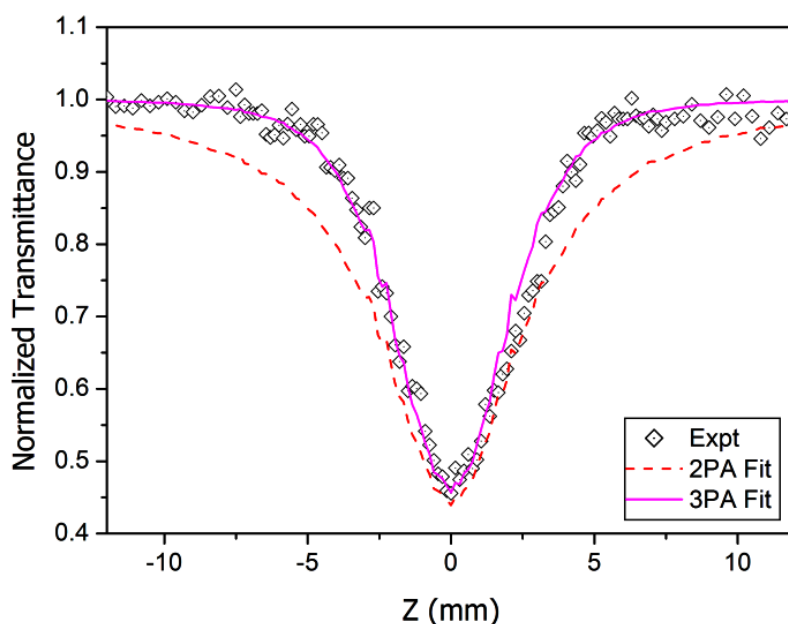


Figure 18: Numerical fits to the Z-scan data assuming 2PA as well as 3PA processes. It can be clearly seen that a 3PA process fits well to the data.

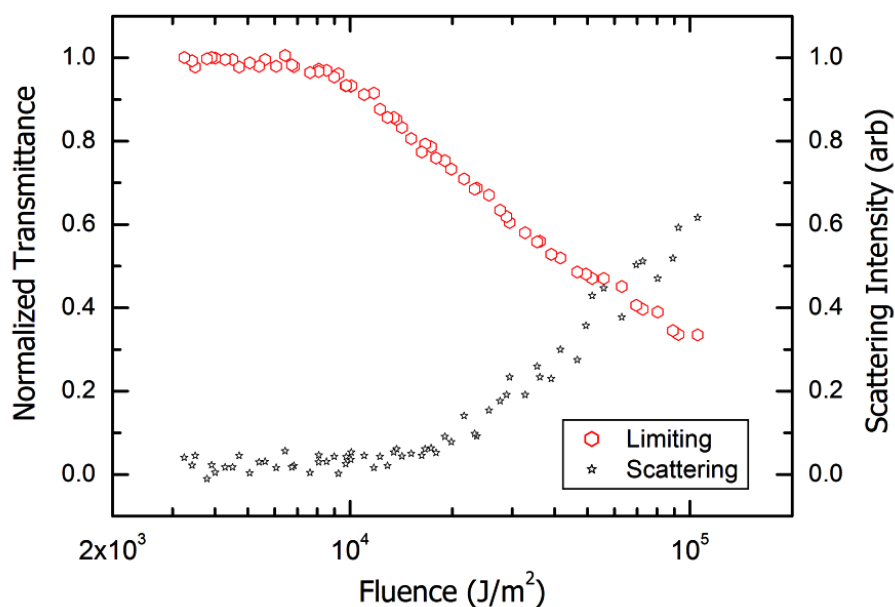


Figure 19: Nonlinear scattering shown by the gold nanosponge at 532 nm plotted against the optical limiting curve. The contribution from scattering becomes significant only at high fluences.

The nanosponges of gold and silver were also tested for surface-enhanced Raman scattering (SERS) activity and were found to enhance the Raman signals of a known dye, Rhodamine 6G, even at lower concentration (10^{-6} M). Since these nanosponges show broad surface plasmon absorption in the visible and IR regions, the SERS shown by these substrates is not restricted to only one excitation wavelength, as is the case for Au or Ag nanoparticles of particular size. The characteristic signals for Rhodamine 6G was enhanced multifold when observed over the Ag and Au substrates whereas the Rhodamine 6G dye of 10^{-4} M concentration over the glass slide without the nanosponge could not be detected (Figure 20a and 20b).

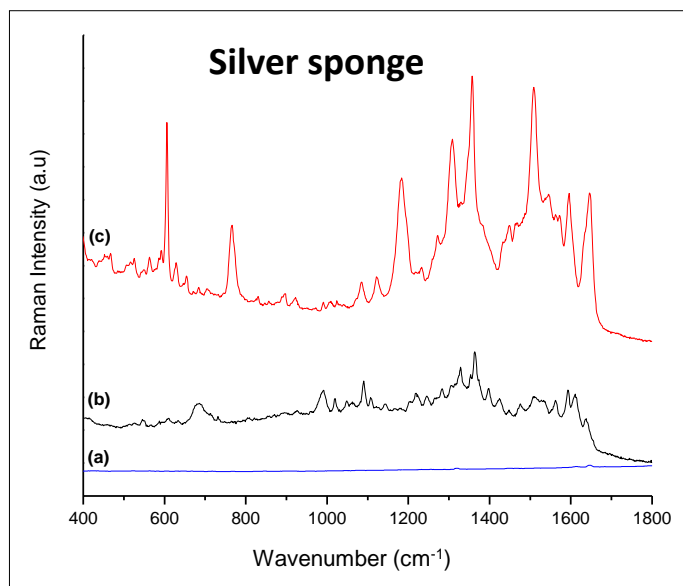


Figure 20a: Surface-enhanced Raman spectra (SERS) of (a) Rhodamine 6G (10^{-4} M), (b) Rhodamine 6G (10^{-6} M) with silver nanosponge and (c) Rhodamine 6G (10^{-4} M) on silver nanosponge

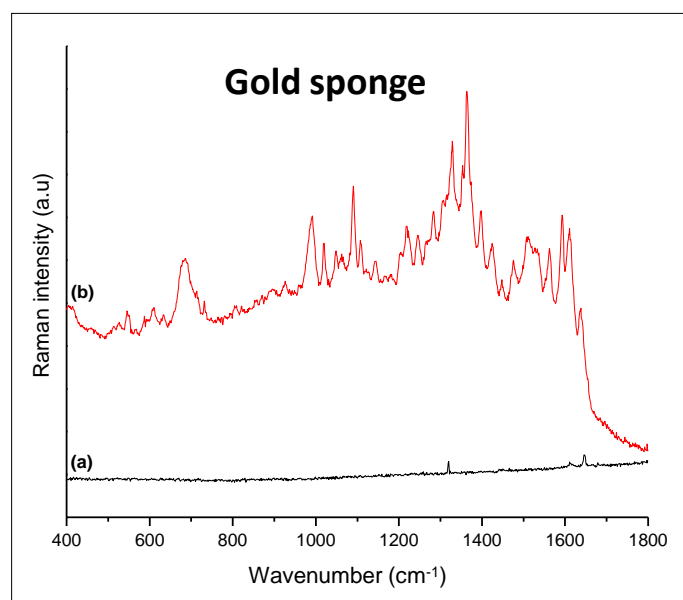


Figure 20b: Surface-enhanced Raman spectra (SERS) of (a) Rhodamine 6G (10^{-4} M) and (b) Rhodamine 6G (10^{-6} M) on gold nanosponge

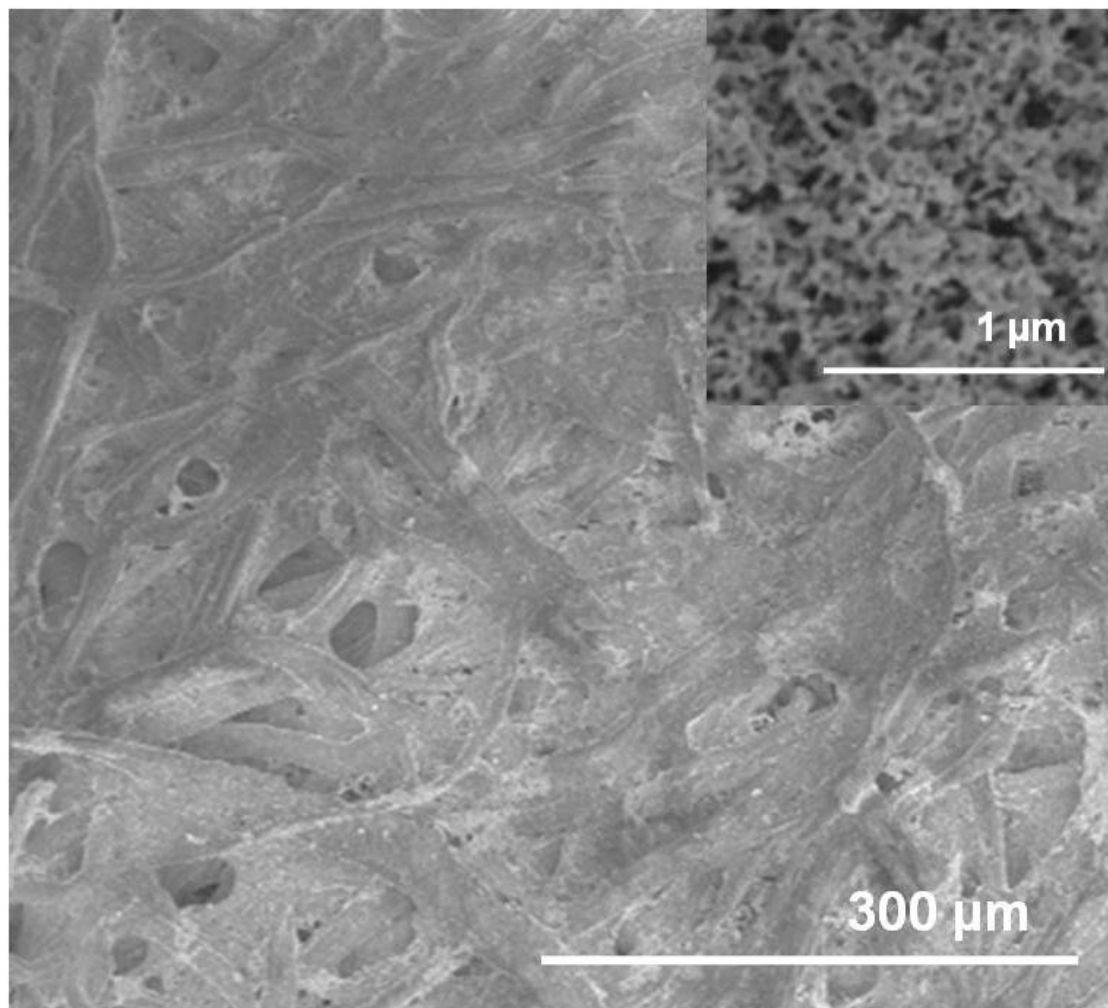


Figure 21: FESEM image of the silver nanosponge – Whatman® filter paper composite. Inset shows the high magnification image of the silver nanosponge deposited on the paper

Besides, these porous nanostructures can be easily deposited onto micrometer-sized porous substrates (*e.g.*, ordinary filter papers) and can be used in biofiltration to sieve, identify, and destroy the harmful bacteria and viruses. The antibacterial activity of a silver spongy network deposited on a Whatman® filter paper was studied with *Escherichia coli* bacteria (see Experimental Section). The

composite membranes were placed in a bacterial growth medium and incubated overnight at 37 °C. The bacterial growth was observed over the entire plates except for the zone where the composite membranes were placed. The silver sponge deposited Whatman® filter paper shows a significant antibacterial effect, as seen from the inhibition zone it created around the silver nanosponge-embedded filter paper (Figure 21 and 22).

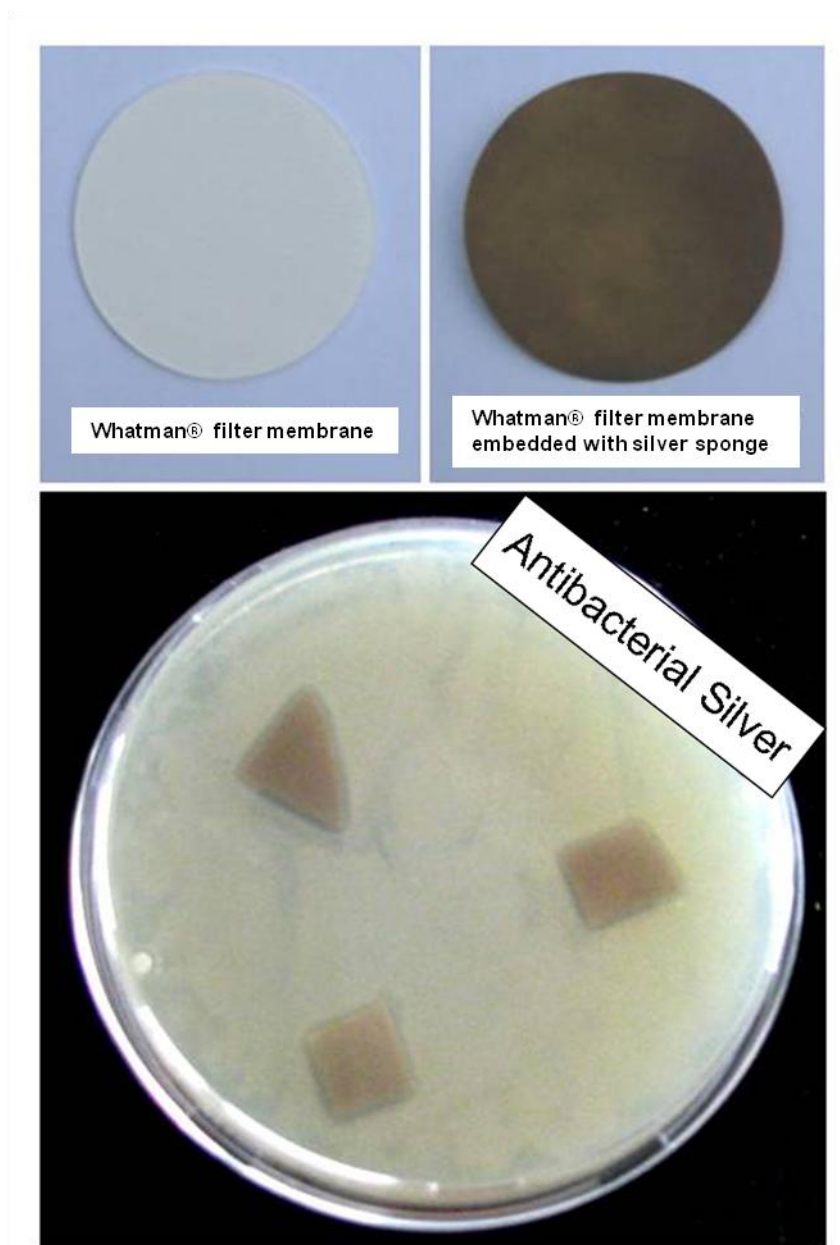


Figure 22: *Photographs showing (a) Whatman® filter membrane and (b) composite membrane embedded with silver nanosponge (c) Anti-bacterial activity of the silver nanosponge - Whatman® filter membrane composite against E. coli bacteria. The inhibition zone against the bacterial growth is visible around the paper strips.*

4.5 Conclusions

In summary, this chapter deals with synthesis of high surface area noble metal nanosponges of Au, Ag, Pd, and Pt by kinetically controlling the simple borohydride reduction process. These 3-D porous nanostructures exhibit efficient broadband optical limiting behavior. Nanosponges of Ag and Au were shown as good substrates for SERS activity. Additionally, the antimicrobial activity of the self-supported nanoporous silver discs or nanoporous silver network incorporated filter papers could be utilized for water purification, particularly to screen and destroy the harmful pathogens. The synthesis strategy in principle could be extended to obtain nanosponges of other metals, metal oxides, and alloys which could find applications as advanced optical sensors and ultrasensitive detectors.

4.6 References

1. D. R. Rolison, *Science* **2003**, 299, 1698.
2. B. C. H. Steele and A. Heinzl, *Nature* **2001**, 414, 345.

3. Y. Ding, M. Chen and J. Erlebacher, *J. Am. Chem. Soc.* **2004**, *126*, 6876.
4. A. P. Padilla, J. A. Rodríguez and H. A. Saitúa, *Desalination* **1997**, *114*, 203.
5. K. Bonroy, J. M. Friedt, F. Frederix, W. Laureyn, S. Langerock, A. Campitelli, M. Sára, G. Borghs, B. Goddeeris and P. Declerck, *Anal. Chem.* **2004**, *76*, 4299.
6. Y.Y. Song, D. Zhang, W. Gao and X. H. Xia, *Chem. Eur. J.* **2005**, *11*, 2177.
7. M. Hieda, R. Garcia, M. Dixon, T. Daniel, D. Allara and M. H. W. Chan, *Appl. Phys. Lett.* **2004**, *84*, 628.
8. J. Biener, A. Wittstock, L. A. Zepeda-Ruiz, M. M. Biener, V. Zielasek, D. Kramer, R. N. Viswanath, J. Weissmüller, M. Bäumer and A. V. Hamza, *Nature Mater.* **2009**, *8*, 47.
9. J. Weissmüller, R. N. Viswanath, D. Kramer, P. Zimmer, R. Würschum and H. Gleiter, *Science* **2003**, *300*, 312.
10. P. Yang, D. Zhao, D. I. Margolese, B.F. Chmelka and G. D. Stucky, *Nature*, **1998**, *396*, 152.
11. M. E. Davis, *Nature* **2002**, *417*, 813.
12. D. Zhao, J. Feng, Q. Huo, N. Melosh, G. H. Fredrickson, B. F. Chmelka and G. D. Stucky, *Science* **1998**, *279*, 548.
13. A.T. Bell, *Science* **2003**, *299*, 1688.
14. A. Roucoux, J. Schulz and H. Patin, *Chem. Rev.* **2002**, *102*, 3757.
15. V. Zielasek, B. Jürgens, C. Schulz, J. Biener, M. M. Biener, A. V. Hamza and M. Bäumer, *Angew. Chem. Int. Ed.* **2006**, *45*, 8241.

16. C. Xu, J. Su, X. Xu, P. Liu, H. Zhao, F. Tian and Y. Ding, *J. Am. Chem. Soc.* **2007**, *129*, 42.
17. M. D. Hughes *et al.*, *Nature* **2005**, *437*, 1132.
18. D. Walsh, L. Arcelli, T. Ikoma, J. Tanaka and S. Mann, *Nature Mater.* **2003**, *2*, 386.
19. F. Khan, M. Eswaramoorthy and C. N. R. Rao, *Solid State Sciences* **2007**, *9*, 27.
20. J. He, T. Kunitake and T. Watanabe, *Chem. Comm.* **2005**, 795.
21. G. S. Attard, C.G. Göltner, J. M. Corker, S. Henke and R. H. Templar, *Angew. Chem. Int. Ed.* **1997**, *36*, 1315.
22. O. D. Velev, P. M. Tessier, A. M. Lenhoff and E.W. Kaler, *Nature* **1999**, *401*, 548.
23. J. Erlebacher, M. J. Aziz, A. Karma, N. Dimitrov and K. Sieradzki, *Nature* **2001**, *410*, 450.
24. Y. Ding and J. Erlebacher, *J. Am. Chem. Soc.* **2003**, *125*, 7772.
25. G. W. Qin, J. Liu, T. Balaji, X. Xu, H. Matsunaga, Y. Hakuta, L. Zuo and P. Raveendran, *J. Phys. Chem. C.* **2008**, *112*, 10352.
26. G. Ramanath, J. D'Arcy-Gall, T. Maddanimath, A. V. Ellis, P. G. Ganesan, R. Goswami, A. Kumar, K. Vijayamohanan, *Langmuir* **2004**, *20*, 5583.
27. B. Vishwanath, S. Patra, N. Munichandraiah, N. Ravishankar, *Langmuir* **2009**, *25*, 3115.

28. Y. Song, R. M. Garcia, R. M. Dorin, H. Wang, Y. Qiu, E. N. Coker, W. A. Steen, J. E. Miller and J. A. Shelnutt, *Nano Lett.* **2007**, 7, 3650.
29. N. C. Bigall, A-K. Herrmann, M. Vogel, M. Rose, P. Simon, W. Carrillo-Cabrera, D. Dorfs, S. Kaskel, N. Gaponik and A. Eychmüller, *Angew. Chem. Int. Ed.* **2009**, 48, 9731.
30. R. Klajn, K. J. M. Bishop, M. Fialkowski, M. Paszewski, C. J. Campbell, T. P. Gray and B. A. Grzybowski, *Science* **2007**, 316, 261.
31. M. Sheik Bahae, A. A. Said, T. M. Wei, D. J. Hagan and E.W. Vanstryland, *IEEE J. Quantum Electron.* **1990**, 26, 760.
32. R. L. Sutherland, In *Hand Book of Nonlinear Optics*, Second Ed, Marcel Dekker, New York, **2003**, 591.
33. A. Tao, F. Kim, C. Hess, J. Goldberger, R. He, Y. Sun, Y. Xia and P. Yang, *Nano lett.* **2003**, 3, 1229.
34. C. J. Orendorff, L. Gearheart, N. R. Jana and C. J. Murphy, *Phys. Chem. Chem. Phys.* **2006**, 8, 165.
35. S. Eutis and M. A. El-Sayed, *Chem. Soc. Rev.* **2006**, 35, 209.
36. L. W. Tutt and A. Kost, *Nature* **1992**, 356, 225.
37. J. W. Perry, *et al.*, *Science* **1996**, 273, 1533.
38. L. W. Tutt and T. F. Boggess, *Prog. Quant. Electr.* **1993**, 17, 299.
39. V. Dentan, P. Feneyrou, F. Soyer, M. Vergnolle, P. Le Barny and Ph. Robin, *Mat. Res. Soc. Symp. Proc.* **1997**, 479, 261.
40. J. Wang, Y. Hernandez, M. Lotya, J. N. Coleman and W. J. Blau, *Adv. Mater.* **2009**, 21, 2430.

41. X. Sun, R. Q. Yu, G. Q. Xu, T. S. A. Hor and W. Ji, *Appl. Phys. Lett.* **1998**, 73, 3632.
42. T. N. Narayanan, C. S. S. Sandeep, M. M. Shaijumon, P. M. Ajayan, R. Philip and M. R. Anantharaman, *Nanotechnology* **2009**, 20, 285702.
43. R. Philip, G. Ravindrakumar, N. Sandhyarani and T. Pradeep, *Phys. Rev. B* **2000**, 62, 13160.
44. S. Porel, S. Singh, S. S. Harsha, D. N. Rao and T. P. Radhakrishnan, *Chem. Mater.* **2005**, 17, 9.

Chapter 5

**Drums & Pencils: ZnO as a versatile template
to obtain unusual morphologies of silica, gold
and carbon nanostructures**

Summary

This chapter deals with the synthesis of unusual drum and pencil-like morphologies of silica, gold and carbon by using ZnO structures as the template. ZnO is widely known to form interesting shapes and structures under different synthetic conditions. Also, ZnO being amphoteric in nature is easily dissolvable in mild acids or bases which makes them ideal template for use in materials synthesis. Core-shell microstructures were prepared by coating the ZnO with silica, gold and carbon. Upon acid treatment, the ZnO core was removed to yield inverse replicas of silica, gold and carbon nanostructures.

Paper based on the above study has been published in *Chem. Comm.* **2010**, 46, 2989.

5.1 Introduction

Controlling the morphology of inorganic nanostructures has become the primary focus of researchers because of their novel shape-dependent properties (1-3). Structures at the macroscale demand different shapes and assembly of building units for many practical applications (4, 5). Similarly, structures at the nanoscale also need to be in different forms to fabricate complex functional devices. Template based method is one of the well established techniques to produce inorganic nanomaterials in different forms (6-10). Organic molecules in the form of self-assembled supramolecular structures often been used as soft templates to replicate their morphology in few inorganic structures, a process which parallels in some aspects the biominerals formation in organisms (11-14). On the other hand, hard templates such as carbon, polymer and silica in the form of spheres, rods, wires, tubes are used to make many inorganic nanostructures, but more or less restricted to spherical, tubular and rod-shaped morphologies (15-17). Creation of complex morphologies using these conventional templates would be hard to realize. Furthermore, making templates of complex structure is in itself difficult to achieve. Therefore, a cheap and simple template which can be produced in different forms can be an ideal substitute to obtain nanostructures of different morphologies. ZnO is one such template which can be produced in the form of wires (18), belts (19), cables and tubes (20, 21), combs (22), tetrapods (23), rings and disks (24, 25), springs (26) flowers (27), and bowls (5). Further, ZnO being amphoteric in nature, can be easily dissolved in mild acids or bases and hence removal would be simpler. Though there were few reports on the use of rod and wire shaped ZnO as templates (28-31), the faceted, complex

morphologies of ZnO nano- and microstructures have not been fully exploited to obtain free-standing replicas of inorganic nanostructures of different architectures. In this chapter, we describe the synthesis of ZnO in the form of microdrums and pencil shaped structures and their utilization as templates to create silica, carbon and gold replicas.

5.2 Scope of the present investigation

ZnO is known to form into exciting shapes by using different synthetic approaches. The present investigation is about using the ZnO structures as templates for the synthesis of silica, gold and carbon structures that are difficult to synthesize using conventional methods. For this, microemulsion and hydrothermal methods were used to synthesize drum and pencil shaped ZnO structures. These structures were used as templates to make silica, gold and carbon nanostructures of complex morphologies.

5.3 Experimental section

5.3.1 Synthetic procedure for ZnO drums

For the preparation of ZnO drums, a NaAOT microemulsion was first prepared by adding 0.3718 g of $\text{Zn}(\text{NO}_3)_2 \cdot 6\text{H}_2\text{O}$ (Merck) to 50 ml of water and

stirred for 5 min to dissolve completely. To this a solution containing 0.22 g of NaAOT (Merck) in 5 ml of 1-butanol was added with vigorous stirring. The stirring was continued for 2 h and then 0.280 ml of liquor ammonia ($\text{NH}_3 \cdot \text{H}_2\text{O}$) was added drop-wise to the well-stirred microemulsion. After addition, stirring was further continued for 3 h at room temperature. The resulting milky white mixture was subsequently kept at 70 °C for 12 h. A white suspension obtained was suction-filtered to separate the precipitate, which was later washed several times with distilled water and absolute ethanol. Finally, a white powder was obtained by drying the solid product in an oven at 60 °C overnight.

5.3.2 Synthetic procedure for ZnO pencils

Hexagonally faceted pencil shaped ZnO rods were synthesized using a reported procedure (26). In a typical synthesis, 5.0 g of NaOH (Merck) and 2.75 g of zinc acetate (Merck), each in 25 ml of water was prepared separately, mixed in a teflon-lined stainless steel autoclave of 65 ml capacity. The autoclave was sealed and heated to 120 °C in an oven for 6 h. It was then allowed to cool naturally to room temperature. The solid product was separated from the solution by filtration, washed with distilled water several times and dried in an air-oven maintained at 50 °C.

5.3.3 Silica-coating of ZnO structures

The zinc oxide-silica core shell structure was obtained by sol-gel method using tetraethylorthosilicate (TEOS) (Aldrich) as the silica precursor (28). In a typical procedure, 30 mg of zinc oxide microdrums/pencils were dispersed in 3.0 ml 2-propanol. Under continuous mechanical stirring, 0.4 ml of deionized water, 0.1 ml of ammonia solution (28 % w/w) and 20 μ l of TEOS (for ~ 10 nm thick silica coating) were consecutively added to the dispersed solution. The amount of TEOS can be varied to vary the coating thickness. The reaction mixture was kept for 3 h without stirring. A white solid product settled at the bottom was obtained after the reaction. The solution was then filtered and washed several times with deionized water and anhydrous ethanol respectively.

Hollow silica nanostructures were obtained by removing the ZnO core by etching in dilute HCl solution. For this, the core-shell structures were added to the 1 M HCl solution. After 3 h of soaking in acid solution, the resultant product was filtered and washed several times with deionized water and anhydrous ethanol respectively.

5.3.4. Gold-coating of ZnO structures

To obtain gold nanostructures, 30 mg of ZnO template was placed over a thin glass wafer and was sputter coated with gold for 2 min using sputter coating machine. The process was carried out in high vacuum and at an optimal applied

voltage. The gold coated ZnO on glass wafer was then soaked in a beaker containing 3 ml of 1 M HCl for 3 h to dissolve the ZnO. The resultant product (gold nanostructures) was then washed with deionized water and ethanol and dried at room temperature.

5.3.5 Carbon-coating of ZnO structures

Carbon coating on ZnO template was done with arc discharge process. By generating an arc between two graphite rod tips at high voltages, carbon vapour was generated inside a vacuum chamber. The vapour was allowed to settle on the ZnO nanostructures (powder) placed on a glass substrate in the vacuum chamber. The process completes within ~ 30 sec resulting in 10 – 20 nm carbon coating over the ZnO structures. The carbon-coated ZnO was then acid treated to remove the ZnO core.

5.3.6 SiO₂@Fe₂O₃ hollow tubes

0.55 g of FeCl₃.6H₂O (S.D. fine-chemicals, India) and 0.77 g of citric acid (S.D. fine-chemicals, India) were dissolved in a solvent mixture containing 0.75 ml of water and 5.25 ml of ethanol (water–ethanol v/v = 1:7). To this solution, 1 ml of polyethylene glycol (PEG) (molecular weight = 600, S.D. fine-chemicals, India) was added as cross-linking agent. The mixture was stirred for 1 h to form a clear solution and then the 65 mg of ZnO@SiO₂ nanorods sample was added under stirring. The

suspension was further stirred for another 3 h, and then the product was separated by filtration. The samples were dried at 100 °C for 1 h immediately afterwards. The dried samples were annealed at 500 °C for 2 h in a furnace with a heating rate of 1 °C/min. Then the preheated samples were annealed to 600 °C with a heating rate of 1 °C/min. The presence of citric acid in the medium dissolves the ZnO leading to the formation of SiO₂@Fe₂O₃ hollow tubes.

5.3.7 Sample characterization

The morphologies of all the samples were analyzed with a field-emission scanning electron microscope (FE-SEM, FEI Nova-Nano SEM-600, The Netherlands). Transmission electron microscopy (TEM) was carried out at 300 kV with a JEOL JEM-3010. Powder X-ray diffraction (XRD) patterns were obtained by using a Rich-Siefert 3000-TT diffractometer employing CuK α radiation.

5.4 Results and discussion

Figure 1 shows the FESEM image of ZnO microdrums obtained by aging the zinc nitrate with sodium salt of Aerosol OT, NaAOT (sodium bis-(2-ethylhexyl)-sulfosuccinate) mixture for 12 h at 70 °C. It is to be noted here that even though we followed a similar procedure reported by Wang and co-workers (24), we often ended up with faceted ZnO microdrums rather than hexagonal nanodiscs probably, due to the variation in the aging method. These microdrums are made up of hexagonally

faceted twinned-crystals having flat surfaces on both the ends (Inset of Figure 1). The crystals are twinned on (0001) plane. The possibility of having a sphalerite ZnO layer at the twinned plane cannot be ruled out though it was not observed in the diffraction pattern. The diameter and the height of the drums are around 900 nm and 600 nm respectively. Occasionally very small drums of ~ 200 nm size were obtained along with the bigger ones.

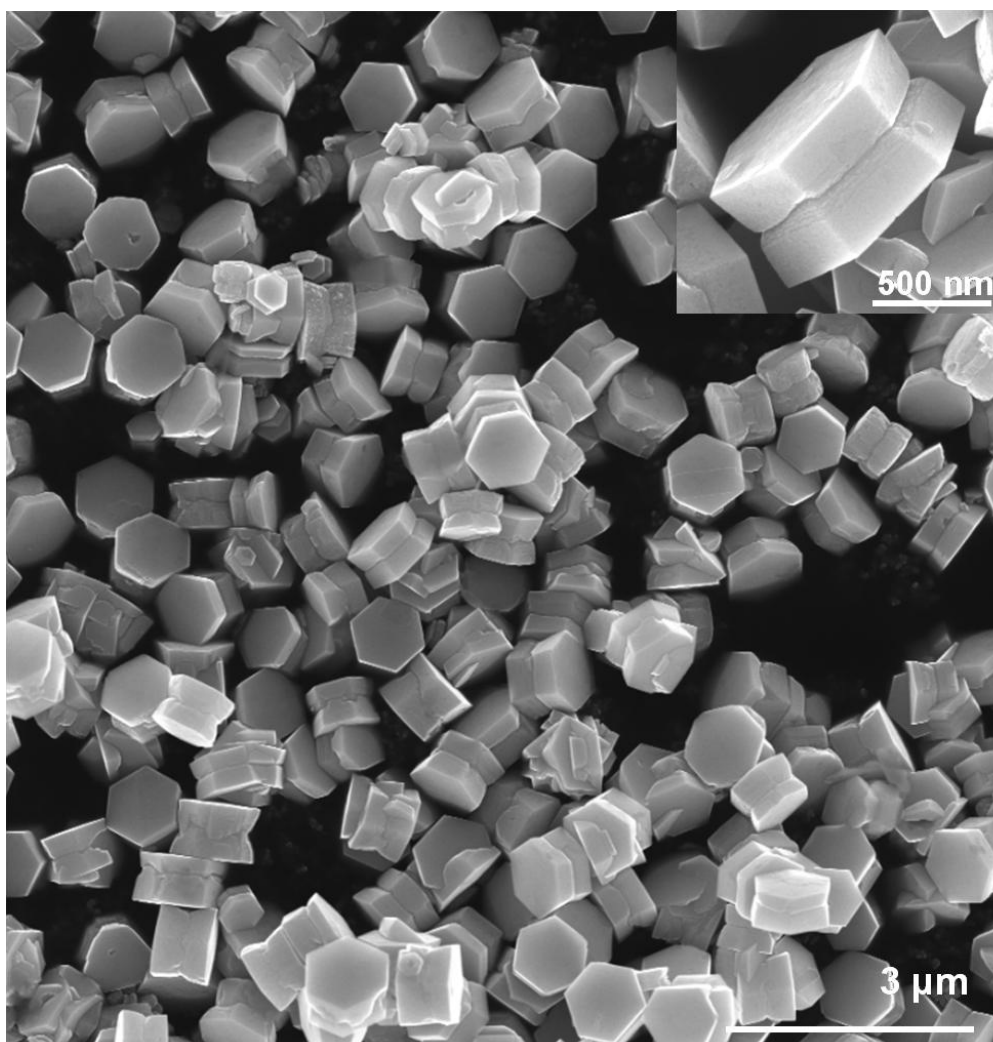


Figure 1: Low-magnification FESEM image of faceted ZnO microdrums. Inset shows a single magnified drum.

TEM images of the faceted ZnO drums are shown in Figure 2a and 2b. Electron diffraction (ED) pattern shows the single-crystalline nature on each side of the drum. Increasing the aging time to 5 days still results in similar morphology but with larger particles sizes of ~ 2.5 microns (Figure 3). Aging the sample under hydrothermal conditions for 1, 2 and 4 days however, resulted in ZnO microstructures with dog-bone and cauliflower-like morphologies (Figure 4).

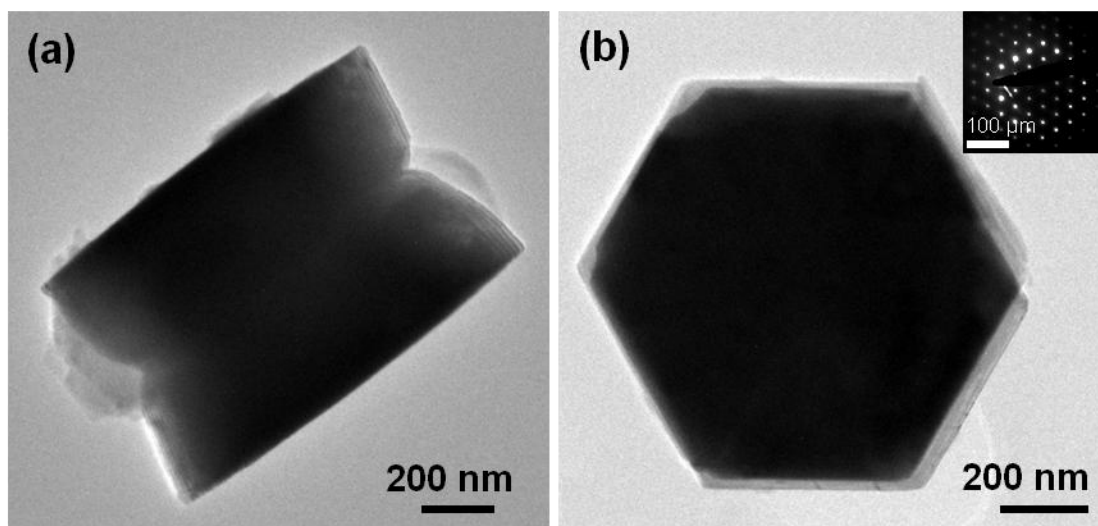


Figure 2: (a) & (b) TEM images of the faceted ZnO microdrums. Inset in (b) shows the ED pattern.

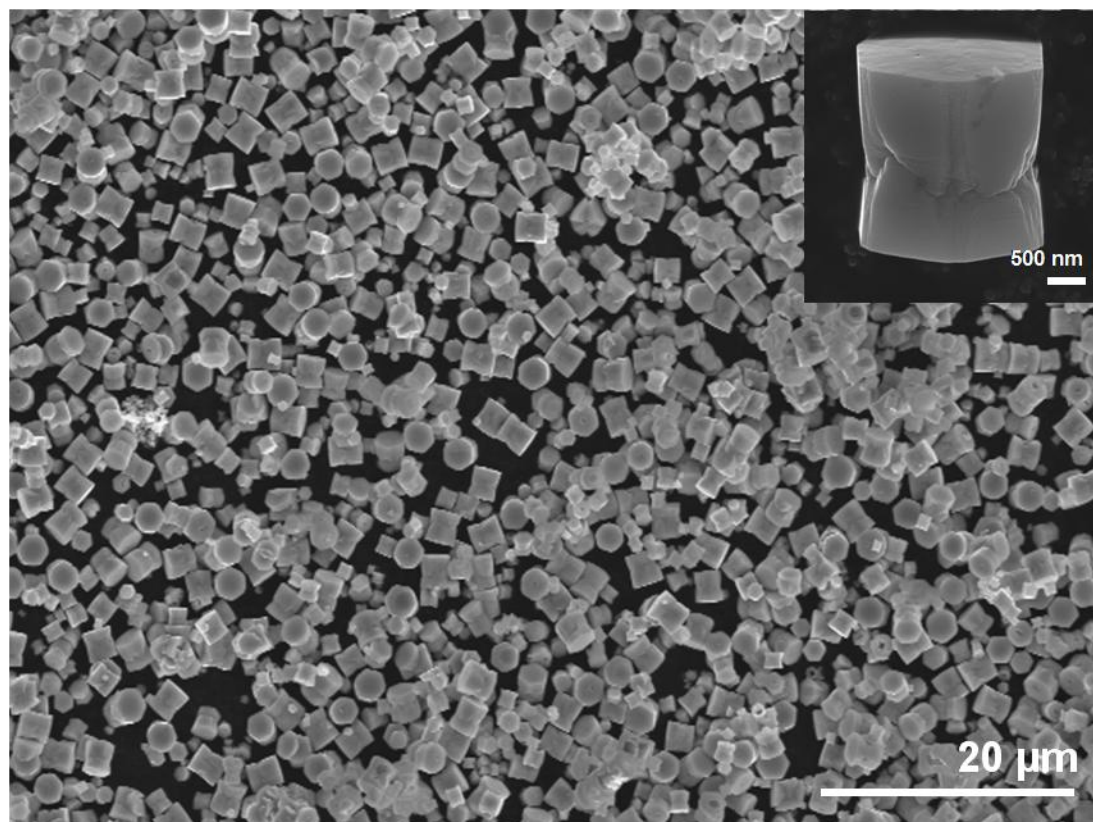


Figure 3: Low-magnification FESEM image of ZnO microdrums formed at 5 days of reaction time. Inset shows a single magnified drum.

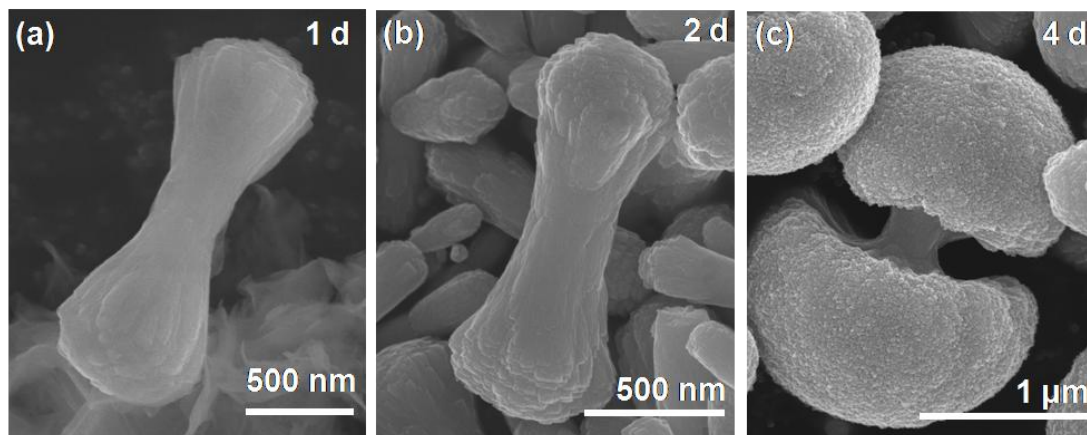


Figure 4: FESEM images of the morphologies of ZnO obtained by hydrothermal treatment for (a) 1 day (b) 2 days and (c) 4 days respectively.

These microdrums were used as hard templates to make silica, gold and carbon nanostructures. To obtain silica nanostructures having inverse replica of the microdrum morphology, ZnO microdrums were first coated with silica using a sol-gel technique reported by Chen *et al* (31). Hexagonally faceted, hollow drums of silica were obtained after the removal of ZnO core by acid treatment. The ZnO template and the silica replicas could be well dispersed as free standing structures in the medium, 2-propanol. By optimizing the conditions, the formation of aggregated silica structures can be avoided during the templating process. Figure 5a shows an FESEM image of the hollow SiO₂ drums obtained in good yield by templating the ZnO microdrums. Figure 5b shows a single drum structure having a light contrast outermost layer of thickness around few tens of nanometer associated with silica coating. EDAX profile confirms the presence of silica (Figure 5c).

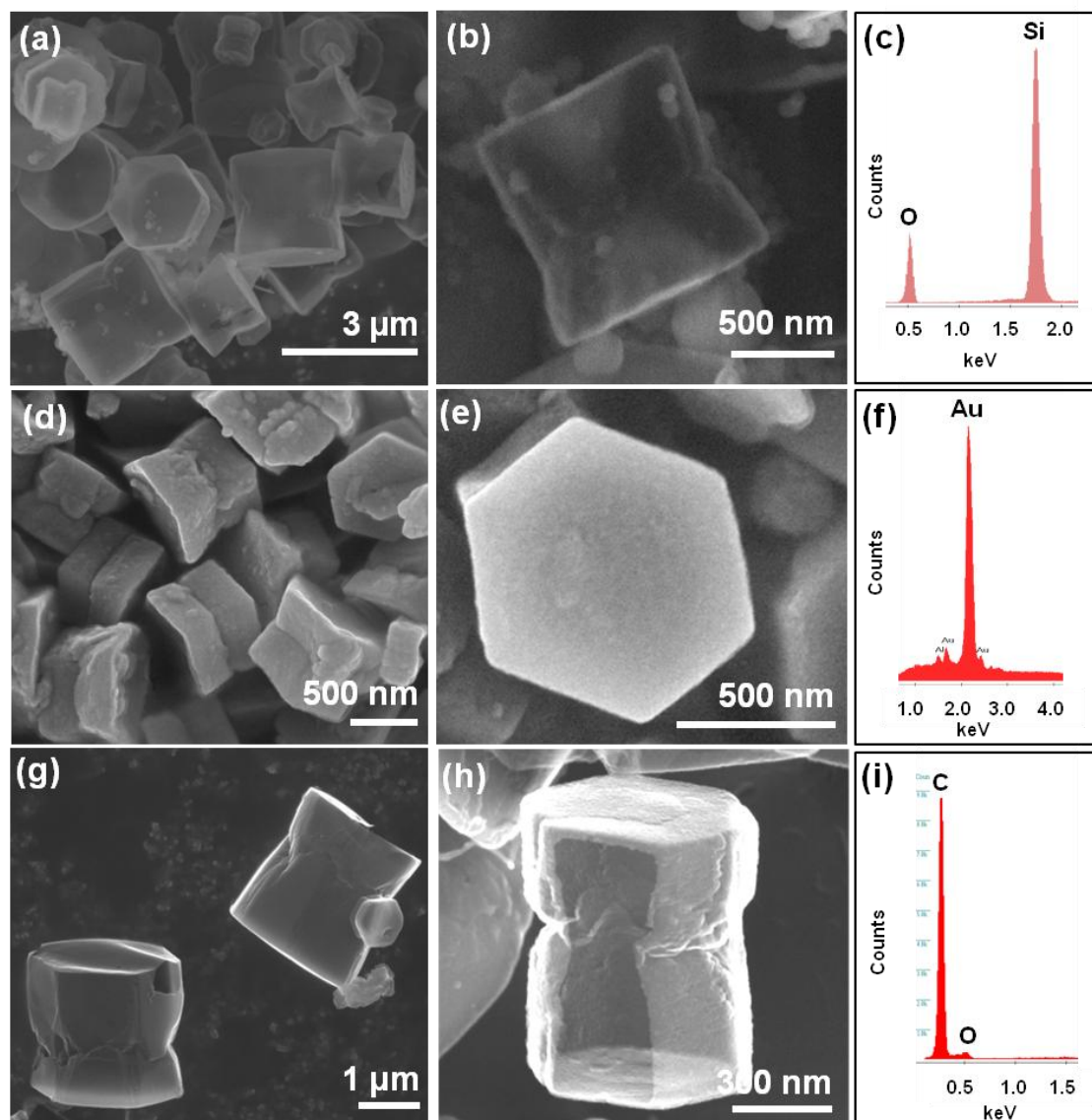


Figure 5: FESEM images of faceted nanostructures obtained from templating ZnO drums. (a) Silica drums (b) Single silica drum (d) Gold drums (e) Single gold drum (g) Carbon drums (h) Fractured carbon drum showing the hollow interior (c), (f), (i) EDAX profiles of the corresponding drums.

Similarly, hollow, gold microdrums having wall thickness of few tens of nanometers were made by sputter coating the gold over ZnO microstructures

followed by etching the template in acid (Figure 5d and 5e). The gold was coated uniformly on all the sides with the wall thickness around 60 ± 15 nm which can be controlled by varying the sputtering time. If the sputtering time is below two minutes, the ZnO drums were not properly coated with Au, resulting in open ended structures upon etching. Close observation of these drums under FESEM shows that the walls are non-porous, slightly buckled inwards at both the ends and are made up of gold nanoparticles of size 15 to 20 nm. Arc discharge process was used to get core-shell ZnO/carbon microstructures, which on treatment with acid leaves carbon microdrums. Figure 5g shows the FESEM image of the hollow faceted carbon drums formed through this process. These drums are very fragile, unlike gold drums and are broken at several places. Figure 5h shows a single fractured carbon drum showing the hollow interior. The hollow microdrums with large inner volume coupled with optical, electronic and pore properties of their nanostructured wall would be expected to find application in biomedical field.

In a similar approach to obtain pencil-shaped nanostructures, ZnO template with hexagonally-faceted nanorods were first synthesized from a hydrothermal procedure reported by Zhang *et al* (26) (see experimental section). A low magnification FESEM image shows dandelion-like ZnO structures assembled from faceted nanorods (Figure 6a). Higher magnification FESEM image (Figure 6b) of these dandelions shows the faceted, pencil-shape of ZnO nanorods.

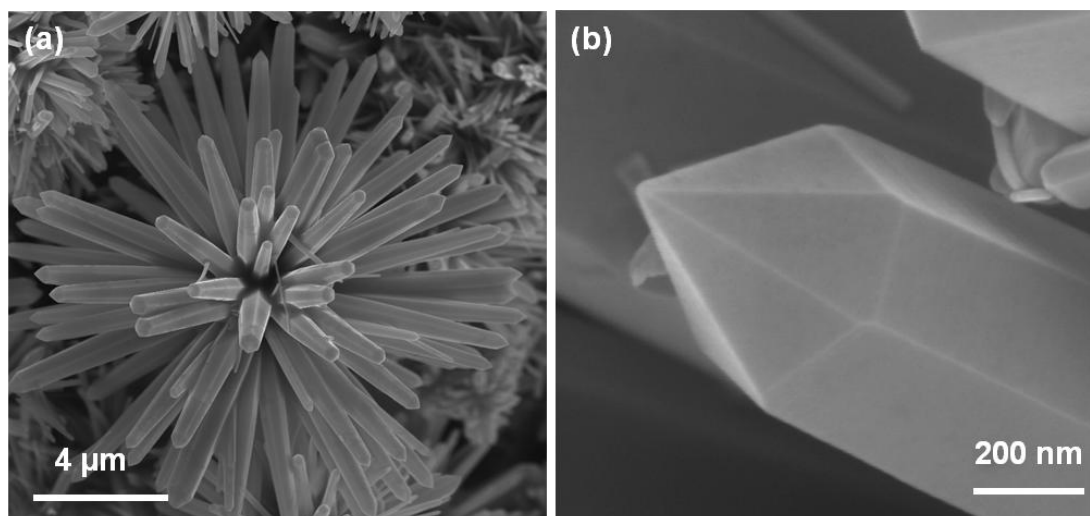


Figure 6: (a) FESEM image of the dandelion-like ZnO structures (b) FESEM image of a single faceted ZnO nanorod resembling pencil shape.

The powder X-ray diffraction (PXRD) pattern obtained for the ZnO nanorods can be indexed to the ZnO wurtzite phase (Figure 7a). TEM image of a single ZnO nanorod in Figure 7b shows that they are solid and dense structures with a sharp tapering tip. The single crystalline nature of these nanorods is evident from the ED pattern (Figure 7c). Silica is coated on to these ZnO nanorods through a sol-gel method to obtain ZnO/SiO₂ core-shell nanorods. TEM image of an individual silica coated ZnO core-shell nanorod shows ~ 10 nm thick silica coating (Figure 8a). Faceted silica nanotubes are obtained after the removal of the ZnO core by acid treatment. Figure 8b shows the scanning transmission electron microscopy (STEM) image of the hollow, faceted silica nanotubes with pencil shape having one end left opened. This open end can be utilized to fill the desired protein or drug molecules for the delivery purpose. For example, the silica nanotubes soaked with ferritin protein showed the presence of protein within the nanotubes (Figure 9).

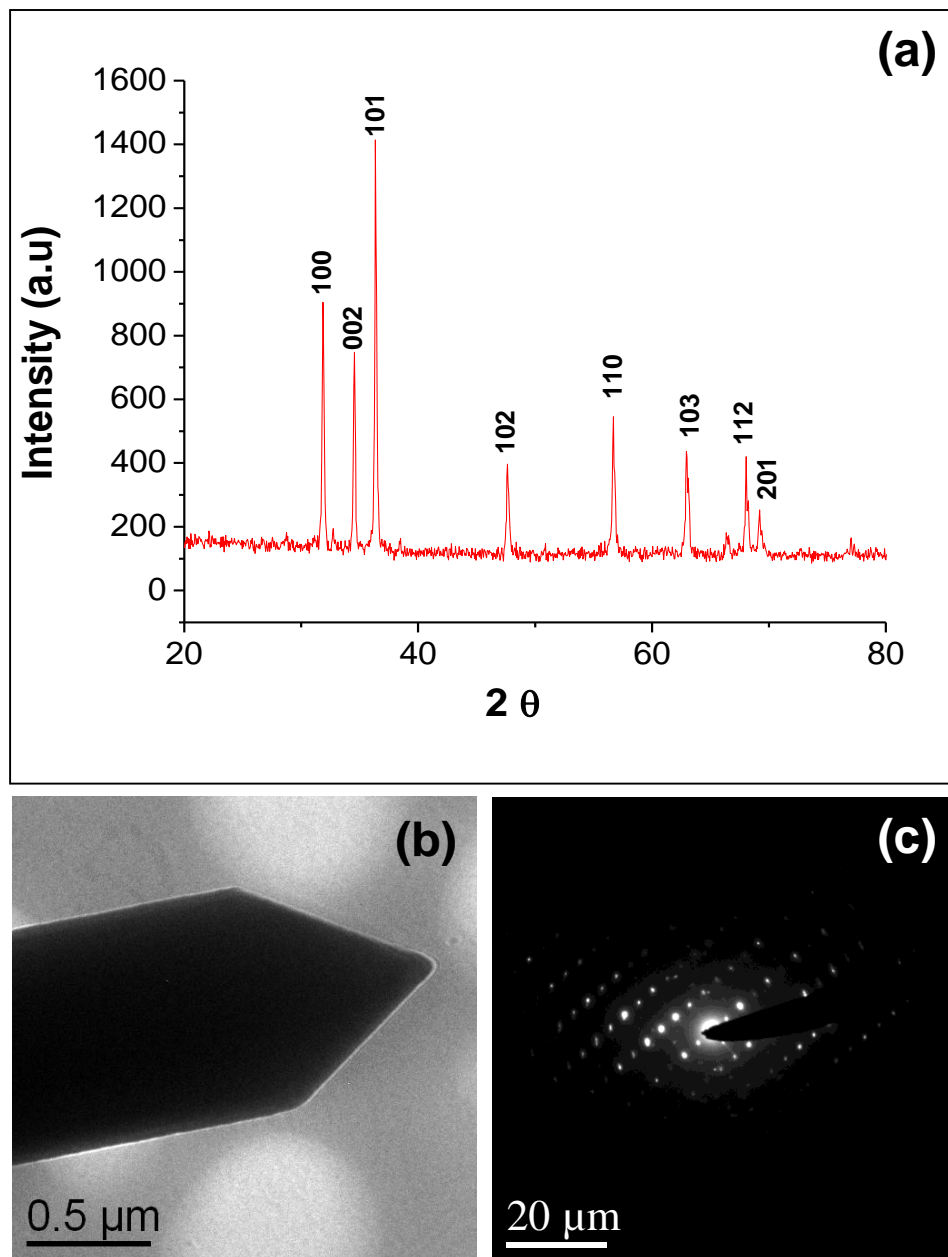


Figure 7: (a) Powder X-ray diffraction (PXRD) pattern obtained for the ZnO nanorods (b) TEM image of a single ZnO nanorod (c) electron diffraction (ED) pattern of the ZnO nanorods.

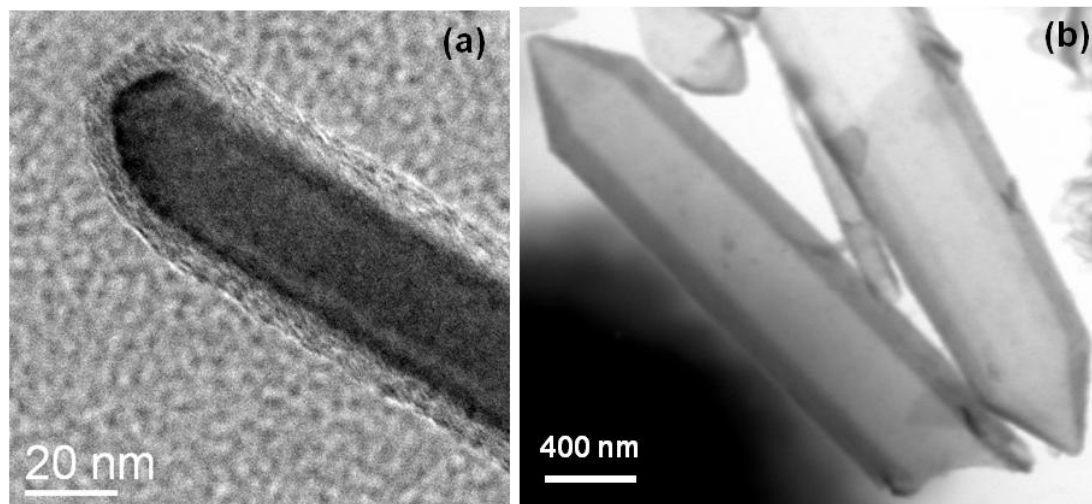


Figure 8: (a) TEM image of a ZnO nanorod with ~ 10 nm thick silica coating (b) Faceted silica nanotubes obtained after removing the ZnO nanorods.

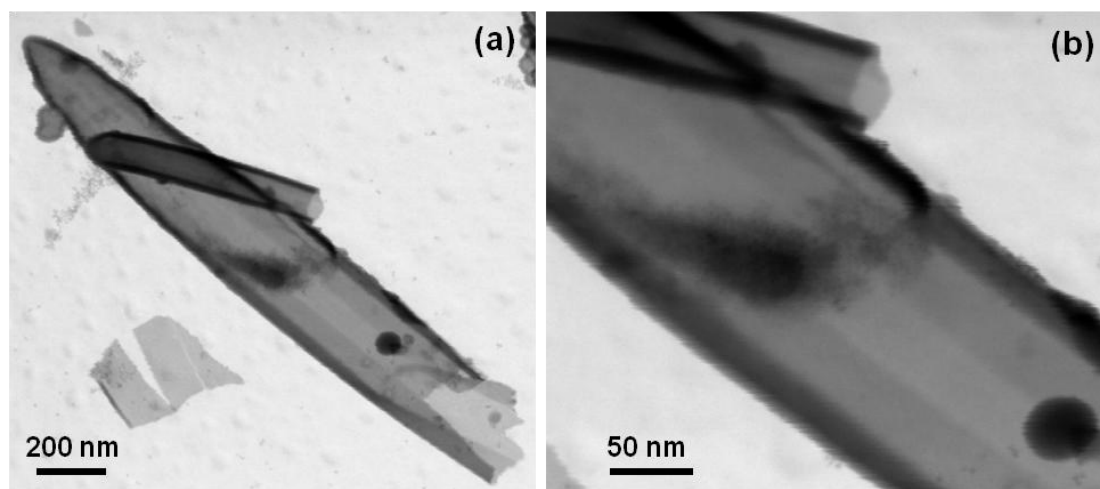


Figure 9: (a) STEM image of a ferritin protein encapsulated silica nanotube that is open at one end and closed at the other. (b) Higher magnification image of the protein encapsulated region.

Gold and carbon nanotubes with faceted pencil shaped morphology were also obtained by similar coating procedures adopted for the microdrums. FESEM images

of the as obtained faceted gold and carbon nanopencils with hexagonal facets are shown in Figure 10. Etching of the nanotips in principle, could lead to faceted nanopipettes, just like carbon nanopipette (32). Further, the synthesis of core-shell nanostructures, like $\text{SiO}_2@\text{Fe}_2\text{O}_3$ hollow tubes was also possible by coating Fe_2O_3 over silica hollow tubes obtained by templating ZnO nanorods (Figure 11).

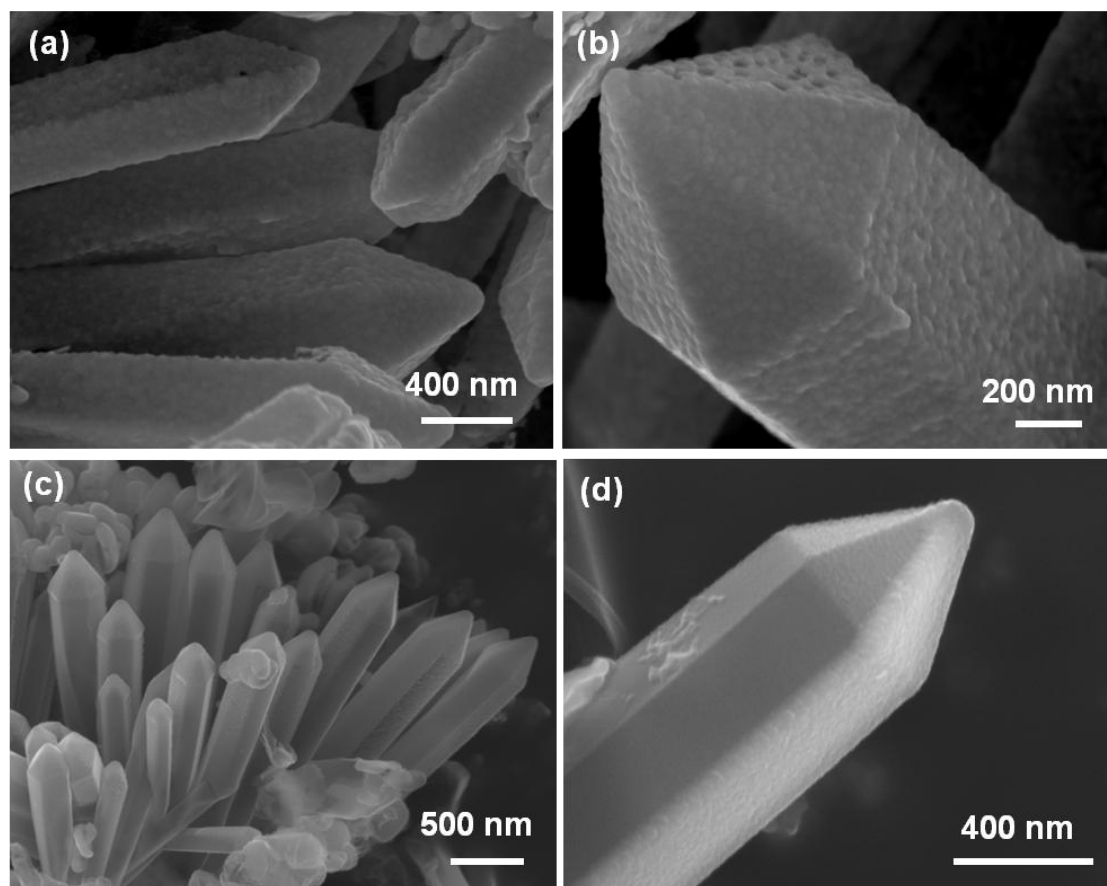


Figure 10: FESEM images of (a) gold nanotubes obtained after removing the ZnO nanorods (b) single faceted gold nanotube (c) carbon nanotubes obtained after removing of ZnO nanorods and (d) single faceted carbon nanotube.

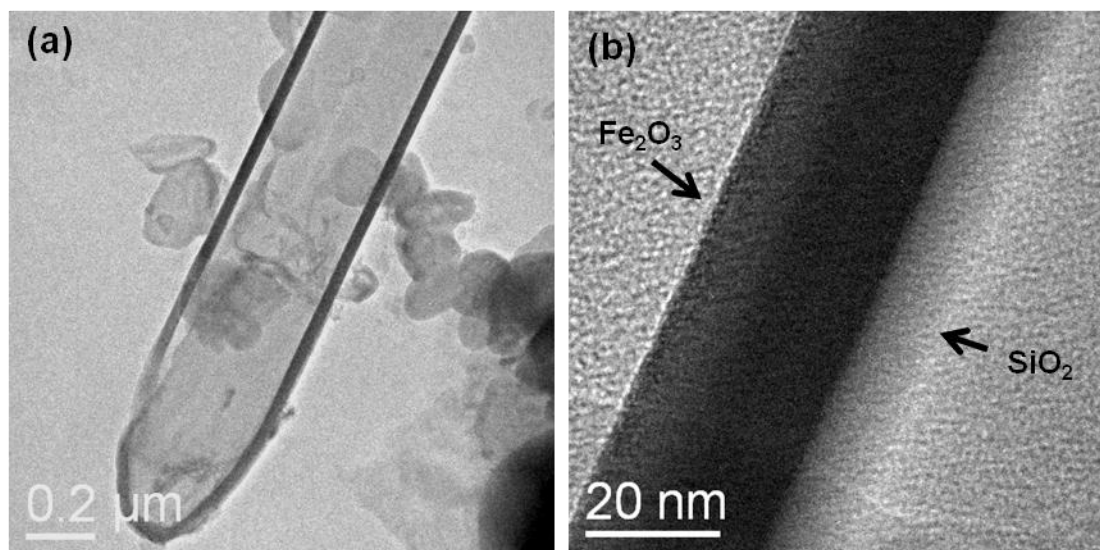


Figure 11: (a) TEM image of Fe₂O₃ coated silica nanotubes (b) Higher magnification image showing Fe₂O₃ coating thickness of ~ 30 nm.

5.5 Conclusions

In conclusion, this chapter describes a simple procedure to synthesize drum and pencil-shaped nanostructures of silica, gold and carbon using ZnO structures as template. These faceted morphologies are difficult to produce by conventional synthetic routes. This template method, in principle, can also be used to obtain different morphologies of other metal and metal oxide nanostructures.

5.6 References

1. C. Burda, X. Chen, R. Narayanan, and M. A. El-Sayed, *Chem. Rev.* **2005**, *105*, 1025.
2. S. Mann and G. A. Ozin, *Nature* **1996**, *382*, 313.
3. Z. L. Wang, *J. Phys. Condens. Matter* **2004**, *16*, R829.
4. G. M. Whitesides and B. Grzybowski, *Science* **2002**, *295*, 2418.
5. K. S. Krishna, U. Mansoori, N. R. Selvi, and M. Eswaramoorthy, *Angew. Chem. Int. Ed.* **2007**, *46*, 5962.
6. C. R. Martin, *Science* **1994**, *266*, 1961.
7. X. Sun, J. Liu, and Yadong Li, *Chem. Eur. J.* **2006**, *12*, 2039.
8. C. Bae, H. Yoo, S. Kim, K. Lee, J. Kim, M. M. Sung, and H. Shin, *Chem. Mater.* **2008**, *20*, 756.
9. K. S. Krishna and M. Eswaramoorthy, *Chem. Phys. Lett.* **2007**, *433*, 327.
10. Y. Sun, B. T. Mayers, and Y. Xia, *Nano Lett.* **2002**, *2*, 481.
11. M. Eswaramoorthy, D. Walsh, and S. Mann, *Adv. Mater.* **2002**, *14*, 969.
12. A. Patil, M. Eswaramoorthy, A. M. Seddon, and S. Mann, *Adv. Mater.* **2003**, *15*, 1816.
13. S. Mann, *Nature Mater.* **2009**, *8*, 781.
14. S. Che, Z. Liu, T. Ohsuna, K. Sakamoto, O. Terasaki, and T. Tatsumi, *Nature* **2004**, *429*, 281.
15. J. Dinesh, M. Eswaramoorthy, and C. N. R. Rao, *J. Phys. Chem. C.* **2007**, *111*, 510.
16. F. Caruso, R.A. Caruso, and H. Mohwald, *Science* **1998**, *282*, 1111.

17. Y. Xia, B. Gates, Y. Yin, and Y. Lu, *Adv. Mater.* **2000**, *12*, 693.
18. M. H. Huang, S. Mao, H. Feick, H. Yan, Y. Wu, H. Kind, E. Weber, R. Russo and P. Yang, *Science*, **2001**, *292*, 1897.
19. Z. W. Pan, Z. R. Dai, and Z. L. Wang, *Science* **2001**, *291*, 1947.
20. S. Kim, M-C. Jeong, B-Y. Oh, W. Lee and J-M. Myoung, *J. Cryst. Growth* **2006**, *290*, 485.
21. Y. J. Xing, Z. H. Xi, Z. Q. Xue, X. D. Zhang, J. H. Song, R. M. Wang, J. Xu, Y. Song, S. L. Zhang, and D. P. Yu, *Appl. Phys. Lett.* **2003**, *83*, 1689.
22. Y. Huang, Y. Zhang, J. He, Y. Dai, Y. Gu, Z. Ji and C. Zhou, *Ceramics Int.* **2006**, *32*, 561.
23. M. C. Newton and P. A. Warburton, *Mater. Today.* **2007**, *10*, 50.
24. F. Li, Y. Ding, P. Gao, X. Xin, and Z. L. Wang, *Angew. Chem.* **2004**, *116*, 5350.
25. Z. R. Tian, J. A. Voigt, J. Liu, B. McKenzie, M. J. McDermott, M. A. Rodriguez, H. Konishi, and H. Xu, *Nat. Mater.* **2003**, *2*, 821.
26. P. X. Gao and Z. L. Wang, *Small* **2005**, *1*, 945.
27. Y. Zhang and J. Mu, *Nanotechnology* **2007**, *18*, 075606.
28. J. Qiu, W. Yu, X. Gao, and X. Li, *J. Sol-Gel Sci. Technol.* **2007**, *44*, 235.
29. J. Qiu, W. Yu, X. Gao, and X. Li, *Nanotechnology* **2006**, *17*, 4695.
30. Z. Li, X. Qian, J. Yin, and Z. Zhu, *J. Solid State Chem.* **2005**, *178*, 1765.
31. Y. Chen, X. Xue, and T. Wang, *Nanotechnology* **2005**, *16*, 1978.
32. M. G. Schrlau, E. M. Falls, B.L. Ziober, and H. H Bau, *Nanotechnology* **2008**, *19*, 015101.

Chapter 6

Pillar arrays: Synthesis, Characterization and

Applications of Amorphous Carbon Nitride

Nanopillar Arrays

Summary

This chapter deals with the formation of nanopillar arrays of amorphous carbon nitride using anodic aluminium oxide (AAO) membrane as template. The process involves polymerization and carbonization of the precursors, ethylenediamine and carbon tetrachloride in very low volume within the channels of the AAO membrane template in a sealed environment. The as-formed nanopillars have $C_{13}N$ composition and have functional amine groups on their surface. The amine groups were exploited for functionalization with oleic acid in order to stabilize the nanostructure at the aqueous-organic interface and also for the immobilization of metal nanoparticles and protein.

6.1 Introduction

Carbon nitrides of the general formula CN_x are fascinating class of materials owing to the ability to tune their electronic, optical, catalytic and mechanical properties based on the structure and the composition of carbon and nitrogen (1-3). For example, amorphous carbon nitride, due to its negative electron affinity was considered as a promising candidate for the field-emitters (4-6). β - C_3N_4 , an isostructure of Si_3N_4 was predicted to have super hardness, high oxidation resistance and chemical inertness (7). Graphitic C_3N_4 was credited for its potential application as organic semiconductors and precursors for super hard material (8). Mesoporous graphitic carbon nitride of composition g - C_3N_4 was shown to have interesting catalytic properties associated with the presence of nitrogen (9, 10). Various methods were used to make the carbon nitrides in the form of nanotubes, nanorods having different C/N ratios as these materials are expected to have interesting optical, electronic and mechanical properties associated with their one dimensional structures in addition to the intrinsic properties bestowed by their composition and structure (11-13). Among various approaches, template based method using anodic aluminum oxide (AAO) membrane is the widely used one to get aligned nanostructures (14). However, the sagging and random array of these one dimensional rod or tube like structures upon removal of the template limits their use in fabricating nanopillar arrays which are emerging as an interesting new class of materials for applications in electron emission (15), optics (16), biosensing (17), biomimetics (18), photovoltaics (19) etc. Nevertheless, there are few reports on the synthesis of nanopillar arrays

using AAO as template (20, 21). This chapter discusses about a modified approach to obtain amorphous carbon nitride nanopillars from AAO membrane template method.

6.2 Scope of present investigation

Nanopillar morphology has several interesting applications as discussed in the previous section. The present investigation is focused on the synthesis of nanopillar arrays of carbon nitrides by carbonizing its precursors, ethylenediamine and carbon tetrachloride within the channels of the AAO membrane template. The use of surface amine groups present on the carbon nitride pillars for different applications is also investigated in this study.

6.3 Experimental section

6.3.1 Synthetic procedure for nanopillar arrays

In a typical synthesis, 0.39 ml (5.84 mmol) of ethylenediamine (Merck) and 0.55 ml (5.57 mmol) of carbon tetrachloride (Merck) are taken in a 20 ml teflon-lined steel autoclave. A porous anodic alumina membrane (13 mm diameter, 60 μm thick with a uniform pore size of 200 nm, Whatman® Anodisc 13) was placed on the solution and the mixture was kept in the oven at 150 °C for 12 hrs. The black colored membrane thus obtained was carefully removed from the teflon container and

carbonized at 600 °C in a tube furnace with continuous N₂ flow, at a heating ramp of 3°C/min and maintained at 600 °C for 5 h. The as-prepared membrane is then treated with 2M NaOH solution for 1 h to dissolve the alumina template and washed with water several times and dried.

6.3.2 Sample characterization

The as-prepared and modified carbon nitride samples were characterized using field-emission scanning electron microscope (FESEM, FEI Nova-Nano SEM-600, The Netherlands), scanning electron microscope (LeicaS-440-I Instrument, U.K), transmission electron microscope (JEOL-JEM 3100 Instrument, Japan) and powder X-ray diffractometer (Bruker D8 discover diffractometer employing CuK α radiation). Raman spectrum was recorded with LabRAM HR Raman spectrometer at an excitation wavelength of 632 nm (HeNe laser source). X-ray photo electron spectrometer (XPS) was used to measure the elemental composition. Fourier-transform infrared (FT-IR) spectrum was recorded using Bruker, IFS 66 V/s.

6.4 Results and discussion

Amorphous carbon nitride nanopillars (CNPs) were obtained by polymerization of ethylenediamine and carbon tetrachloride within the channels of anodic aluminium oxide (AAO) membrane at 150 °C for 12 h. Figure 1 shows the

low magnification FESEM image of CNPs supported on a 5 μm thick slab of amorphous carbon nitride. The lengths of the nanopillars are in the range of 40 to 60 μm , equivalent to the thickness of the AAO membrane, confirming their formation within the membrane.

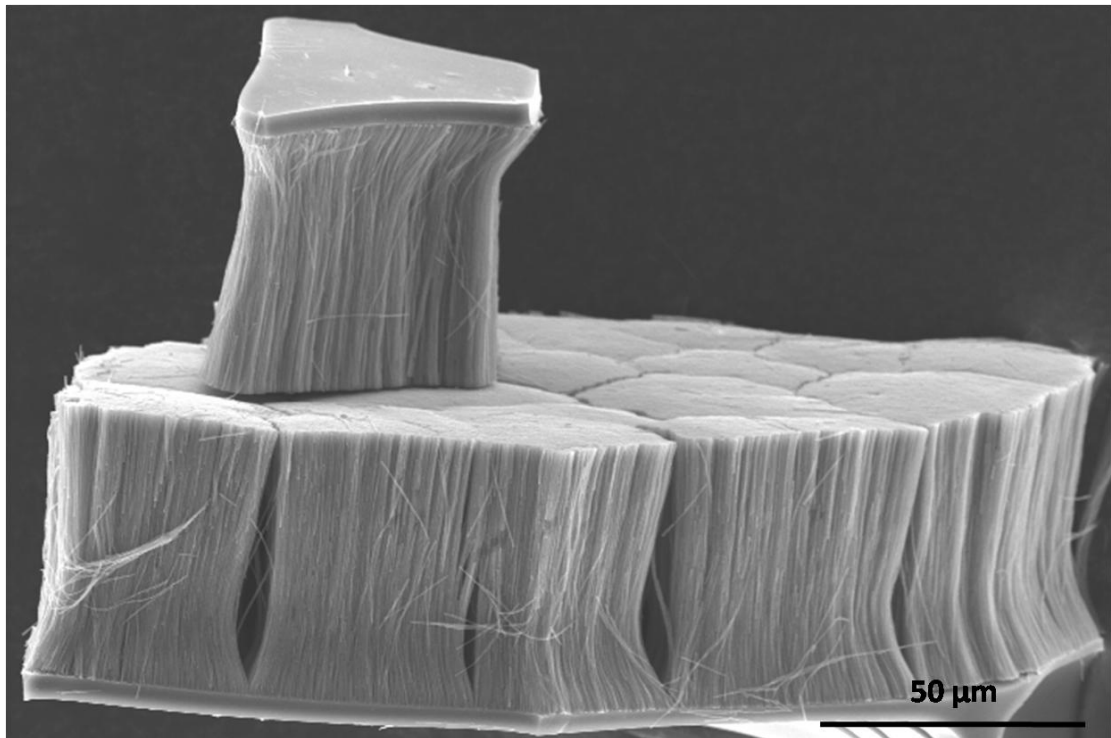


Figure 1: *Low-magnification FESEM image of nanopillar arrays of amorphous carbon nitride.*

Figure 2 shows a magnified portion of the CNPs, which is analogous to a natural brush having hair-like bristles (Inset shows the magnified portion of the marked region). The nanorods are of uniform size and are not interconnected with each other. These nanorods have diameters ranging from 250 to 300 nm, which is usually depended upon the pore size of the AAO membrane template.

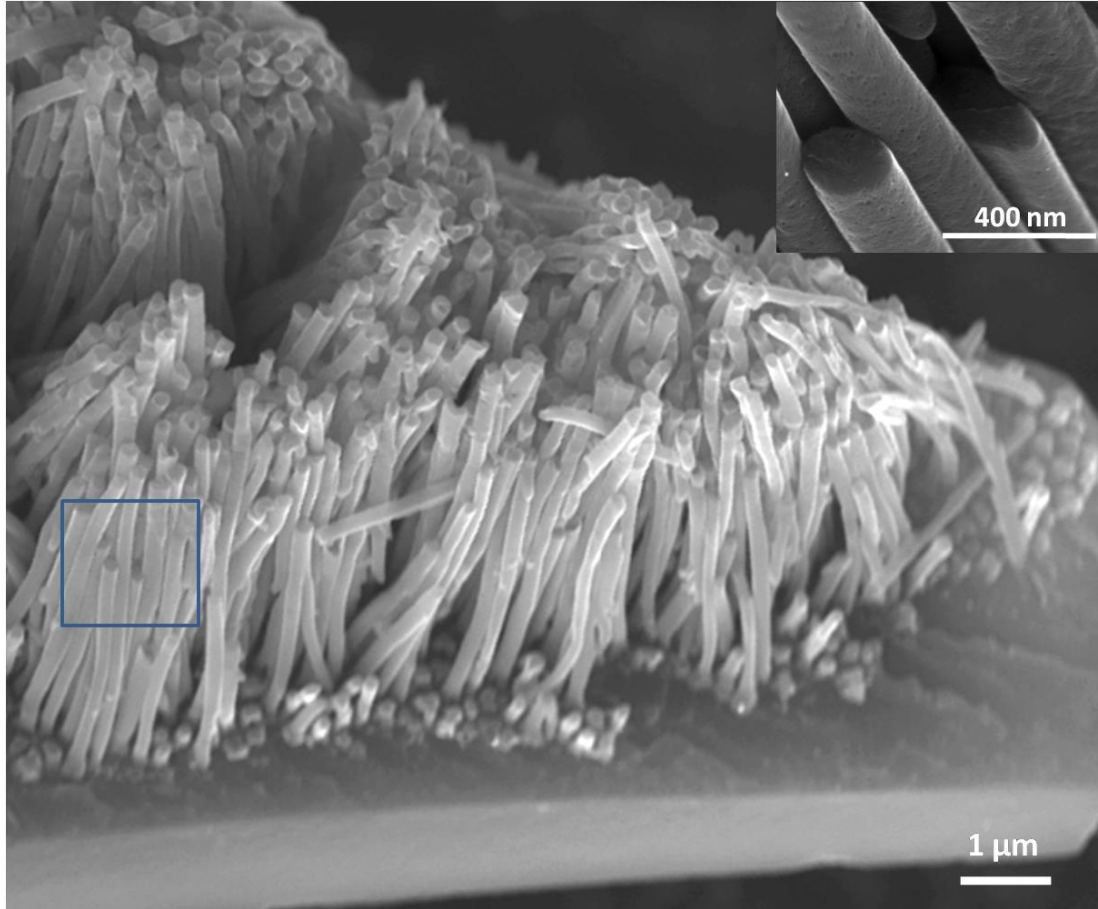


Figure 2: Higher magnification FESEM image of CNPs supported on a slab. Inset shows the closer view of the nanorods (of marked portion).

Figure 3a shows SEM image of the top-view of nanopillar array, which appears more like nanotubes rather than nanorod array. However, the TEM image (Inset of figure 3) shows a single nanorod with concave tip at its end. Such appearance originate from the formation of lower meniscus by the precursor mixture, ethylenediamine and carbon tetrachloride within the AAO pores during the capillary pore-filling (see schematic in Figure 4).

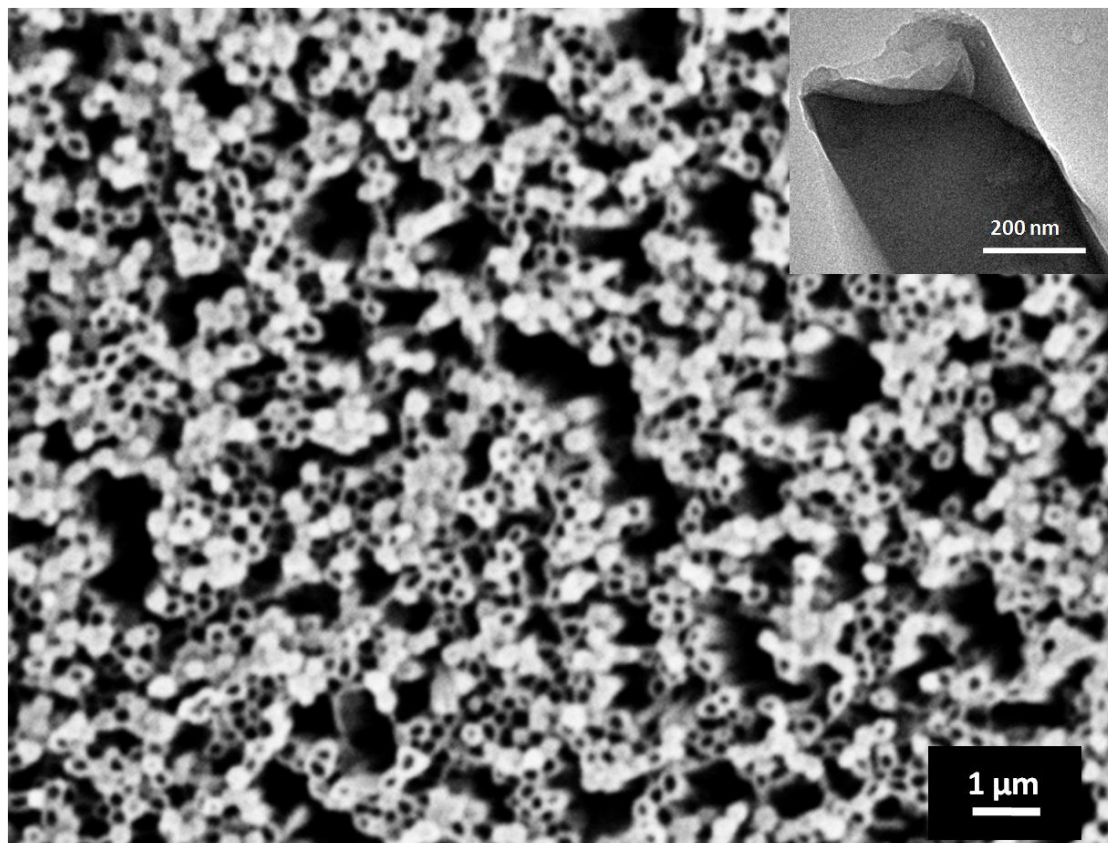


Figure 3: SEM image of the top-view of the CNPs. Inset shows the TEM image of a single nanorod showing a concave tip.

Unlike earlier methods, where amorphous carbon nitride nanotubes were obtained by soaking AAO membrane in excess carbon nitride polymer solution (11), we have used a modified process wherein the precursors were allowed to wet the AAO from one-side. Here, the precursor solution fills the pores of the anodic alumina membrane from one-side by capillary rising. This step was followed by the polymerization of the precursors within the AAO template at 150 °C for 6 h in a Teflon-lined steel autoclave. The polymerized product was then carbonized in a

nitrogen atmosphere at 600 °C for 5 h. This has left a thick slab of carbon nitride on one-side of the membrane over which the pillars were supported.

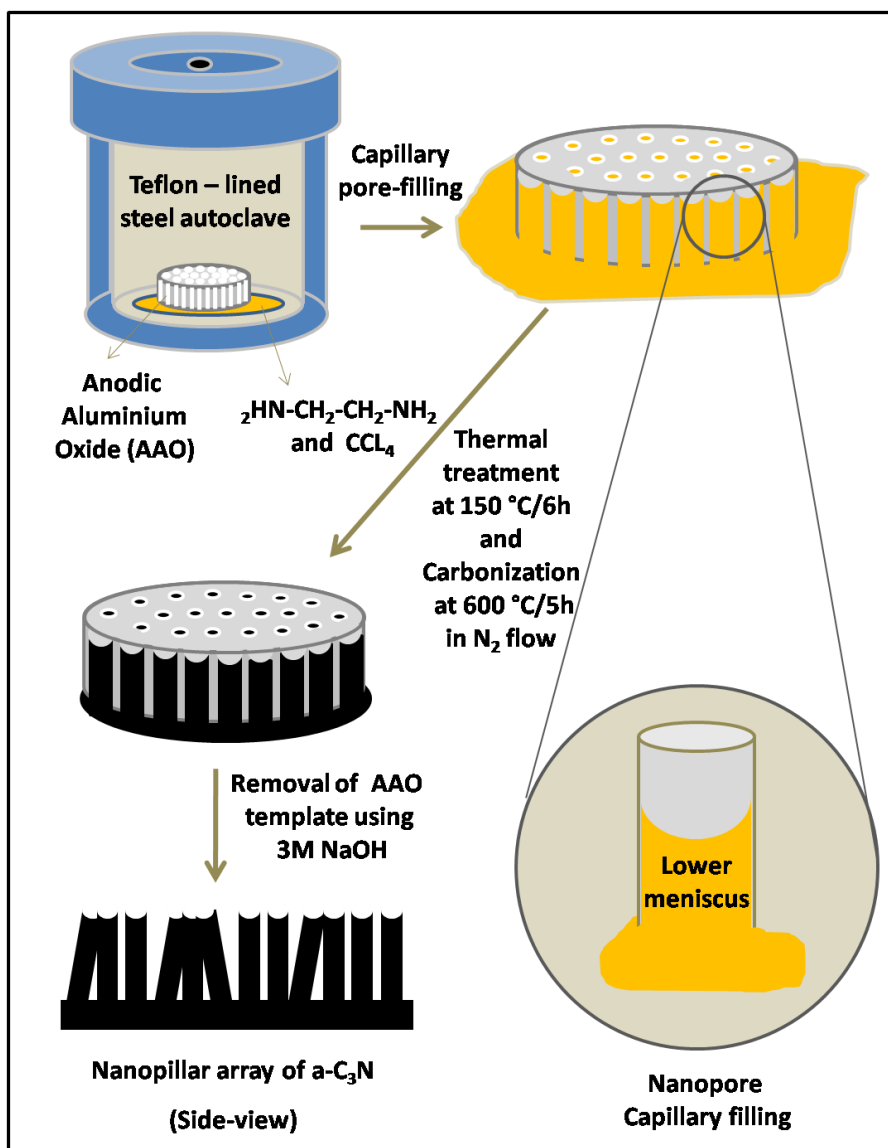


Figure 4: Schematic illustration of the formation process of CNPs

The X-ray diffraction (XRD) pattern of the CNPs shows a broad 2θ peaks at 10.5° and 23.5° respectively (Figure 5a). The former peak is attributed to the formation of a disordered graphitic oxide structure during the alkali treatment to

remove the AAO template. However, this peak disappeared when the sample was reduced with hydrazine hydrate. The latter peak corresponds to 002 reflection of disordered graphitic structure (Figure 5b).

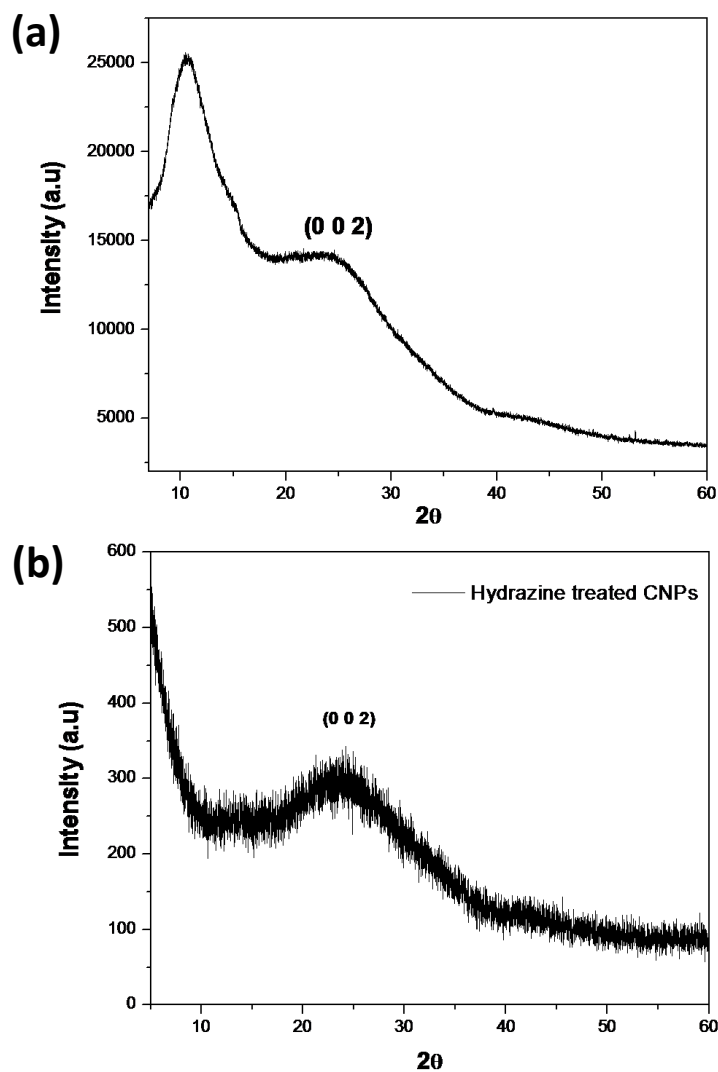


Figure 5: (a) XRD pattern of the CNPs showing the broad 2θ peaks at 10.5° and 23.5° respectively (b) disappearance of the 2θ peak at 10.5° after reducing with hydrazine hydrate.

The Raman spectrum of CNPs shows a broad D-band at 1325 cm^{-1} corresponding to the presence of sp^3 bonded carbon nitride, which is predominantly amorphous in nature (Figure 6). However, a weak G-band at 1569 cm^{-1} shows the presence of sp^2 bonded carbon nitride phases in the amorphous matrix.

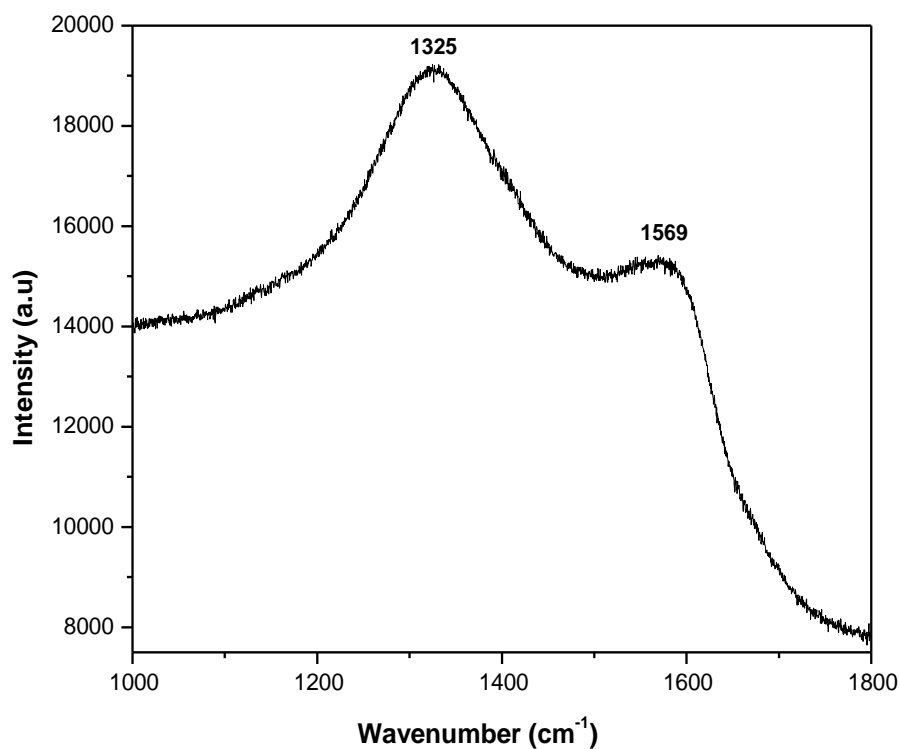


Figure 6: Raman spectrum of the CNPs showing the presence of D-band and G-band.

The carbon (1s) spectrum of the XPS analysis shows a peak around 285 eV which is attributed to the C-C bond (22). The nitrogen (1s) peak around 399 eV is attributed to the C-N bond (Figure 7). The nitrogen to carbon ratio (N/C ratio) of the

as-synthesized CNPs calculated from the XPS analysis shows 7.3% nitrogen content with a composition of $C_{13}N$.

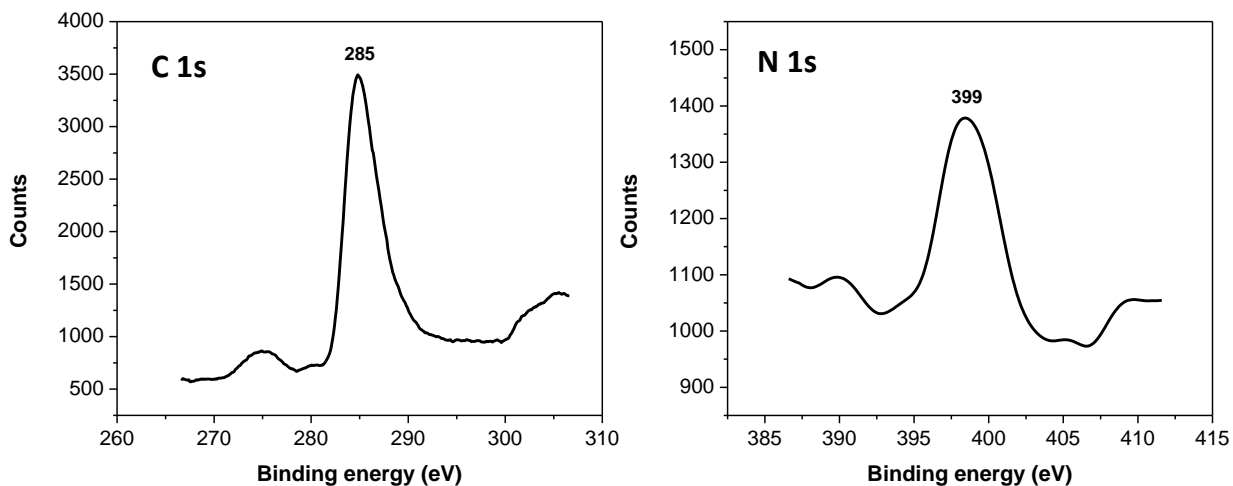


Figure 7: XPS analysis showing the C 1s and N 1s spectra of the CNPs confirming the presence of carbon and nitrogen.

The chemical bonding between the carbon and nitrogen is also analyzed by fourier transform infrared (FT-IR) spectroscopy. The FT-IR spectrum of the CNPs sample shows broad bands corresponding to the stretching and deformation modes of NH_2 group at 3409 cm^{-1} and 1567 cm^{-1} (Figure 8). The doublet at 3409 cm^{-1} (asymmetric) and 3511 cm^{-1} (symmetric) is attributed to the N-H stretch of the primary amines.

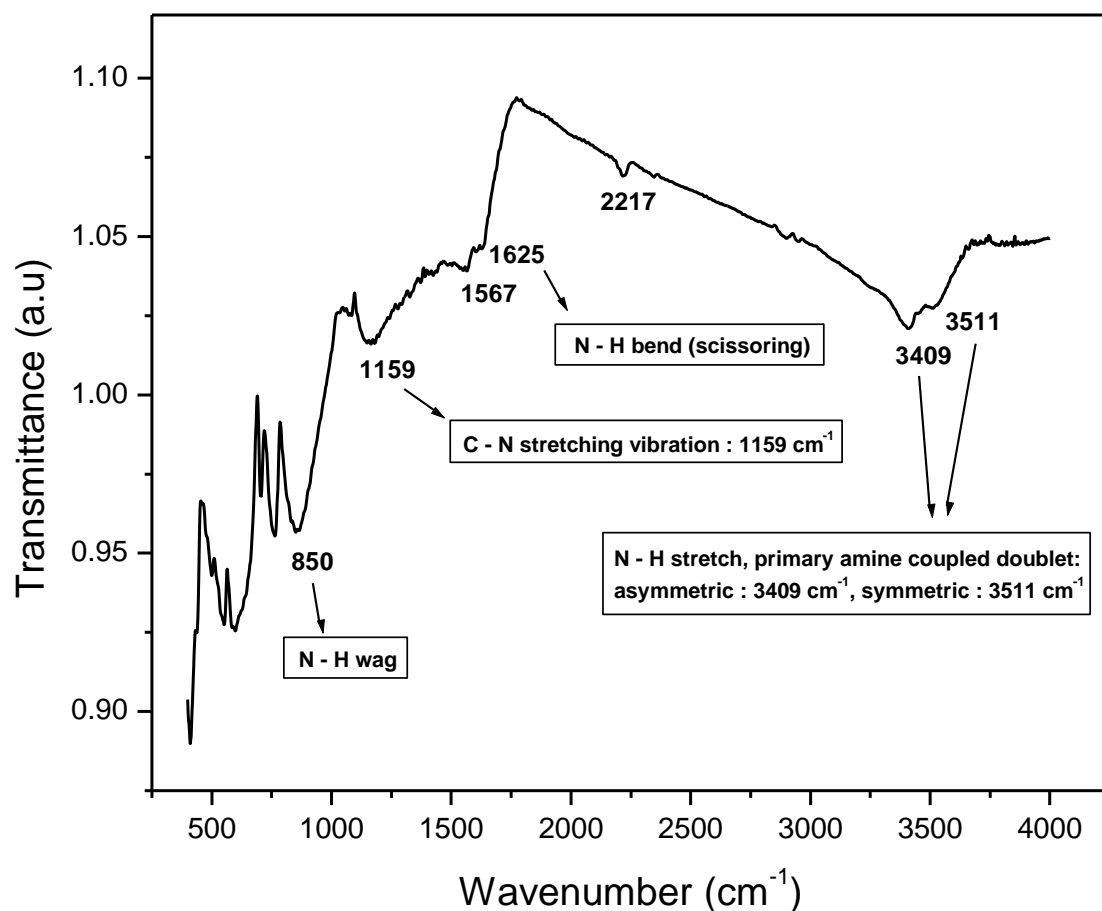


Figure 8: FT-IR spectrum of the CNPs

Nanopillar and nanotube arrays, due to their unique morphology could find application in sensors. For example, carbon nanotube arrays (23) coated with conducting polymers showed a significant increase in selectivity and sensitivity in glucose and H₂O₂ sensing. Similarly, electrodes modified with peptide nanotubes (24) showed a 2.5-fold increase in amperometric response compared with non-modified electrodes. Recently, nitrogen-rich, polymer-like amorphous carbon nitride

films were used in humidity and gas sensors (25). The nanopillar morphology of our CNPs can also be considered as a promising material for various sensor applications. The presence of amine groups on CNPs would enhance their sensor applicability as these amine groups could be used to immobilize nanoparticles and proteins. We have shown that these amine groups help to immobilize Au and Pt nanoparticles and ferritin protein on to the surface of the carbon nitride nanorods (Figure 9). Additionally, the amine groups can also be modified to get hydrophobic surface by interacting them with a long chain alkyl group fatty acid, like oleic acid. Figure 10 shows the schematic of the functionalization process, which is performed by an amidation reaction between oleoyl chloride and carbon nitride nanorods. The resulting functionalized nanorods have a hydrophobic surface which brings them to the oil-water interface in a toluene-water mixture. Figure 11 shows the FESEM image of these nanorods dispersed at the toluene-water interface.

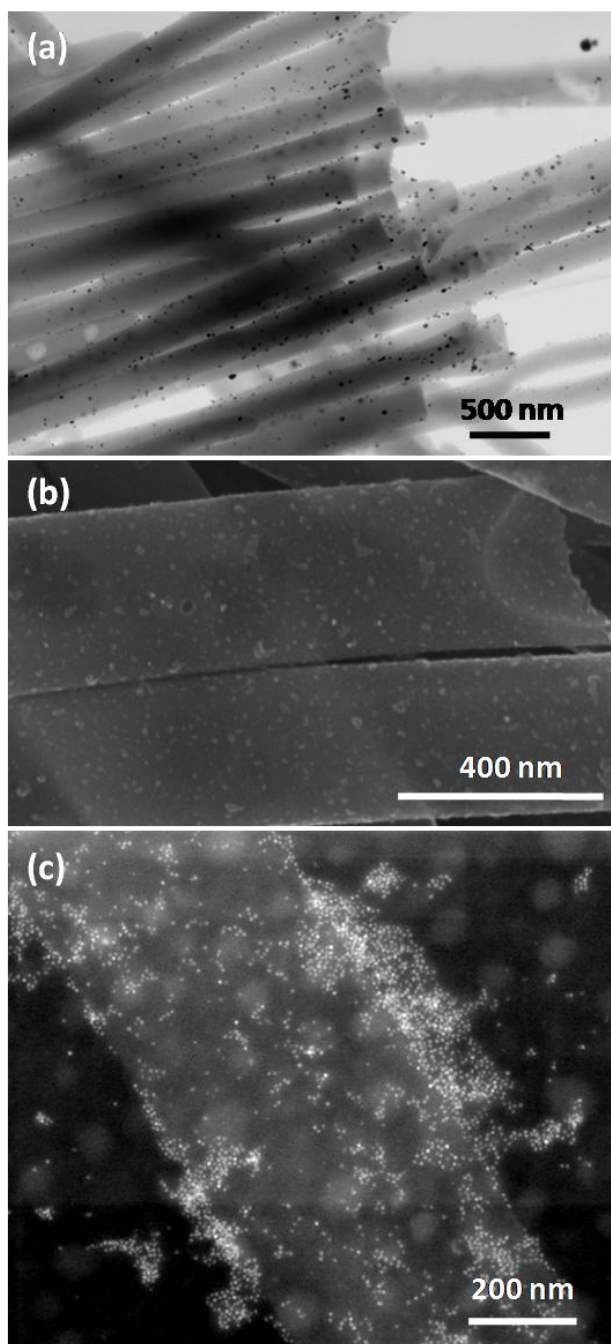


Figure 9: (a) STEM image of Pt nanoparticles, (b) FESEM image of Au nanoparticles, (c) STEM image of ferritin protein, immobilized onto carbon nitride nanorods (~ 5 -10 nm size Fe₂O₃ nanoparticles, co-factors of the ferritin protein are clearly seen).

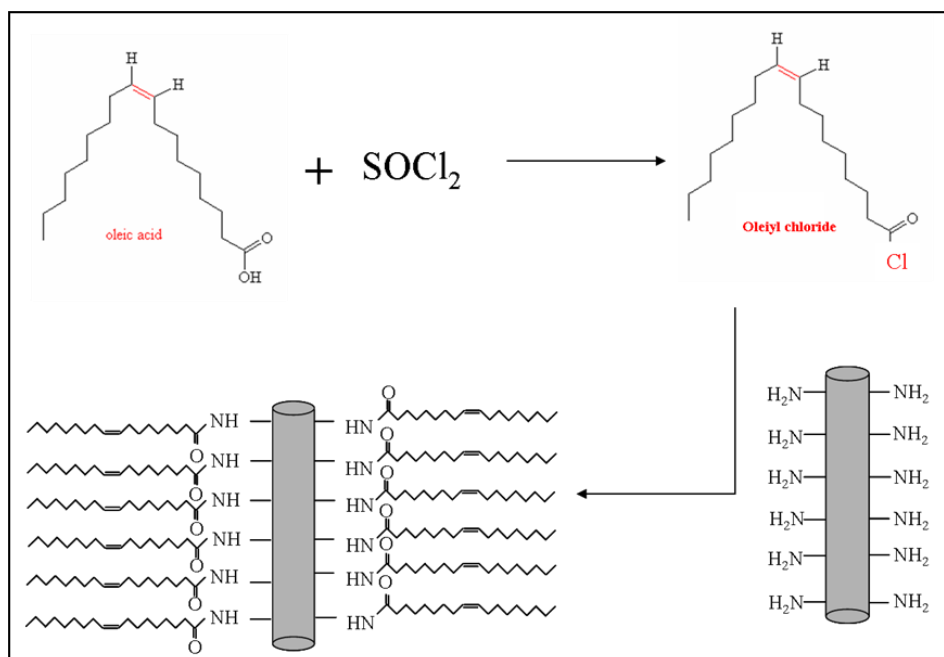


Figure 10: Schematic of the functionalization process of carbon nitride nanorods with oleic acid.

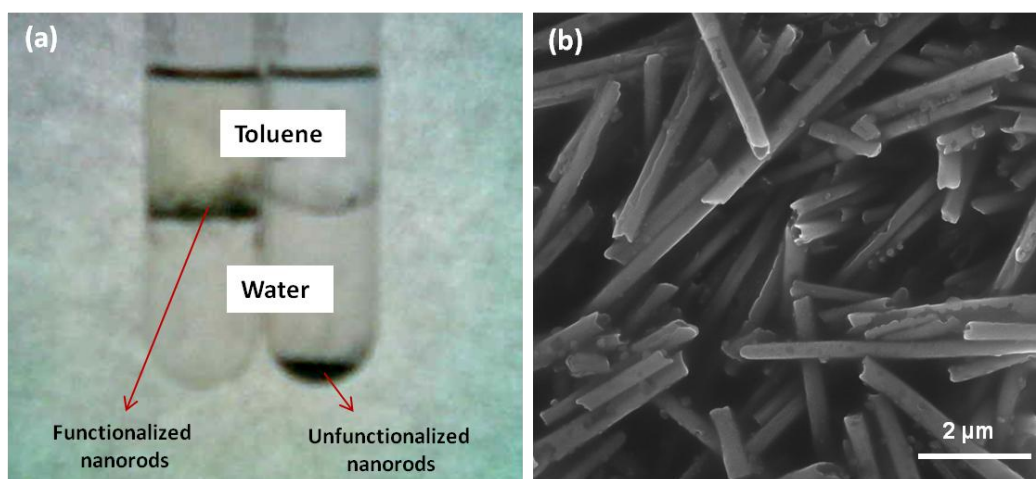


Figure 11: (a) Photograph of the carbon nitride nanorods at the interface of toluene-water mixture after functionalization (b) FESEM image of the oleic acid functionalized nanorods taken from the toluene-water interface.

6.5 Conclusions

In conclusion, this chapter describes the synthesis of amorphous carbon nitride nanopillar arrays (CNPs) using ethylenediamine and carbon tetrachloride as precursors with anodic aluminium oxide (AAO) membrane as a template. The as-synthesised CNPs have surface functional amine groups that were utilized to bind/stabilize gold, platinum nanoparticles and ferritin protein. The amine groups were also exploited for functionalization with long chain organic acids, like oleic acid for changing the hydrophilic nature of the carbon nitride surface so that they can be brought to aqueous-organic interface.

6.6 References

1. E. Kroke and M. Schwarz, *Coord. Chem. Rev.* **2004**, 248, 493.
2. X. Wang, K. Maeda, A. Thomas, K. Takanabe, G. Xin, J. M. Carlsson, K. Domen and M. Antonietti, *Nat. Mater.* **2009**, 8, 76.
3. C. M. Lieber and Z. J. Zhang, *Adv. Mater.* **1994**, 6, 497.
4. X. W. Liu, C. H. Lin, L. T. Chao and H.C. Shih, *Mater. Lett.* **2000**, 44, 304.
5. A. Modinos and J. P. Xanthakis, *Appl. Phys. Lett.* **1998**, 73, 1874.
6. X. W. Liu, S. H. Tsai, L. H. Lee, M. X. Yang, A. C. M. Yang, I. N. Lin and H. C. Shih, *J. Vac. Sci. Technol. B.* **2000**, 18, 1840.
7. A. Y. Liu and M. L. Cohen, *Science* **1989**, 245, 841.

8. J. L. Zimmerman, R. Williams, V. N. Khabashesku, and J. L. Margrave, *Nano Lett.* **2001**, *1*, 731.
9. F. Goettmann, A. Fischer, M. Antonietti and A. Thomas, *Angew. Chem. Int. Ed.* **2006**, *45*, 4467.
10. F. Goettmann, A. Thomas and M. Antonietti, *Angew. Chem. Int. Ed.* **2007**, *46*, 2717.
11. S. W. Bian, Z. Ma and W. G. Song, *J. Phys. Chem. C.* **2009**, *113*, 8668.
12. S. L. Sung, S. H. Tsai, C. H. Tseng, F. K. Chiang, X. W. Liu, and H. C. Shih, *Appl. Phys. Lett.* **1999**, *74*, 197.
13. Q. Guo, Y. Xie, X. Wang, S. Zhang, T. Hou and S. Lv, *Chem. Comm.* **2004**, 26.
14. C. R. Martin, *Science* **1994**, *266*, 1961.
15. A. Z. Jinl, Q. Wang, Y. L. Li, H. F. Yang, J. J. Li, Q. Luo, Z. Cui and C. Z. Gu, *IEEE Xplore* **2006**, 129.
16. Y. D. Wang, S. J. Chua, S. Tripathy, M. S. Sander, P. Chen and C. G. Fonstad, *Appl. Phys. Lett.* **2005**, *86*, 071917.
17. V. Anandan, Y. L. Rao and G. Zhang, *Int. J. Nanomed.* **2006**, *1*, 73.
18. H. Xu, N. Lu, D. Qi, J. Hao, L. Gao, B. Zhang and L. Chi, *Small* **2008**, *4*, 1972.
19. Z. Fan, H. Razavi, J. W. Do, A. Moriwaki, O. Ergen, Y. L. Chueh, P. W. Leu, J. C. Ho, T. Takahashi, L. A. Reichertz, S. Neale, K. Yu, M. Wu, J. W. Ager and A. Javey, *Nat. Mater.* **2009**, *8*, 648.
20. C. Shin, W. Shin and H. G. Hong, *Electrochimica Acta* **2007**, *53*, 720.

21. S. Rahman and H. Yang, *Nano Lett.* **2003**, 3, 439.
22. Y. Qiu and L. Gao, *Chem. Comm.* **2003**, 2378.
23. M. Gao, L. Dai and G. G. Wallace, *Electroanalysis* **2003**, 15, 1089.
24. M. Yemini, M. Reches, J. Rishpon and E. Gazit, *Nano Lett.* **2005**, 5, 183.
25. L. M. Zambov, C. Popov, N. Abedinov, M. F. Plass, W. Kulisch, T. Gotszalk, P. Grabiec, I. W. Rangelow and R. Kassing, *Adv. Mater.* **2000**, 12, 656.